THE UNIVERSITY *of* EDINBURGH

The Dynamics of Hygrotactic Fronts - From Fundamentals of Soft-Matter Systems to Smart Materials Engineering Applications

Hernán Barrio-Zhang

A thesis submitted in fulfillment of the requirements for the degree of Doctor of Philosophy

Institute of Multiscale Thermofluids, School of Engineering
The University of Edinburgh

2022

Abstract of Thesis

THE UNIVERSITY of EDINBURGH

See the Postgraduate Assessment Regulations for Research Degrees: https://www.ed.ac.uk/files/atoms/files/pgr_assessmentregulations.pdf

Name of student:	Hernán Barrio Zhang	UUN	S2130994
University email:			
Degree sought:	Doctor of Philosophy	Estimated number of words in the main text of thesis*:	37000
Title of thesis:	The Dynamics of Hygrotactic Fronts – from Fundamentals of Soft-matter Systems to Smart Materials Engineering Applications		

*The thesis must not exceed a maximum word count of 100,000, or other limit as detailed in the specific regulations detailed in the Degree Regulations and Programmes of Study. In exceptional circumstances, on the recommendation of the supervisor, permission may be granted by the College to exceed the stated length on the ground that such extension is required for adequate treatment of the thesis topic.

Insert the abstract text here - the space will expand as you type.

Tactic behaviour is understood as the ability of a system to sense and respond to external stimuli. This tactic behaviour is present in many complex systems, many of which can be found in nature. Tactic systems are able to sense external stimuli (for example, chemical or temperature gradients) and convert this sensory information into large-scale self-propulsion. This PhD thesis aims to explore a transformative concept for tactic behaviour in soft-matter physics and smart-materials engineering called hygrotaxis, defined as the motion of a droplet on a solid surface caused by the presence of a humidity gradient.

The interactions present in this effect give rise to very small forces. Hence, experiments are carried out on Slippery Omniphobic Covalently Attached Liquid-like (SOCAL) surfaces, a type of ultra-smooth surface which exhibits remarkably low contact angle hysteresis (< 3°). Base studies on the evaporation dynamics of water droplets on ultra-smooth surfaces show that SOCAL was successfully grafted into glass substrates. Studies of the contact angle hysteresis on these surfaces shows there are different friction regimes that make measurement of contact angle hysteresis challenging. Hence, a novel method of characterisation of ultrasmooth surfaces is developed to use the relaxation of interfaces to measure contact angle hysteresis on SOCAL surfaces. The relaxation times obtained in these studies allow for the analysis of the physical mechanisms guiding the motion of the droplet, which depends on the kinematics of the contact line rather than the hydrodynamics.

Lattice Boltzmann simulations are implemented to study the effect of humidity gradients on liquid droplets inside a square channel. Base simulations show that the Lattice Boltzmann algorithm is accurate in modelling the dynamics as predicted by the Cahn-Hilliard equation. Gradients inside the channel are generated by introducing a chemical potential difference in

Document control

If you require this document in an alternative format please email Academic.Services@ed.ac.uk or telephone 0131 651 4990.	Date last revised: 22.11.21

the ambient phase. These simulations show that chemical potential gradients are able to affect the liquid-gas interface, generating surface flows that guide the droplet towards more humid environments.

Based on the findings in this thesis, two experimental approaches are developed to study hygrotaxis. The first approach aims to generate a gradient in relative humidity by placing two droplets of significantly different sizes in close proximity (~0.1mm) in an ambient relative humidity of 10%. The effect observed is a consistent displacement of the centre of mass of the small droplet towards the larger one. Comparisons between experiments and simulation show an overall agreement in the behaviour of the droplet in such configuration. The second approach consists of separating the exposed surface of a small amount water into two different interfaces. This is done by developing a method to coat and characterise the inside of glass capillary tubes with the SOCAL coating. Comparisons between coated and uncoated samples show that SOCAL has been successfully applied, exhibiting contact angle hysteresis measurements of 2.9°±1.9°. Although pinning events are prevalent in SOCAL coated samples, evaporation of 2µL liquid slugs indicate the possible existence of a pressure driven effect which drives the contact line to recede from the humid side rather than the dry one. Even though improvements in the experiments still have to be implemented, these results are motivating and serve a proof of concept for future studies.

The methods and the results presented in this work improve our understanding of the interaction of water droplets, ultra-smooth surfaces and relative humidity gradients.

Lay Summary of Thesis

THE UNIVERSITY of EDINBURGH

Name of student:	Hernán Barrio-Zhang	UUN	S2130994
University email:			
Degree sought:	Doctor of Philosophy	No. of words in the main text of thesis:	37000
Title of thesis:	The Dynamics of Hygrotactic Fronts – from Fundamentals of Soft-matter Systems to Smart Materials Engineering Applications		

Insert the lay summary text here - the space will expand as you type.

The study of the interaction between liquid droplets, solids and their environments forms an essential part of nature and our everyday lives. Examples of the importance of these interactions are numerous in nature, from animals such as ducks, which have developed water repellent feathers, to small desert beetles that use the small bumps on their bodies to gather water from the morning dew in the desert dunes. The advancement in our understanding of these types of interactions has enabled us to manipulate surfaces that allow liquids to slide without resistance, which allows us to create simple commodities such as raincoats to more complex applications such as self-cleaning and antibacterial surfaces.

Over the years, we have taken inspiration from the beginning of life in our planet to try to explain how some of simplest organisms, such as cells, use chemical signals to guide their motion automatically towards sources of food. One can extend the ideas drawn from these systems to liquid droplets that use different spreading and chemical strategies to achieve self-propulsion. As our understanding behind these mechanisms progresses, we are able to develop remarkably effective surfaces that produce spontaneous droplet self-propulsion without the need of supplying an external source of mechanical energy.

In this thesis, I study a special case of self-propulsion named ”Hygrotaxis”, referring to the motion generated by differences in the ambient humidity. The forces involved in this interaction are very small, which is why determining a suitable low friction surface where droplets can overcome static friction becomes a key challenge. Hence, this thesis begins by studying the interaction between water droplets and a low-friction surface named “Slippery Omniphobic Covalently Attached Liquid-like” (SOCAL) surface. This study sheds light on the statics and dynamics of motion of liquids in low friction surfaces such as SOCAL, which requires an exceptionally low force to initiate motion of a liquid droplet but its motion is surprisingly slow. This makes classical ways of quantifying these forces challenging. In this work, a novel method is developed to improve the accuracy of this measurement by using the relaxation of a droplet after it is inflated or deflated. Experiments show that droplets on SOCAL surfaces change their spreading behaviour depending on the ambient humidity, supporting that SOCAL surfaces are a prime candidate in the study of hygrotaxis.

To complement the experimental results, I carry out numerical simulations using the “Lattice Boltzmann Method” to model a droplet evaporating in a humidity gradient. The results show

Document control

K:\AAPS\D-AcademicAdministration\02-CodesOfPractice,Guidelines&Regulations\24-MainReferencesCopiesPolicies\01-Current\Assessment BOE SCC & Feedback\Forms\ThesisLaySummary	
If you require this document in an alternative format please email Academic.Services@ed.ac.uk or telephone 0131 651 4990.	Date last revised: 20.06.19

Lay Summary of Thesis

THE UNIVERSITY of EDINBURGH

that the driving mechanism of hygrotaxis is attributed to the Marangoni effect, the same effect that creates the tears of wine in glass cups.

In the last part of this thesis, I apply the findings from the studies on SOCAL surfaces and the Lattice Boltzmann Method simulations to practical approaches. When a very small droplet is placed next to one over ten times its size, the small one is trapped between the vapour field of the larger one and the ambient humidity, effectively creating a humidity gradient around the small droplet. The results of this experiment show that the small droplet evaporates at a rate much slower than the one predicted by the corresponding ambient humidity, confirming the influence and the generation of a humidity gradient around the droplet. Most significantly, however, under these conditions the centre of mass droplet shows motion towards the larger one, in agreement with the simulations.

To study the effect of confinement, where a small amount of liquid is exposed to differing values of ambient humidity on each side, a method to coat the inside of thin tubes with SOCAL is developed. A small liquid slug is placed in a SOCAL coated thin tube where each end is exposed to high and low ambient humidity, respectively. Although there are still challenges to overcome in the resistance present inside the thin tubes, results show that the liquid edge that recedes is not the dry one as we would expect, but the humid one. This indicates that the relative humidity controlled spreading of liquid inside thin tubes has the potential to induce motion towards regions with low ambient humidity.

The results presented in this thesis expand our understanding of the interaction between ultra-smooth surfaces, such as SOCAL, and liquid droplets. Additionally, the simulation and experimental findings of droplets interacting with humidity gradients serve as proof of concept for hygrotaxis and motivate the continued study into this effect.

Document control

K:\AAPS\D-AcademicAdministration\02-CodesOfPractice,Guidelines&Regulations\24-MainReferencesCopiesPolicies\01-Current\Assessment BOE SCC & Feedback\Forms\ThesisLaySummary	
If you require this document in an alternative format please email Academic.Services@ed.ac.uk or telephone 0131 651 4990.	Date last revised: 20.06.19

Abstract

Tactic behaviour is understood as the ability of a system to sense and respond to external stimuli. This tactic behaviour is present in many complex systems, many of which can be found in nature. Tactic systems are able to sense external stimuli (for example, chemical or temperature gradients) and convert this sensory information into large-scale self-propulsion. This PhD thesis aims to explore a transformative concept for tactic behaviour in soft-matter physics and smart-materials engineering called hygrotaxis, defined as the motion of a droplet on a solid surface caused by the presence of a humidity gradient.

The interactions present in this effect give rise to very small forces. Hence, experiments are carried out on Slippery Omniphobic Covalently Attached Liquid-like (SOCAL) surfaces, a type of ultra-smooth surface which exhibits remarkably low contact angle hysteresis ($< 3^\circ$). Base studies on the evaporation dynamics of water droplets on ultra-smooth surfaces show that SOCAL was successfully grafted into glass substrates. Studies of the contact angle hysteresis on these surfaces shows there are different friction regimes that make measurement of contact angle hysteresis challenging. Hence, a novel method of characterisation of ultra-smooth surfaces is developed to use the relaxation of interfaces to measure contact angle hysteresis on SOCAL surfaces. The relaxation times obtained in these studies allow for the analysis of the physical mechanisms guiding the motion of the droplet, which depends on the kinematics of the contact line rather than the hydrodynamics.

Lattice Boltzmann simulations are implemented to study the effect of humidity gradients on liquid droplets inside a square channel. Base simulations show that the Lattice Boltzmann algorithm is accurate in modelling the dynamics as predicted by the Cahn-Hilliard equation. Gradients inside the channel are generated by introducing a chemical potential difference in the ambient phase. These simulations show that chemical potential gradients are able to affect the liquid-gas interface, generating surface flows that guide the droplet towards more humid environments.

Based on the findings in this thesis, two experimental approaches are developed to study hygrotaxis. The first approach aims to generate a gradient in relative humidity by placing two droplets of significantly different sizes in close proximity ($\sim 0.1\,\mathrm{mm}$) in an ambient relative humidity of 10%. The effect observed is a consistent displacement of the centre of mass of the small droplet towards the larger one. Comparisons between experiments and simulation show an overall agreement in the behaviour of the droplet in such configuration. The second approach consists of separating the exposed surface of a small amount water into two different interfaces. This is done by developing a method to coat and characterise the inside of glass capillary tubes with the SOCAL coating. Comparisons between coated and

uncoated samples show that SOCAL has been successfully applied, exhibiting contact angle hysteresis measurements of $2.9^\circ \pm 1.9^\circ$. Although pinning events are prevalent in SOCAL coated samples, evaporation of $2\,\mu L$ liquid slugs indicate the possible existence of a pressure driven effect which drives the contact line to recede from the humid side rather than the dry one. Even though improvements in the experiments still have to be implemented, these results are motivating and serve a proof of concept for future studies.

The methods and the results presented in this work improve our understanding of the interaction of water droplets, ultra-smooth surfaces and relative humidity gradients.

Lay Summary

The study of the interaction between liquid droplets, solids and their environments forms an essential part of nature and our everyday lives. Examples of the importance of these interactions are numerous in nature, from animals such as ducks, which have developed water repellent feathers, to small desert beetles that use the small bumps on their bodies to gather water from the morning dew in the desert dunes. The advancement in our understanding of these types of interactions has enabled us to manipulate surfaces that allow liquids to slide without resistance, which allows us to create simple commodities such as raincoats to more complex applications such as self-cleaning and antibacterial surfaces.

Over the years, we have taken inspiration from the beginning of life in our planet to try to explain how some of simplest organisms, such as cells, use chemical signals to guide their motion automatically towards sources of food. One can extend the ideas drawn from these systems to liquid droplets that use different spreading and chemical strategies to achieve self-propulsion. As our understanding behind these mechanisms progresses, we are able to develop remarkably effective surfaces that produce spontaneous droplet self-propulsion without the need of supplying an external source of mechanical energy.

In this thesis, I study a special case of self-propulsion named ”Hygrotaxis”, referring to the motion generated by differences in the ambient humidity. The forces involved in this interaction are very small, which is why determining a suitable low friction surface where droplets can overcome static friction becomes a key challenge. Hence, this thesis begins by studying the interaction between water droplets and a low-friction surface named “Slippery Omniphobic Covalently Attached Liquid-like” (SOCAL) surface. This study sheds light on the statics and dynamics of motion of liquids in low friction surfaces such as SOCAL, which requires an exceptionally low force to initiate motion of a liquid droplet but its motion is surprisingly slow. This makes classical ways of quantifying these forces challenging. In this work, a novel method is developed to improve the accuracy of this measurement by using the relaxation of a droplet after it is inflated or deflated. Experiments show that droplets on SOCAL surfaces change their spreading behaviour depending on the ambient humidity, supporting that SOCAL surfaces are a prime candidate in the study of hygrotaxis.

To complement the experimental results, I carry out numerical simulations using the “Lattice Boltzmann Method” to model a droplet evaporating in a humidity gradient. The results show that the driving mechanism of hygrotaxis is attributed to the Marangoni effect, the same effect that creates the tears of wine in glass cups.

In the last part of this thesis, I apply the findings from the studies on SOCAL surfaces and the Lattice Boltzmann Method simulations to practical approaches. When a very small droplet is placed next to one over ten times its size, the small one is trapped between the vapour field of the larger one and the ambient humidity, effectively creating a humidity gradient around the small droplet. The results of this experiment show that the small droplet evaporates at a rate much slower than the one predicted by the corresponding ambient humidity, confirming the influence and the generation of a humidity gradient around the droplet. Most significantly, however, under these conditions the centre of mass droplet shows motion towards the larger one, in agreement with the simulations.

To study the effect of confinement, where a small amount of liquid is exposed to differing values of ambient humidity on each side, a method to coat the inside of thin tubes with SOCAL is developed. A small liquid slug is placed in a SOCAL coated thin tube where each end is exposed to high and low ambient humidity, respectively. Although there are still challenges to overcome in the resistance present inside the thin tubes, results show that the liquid edge that recedes is not the dry one as we would expect, but the humid one. This indicates that the relative humidity controlled spreading of liquid inside thin tubes has the potential to induce motion towards regions with low ambient humidity.

The results presented in this thesis expand our understanding of the interaction between ultra-smooth surfaces, such as SOCAL, and liquid droplets. Additionally, the simulation and experimental findings of droplets interacting with humidity gradients serve as proof of concept for hygrotaxis and motivate the continued study into this effect.

Acknowledgements

I would like to express my deepest gratitude to my principal supervisor Dr. Rodrigo Ledesma-Aguilar and co-supervisors Dr. Gary G. Wells and Dr. Daniel Orejon for their unending support and guidance throughout my PhD, the pandemic and this process. I would also like to extend this gratitude to Dr. Élfego Ruiz-Gutiérrez for his continuous support, precious advice and invaluable discussions. Their extensive experimental and theoretical knowledge provided essential contributions towards this project and my own development as a researcher.

I would like to thank the University of Edinburgh and Northumbria University for providing me with so much support in what has been an unexpected pandemic. Additionally, I would like to thank these Institutions for providing me with the scholarship and the facilities to carry out my research, and for enabling me to attend and present my research in conferences and academic meetings.

I would like to express my sincere gratitude to colleagues and friends made during this PhD: Dr. Steven Armstrong, Dr. Prashant Agrawal, Dr. Bethany Orme, Dr. Dominka Zabiegaj, Dr. Gaby Launay, Dr. Neeru Bala, Manish Yadav, Preeti Singh, Balaji Aresh, old and new friends for their collaborations, friendship and support which have made this PhD so much more enjoyable and interesting.

I would also like to thank Prof. Aurora Hernandez Machado for helping start my interest in this field and Prof. Glen McHale for his valuable insight and support.

Last, but certainly not least, I owe a special thanks to my parents (Rafael and Limei), my brothers (Férmin and Andres), my family and my friends for their continuous love and support through the best, the uneventful and the difficult times.

Declaration

I declare that this thesis was composed by myself, that the work contained herein is my own except where explicitly stated otherwise in the text, and that this work has not been submitted for any other degree or professional qualification except as specified.

Hernán Barrio-Zhang

Contents

Figures and Tables

Figures

Tables

Acronyms

CC Condensation-Condensation. 91
CCA Constant Contact Angle. 24–26, 64–66, 77, 110, 112, 113, 115, 128
CCR Constant Contact Radius. 23–25, 77
CE Condensation-Evaporation. 91
CFD Computational fluid dynamics. 33

DI De-ionised. 42, 45–48, 56, 65, 71, 112, 118, 120
DMDS dimethyldimethoxysilane. 43, 44, 46, 61, 63
DSA Droplet Shape Analyser. 58

EC Evaporation-Condensation. 91, 98, 103
ECEQ Evaporation-Condensation at Equilibrium. 98
EE Evaporation-Evaporation. 91, 110
EQC Equilbrium-Condensation. 98
EQE Equilibrium-Evaporation. 94, 98

ID Inner Diameter. 46, 47, 117, 119, 120, 125
IPA Isopropyl Alcohol. 42–48, 61

LIS Liquid Infused Surfaces. 19, 20, 51, 63

MKT Molecular Kinetic Theory. 17, 64, 69, 70, 79, 128

OD Outer Diameter. 47, 109, 120
OH Oxygen-Hydrogen. 44, 46, 47, 61
OpenCV Open Source Computer Vision Library. 58

PDMS Polydimethylsiloxane. 20, 43, 45, 46, 61
PyDSA Python Droplet Shape Analyzer. 58, 61, 71, 109

RH Relative Humidity. 26, 46, 74

SEM Scanning Electron Microscopy. 47
SLIP Slippery Liquid Infused Porous. 19, 20, 25, 26, 39, 63
SOCAL Slippery Omniphobic Covalently Attached Liquid. 2–4, 20, 26, 40–48, 50–52, 54, 56, 61–65, 70, 71, 73, 75, 77, 79–81, 108, 109, 114, 117–122, 125, 127, 128, 130, 131

Nomenclature

α	Sliding angle
χ	Wetting potential
$\Delta\theta$	Contact angle hysteresis
$\delta\theta$	Deformation angle
$\Delta\theta_0$	Amplitude of relaxation
$\dot{q}$	Flow-rate
η	Dynamic viscosity
γ	Liquid-Gas surface tension
γ_0	Liquid-Gas surface tension at equilibrium
γ_{sl}	Solid-Liquid surface tension.
γ_{sv}	Solid-Vapour surface tension.
κ^{-1}	Capillary length
$\mathscr{F}$	Helmholtz free energy
g	Gravitational acceleration
μ	Chemical potential
μ_0	Equilibrium chemical potential
ω	Correction constant contact angle relaxation
ϕ	Order parameter or Phase field
ϕ_s	Surface fraction
Π	Total pressure
ψ	Free energy density
ρ	Density
τ	Relaxation time
τ_{CV}	Cox-Voinov relaxation time
τ_{MKT}	MKT relaxation time
P	Capillary pressure
θ_A	Advancing contact angle
θ_l	Left contact angle
θ_m	Mean contact angle
θ_R	Receding contact angle
θ_r	Right contact angle
θ_S	Static contact angle
θ_∞	Asymptotic contact angle
θ_e	Young's equilibrium contact angle
θ_{mic}	Microscopic contact angle

θ_{tilt}	Tilting angle
ϑ	Kinematic viscosity
Ξ	Collision operator
ξ	Intermolecular distance
ζ	Binding energy
A	Area
c_q	Lattice velocities
c_s	Speed of sound in the system
D	Diffusion constant
F	Force
F_D	Driving force
f_q	Distribution function
f_{cap}	Capillary force
$F_{pinning}$	Pinning force
J	Mass flux
K_0	Adsorption-desorption frequency
L	Length
l	Interface thickness
l_m	Microscopic length
L_x	Channel length
L_y	Channel height
Ma	Marangoni number
N	Number of particles
p	Pressure
p	pressure
Pe	Péclet number
R	Spherical Radius
r	Base radius
r_w	Roughness factor
RH	Relative humidity
S	Spreading parameter
s	Arclength
$S*$	Entropy
S_q	Sources term
T	Temperature
t	Time
u	Flow velocity
u_c	Characteristic velocity
u_{cm}	Velocity of the centre of mass

V	Volume
v	Contact line velocity
v_d	Velocity of the centre of the droplet

Chapter 1

Introduction

Capillarity and wetting is the study of the interaction of the interfaces of multiple immiscible fluids and their behaviour on solid surfaces [5]. These type of phenomena have come to form a integral part of our lives and the natural world. From the capillary forces involved in the transport of water inside the tallest of trees to the water repellent aspects of a raincoat on a rainy day, this field offers fundamental understanding of science and moves technology forward [6, 7].

Over the years, special interest in the accurate control and manipulation of droplets in small scales has been developed due to their potential applications in the food industry, heat transfer systems, medicine, water harvesting and fundamental science [7, 8]. This interest has been enhanced by the advancement in the ability to manipulate the chemistry and the topography of surfaces which enable the precise control of wetting behaviour of liquid droplets on them [9]. Additionally, research into surface engineering has allowed for the development of solid surfaces that exhibit remarkably low friction to the motion of droplets [2]. When the scale of the droplet is below the influence of external forces, such as gravity, and surface interactions are reduced to quasi-ideal interactions, molecular forces like surface tension become dominant in the behaviour of the droplet. This allows the study of the forces generated by changes in the surface energy between the solid-liquid and the liquid-gas interface to induce self-propulsion of droplets on surfaces. This type of surface tension driven motion can be described as tactic behaviour of liquid. Examples of self-propulsion of droplets can be seen in effects such as *chemotaxis*, the motion induced by chemical gradient stimuli [10, 11], *magnetotaxis*, the motion generated by electromagnetic gradients in magnetic sensitive droplets [12], *durotaxis*, the motion induced by surface rigidity gradients [13], and Marangoni driven motion generated by the difference in surface tension between binary mixtures [14, 15].

In this thesis, focus is directed to an effect named in this work as *Hygrotaxis*. This effect is defined as droplet self-propulsion generated by relative humidity gradients, also referred to as vapour gradients, in the ambient phase of the same species as the liquid droplet. In the literature, there are reports that show that vapour gradients can induce motion of droplets on surfaces generated by surface tension differences which induce Marangoni flows that drive the motion of the droplet [7, 15, 16]. However, this type of vapour driven motion has only

been achieved through high surface energy interactions caused by significant surface tension differences in binary mixtures of liquids of different surface tensions [15–18]. The novelty of hygrotaxis lies in the potential motion produced by surface tension changes generated by the effects induced by a vapour field of the same species as the liquid droplet. Since the forces generated by these interactions are normally smaller than the forces needed to overcome the lateral resistance of the surface, ultra-smooth surfaces offer great potential to study this type of systems. Hence, this thesis studies the effect of relative humidity gradients on water droplets on a novel ultra smooth surface called Slippery Omniphobic Convalently Attached Liquid-like (SOCAL) surface. This type of motion has the potential to be used in optimization of heat trasfer systems via the easy shedding of droplets from cooling surfaces and for water harvesting systems.

This thesis starts by providing a general overview of the key concepts and relevant literature necessary to approach this problem. A section devoted to wetting an capillarity reviews concepts such as surface tension, the force that originates from the cohesive nature of molecular interactions, which plays a key role in the study of droplets. These forces give rise to effects such as droplet spreading and explains the origin of the concepts of inner pressure in liquids and capillary effects stemming from the fundamental forces of surface tension. Another aspect that determines the behaviour of liquid droplets on surfaces is the effect of surface chemical and topographical heterogeneity in the lateral motion of droplets. The origins of these resistive forces is discussed, and strategies to overcome these resistive effects are presented.

An important consequence of relative humidity gradients is the phase change produced by the constant thermodynamic exchange of liquid molecules between the ambient and the liquid phases. A review on the theory of phase transitions is provided which looks into diffusion limited evaporation, evaporation driven contact line behaviour on rough and smooth surfaces, and phase transition approximations. An overview of the Lattice Boltzmann Method is presented, giving a general description into how problems are approached using this numerical solver for computational fluid dynamics. Chapter 2 finishes with an overview of the known mechanisms of self-propulsion of droplets on solid surfaces, which focus on wettability gradients and surface tension gradients as driving forces in this motion.

Chapter 3 presents the materials, methods and experimental techniques used throughout this study. Substrate cleaning procedures are outlined and a humidity chamber is built to control the relative humidity conditions in surface production. The procedure to create Slippery Omniphobic Covalently Attached Liquid (SOCAL) surfaces is detailed, where an acid-catalyzed chemical reaction induces the deposition of nanometric polymer chains on the surface, leaving an ultra-smooth coating. In order to characterise friction on surfaces, contact angle hysteresis, $\Delta\theta$, measurements based on the wettability of droplets on solid surfaces are done by determining the advancing, θ_a, and receding, θ_r, contact angles. Hence, relevant

surface characterisation techniques are presented in detail, where the focus is directed to the characterisation using the volumetric changes and tilting of a surface induce the motion of droplets. Initial measurements using the volumetric variation method shows contact angle hysteresis measurements are comparable to those reported in literature.

A fundamental aspect of contact angle hysteresis measurements is the ability to obtain morphological parameters of the droplet from images or video recordings. The fundamental parameters that need to be acquired for this study are the contact angle measurements at the contact points of the droplet and measurements of the base radius of the droplet. Hence, a description into the imaging processing techniques is done focused on the fitting of the contour of the droplet and interpolation techniques to measure these key parameters.

Chapter 4 presents a study of the static and dynamic friction on SOCAL surfaces. Evaporation experiments are performed on SOCAL surfaces which show constant contact angle evaporation, reflecting high surface homogeneity, comparable to results reported in the literature. Contact line friction on SOCAL surfaces presents unique behaviour when compared to other low hysteresis surfaces. While they exhibit very low contact angle hysteresis ($\sim 2^\circ$), the contact line on these surfaces moves much slower than on superhygdrophobic or lubricated surfaces. This behaviour can be appreciated in the onset of motion of the contact line, where the base radius of the droplet undergoes a smooth transition from static to dynamic configurations. This behaviour negatively impacts current surface characterisation techniques based on the measurement of contact line motion and it is shown that this behaviour translates to errors that are of the same order of the contact angle hysteresis measurement itself. To provide more accurate measurements on contact angle hysteresis on SOCAL surfaces, a new method is developed by observing the relaxation to equilibrium of a relaxing contact line. An exponential fit to this relaxation allows for the asymptotic measurement of the advancing and receding contact angles, resulting in a more robust and accurate measurement of contact angle hysteresis on SOCAL surfaces in high relative humidity environments. The fitting parameters of this method are then used to obtain experimental relaxation times which are compared to the hydrodynamic theory [19], based on viscous stresses and surface tension, and the Molecular Kinetic Theory (MKT) [20] based on the kinematic attributes of the contact line. The results shows that contact line of water droplets on SOCAL surfaces follow the prediction set by the MKT more accurately, highlighting the importance of the surface morphology for moving contact lines. This provides insight into the motion mechanism of liquids on SOCAL surfaces, providing an explanation as to why SOCAL surfaces exhibit such relationship between static and dynamic configurations.

The Lattice Boltzmann Method is used in Chapter 5 to simulate a 2D droplet undergoing phase transition in different chemical potential gradients. To ensure that the Lattice Boltzmann Method was modelling phase transition correctly, benchmarking simulations are done for a droplet evaporating on a solid surface. The results show agreement between the theory and

the simulations, confirming their accuracy. Then, simulations are done in a confined domain which emulates a droplet in a small square channel exposed to different chemical potential gradients. The gradients explored are a combination of chemical potential which induce the differential evaporation or condensation of liquid fronts. In this chemical potential regimes, motion of the centre of mass of the droplet is observed in all cases, with the most prominent motion located in the regimes the condensing and evaporating fronts are combined. Analysis of the velocity fields and surface tension values at the interface of the droplet shows that a surface gradient generates flows inside the droplet that enable it to move towards regions of higher values of chemical potential. A comparison of the advective and diffusive transport rates shows that the motions of the droplet is indeed caused by a driving force coming from advective motion rather than diffusive one, as is the case for differential evaporation. Thereby confirming that under a chemical potential gradient, hygrotaxis is possible. Additionally, studies done at varying viscosities show that this effect is not significantly affected since the translation of the droplet is not affected. However, there are significant effects on the lifetime of moving droplets when the thickness of the channel is changed, where the rectification of the flux field around the droplet limits the rate of evaporation while keeping the surface tension effect active and allowing for longer self-propulsion of droplets.

Chapter 6 is focused on preliminary experimental approaches to expose the interface of a small body of liquid to a difference in relative humidity. The first approach is a case similar to the ones done in the simulations, where a small droplet ($\sim 0.08\,\mu\text{L}$) is left to evaporate at a relative humidity of 10% near a larger one, effectively creating a relative humidity gradient around the small droplet. Although more experiments are needed, the results of these experiments are motivating since displacement of the centre of mass of the droplet is observed in all experimental trials. Initial comparisons between experiments and simulations show a similar trend to a droplet evaporating in a regime where there are different rates of evaporation on each side.

The second experimental approach in this chapter focuses on separating the interface of a small body of water into two interfaces exposed to different values of relative humidity. To achieve this, a method to coat the inside of thin capillary tubes (inner diameter = $\sim 1\,\text{mm}$) is developed. To characterise the samples made, a surface characterisation method based on the contact angle relaxation method and capillary action laws are used to determine the contact angle hysteresis inside the tubes. The contact angle measurements show contact angle hysteresis values similar to those measured in flat substrates. An experiment to expose both ends of the SOCAL capillary tubes is designed by creating a dry reservoir using silica beads which drive the relative humidity down to $< 5\%$ on one side of the tube and exposing the other end to the environmental humidity chamber set to a relative humidity of 94%. Experiments showed that there was significant presence of pinning during the evaporation of the liquid inside the capillary tubes. However, when pinning did not present an issue, the liquid

slug inside the capillary tube preferentially evaporates on the humid side rather than the dry side, which is unexpected. Such results suggest to the possibility of a Laplace pressure driven effect stopping the dry contact line from receding. Although more experiments are needed to confirm these effects, Chapter 6 serves as a base study to continue researching hygrotaxis in the future.

Finally, a general summary and reflection on future work is provided in Chapter 7.

Chapter 2

Theoretical framework and literature review

This chapter explores the relevant theoretical framework for the work presented in this thesis in order to provide a basis for the research of hygrotactic fronts. The topics in this section are the theory of wetting and capillarity, the origin and characterization of contact line friction, the evaporation mechanics on surfaces of liquid droplets, multiphase fluid, the Lattice Boltzmann method and approaches to tactic phenomena.

Wetting and capillarity play a fundamental part in interfacial fluid mechanics, particularly in the research of droplets, their interactions with solids and the forces driving the behaviour of the droplets. How a liquid moves on the surface is dictated by the properties of the liquid-solid interaction. These interfacial interactions have significant implications and consequences in the mechanics of a fluid, paving the way to concepts such as surface tension, capillary action, contact line friction and even influence the dynamics of evaporation and condensation of a droplet on a solid surface.

2.1 Hygrotaxis

Tactic behaviour, the ability of a system to sense and respond to external stimuli, underpins the dynamics of many complex systems, for instance in biology. Biological tactic behaviour consists of (i) an ability to sense external stimuli (e.g., concentration or temperature gradients), and (ii) a transducing mechanism to convert sensory information into large-scale motion. Bio-tactic mechanisms can increasingly inform developments in smart-materials science, from artificial swimmers [14] inspired by bacterial magnetotaxis [12] to self-propelling droplets on surfaces with rigidity gradients [13] motivated by cell durotaxis [21].

Hygrotaxis is defined as the motion caused by the presence of a humidity gradient, where evaporating or condensing liquid fronts on low-friction surfaces are capable of transducing humidity gradients into large-scale motion.

To understand hygrotaxis, one must look at key concepts governing liquid behaviour, particularly at small scales. Droplets which are smaller than the “capillary length" overcome gravitational forces, leaving interfacial interactions as the most prominent forces ruling droplet behaviour, which is why understanding wetting, capillarity and evaporation phenomena become of special importance.

Understanding wetting and capillarity, for both liquids and surfaces, enables us to explain phenomena such as why water spreads easily on glass but not on plastic. By using changes in chemistry and topography, one can create surfaces to “control" this effect, for instance, by turning a non-wettable solid into a wettable one, and viceversa.

Wetting, as a research area, refers to the study of how a liquid deposited on a substrate (solid or liquid) spreads out [5]. It has important academic and practical applications, for example, in the chemical industry, the food industry, soil science, inflation of lungs and sap rise in plants [5, 22]. Surfaces are crucial in this study since both chemical and physical properties of the surface dictate the way a given substance will behave on it, if it will spread, pin or slide on it.

Finally, evaporation is not only of great relevance in fundamental terms but also offers a wide range of applications today that range from pesticide spraying, DNA microarray analysis, ink jet printing and many more [23]. It is a phenomenon that we see everyday, from starting the day with a hot shower or looking at the cloud spotted skies. Evaporation occurs due to the difference in saturation of liquid molecules around the liquid’s body [24]. A liquid loses molecules to collisions and inner pressure which allow particles to go beyond the interface of the droplet and join the less saturated environment [25].

All of these concepts and phenomena will play a key role in the observation and studying of an effect such as hygrotaxis and, conceivably, explain the underlying mechanisms in this phenomenon.

2.2 Wetting and capillarity

Consider a liquid coming in contact with a solid surface. Experience tells us that the liquid will spread on the surface. However, not all liquids spread in the same way, some will spread into a film, similar to when water is immediately absorbed by the soil in our plant pots, and others will spread into puddles or droplets, like when rain falls on our raincoats. The reason liquids spread on surfaces is strongly linked to the intermolecular interactions between the interfaces and the degree of spreading is known as wetting.

Studying and manipulating this phenomenon provides us with fundamental understanding of the physics of interfaces and comes at the benefit of many industrial applications, making this topic particularly significant and relevant to our every day lives [26]. Some of the most prominent applications of this field of study include inkjet printing [27], heat transfer [28] and oil recovery [29]. Recent advances in the understanding of wetting have allowed the creation wetting systems that use capillarity effects to achieve self propulsion of droplets such as vapour driven motion of droplets [15] and rigidity gradient driven motion droplets [30–32].

2.2.1 Surface tension

A key concept involving interfacial interactions between substances is a physical quantity known as surface tension. All condensed matter, regardless of what state of matter they are in (liquid, solid or gas), are formed by an agglomeration of molecules or particles. The state of matter is determined by the degree of movement of particles, regulated by the cohesive forces keeping them together.

These forces at molecular level help keep the individual molecules together [33] and are the reason why surface tension exists. A good way to envision surface tension is by imagining a liquid droplet suspended in the air, similar to Figure 2.1. The liquid forming the droplet is an arrangement of condensed molecules held together by cohesive forces, mainly weak forces of the Van der Waals type [5]. The droplet's surface is similar to a stretched membrane that interacts with the surrounding environment. Inside this membrane, the liquid molecules are in a minimum state of energy since the cohesive forces affecting them are cancelled in every direction, as can be seen in Figure 2.1(a). At the membrane, however, molecules face an unfavourable energy state since the amount of cohesive forces holding them together is roughly halved, this forces the molecules to minimize the surface area of the interface. This imbalance of forces at the surface drives the liquid to deform into the shape that is most effective in reducing the surface area, a sphere.

Surface tension, denoted as γ, is formally defined as the energy that must be supplied in order to increase the surface area by one unit [5, 33]. From this definition, at a constant value of temperature, volume and number of molecules, one can link the increase in surface area (A) to the free energy (F) as:

$$\gamma = \left[\frac{\delta F}{\delta A}\right]_{T,V,n}, \tag{2.1}$$

where T is the temperature, V is the volume and n is the number of molecules. This quantity reflects the energy it takes for a substance to adopt a certain shape and can also be referred to as the free surface energy or a force per unit length at which one phase opposes the other. As an example, the surface tension of water surrounded by air at $25^{\circ}\mathrm{C}$ is $72.8\,\mathrm{mNm}^{-1}$.

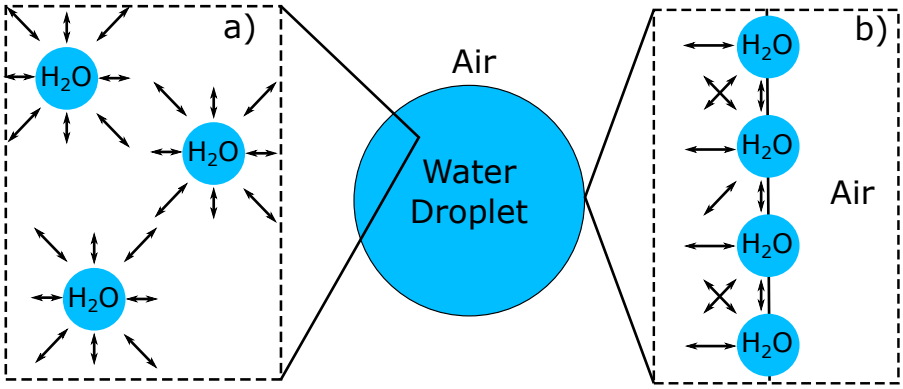

Figure 2.1: Molecules in and out of equilibrium. Schematic showing the attractive forces that water particles experience at a molecular level. Inside the bulk (a) of the liquid, the molecules are in a stable state due to the attractive forces cancelling each other but at the interface (b) there is at an imbalance of these forces, generating the tension force known as surface tension.

2.2.2 Laplace pressure

If we look at Figure 2.1(b) and localize a single molecule at the surface of the liquid, then there is a net force normal to the surface due to the imbalance on forces located there, which induces an overpressure known as the Laplace pressure [5]. In the case of our water droplet suspended in the air, since the shape is not changing then the total work done on the surface is zero, hence,

$$\delta W = p_w dV_w - p_a dV_a + \gamma dA = 0, \tag{2.2}$$

where p_w is the pressure inside the water droplet, p_a is the pressure exerted by the air, V_w is the volume of the water droplet, V_a is the air volume and γ is the surface tension of the water/air interface. Expressing equation 2.2 in terms of the radius of the droplet, R, allows us to obtain the following expression for the laplace pressure for spherical droplets [5],

$$\Delta p = p_w - p_a = 2\frac{\gamma}{R}. \tag{2.3}$$

This equation can be generalized to any shape by taking a infinitesimally small displacement, dR, leaving us to Laplace's law which says that the increase in hydrostatic pressure, Δp, which occurs upon traversing the boundary between two fluids is equal to the product of the surface tension γ and the curvature of the surface $C = \frac{1}{R} + \frac{1}{R'}$ [5]:

$$\Delta p = \gamma\left(\frac{1}{R} + \frac{1}{R'}\right) = \gamma C, \tag{2.4}$$

where R and R' are the main radii of curvature of the surface.

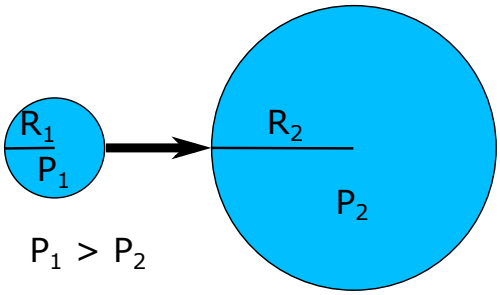

Figure 2.2: Radius dependent Laplace pressure. A droplet with a smaller spherical radius, R_1, has a larger pressure P_1 than the P_2 which has a larger radius. Leading the smaller droplet to coalesce with the larger one.

The Laplace pressure has a variety of consequences, for instance, it is the reason why small droplets will always merge towards bigger droplets since the overall pressure inside the small droplet is greater than the pressure inside the bigger droplet as can be appreciated in Figure 2.2. It is also explains why smaller droplets evaporate more rapidly than larger ones, as happens when using aerosols [5], and why capillary bridges can form strong adhesion, for instance when hair clumps together when wet or when wet sand can be shaped into sand-castles at the beach.

2.2.3 Spreading Coefficient

Currently, all of the concepts reviewed have assumed that the only relevant forces stem from the interaction of the molecules in the liquid and gaseous phases. Consider a droplet of a constant volume similar to the one shown in Figure 2.3, when we place the droplet on a thoroughly cleaned piece of glass, the droplet spreads into a thin film. On the other hand, if the same droplet is placed on a piece of plastic, we see that it beads up into a spherical cap. This shows that there are two extremes of a liquid spreading over surface which are regulated by the interaction of the free surface energies of the interfaces. The parameter that distinguishes them is known as the spreading coefficient, denoted by S. This parameter measures the difference between the surface tension of the solid substrate when dry and wet. According to the spreading parameter, the difference between the energy per unit area between the wet and dry states states is expressed as

$$S = \gamma_{SG} - (\gamma_{SL} + \gamma), \tag{2.5}$$

where γ_{SG} is the surface tension of the Solid-Gas interface and γ_{SL}.

The regime when $S \geq 0$ is called total wetting. This is when the combined interfacial energy of the wetting state, $\gamma_{SL} + \gamma$, is lower than the surface energy of the Solid-Gas interface, γ_{SG}. This results in the spreading of the liquid layer on the solid surface towards a liquid film driving the contact angle, θ_e to zero [5].

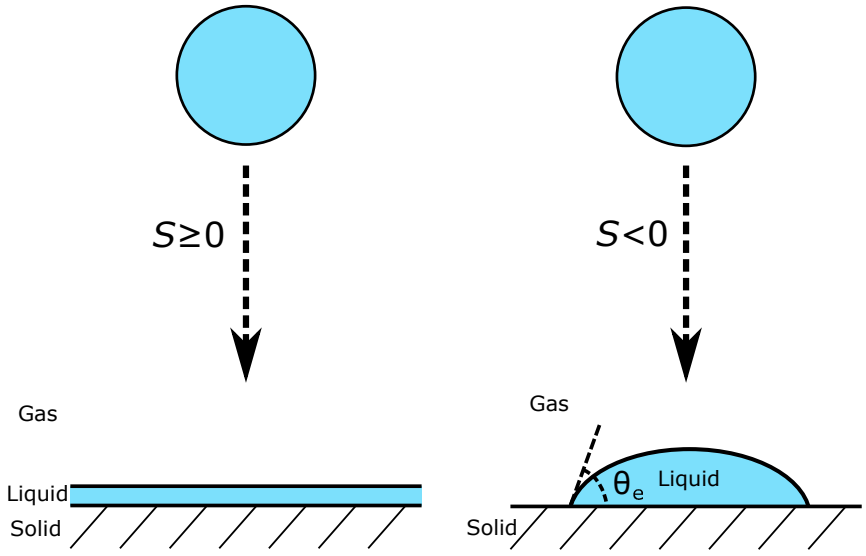

Figure 2.3: Spreading Parameter. When the spreading parameter, S, is greater or equal to zero, the droplet spreads completely into a thin film on the surface. On the other hand, when the droplet interacts with a surface with a negative spreading parameter, it forms a spherical cap and rests at a given contact angle, θ_e, with the surface.

On the other hand, the regime when $S < 0$ is referred to as partial wetting. In this case, the surface energy of the solid surface is higher when it is wet than when dry. This will cause the droplet to spread into a spherical cap, which is resting on the surface at a particular θ_e. A liquid is "wetting" if the contact angle lies between $0^\circ < \theta_e < 90^\circ$ and "non-wetting" if the contact angle lies between $90^\circ < \theta_e < 180^\circ$. The case when the $\theta_e = 90^\circ$ is referred as neutral wetting.

2.2.4 Young's Law

The spreading coefficient allows us to predict if the droplet will present complete or partial wetting depending on the interaction of the surface tension of the liquid-solid-gas phases. Consider a small droplet sitting on a perfectly flat and smooth surface, similar to Figure 2.4. The shape of the liquid spherical cap is defined be the attractive forces of the relationship of the surface tensions. Within the framework of classical thermodynamics, the equilibrium state of the droplet is given by a minimum in the total surface energy of the system. This corresponds to a spherical cap shape defined by an equilibrium contact angle θ_e, also known as Young's angle, which is determined by the Young-Dupré equation:

$$\cos\theta_e = \frac{\gamma_{SG} - \gamma_{SL}}{\gamma}, \tag{2.6}$$

where γ is the liquid-gas surface tension, γ_{SG} is the solid-gas surface tension and γ_{SL} is the solid-liquid surface tension.

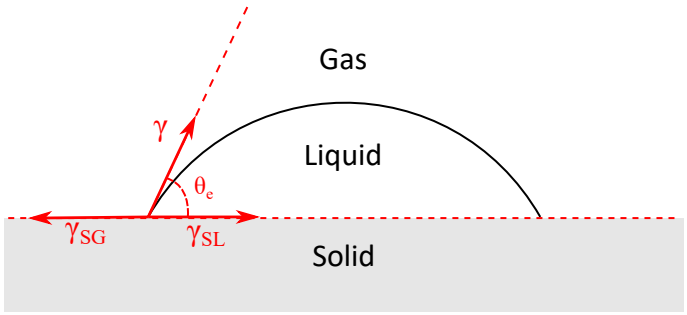

Figure 2.4: Forces defining the contact angle. The balance between the surface tension of the liquid-gas (γ), solid-liquid (γ_{SG}) and solid-gas (γ_{SL} defines the equilibrium contact angle (θ_e) and the shape the droplets rests on a surface.

Equation 2.6 describes the interaction between three phases of matter in the ideal case. Consequently, θ_e is a unique characteristic physical quantity which corresponds to the balance of interfacial forces given by a specific liquid-solid-gas system. However, in practice, there are important considerations to be made such as the effect of gravity and the effect of roughness on a solid surface.

2.2.5 Capillary length

Up to this point, the droplets we have used have ignored the effects of gravity. This force is by no means trivial in wetting and fluid behaviour, in fact, gravity is the reason we normally do not see big spherical caps (beyond a couple of centimetres) of any liquid on surfaces since the pressure exerted by gravity on the liquid makes them flatten into the familiar puddle.

However, experience tells us that small droplets form perfectly spherical liquid caps when resting on a surface. For instance, when we spill coffee and it splashes on the ground, the main body of liquid is compressed into a pancake shape puddle while the small satellite droplets form spherical caps. This shows the existence of a transition, a particular threshold in length scale, where the forces of gravity become negligible and the interfacial forces dominate in the shape of the droplet. This length is known as the capillary length and is commonly denoted as κ^{-1} [5, 34]

It is possible to find a physical expression for this capillary length through dimensional analysis. At small length scales, the surface tension forces scale as a function of R, as we discussed in the previous section. On the other hand, in larger length scales the gravitational forces scale with mass of the liquid, which depends on the volume, R^3, and the density of the liquid, ρ. The ratio between gravitational and surface tension forces then scales as

$$\frac{\rho g R^3}{\gamma R} \sim R^2. \tag{2.7}$$

As the length grows, the forces that dominate stem from gravity but as the lengths grows smaller, it is the surface tension forces that take over. If these forces are equal then the capillary length is defined as

$$\kappa^{-1} = \sqrt{\frac{\gamma}{\rho g}}. \tag{2.8}$$

The capillary length for water can be obtained by choosing the corresponding values for equation 2.8, $\gamma = 72.8\,\mathrm{mN\,m^{-1}}$, $\rho = 997\,\mathrm{kg\,m^{-3}}$, and $g = 9.8\,\mathrm{m\,s^{-2}}$, giving $\kappa^{-1} = 2.7\,\mathrm{mm}$.

The concept of capillary length is useful, for it enables the development of experiments to study pure interfacial interactions without having to take the effects of gravity into account.

2.2.6 Jurin's Law

The spontaneous capillary filling of a liquid in a tube is defined by the relationship between the solid-gas surface tension, γ_{SG}, and the solid-liquid surface tension, γ_{SL}, as follows,

$$I = \gamma_{SG} - \gamma_{SL}, \tag{2.9}$$

where I is defined as the imbibition parameter. Similar to the spreading coefficient, the value of this parameter describes the type of capillary action expected. When $I > 0$, the solid surface is in a lower state of energy when wet by the liquid, resulting in the invasion of the liquid to the tube. Analogously, when $I < 0$, the solid surface has lower surface energy in a dry state which results in the liquid being expelled from the tube.

In the presence of gravity, the energy, E, of a liquid pillar inside the tube can be expressed as,

$$E = -2\pi rhI + \pi r^2 h^2 \rho g, \tag{2.10}$$

where r is the inner radius of the tube, h is the height difference between the liquid pillar and the liquid bulk, ρ is the density of the liquid and g is the acceleration due to gravity. The first term of the right hand side of Equation 2.10 is the energy contribution related to the gain in surface energy and the second term is the gravitational potential energy. The imbibition parameter can be related to the equilibrium contact angle via Young's law and can be re-written as,

$$\gamma \cos\theta_e = \gamma_{SG} - \gamma_{SL} = I, \tag{2.11}$$

At equilibrium, the energy is minimized which reduces Equation 2.10 to Jurin's law for capillary rise,

$$H = \frac{2\gamma\cos\theta_e}{\rho g r}, \tag{2.12}$$

where H is the equilibrium height of the pillar, also known as Jurin's height [5]. Figure 2.5 shows a diagram of the behaviour of capillary action according to the different imbibition parameter regimes.

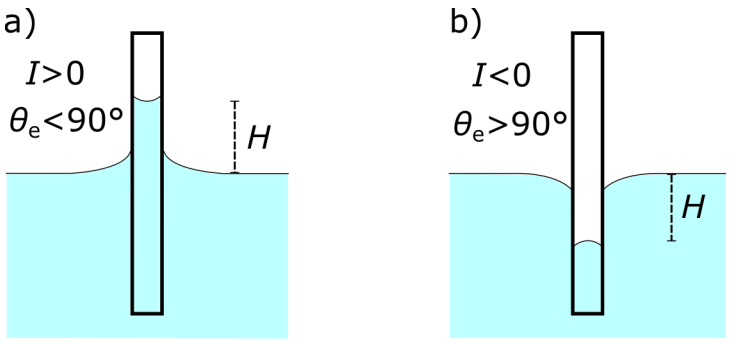

Figure 2.5: Capillary action: rise and descent of a liquid pillar. The behaviour of the liquid encased inside the tube is determined by the imbibition parameter, I. When a) I is positive, the liquid rises up the tube and when b) I is negative, the liquid descends. The rise or descent of the liquid pillar describes the wetting properties, such as the equilibrium contact angle, θ_e, at the interface of the liquid-solid-gas and is tied to the height difference between the meniscus of the pillar and the surface of the bulk of the liquid. This height is also known as Jurin's height (H).

2.3 Contact line pinning and surface heterogeneity

2.3.1 Origin of pinning and friction forces

The Young-Dupré equation (Equation 2.6) asserts that the equilibrium contact angle is uniquely determined by the combination of the surface tensions. Any deviation from this ideal shape would force the droplet to deform and adjust in order to return to the equilibrium configuration. However, this statement is only true for the ideal case of a solid which is perfectly flat and smooth. In practice, solids are naturally rough and heterogeneous at small scales because of imperfections on the surface. These imperfections, also referred to as roughness, can be present in the form of chemical heterogeneity, topographical variations, dimples or protrusions [26, 34–37]. The effect of these physical or chemical variations generate resistive forces at the contact line, removing the ideal behaviour of the equilibrium contact angle and allowing the droplet to have an interval of static static contact angle, θ_S, configurations. This means that θ_e is contained in the range of θ_S. This is the reason why Young's equilibrium contact angle, θ_e, has seldom been observed; instead, one observes a static contact angle whose range of variation depends on the roughness of the surface. Additionally, in motion, the droplet can adopt dynamic configurations for the contact angle that are not in the static contact angle envelope. Therefore, any contact angle that differs from the one specified by the equilibrium contact angle is referred to as the apparent contact angle, θ, since it will be a product of surface roughness, dynamic behaviour or a combination of both.

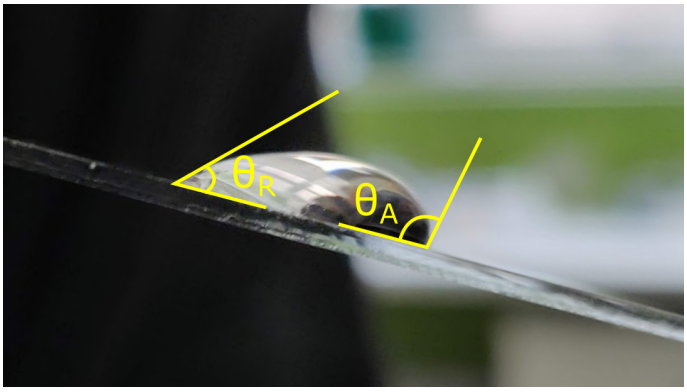

Figure 2.6: Droplet on a tilted surface. At the onset of motion, the droplet has a advancing receding contact angle, θ_A, and a receding contact angle, θ_R.

2.3.2 Contact angle hysteresis

The resistive force that comes from surface heterogeneity of a solid is defined as contact line pinning. The presence of pinning provides an indication of the static friction that a droplet must to overcome to start moving on the solid [5]. In practice, it is possible to observe this effect at play when a droplet is placed on a surface and then is inclined, as seen in Figure 2.6. The droplet resists motion up to a maximum inclination, at which point it begins to slide. The corresponding combination of contact angles at the onset of motion is defined by an advancing and receding configuration. At the limit of transition from static to motion of the contact line, the contact angle of an advancing liquid-gas interface is referred to as the advancing contact angle, θ_A. Similarly, the contact angle at the limit of a receding motion is called the receding angle, θ_R. Hence, the range of the static contact angles, θ_S, which refers to all the contact angles where the droplet remains static on the surface due to the effect of roughness, is defined as

$$\theta_R \leq \theta_S \leq \theta_A, \tag{2.13}$$

and the amplitude of this range is a measure of the contact angle hysteresis caused by the surface heterogeneity, typically called the contact-angle hysteresis:

$$\Delta\theta = \theta_A - \theta_R. \tag{2.14}$$

The magnitude of this quantity is proportional to the pinning force needed to move a liquid on a surface, i.e, [5, 38, 39]

$$F_{\text{pinning}} = 2\gamma r(\cos\theta_R - \cos\theta_A), \tag{2.15}$$

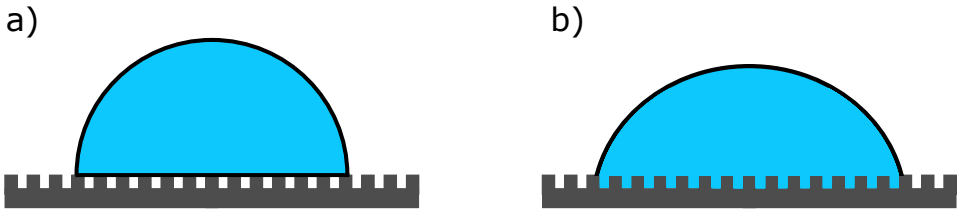

Figure 2.7: Extreme effects of surface roughness in wetting behaviour. a) Cassie-Baxter state and b) Wenzel state.

2.3.3 Cassie-Baxter and Wenzel states

Roughness can also alter the interaction between liquid and solid surfaces. When a droplet is contact with a rough surface, it can adopt a Cassie Baxter state [40], a Wenzel state [41] or mixed state of the two.

The Cassie-Baxter state is the case where a droplet is suspended on the surface heterogeneity as seen in Figure 2.7(a). In this type of state, the surface contact of the droplet is minimized, which causes the droplet to adopt a configuration of an apparently larger contact angle and decrease the force needed to move the droplet on the surface [42]. When taking the horizontal bridging of the liquid across the pillars, the value of the Cassie-Baxter contact angle, θ_e^{CB}, can be expressed in terms of the equilibrium contact angle, θ_e, on the flat surface of the solid, i.e.,

$$\cos\theta_e^{CB} = \phi_s \cos\theta_e - (1-\phi_s), \tag{2.16}$$

where ϕ_s is the solid-vapour fraction of the surface.

The Wenzel state describes an interaction where the droplet is able to penetrate the surface roughness, achieving complete contact with it. The roughness increases the contact area of the droplet, hence the pinning forces increase due to the need to move a larger amount of liquid on the surface [43]. The Wenzel contact angle, θ_e^W, is given by

$$\cos\theta_e^W = r_w \cos\theta_e \tag{2.17}$$

where r_w is the ratio between the real surface area against the apparent surface area of the solid. Note that in this wetting case, r_w, acts as an amplification of wetting term, $\cos\theta_e$. Therefore, small changes in θ_e translate to bigger changes in θ_e^w. This highlights the importance of neutral wetting ($\theta_e = 90^\circ$) in this wetting case since it marks the an decrease in the Wenzel contact angle ($\theta_e < 90^\circ$) towards zero, and the increase in the Wenzel contact angle ($\theta_e > 90^\circ$) towards 180°.

2.3.4 Contact line dynamics

When a contact line is moving, the shape of the droplets changes and adjusts to a dynamic angle, $\theta(v)$, which depends on the velocity of the contact line, v [5, 26]. For an advancing contact line, the dynamic contact angle is higher than the advancing angle, $\theta(v) > \theta_A$, and one expects that θ approaches θ_A as $v \to 0$. Similarly, for a receding contact line $\theta(v) < \theta_R$, and $\theta \to \theta_R$ as the contact line comes to a rest. In this thesis, the analysis is based on two theoretical models that aim to shed light on the motion of contact lines: the Cox-Voinov theory, also known as the hydrodynamic theory, and the Molecular Kinetic Theory (MKT).

The deviation of the dynamic contact angle from the static value is governed by the competition between driving and dissipative forces. On the one hand, the Cox-Voinov theory [19, 44] states that the large-scale deformation of the liquid-gas interface is governed by the competition between viscous stresses and surface tension. This yields the following prediction of the apparent contact angle as a function of the velocity of the interface:

$$\theta^3 = \theta_{mic}^3 + 9\mathrm{Ca}\ln\left(\frac{\mathrm{L}}{\mathrm{l_m}}\right), \tag{2.18}$$

where θ is the apparent contact angle, θ_{mic} is the microscopic contact angle, $\mathrm{Ca} = \eta\,\mathrm{v}/\gamma$ is the capillary number, L is the typical macroscopic length scale where the dynamic contact angle is measured, and θ_{mic} is the microscopic contact angle, measured at a microscopic cut-off length scale, or slip-length, l_m [26]. L is a length scale in the order of the capillary length and l_m is is a length of the order of the size of the molecules of the solid surface, or the length scale where the no-slip boundary condition does not apply [45].

On the other hand, the driving and dissipative forces may be regulated by microscopic processes on the motion of the contact line on the solid surface. Haynes and Blake developed the MKT model to describe the motion of the contact line considering these processes [46] which was subsequently used to describe the spreading of droplets on solid surfaces [47]. In the framework of MKT, the contact line motion is governed kinetic properties such as the rate of adsorption and desorption of molecules from the solid and the distance between molecules on the surface. The balance between both processes sets the contact-line velocity [2], which is given by

$$v = 2K_0\xi\,\sinh\left(\frac{\gamma\xi^2(\cos\theta_S - \cos\theta)}{2k_BT}\right), \tag{2.19}$$

where K_0 is the frequency of adsorption-desorption of molecules at the contact line, ξ is the average distance of molecular displacements and k_BT is the thermal energy.

2.3.5 Overcoming pinning

In nature, there are many examples of surfaces which have adapted to overcome pinning, allowing water droplets to slide easily from lotus leaves, ensuring they remain clear of contaminants [48, 49], or the Nepenthes pitcher plant which uses a lubricated surface to lead unsuspecting insects into a slippery demise [50, 51]. These have served as inspiration to create smart-engineered surfaces that aim to reduce surface pinning to allow surfaces to remain dry, self-clean and exhibit anti-fouling capabilities [52]. In recent years, there have been significant advances in surface modification for water repellency and interest in these surfaces has greatly increased due to their potential applications in fields such as medicine, biotechnology and heat transfer [52].

Superhydrophobic surfaces

One of the most well-known superhydrophobic phenomena is the “lotus leaf effect", first coined by Barthlott & Neinhuis. The lotus leaf is covered in waxy bumps that induces droplets to roll of the surface of the leaf [34, 48]. These bumps, or roughness, are small enough that water droplets sit on top of them in a Cassie-Baxter state, enabling the droplets to increase the contact angle of the triple line to superhydrophobic values ($> 150^\circ$) and allowing the droplets to shed off easily from its surface. This principle is the basis of laboratory engineering of superhydrophobic surfaces using a range of different techniques. For instance, the utilization of fractal wax surfaces has shown that droplets can reach contact angles of $\theta = 174^\circ$ [53]. Lithographic techniques have allowed the manufacturing of different geometries for surface roughness, reaching values of $\theta = 170^\circ$ [54, 55]. Chemical deposition of gels and metals to roughen substrates has been successful in delivering similar results in smaller scales [56, 57]. In recent years, the advancement in the production of superhydrophobic surfaces has allowed the scale of the roughness to be reduced to remarkably small length scales via the use of nanometric particles to coat the surface of a solid [58, 59].

Although superhydrophobic surfaces offer water repellent qualities, they are seldom used in practice due to structures comprising the surfaces are not durable. Additionally, if sufficient pressure is applied on the surface, the liquid can penetrate the surface geometry, driving the droplet to a Wenzel state and consequently lose it’s water shedding properties. However, this weakness is not fundamental since a recent work by Wang *et al* [52] has developed a geometry which is pressure resistant and durable, opening opportunities to put superhydrophobic surfaces in more practical perspectives.

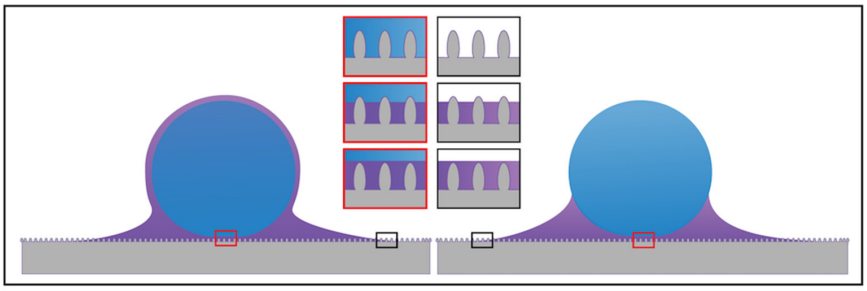

Figure 2.8: Liquid infused surfaces (LIS). Schematic of droplet sitting on a LIS which can be completely coated (left diagram) or partially coated (right diagram) by the lubricating layer, both cases exhibiting a wetting ridge between the droplet and the lubricating layer. The insets in red show the possible interactions between the liquid droplet: Complete wetting (top), partial wetting (middle), or separated by the lubricating liquid completely (bottom). The interaction of the substrate and the lubricating liquid are shown in the black insets: lack of lubricant (top), partially coated (middle), and completely impregnated (bottom). Taken from ref [1].

Liquid infused surfaces

Liquid Infused Surfaces (LIS) utilize a lubricating layer to minimize surface pinning. This is reminiscent to the Nepethes pitcher plant, which uses a highly water wetting surface in combination with surface geometry to create a thin layer of water which minimizes the friction with the oils found on the feet of insects, making them slip into the plant's digestive system [50, 51]. Studies have been made to reproduce this effect in laboratory conditions which mix surface geometry, wetting attributes and liquid retention in order to reduce surface pinning [1]. Figure 2.8 shows characteristic attributes of LIS, when in contact with the lubricating layer, a wetting ridge is formed between the droplet and the lubricating layer. The lubricating layer either completely or partially coated the droplet depending on the interfacial interactions of the two liquids. The interaction between the liquid and the surface can be present in the form of complete wetting of the solid, partial interaction with the solid or no interaction with the solid. Similarly, the interaction of the lubricating layer can either be a thin film on the surface, partially impregnated or completely impregnated. The limitation of these type of surfaces lie in the metastable state of the lubricating liquid on the solid substrate, which can be destroyed by the depletion of the lubricating layer by flow of liquid or evaporation [60].

However, perhaps one of the most outstanding types of LIS are Slippery Liquid Infused Porous (SLIP) surfaces. The principle behind these surfaces is to increase the surface area of the solid via the deposition of a nanometric porous coating which is preferentially wet by a lubricating liquid, creating a thermodynamicaly stable lubricating layer that exhibits very low friction and is capable to withstand lubricant shedding, allowing for conformal lubrication of engineered surfaces [61].

Slippery Omniphobic Covalently Attached Liquid (SOCAL) surfaces

In this thesis, special attention is directed to SOCAL surfaces since they are the prime solid low friction surfaces where hygrotaxis is going to be studied.

In 2016, Wang & McCarthy [62] developed a method to produce a hydrophobic surface, named SOCAL, that serves as an alternative to low friction surfaces such as SLIP surfaces. SOCAL surfaces are created through acid-catalysed graft polycondensation of dimethyldimethoxysilane onto a smooth flat surface, such as glass, or silicon. The result of this process leaves a homogeneous layer of Polydimethylsiloxane (PDMS) chains grafted to the surface. This layer of PDMS acts as a liquid-like coating which exhibits uniquely low static resistance to motion of droplets. This low static friction translates into contact angle hysteresis values that average at $\sim 3^\circ$ in the literature, with some works achieving values below $< 1^\circ$ [4, 62], reportedly the lowest achieved for a solid smooth flat surface. Due to these surfaces exhibiting such low values of contact angle hysteresis, some works have proposed that the value of the static contact angle, or evaporation contact angle, can be considered as the ideal equilibrium contact angle defined by the Young-Dupré equation [4].

One of the most interesting aspects of SOCAL surfaces is that although they report uniquely low values of contact angle hysteresis, the behaviour of the motion of droplets shows an higher level of complexity. This can be appreciated in Figure 2.9, where $10\,\mu$L droplets are placed on low hysteresis surfaces at fixed tilting angles, θ_{tilt}, of 5° and 15°. If one starts by looking at the results of a tilting angle of 5°, only the droplet resting on the lubricated surface seems to exhibit motion. This result apparently shows some degree of discrepancy since LIS surfaces and SOCAL surfaces are reported to have contact angle hysteresis values comparable to each other ($\sim 1^\circ$), therefore one would expect that they would exhibit similar behaviour, as opposed to a large difference. Furthermore, moving onto the results for $\theta_{tilt} = 15^\circ$, it seems like the contact line on SOCAL surfaces is significantly lower than other low hysteresis surfaces. The apparent difference between static and dynamic states compared to other low hysteresis surfaces seems to suggest that there is a large timescale in the motion on SOCAL surfaces, which will be further explored in Chapter 4.

SOCAL surfaces offer great opportunities to further undertand the physics of liquid contact lines on solid surfaces of unprecedented contact angle hysteresis. Additionally, some of the most notable research into applications for this type of surface has been done in topics such as fog harvesting [63] and is considered a prime candidate for the control of soil wettability [64], an application particularly important in rare mineral harvesting.

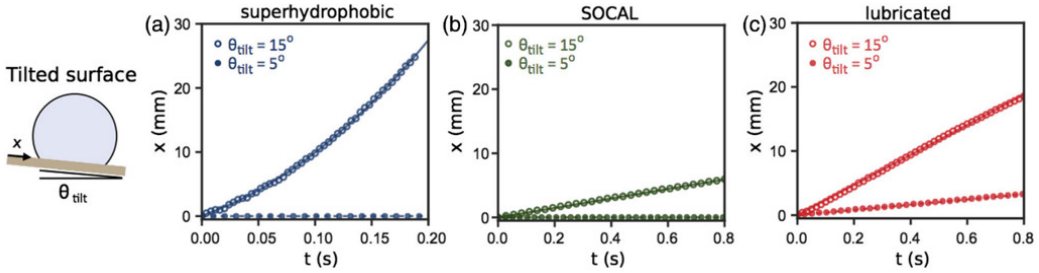

Figure 2.9: Droplet motion on low hysteresis surfaces Experiments of moving droplets at tilt angles, θ_{tilt}, of 5° and 15°. a) Superhydrophobic surfaces, b) SOCAL surfaces and c) LIS. Figure adapted from Dan Daniel, *et al* [2]

2.4 Droplet evaporation

Evaporation of liquids is a natural phenomena that is present whenever a liquid is surrounded by an atmosphere that is not saturated with the liquids own molecules [24]. Evaporation has been extensively studied in the literature, with significant amount of research into the applications and dynamics of evaporation [24, 65, 66]. For instance, the coffee ring effect, named after the stains left by evaporated spilled coffee, has shown the existence of capillary flows able to deposit particles on the edges of the droplet footprint and it's applicability for particle deposition purposes [67]. More recent studies, particularly involving binary mixtures, have shown that evaporation can induce self-propulsion of droplets via evaporative cooling or vapour induced surface tension gradients, allowing the understanding of the fundamental mechanisms behind evaporation driven effects and its applicability in substance transport and sensors [15, 16]. These show the importance that evaporation has in expanding our understanding of fundamental concepts and it's significance in different fields of study, justifying the extensive and continued research done in this phenomenon.

2.4.1 Aerosol droplets

Consider a droplet of liquid suspended in air with a radius below the capillary length, similar to the droplets formed in aerosols. If the ambient around the droplet is not saturated with the liquid's vapour molecules, then it evaporates radially and isotropically [24], as seen in Figure 2.10(a). As discussed previously, surface tension drives the shape of the droplet to be that of a sphere, therefore the volume of the liquid V is given by

$$V = \frac{4}{3}\pi R^3, \tag{2.20}$$

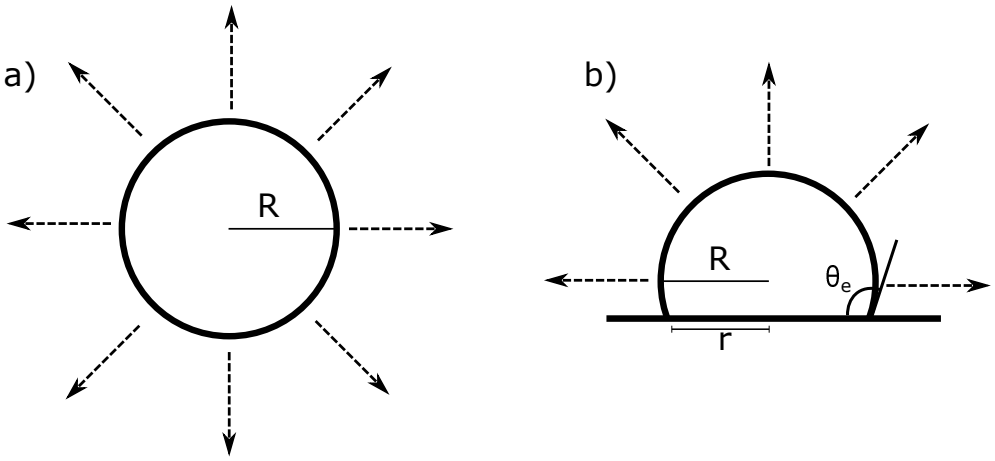

Figure 2.10: Free and limited diffusion evaporation. a) Isotropic evaporation of a suspended droplet. b) diffusion limited evaporation due to the interaction with a solid surface.

where R is the spherical radius of the droplet. Picknett & Bexon developed a theory of evaporation which describes the mass flux in evaporation in terms of concentration at the interface of the droplet, c_0, and the concentration far away from the droplet, c_∞. In this approximation, the rate of volume loss in time through the surface of the sphere is expressed as [25]

$$\frac{dV}{dt} = -\frac{4\pi RD\Delta c}{\rho}, \tag{2.21}$$

where $\Delta c = c_\infty - c_0$.

2.4.2 Sessile Droplets

When a liquid droplet interacts with a solid surface, it spreads and takes the shape of a spherical cap defined by a contact angle, θ_e, and a base radius, r. The effect of the solid surface limits the diffusion of the vapour molecules, since evaporation can only occur throughout the liquid-gas interface, as seen in Figure 2.10(b). This breaks the symmetry of the isotropic diffusion of the molecules during evaporation of a sessile droplet. This delimited diffusion is regulated by the amount of surface exposed to the environment, as shown in Figure 2.10(b). Therefore, the shape, or contact angle, that the droplet has on a surface will affect the rate of evaporation of the liquid droplet.

When a droplet below the capillary length, $R < \kappa^{-1}$, is placed on a surface with a partial wetting spreading parameter, $S > 0$, the droplet takes the shape of a symmetrical spherical cap. This allows to approximate the volume V of the droplet using geometric relations, hence

$$V = \frac{\pi R^3(2+\cos\theta_e)(1-\cos\theta_e)^2}{3}. \tag{2.22}$$

This geometrical approximation allows us to obtain key parameters from a side profile of the droplet. Such parameters include the spherical radius R, the contact radius r, the apparent contact angle θ, and the height of the droplet h. Therefore, considering Equation 2.22, one obtains

$$R = \left(\frac{3V}{\pi(2 - 3\cos\theta + \cos^3\theta)} \right)^{1/3}, \tag{2.23}$$

$$h = R(1 - \cos\theta), \tag{2.24}$$

$$r = R\sin\theta, \tag{2.25}$$

$$\tan\left(\frac{\theta}{2}\right) = \frac{h}{r}. \tag{2.26}$$

As for the aerosol droplet, the relationship of the concentration in this geometry follows $(c_\infty - c_0)/R$. These geometric relations give an expression for the loss of volume of the droplet in time [4]

$$\frac{dV}{dt} = \frac{4\pi RD\Delta c}{\rho} f(\theta), \tag{2.27}$$

which one can express in terms of the base radius using Equation 2.25,

$$\frac{dV}{dt} = \frac{4\pi rD\Delta c}{\rho \sin\theta} f(\theta), \tag{2.28}$$

where $f(\theta)$ is a contact angle dependent function which gives an exact solution to Equation 2.27 [25].

2.4.3 Ideal modes of evaporation

Surface roughness plays a significant role in the evaporation of a droplet. This is because contact line pinning affects the apparent contact angle a droplet will adopt on a surface, changing the dynamics of evaporation. This problem was explored by Picknett & Bexon in 1977 [25], where they proposed an analytical model outlining two ideal modes of evaporation for perfectly rough and perfectly smooth surfaces. Their model provides exact solutions for the for the contact angle dependent function $f(\theta)$ by the interpolation of a polynomial function [25].

Constant contact radius evaporation

The first ideal mode, reflecting the interaction of a droplet with a perfectly rough surface, is called Constant Contact Radius (CCR) mode. In this mode of evaporation, the contact line is pinned to the surface, resulting in the decrease of the contact angle of the droplet as it evaporates while it's base radius remains constant, as shown in Figure 2.11(a). Although this is an ideal mode of evaporation, CCR evaporation has been experimentally observed and studied in the literature [68]. Since this mode of evaporation falls out of scope of this project, the reader is invited to read references [25, 68] for additional details on this mode.

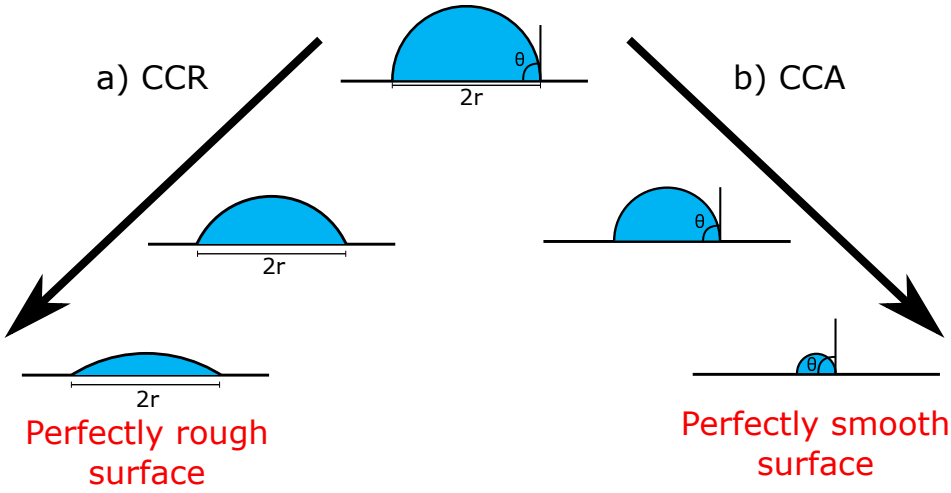

Figure 2.11: Ideal evaporation modes. a) Constant Contact Radius (CCR) mode, the base radius of the droplet remains constant throughout the evaporation. b) Constant Contact angle (CCA) mode, the contact angle remains constant throughout the evaporation

Constant contact angle evaporation

The second mode of evaporation describes the scenario where a droplet evaporates in the absence of pinning, or a perfectly smooth surface, and is called Constant Contact Angle (CCA) mode. In contrast to CCR mode, here the contact angle remains constant while the base radius decays throughout the evaporation. Due to the absence of resistive pinning forces, the droplet evaporates at Young's equilibrium contact angle, hence for this section $\theta_e = \theta$.

Picknett & Bexon derived an exact solution for $f(\theta)$ and provided a numerically accurate polynomial interpolation solution, $f_{PB}(\theta)$, for the possible contact angles a droplet can have have on the surface ($0^\circ < \theta < 180^\circ$),

$$f_{PB}(\theta) = \begin{cases} \frac{1}{2}(0.6366\theta + 0.09591\theta^2 - 0.06144\theta^3) & 0^\circ < \theta \leq 10^\circ \\ \frac{1}{2}(0.00008957 + 0.6333\theta + 0.116\theta^2 - 0.08878\theta^3 + 0.01033\theta^4) & 10^\circ < \theta \leq 180^\circ \end{cases} \tag{2.29}$$

where θ is given in radians.

It is possible obtain the base radius dependent expression of the volume by using equation 2.22 and 2.25, which reads

$$V = \frac{\pi r^3 (1 - \cos\theta)^2 (2 + \cos\theta)}{3 \sin^3\theta}, \tag{2.30}$$

which when differentiated with respect to time gives

$$\frac{dV}{dt} = \frac{\pi r^2 (1 - \cos\theta)^2 (2 + \cos\theta)}{\sin^3\theta} \frac{dr}{dt}. \tag{2.31}$$

Combining Equation 2.28 and 2.31 gives

$$\frac{\pi r^2(1-\cos\theta)^2(2+\cos\theta)}{\sin^3\theta}\frac{dr}{dt} = \frac{4\pi rD\Delta c}{\rho\sin\theta}f_{PB}(\theta). \tag{2.32}$$

Solving Equation 2.32 for r yields

$$\pi r dr = \frac{4\pi\sin^2\theta D\Delta c}{\rho(1-\cos\theta)^2(2+\cos\theta)}f_{PB}(\theta)dt, \tag{2.33}$$

which integrated with the following boundary conditions: $r_i = r$, $r_f = 0$, $t_i = 0$ and $t_f = t$, yields

$$A = \pi r^2 = A_0 - \frac{8\pi\sin^2\theta D\Delta c}{\rho(1-\cos\theta)^2(2+\cos\theta)}f_{PB}(\theta)t, \tag{2.34}$$

where A is the contact area of the droplet and A_0 is the initial contact area of the droplet. Hence, under CCA evaporation, the contact area of the droplet decays linearly in time, i.e. $A = A_0 - mt$, where the gradient m is associated with the dynamics described in the Picknett & Bexon evaporation dynamics.

In terms of the observation of this evaporation mode, this phenomena has been difficult to observe due to the non-ideal behaviour of surfaces in impeding the complete motion of the contact line. In reality, liquid droplets evaporate from surfaces in a mixed mode known as slick-slip mode of evaporation [69]. In this mode, the contact radius of the droplet changes due to the contact angle decreasing beyond the drag forces of the surface while the contact angle decreases due to the pinning the surface induces on the droplet.

However, engineered surfaces that are able to decrease the pinning forces to near zero, as discussed in the previous sections, have allowed the observation of CCA evaporation. Attempts to do this have been made on superhydrophobic surfaces and SLIP surfaces [51, 60]. On superhydrophobic surfaces, contact line hysteresis is minimized by reducing the effective contact area between the droplet and the solid via patterns or roughness on the surface, suspending the droplet in a Cassie-Baxter state. Although CCR has been observed in superhygrophobic surfaces [70] since the transition between Cassie-Baxter into Wenzel state induces complete pinnning of the droplet, McHale *et al* [71] reported CCA intervals on a SU-8 textured surface. Since then, the study of evaporation on superhydrophobic surfaces has contributed to the understanding of the effects of contact angle hysteresis and superhydrophobicity on this phenomenon [70–76].

The observation of this effect on lubricated surfaces has been more successful, particularly on SLIP surfaces. Guan, *et al.* [77] observed CCA mode of evaporation on SLIP surfaces coated with a hygrophobic layer imbibed with oil. The lubricant allows droplets to become extremely mobile on the surface which allows this phenomenon to take place. However, the interaction of the droplet and the SLIP surface does not follow the direct mechanics of solid-liquid interactions due to the immiscible lubricating layer interacting with the liquid.

More recently, however, Armstrong *et al* [4] reported consistent CCA evaporation of SOCAL surfaces for the first time. As mentioned previously, SOCAL surfaces have been reported to decrease the contact angle hysteresis to an interval between 1° to 5° while keeping direct contact with the solid. This is significant because it is the first time this effect was observed on a solid flat surface which allows the use classic descriptions of this interaction.

2.4.4 Diffusion constant and relative humidity

On one hand, Relative Humidity (RH) is essential to the study of evaporation since it is a quantity that regulates the amount of molecules in the vapour phase surrounding the evaporating droplet. This quantity is tied to the relative concentration of vapour molecules in the environment, $\Delta c = c_\infty - c_0$. On the other hand, the diffusion coefficient D is a proportionality constant that describes the relation between the mass flux and concentration of the vapour molecules. Being able to obtain both quantities is beneficial since it allows the calculation of theoretical evaporation times of droplets of a given liquid, volume and temperature.

To obtain the expression for the diffusion constant, Equation 2.34 can be solved to yield a prediction of the diffusion constant, which takes the form

$$D = \frac{m\rho(1-\cos\theta)^2(2+\cos\theta)}{8\pi\sin^2\theta(c_\infty - c_0)f_{PB}}. \tag{2.35}$$

The vapour concentration at the surface of the droplet, c_0, cannot exceed the one determined by the saturation vapour density at a fixed temperature. Therefore, to approximate the value of c_0, a polynomial function can be fit to data provided by Kaye & Laby [78] to predict the value of the saturation vapour density as a function of temperature, i.e,

$$c_0 \approx 0.0004T^3 + 0.0053T^2 + 0.3759T + 4.7736, \tag{2.36}$$

Where T is in $^\circ$C and is c_0 is given in $\mathrm{g\,m^{-3}}$.

Relative humidity is the relationship between the saturation vapour density (at the interface of the droplet) and the actual vapour density (ambient). The actual vapour density can be considered as a good approximation for the vapour concentration far away from the droplet since it represents the average concentration of vapour in the room. The expression to obtain

the relative humidity percentage is given by the following expression,

$$RH = \frac{\text{Actual vapour density}}{\text{Saturation vapour density}} \times 100\% \approx \frac{c_\infty}{c_0} \times 100\%. \tag{2.37}$$

Hence, under the considerations done, the value of c_∞ can be approximated as

$$c_\infty \approx \frac{RH}{100\%} \times c_0. \tag{2.38}$$

The temperature dependence of the diffusion constant, D_{theo}, can be obtained from the "CRC handbook of chemistry and physical constants" [79] and reads

$$D_{lit} = 0.0024T - 0.4677, \tag{2.39}$$

where the temperature units are in K and D_{theo} is given in $\mathrm{cm}^2\,\mathrm{s}^{-1}$.

2.5 Hydrodynamic equations

In order to describe the interaction between a liquid droplet and the surrounding gas phase, it is necessary to define the governing equations. The flow of fluid substances is defined by the conservation of momentum and the conservation of energy. These conservation laws are defined in the Navier-Stokes equations and play a key role in the study the physics of fluids. For the Lattice Boltzmann simulations, the expression of the imcompressible limit of the Navier-Stokes equations is used. Although these equations do not account for fluid compressibility in gases, thermal effects, chemical reactions and many more, they are very frequently and successfully used for both liquid and gases, including droplet dynamics [80–83].

Under the incompressible limit, the conservation of energy is described by the continuity equation, defined as

$$\nabla \cdot \mathbf{u} = 0, \tag{2.40}$$

where **u** represents the fluid velocity. The conservation of momentum, on the other hand, is expressed as

$$\rho(\delta_t \mathbf{u} + \mathbf{u} \cdot \nabla)\mathbf{u} = -\nabla \cdot \Pi + \eta \nabla^2 \mathbf{u} + \mathbf{F}_{ext}, \tag{2.41}$$

where δ_t denotes the partial derivative with respect to time, η is the dynamic viscosity which represents the resistance to shearing forces and $\mathbf{F}_{ext}$ is the external force contribution. The left hand side of Equation 2.41 describes the inertia of the fluid which includes the flow acceleration as the first term and the convective acceleration in the second term. The right hand side describes the divergence of the stresses and the external force which include the

total pressure as the first term, the viscous dissipation as the second term and the external force as the last term. The central quantity in the Navier-Stokes equations is the velocity, which means that when values of the velocity are known at every point in time and space, the Navier-Stokes equation is considered to be solved.

Relative humidity has a significant effect on evaporation and condensation phenomena since both of these processes are regulated by the mass exchange generated by gradients of concentration of molecules of the same species in the ambient phase [4, 84]. For isothermal systems, the mass flux exchange of the system can be modelled by the Cahn-Hilliard convection-diffusion equation [80]. This model developed by Cahn & Hilliard in 1958 [85], aims to provide an expression of the conservation of the order parameter associated with mass fluxes, which reads as

$$\delta_t \phi + \mathbf{u} \cdot \nabla \phi = -\nabla J \tag{2.42}$$

where the key component in the Cahn-Hilliard model is the diffusive flux, J, which obeys the following constitutive equation

$$J = -M \nabla \mu, \tag{2.43}$$

where M is known as the mobility parameter and plays a role akin to diffusivity [80]. Therefore, Equation 2.42 can be given as

$$\delta_t \phi + \mathbf{u} \cdot \nabla \phi = M \nabla \mu. \tag{2.44}$$

2.6 Multiphase fluids

2.6.1 Thermodynamics of phase transition

Consider a system composed of two different immiscible pure liquids. The liquids are composed of molecules of different species which can be differentiated by introducing an order parameter, ϕ, defined as

$$\phi = \frac{n_2 - n_1}{n_2 + n_1}, \tag{2.45}$$

where n_1 and n_2 represent the number densities of the two different species of molecules [86, 87]. According to Equation 2.45, the order parameter can adopt any value in the interval $[1, -1]$, so that $-1 \leq \phi \leq 1$. The boundary values of this interval represent pure states of the each of the molecule species. Any intermediate value of the order parameter describes the relative concentration of a particular molecule species in a mixture. The concept of the order parameter can be extended to be used in the phase transition of a single component fluid, where n_1 and n_2 now represent the particle densities in the domain. For instance, the density of particles defines the vapour and the liquid phases of a substance.

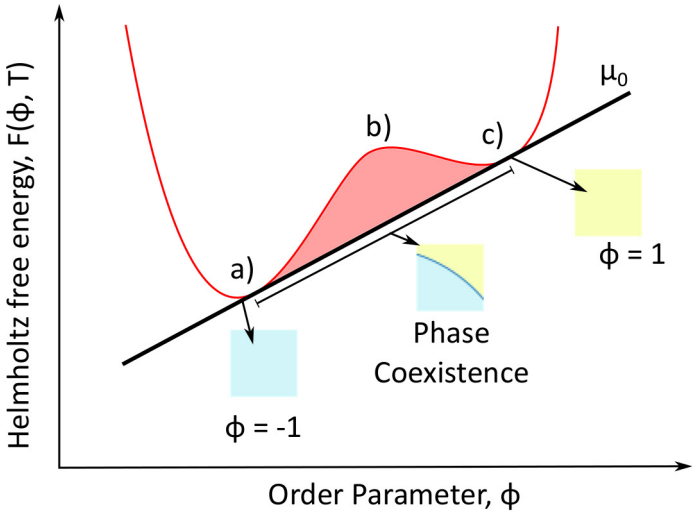

Figure 2.12: Helmholtz free energy of a binary mixture. a) Free energy minimum corresponding to the phase defined by $\phi = -1$. b) Region where the mixture is in phase coexistence, $-1 < \phi < 1$. c) Free energy minimum corresponding to the phase defined by $\phi = 1$.

In liquids, particles are held together by attractive forces as discussed in Section 2.2.1 and interact with each other through collisions. If the cohesive forces between molecules of different species is weaker than the ones of the same species, the mixture tends to separate into differentiated phases. This is the main reason why mixtures are normally less stable than pure phases [88].

Now consider a phase transition system that is reaching equilibrium in a fixed the volume and at constant temperature. Under these conditions, the expression of the free energy that must be minimised is the Helmholtz free energy, $\mathscr{F}$, which one can express for the stationary values of the free energy of the molecules as

$$d[\mathscr{F}(\phi, T) - \mu_0 \phi] = 0, \tag{2.46}$$

where μ_0 is a Lagrange multiplier that allows you to do Equation 2.46 without falling into the trivial solution of F = 0. As a result, $\mu_0 = d\mathscr{F}/d\phi$ and defined as the equilibrium chemical potential of a multiphase system. The free energy of the system can be visualized in Figure 2.12, where there are two energy minimum values ((a) and (c)) which define the phases while the phase coexistence region, shown in (b), the energy values show an unstable homogeneous mixture. Note that the energy profile defined by μ_0 is below the unstable mixture region, explaining why mixtures tend to separate into separate phases.

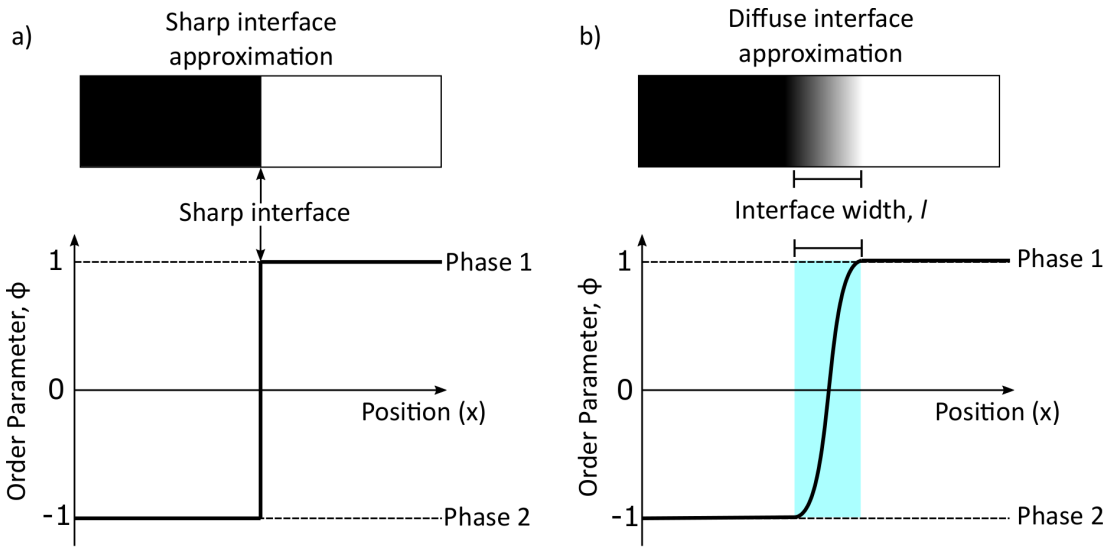

Figure 2.13: Visualization of the sharp and diffuse interface approximations. a) Sharp interface approximation. b) Diffuse interface approximation.

2.6.2 The sharp interface approximation

The sharp interface approximation considers the interface between phases as infinitesimally small, where the differences between two different phases are absolute. The interface in this approximation is a two dimensional boundary, as seen in Figure 2.13(a), subject to a continuous flow velocity and balanced by a pressure normal to the interface surface.

In this approximation, the Helmholtz free energy, $\mathscr{F}$, for a capillary system is defined as [5, 43]

$$d\mathscr{F} = S^* dT - pdV - \gamma dA, \tag{2.47}$$

where S^* is enthropy, V is volume, N is the number of particles and A is the surface area of the interface.

Assuming that the force density stemming from the surface energy is balanced by the change in pressure, one can apply the Gibbs-Thomson condition [89]. This condition relates the Laplace pressure (Equation 2.4) with changes in the order parameter, $\Delta\phi$, so that small changes of chemical potential, $\Delta\mu$, close to the interface are defined as

$$\Delta\mu = -\frac{2\gamma C}{\Delta\phi}, \tag{2.48}$$

where C is the curvature of the interface.

2.6.3 The diffuse interface approximation

In reality, phase transitions from one state to the other are not infinitely sharp since the strength of interactions between molecules depends on the distance between them. This is especially true in liquids since small thermal fluctuations induce flows in the liquid, meaning that liquid molecules cannot remain static and the interactions at the interface are continually changing. Hence, liquids cannot have a sharp interface in equilibrium [90], which implies that the order parameter must adopt intermediate values and change according to the influence of molecular interactions at the interface as a function of distance, as seen in Figure 2.13(b). The distance of influence of the interface is a characteristic length referred in the literature as the interface thickness, l. There have been works that have measured the interface thickness of simple liquids, determining it to be only a few nanometres in length [85, 89, 90].

Under this model, the interaction between molecules is dependent on the spatial energy contribution in the order parameter. Hence, the order parameter turns into a scalar field, also known as the phase field or $\phi = \phi(\mathbf{x})$, where $\mathbf{x}$ is a vector in the domain and (from this point onward, bold letters indicate vectorial notation). Close to the interface between phases, the phase field is determined by a hyperbolic tangent, hence

$$\phi(\mathbf{x}) = \phi_{eq} \tanh(\frac{x}{l}) \tag{2.49}$$

where ϕ_{eq} is the bulk equilibrium order parameter.

The Helmholtz free energy, $\mathscr{F}$, and the capillary behaviour of the droplet for the diffuse interface approximation and the Lattice Boltzmann simulations in Chapter 5 are defined as

$$\mathscr{F}[\rho, \phi] = \int_V [\psi(\phi, \nabla\phi) + \rho c_s^2 \log\rho]\, dV + \int_{\delta V} \zeta(\phi) dS, \tag{2.50}$$

where ρ corresponds to the density number of particles per unit volume, c_s corresponds to the speed of sound as defined in the Lattice Boltzmann system and ϕ corresponds to the phase field, such that $\phi > 0$ indicates the droplet and $\phi < 0$ the surrounding phase, thus defining $\phi = 0$ the interface between the two fluid components. The first term on the right hand side of Equation 2.50 is the volumetric contribution to the energy describing the interaction between the components of the fluid. This interaction energy is defined as,

$$\psi(\phi, \nabla\phi) = \frac{3\gamma_0}{\sqrt{8}l}\left(\frac{1}{4}\phi^4 - \frac{1}{2}\phi^2 + \frac{1}{2}l^2|\nabla\phi|^2\right), \tag{2.51}$$

which corresponds to a double-well potential with minima at $\phi = \pm 1$ which correspond to the saturation values for a flat interface. The terms γ_0 and l correspond to the surface tension and interface thickness, respectively, in thermodynamic equilibrium. The following term in the integrand, which includes the density of the fluid, corresponds to the ideal-gas contribution. The second integral represents the free energy contribution from the interaction of the fluid and the solid surface, δV, where $\zeta(\phi)$ is a function that imposes the wetting condition.

Under this model, the corresponding equations of state are defined as

$$\mu_\rho = \frac{\delta \mathscr{F}}{\delta \rho} = c_s^2(\log \rho + 1), \tag{2.52}$$

and

$$\mu_\phi = \frac{\delta \mathscr{F}}{\delta \phi} = \frac{3\gamma}{\sqrt{8}l}(\phi^3 - \phi - l^2\nabla^2\phi), \tag{2.53}$$

which are the chemical potentials of the ideal gas and the fluid mixture interaction, respectively. One can express these equations in terms of the partial pressures, for the ideal gas pressure this is defined as

$$p = \rho\mu_\rho - \rho c_s^2 \log \rho = \rho c_s^2, \tag{2.54}$$

and for the capillary stresses

$$\mathbf{P} = (\phi\mu_\phi - \psi)\mathbf{I} + \frac{3\gamma l}{\sqrt{8}}\nabla\phi\nabla\phi^T. \tag{2.55}$$

Therefore, the total pressure, Π, is the sum of both contributions which yields

$$\Pi = p\mathbf{I} + \mathbf{P}. \tag{2.56}$$

Equation 2.54 is often referred as the hydrodynamic pressure and is built into the Lattice-Boltzmann. Additionally the phase field dependent equation of state is equivalent to the ones used in previous notation and is referred as $\mu_\phi = \mu$ for consistency.

To obtain the energy cost of transitioning between the two phases can be obtained from Cahn & Hilliard's work on interfacial energy [85] where the surface tension is defined as

$$\gamma \overset{\text{def}}{=} \int [\psi(\phi, \nabla\phi) - \mu_0\phi + p_0]dx, \tag{2.57}$$

where μ_0 is the value of the chemical potential at equilibrium and x is denoted as the normal coordinate to the interface of the phases.

The binding energy, $\zeta(\phi)$, is necessary to impose the wetting condition of the liquid onto a solid interface by introducing a parameter called the wetting potential, χ, which induces an increment in the energy of the liquid proportional to the contact area with the solid interface. Cahn and Briant, *et al.* [91, 92] found that the expression of the binding energy can be given

as

$$\zeta(\phi) = -\chi\phi, \tag{2.58}$$

where χ is a function dependent on the equilibrium contact angle and is known as the wetting potential, θ_e, the liquid does with the solid, which reads as [91, 92]

$$\chi(\theta_e) = \frac{3}{2}\gamma \operatorname{sgn}\left(\frac{\pi}{2} - \theta_e\right) \sqrt{\cos\left[\frac{\arccos(\sin^2\theta_e)}{3}\right]\left[1 - \cos\left[\frac{\arccos(\sin^2\theta_e)}{3}\right]\right]}. \tag{2.59}$$

This equation allows the model the interaction of a droplet sitting on a surface at a defined equilibrium contact angle.

2.7 Numerical methods

Since the focus of this work is not on the development of a Lattice Boltzmann Method infrastructure, the framework used in this thesis is one developed by Élfego Ruiz-Gutiérrez [81–83]. Hence, a general overview of computational fluid dynamics, the governing equations involved and the framework of the Lattice Boltzmann method are reviewed in this section.

2.7.1 Computational fluid dynamics

A fluid is a substance that continually deforms under stress, it resists deformations only lightly because of viscosity and can adopt the shape of any container into which it flows. Up until 1960, fluid dynamics was understood from a perspective of a "two-approach world" where problems regarding fluids would be focused on from either a purely experimental or theoretical perspective [93]. However, with the development of accurate and fast-processing numerical solvers has enabled to add yet another perspective in fluid dynamics, this branch of research is known as Computational fluid dynamics (CFD). Since then, CFD has become a reliable and important tool in research to understand fluid mechanics to the point that CFD now bears the same importance in the field of fluids to merit the description of a "three-approach world" [93].

The main idea in CFD is to numerically approximate solutions to the governing equations of the continuous mechanics used to describe fluid dynamics. This is generally done by providing a solution to the Navier-Stokes equations to the determine the behaviour of the fluid. One can approach computational fluid dynamics on three different relevant length scales, as seen in Figure 2.14: the macroscopic, the mesoscopic and the microscopic approach[94].

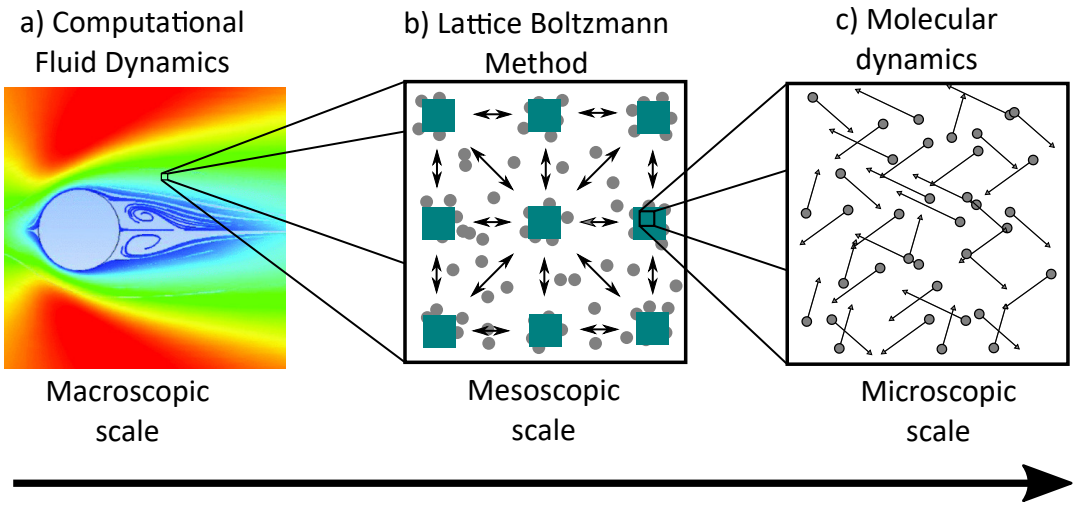

Figure 2.14: Scale of computational approaches to CFD. a) Classic CFD uses macroscopic quantities to describe the motion of the fluid, example image taken from Alhamad *et al* [3]. b) The Lattice Boltzmann Method uses discrete particle populations (black arrows) around lattice nodes (green squares) to model fluid motion. c) Molecular dynamics aims to track the kinetic behaviour of all individual particles in time.

The macroscopic approach aims to describe the dynamics of fluids using continuum mechanics. In this scope, this approach aims to solve the Navier-Stoke equations using macroscopic tangible quantities such as the fluid velocity, pressure and density [94]. However, this approach comes at a cost, since a macroscopic standpoint ignores the molecular nature of matter. This approach has been successful in the modelling of fluids but is not as effective when it comes to modelling turbulent or multiphase flows.

The microscopic approach aims to track the kinetic mechanics of every molecule in the system to simulate the flow of a fluid [95], as seen in Figure 2.14(c). Due to the high discretization, the mechanics followed in this kind of approach are more akin to those in Newtonian dynamics, rather than continuum ones such as the Navier-Stokes equation [94]. Although this methods are highly effective in the accurate simulation of fluids, the biggest disadvantage comes from the high computing power required to run simulations with a significant amount of molecules.

The Lattice Boltzmann Method is a mesoscopic approach that lies in between the macroscopic and microscopic scales. In the mesoscopic scale descriptions aim to describe the dynamics of fluid by tracking distributions or representative groups of molecules acting upon pseudo-particles in a lattice or an off lattice (Figure 2.14(b)). Although the discretization of the fluid system is higher than in macroscopic approaches, mesoscopic approaches are described using kinetic theory which are the main mechanics in the Lattice Boltzmann method [94].

2.7.2 General description of the Lattice Boltzmann Method

The Lattice Boltzmann Method fluid dynamics simulator aims to numerically solve the Boltzmann equation using kinetic theory [96] and describes the system at a mesoscopic level. The Boltzmann equation, which arises from the Kinetic Theory of Gases [97], is a statistical description of the evolution of a fluid by means of the a distribution function, $f_q(x)$, that corresponds to the mean density of particles found at an instance in time t in a discrete position x and a velocity c_q [83]. The discretised form of the Boltzmann equation is what is referred to a the Lattice Boltzmann equation [94, 98].

The Lattice-Boltzmann Method consists of two main steps [80, 83, 94], the first one is called the streaming step which describes the mean density of particles in a given position and velocity at a certain time and is given by the distribution function

$$f_q(x+c_q,t+1) = f_q^*(x,t). \tag{2.60}$$

The second step is called the collision step, which along post-collision terms, describes how the distribution of particles has changed due to interactions in the streaming step. The distribution function associated with the collision step is expressed as follows

$$f_q^*(x,t) = f_q(x,t) + \Xi[f]_q + S_q, \tag{2.61}$$

where $\Xi[f]_q$ is the collision operator and S_q is the sources term.

During the streaming step, the particle populations interact with neighboring lattice nodes by means of the velocity c_q over a unitary time step such that $x \to x + c_q$. This defines a set of velocities associated with neighboring lattice points (depending on the dimension of the domain) in the form of $c_q \in \{c_q\}_{q=0}^{Q-1}$. The result of this interaction are a Q D-dimensional integer vectors that describe the connectivity between the lattice points. This is synthesized by the Q-D notation in the Lattice Boltzmann model. For the case presented in Figure 2.14(b) and the cases in Chapter 5, the corresponding notation is $D2Q9$ in the Lattice Boltzmann model.

On one hand, the collision operator in Equation 2.61 is defined using the Multiple-Relaxation Time (MRT) scheme [99], where a local equilibrium distribution function, f_q^e, is defined. This function defines different relaxation rates for each component of the distribution function. The collision term bears a significant amount of importance in physical terms since it enables the user to tune trasport coefficients such as the viscosity and thermal conductance [83].

The source term in Equation 2.61, on the other hand, can take many forms which depend on the type of sources the user wants to be considered in the simulation, for instance, defining sources of mass, forces, or stresses.

Integration of the Navier-Stokes equations

From the Navier-Stokes equation (Equation 2.41), it is possible to obtain macroscopic parameters such as the density and the velocity. By using the Lattice Boltzmann Method to numerically integrate the Navier-Stokes equations, one can define the expression of macroscopic variables in terms of the distribution function [83]. The mass density flux density yields

$$\rho = \sum_{q=0}^{Q-1} f_q, \tag{2.62}$$

and the momentum of the density, from where one can obtain the velocity field, is defined as [81]

$$\rho u = \sum_{q=0}^{Q-1} c_q f_q, \tag{2.63}$$

Integration of the Cahn-Hilliard

The Cahn-Hilliard equation (Equation 2.44) allows one to obtain the value of the phase field associated to the simulation. In order to compute this phase field, a second distribution function, g_q, of similar form as Equations 2.60 and 2.61 where the moments and collision parameters differ from f_q. The zeroth moment of this distribution function defines the phase field as [81]

$$\phi = \sum_{q=0}^{Q-1} g_q, \tag{2.64}$$

Equations of state

To calculate the values of the pressure tensor field (Equation 2.56) and the chemical potential (Equations 2.53), it is necessary to obtain the gradient and the Laplacian of the phase field as defined in the Lattice Boltzman Method. These can be approximated by using the finite difference stencils, which for the gradient yields

$$\nabla\phi \approx \frac{1}{c_s^2} \sum_{q\neq 0} w_q c_q \phi(x + c_q), \tag{2.65}$$

and for the Laplacian

$$\nabla^2\phi \approx \frac{2}{c_s^2} \sum_{q\neq 0} w_q [\phi(x + c_q) - \phi(x)], \tag{2.66}$$

where w_q is used as weighting factors that optimise the accuracy of the approximation [100].

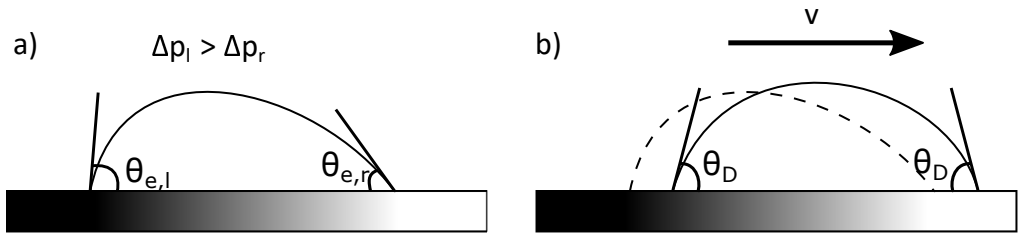

Figure 2.15: Wettability gradient driven motion. Droplet sitting on a surface with a wettability gradient (Colour gradient). a) On the wettability gradient, the contact points of the droplet have different values for the equilibrium contact angle, $\theta_{e,l}$ for the left contact point of the droplet of the droplet and $\theta_{e,r}$ for the right contact point. b) Droplet motion is generated to compensate for the laplace pressure difference.

2.8 Self-propulsion mechanisms of droplets on solid surfaces

Hygrotaxis is a novel mechanism of droplet self-propulsion based on the effects a relative humidity gradient field may have on a pure liquid droplet of the same species as the vapour. This section provides an overview of transport phenomena in the literature which serve as a base to the study of hygrotaxis.

2.8.1 Transport phenomena for self-propulsing droplets

In the absence of strong drag forces such a high contact angle hysteresis on solid surfaces, molecular forces become strong enough to drive motion of the droplets [6]. For hygrotaxis, there are two main mechanisms of transport that have the potential to generate motion on the surface: wettability gradients and surface tension gradients.

Wettability gradients

Wettability gradients affect the wetting behaviour of a liquid on a solid by means of changing the surface chemistry or the roughness of the surface [5, 7]. The general principle behind the motion of this type of transport can be appreciated in Figure 2.15. When a droplet is resting on a wettability gradient, the surface tension changes along the solid surface changes. As a consequence of this, the equilibrium contact angle on left and right contact points of the droplet, $\theta_{e,l}$ and $\theta_{e,r}$ respectively, are different since the balance of surface tensions at those points differ as predicted by the Young-Dupré equation (Equation 2.6) (Figure 2.15(a)). This difference in contact angle changes the curvature along the interface of the droplet, and since the curvature of the droplet is larger at the trailing edge, it will experience an overpressure defined by the Laplace pressure (Equation 2.4). This pressure gradient drives the motion of the droplet towards more wettable regions, defining a dynamic contact angle θ_D while in motion.

The driving forces in wettability gradients can either be dependent on the surface roughness or on the chemical composition of the surface. In the case of surface roughness, the droplet can be in a Wenzel or Cassie Baxter state, as mentioned in Section2.3. However, regardless of which state the droplet rests on the rough surface, r_w and ϕ_s are both functions of surface texture, which can generate surface energy gradients to generate motion. Hence, the net driving force, F_D, in a surface roughness gradient can be given by [7]

$$F_D = \pi R^2 \gamma \frac{d\phi_s}{dx}(\cos\theta_e + 1)\hat{\mathbf{e}}_\mathbf{x}, \tag{2.67}$$

which can be given terms of the curvature of the droplet and the Laplace pressure as

$$F_D = \pi R^2 \frac{\Delta p}{C}\frac{d\phi_s}{dx}(\cos\theta_e + 1)\hat{\mathbf{e}}_\mathbf{x}, \tag{2.68}$$

where $\hat{\mathbf{e}}_\mathbf{x}$ is the unit vector in the direction of the wettability gradient.

In the alternative case, wettability gradients are achieved by changing the chemical composition of the surface. On this type of surfaces, the equilibrium contact angle is a function dependent on the position of the interface of the droplet. The driving force in this case is defined as [7]

$$F_D = \pi R^2 \frac{\Delta p}{C}\frac{d\cos\theta_e}{dx}\hat{\mathbf{e}}_\mathbf{x}. \tag{2.69}$$

Surface tension gradients

The general concept in this type of motion is based on the motion via Marangoni flows inside the droplet generated by gradients in surface tension of the liquid-gas interface γ [7, 15, 16]. These type of flows force the droplet to move from low to high values of surface tension. The motion associated with this type of gradients is subject to the viscous stress that the Marangoni flows enact on the base of the droplet [101]. Since surface tension represents an energy per unit area, one can generate surface tension gradients through thermal differences between the droplet and solid surface and concentration differences between 2 immiscible liquids with different surface tensions.

In the case of thermal differences as a source of surface tension gradients and negligible effects from the solid surface, the driving force can be expressed as [7]

$$F_D = \frac{\pi}{2} R^2 \frac{d\gamma}{dT}\frac{dT}{dx}\hat{\mathbf{e}}_\mathbf{x}. \tag{2.70}$$

Note that since the $\frac{d\gamma}{dT} < 0$, which means that the droplets affected by this mechanism always move towards colder regions.

In the case of concentration gradients, it is assumed that the droplet is in an isothermal system. Therefore, the driving force associated with this type of motion can be expressed as the more general expression of Equation 2.70, hence

$$F_D = \frac{\pi}{2} R^2 \frac{d\gamma}{dx} \hat{\mathbf{e}}_{\mathbf{x}}. \tag{2.71}$$

2.8.2 Applications

The ability to move droplets without having to spend mechanical energy opens the door to many potential applications which highlight the importance of this subject, not only from a fundamental perspective, but also from a practical one. Some of the practical uses of self-propulsion of droplets include [7]:

- *Water harvesting:* Surface geometry has been proven to have an influence on condensation of water vapour and enable the transport of droplets towards collection points. This effect is significantly inspired by nature, such as the surface roughness induced condensation and transport of water on the exo-skeleton of the namibian dessert beetle or the capillary transport of water in the spines of cacti [30]. This has resulted in man-made systems to collect water from vapour sources like fog [102].

- *Heat transfer:* Droplet motion can be used to improve the performance of heat exchangers by optimizing droplet removal from surfaces to maximize the cooling effect [103].

- *Microreactors:* Droplets can be used as small scale mixers. For instance, magnetotaxis, which refers to wetabillity gradient formed by droplets of magnetic fluids, was used to successfully synthesize nylon 6-6 on SLIP surfaces[104].

- *Deposition and Printing:* Moving droplets containing particles like colloids and polymers can be used to deposition devices of these substances [105]. This offers alternative printing options to current printing techniques on flat surfaces.

- *Medicine:* Droplet transport has found a specialized application in the field of medicine since it exhibits broad applicability in *in-vitro* biological and clinical assays [7].

These are some of the applications of these type of transport of droplets. However, this field continues to evolve and further advances and applications are developed continuously [7].

2.9 Conclusion

This chapter has given an overview of the key concepts and relevant literature on the theory behind the interaction of liquid droplets and solids. The understanding of wetting and capillarity, the forces involved in the motion of droplets on surfaces and the important surface tension is key in order to study an effect such as hygrotaxis, the motion generated by a gradient in relative humidity. Hygrotaxis is an effect which depends on the molecular interaction of the liquid with its surroundings. This forces are normally negligible due to the drag forces generated by the surface are larger than the molecular driving forces. For this reason, this chapter highlights the importance of pinning-free surfaces, with a focus on SOCAL surfaces due to their unique combination of low static friction qualities and the conservation of a liquid-solid contact line. Relative humidity has a fundamental effect on the evaporation/condensation dynamics and, thus, the theory surrounding evaporation of droplet on surfaces is reviewed.

This PhD project also includes theoretical studies of this effect via the Lattice Boltzmann simulations of the phase change of liquid droplets subjected to chemical potential gradients. Hence, multiphase thermodynamics are reviewed along with a broad description of the Lattice Boltzmann method.

This chapter finishes by exploring the possible mechanisms that may be involved in hygrotaxis, where concepts regarding the possible relative humidity driven gradient effects may induce the motion of a droplet on a pinning-free surface.

Chapter 3

Materials, methods and experimental techniques

This thesis focuses on Slippery Omniphobic Covalently Attached Liquid (SOCAL) surfaces. These surfaces are a type of ultra-smooth surface consisting of an acid-catalyzed polycondensation of polymer chains onto the surface, rendering a solid liquid-like coating that exhibits remarkably low static friction. This chapter begins by providing a detailed description of the necessary steps to produce SOCAL surfaces on glass substrates. This includes the cleaning and preparation of glass substrates for the SOCAL procedure and bespoke equipment built to control ambient conditions during the procedure. Then, a description of the coating process for flat substrates is described, providing justification for the coating parameters chosen to coat the surfaces. Additionally, a method developed to coat the inside of thin capillary tubes ($\sim 1\,\mathrm{mm}$) with SOCAL is also presented and detailed.

The following section presents two field standard methods of surface characterisation based on surface wettability to quantify surface friction on ultra-smooth surfaces: the volumetric variation method and the sliding angle method. Initial results of surface characterisation via the volumetric variation method confirms that the SOCAL coating parameters chosen deliver results comparable to those in the literature. These results, supported by literature values of the sliding angle on SOCAL surfaces, highlight unique surface friction attributes of these surfaces, where they exhibit remarkably low static friction behaviour while presenting slow moving contact lines.

In this thesis, two methods of surface characterisation are developed and presented: the contact line relaxation method and the capillary action method. In the former, the static friction of a surface is characterized by measuring the advancing and receding angles asymptotically, using the relaxation of a moving contact line on SOCAL where comparisons to the volumetric variation method and the consequences in the dynamics of contact lines of this effect are explored in Chapter 4. In the latter, the advancing and receding contact angles are measured by using the capillary force driven rise and descent of a liquid column inside capillary tubes.

The third section of this chapter describes the image processing methods used to obtain characteristic parameters, such as the apparent contact angle and the base radius, from experimental and simulation raw data.

3.1 Surface production

3.1.1 Substrate cleaning procedure

It is important to thoroughly clean the substrates, or samples, before moving into the coating procedure since this pre-coating process ensures that the surface of the substrate is free from any contaminants and small particles which may affect the consistency of the SOCAL surface. The samples used in this work are standard laboratory glass slides (Width $= 25\,\mathrm{mm}$, Length $= 75\,\mathrm{mm}$, thickness $= 1\,\mathrm{mm}$). New samples are taken out of the packaging and thoroughly rinsed with De-ionised (DI) water in order to remove any large particles from the surface. Then, the samples are placed vertically in a slide holder, ensuring that the samples are not in contact with each other. A 2% Decon90 (Decon Laboratories Limited) and DI water cleaning solution is prepared inside a standard $500\,\mathrm{mL}$ Pyrex glass laboratory beaker. The sample holder containing the slides is then submerged into the solution and placed inside an ultrasonic bath (Fisherbrand$^{\mathrm{TM}}$ S-Series) at room temperature. The sonication agitates the sample at ultrasonic frequencies, easing the removal impurities from the surface. The samples are sonicated for 30 minutes as indicated in the manufacturer guidelines of Decon90, which ensures that trace contaminants are removed from the sample surfaces which may not have been washed off during the DI water rinsing. After the first sonication, the sample holder is removed from the cleaning solution and submerged into another beaker filled with DI water and sonicated to remove any trace of Decon90 from the surface of the substrates.

Once the sonication process is finished, the samples are removed from the solution to be rinsed individually with solvents. Each sample is thoroughly rinsed in a fume-cupboard with acetone (Fisher Chemical) and Isopropyl Alcohol (IPA) (Fisher chemical) and DI water. Acetone is a highly volatile solvent which helps the removal of any particles or detergent agent left after the sonication process, however, if not rinsed properly, it can leave chemical residues on the surface. Acetone is then rinsed off with IPA since this substance does not leave chemical traces on the surface once it evaporates. The sample is then dried and inspected by eye for any possible chemical residues left, which appear against the light as opaque streaks on the surface. If the sample still shows signs of chemical residues after inspection, the acetone and IPA rinsing process is repeated.

Once the cleaning process is finished, the clean samples are stored individually in laboratory grade petri dishes to await the SOCAL procedure.

3.1.2 Humidity chamber

In order to produce SOCAL surfaces, careful control of the relative humidity environment is required [4, 62]. For this purpose, a bespoke humidity chamber was built to be used inside a fume-cupboard. The humidity chamber is built using transparent plastic perspex (thickness = $3\,\mathrm{mm}$) which is laser cut to form a box. These pieces are then bonded together with capillary glue which seals the gaps in the chamber and ensures that there are no unintended leaks of air. Figure 3.1 shows the schematic of the function of the relative humidity control system. Compressed air at $\sim 1.3\,\mathrm{bar}$ is fed into a splitter (Figure 3.1(a)) which guides the air into two air lines: a humid line and a dry line. In the humid line, air is passed through a valve controlled by a stepper motor, regulating the amount of air that flows through the humid line (Figure 3.1(b)). The air then goes into a saturation process which consists of passing air through a water reservoir inside a gas washing bottle (Fisher Scientific) (Figure 3.1(e)). In order to ensure that no large droplets pass through into the humidity chamber, the saturated air is passed through a second gas washing bottle to capture large satellite droplets (Figure 3.1(f)). The air is then joined to the dry line to provide saturated air into the environment of the humidity chamber (Figure 3.1(g)).

Similar to the humid line, the dry line is regulated by a valve controlled by a stepper motor and then joined with the humid line to provide dry air into the humidity chamber (Figure 3.1(g)). The stepper motors are controlled by a Raspeberry Pi microcontroller (Figure 3.1(d)) which runs a bespoke program to control the flow rate of air in the airlines via a proportional control system (Figure 3.1(f)). This control system seeks maintain input variable (fixed relative humidity) close to a desired value by adjusting the output. When the relative humidity is off target, the microcontroller sends a signal to the stepper motors to adjust the flow of saturated air into the humidity chamber. This relative humidity control system allows the environment inside the humidity chamber to be controlled between $10\% - 80\%$ relative humidity with an error of $\pm 1\%$ of the target value.

3.1.3 Preparation of SOCAL surfaces

The SOCAL process was first developed seminal work by Wang & McCarthy in 2016 [62] and has obtained increasing attention since its publication [4, 52, 62, 63, 106–109]. The general concept of the SOCAL coating lies in the rapid condensation of PDMS chains on the surface of a substrate. This is achieved via an acid-catalyzed chemical reaction between an activated surface and a SOCAL reactive solution to allow polymer chains to be deposited in the surface of the substrate. The SOCAL reactive solution is made out of a mixture of IPA, dimethyldimethoxysilane (DMDS) and sulphuric acid (90, 9 and 1% wt., respectively) and must be mixed in that order to avoid exothermic reactions.

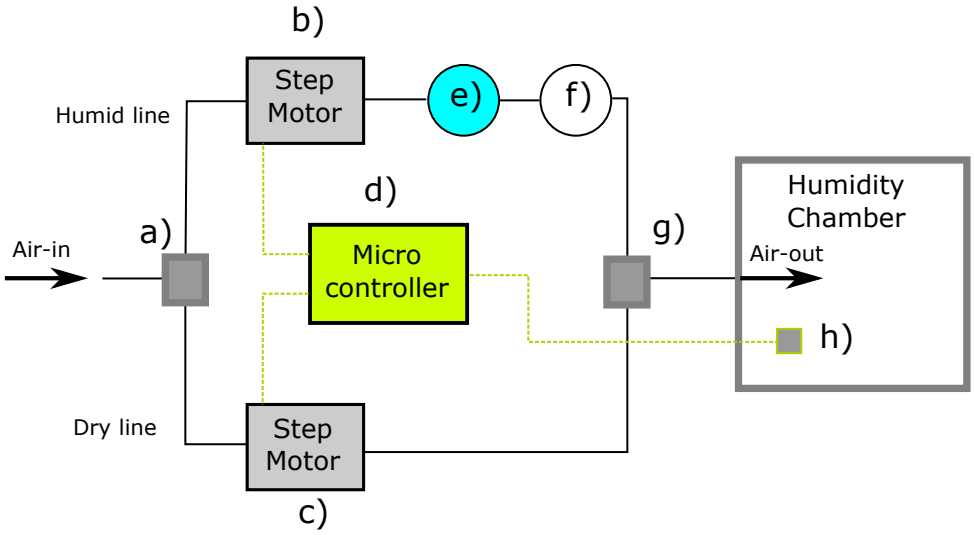

Figure 3.1: Humidity chamber schematic. a) The airflow is split into 2 lines, a humid air line and dry air line. b) The humid air line is regulated by a stepper motor controlled valve. c) dry air line regulated by a stepper motor controlled valve. d) Microcontroller regulating the air valves. e) The humid air line is saturated by passing air through water reservoir inside a gas washing bottle (blue circle). f) After saturation, large droplets in the air are captured in a second empty gas washing bottle (white circle). g) The humid and dry air lines merge into one to provide the humidity chamber with the air source. h) Relative humidity and temperature sensor controlling the stepper motors through the use of the microcontroller.

The SOCAL reactive solution is then prepared inside a $100\,\mathrm{mL}$ screw top bottle, with a bottle-mouth wide enough to allow the unimpeded passage of a laboratory glass slide vertically. To prepare the reactive solution, $92\,\mathrm{mL}$ of IPA is measured in a $100\,\mathrm{mL}$ graduated cylinder and poured into the screw-top bottle. Then, $8\,\mathrm{mL}$ of DMDS is withrawn with a $10\,\mathrm{mL}$ syringe inserted into the membrane of the air-tight DMDS container. The DMDS in the syringe is then added to the IPA and stirred manually using a glass stirrer for a period of $30\,\mathrm{s}$. The following step is to use a micrometric pipette to carefully extract $390\,\mu\mathrm{L}$ of sulphuric acid from its container. The solution is slowly stirred as the acid is added slowly, drop by drop, to avoid a potentially dangerous exothermic reactions. Then the screw-top bottle is closed and the solution is left to rest for 30 mins at room temperature before use. To avoid inconsistencies stemming from the hygroscopic nature of DMDS, the solution was re-made once the current batch exceeded 3 months from the creation date, ensuring that the reactive solution remains fresh and viable.

Once the substrates are cleaned and the reactive solution has been prepared, the coating process may begin. The samples were coated according to the method used by Wang & McCarthy [62]. To obtain surfaces with reproducible low-contact angle hysteresis attributes, there are four main phases SOCAL coating procedure, as seen in Figure 3.2. The first phase consists of activating Oxygen-Hydrogen (OH) radicals on the surface of the substrate via air

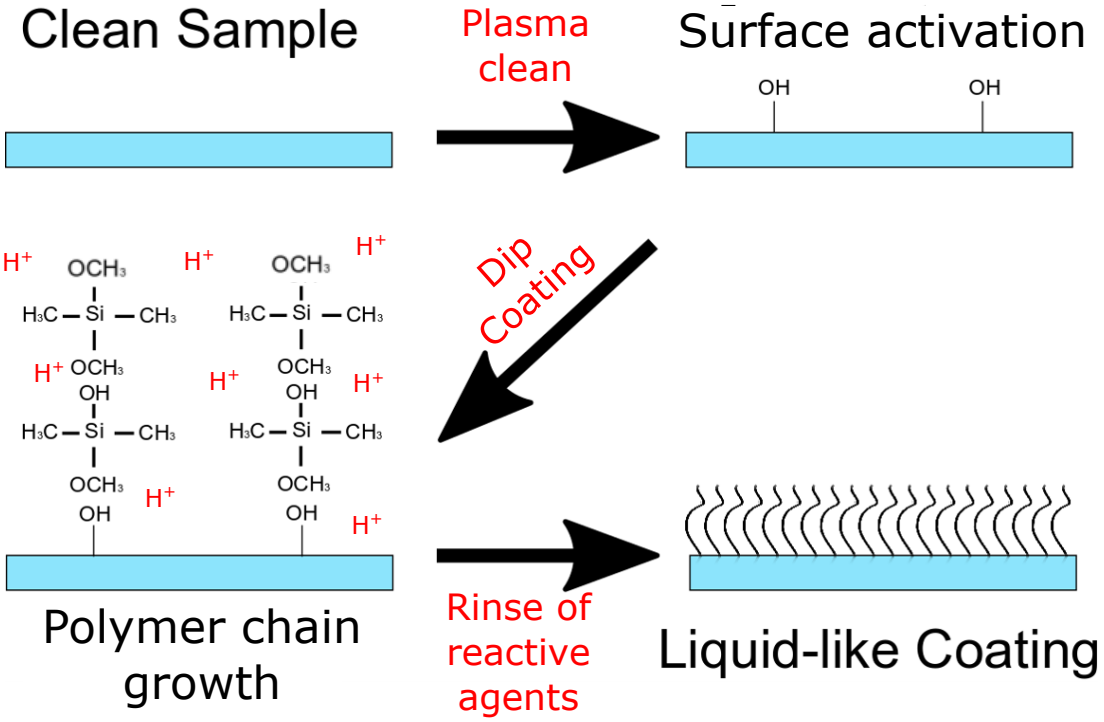

Figure 3.2: SOCAL process diagram. The surface of the clean sample is activated using exposure to air plasma, this opens surface OH radicals. The sample is dipped into the SOCAL solution which begins the condensation of PDMS chains on the surface. Once the chains have been created, the surface is rinsed from any acid and left over reactive agents. This leaves a hair-like flexible nanometric coating on the surface.

plasma exposure. In the second phase, the activated sample is dip-coated in the SOCAL reactive solution and slowly removed at constant speed. Once the sample is removed from the reactive solution, the third phase consist of letting the sample dry for a fixed amount of time in a temperature and relative humidity controlled environment to allow the rapid formation of the PDMS chains. The fourth and final phase consists of rinsing the coated substrate with Toluene, IPA and DI water to stop the chemical reaction and remove any left-over unreacted substances from the surface of the sample. This leaves a nanometric, flexible, hair-like landscape on the surface of the sample, giving the surface the so-called liquid-like qualities as described in Wang & McCarthy's work [62].

To produce the SOCAL surfaces, there are key parameters that must be optimized which include: plasma power, plasma exposure time, relative humidity, temperature and drying time. In this work, the SOCAL production parameters used are based on the optimization parameters that Armstrong *et al* utilized to study water droplet evaporation on SOCAL surfaces [4]. A clean sample is taken and placed inside a Henninker plasma cleaner (HPT-100) at a power

of 30 W for 30 min. The long exposure of the surface to plasma ensures that the OH radicals are added consistently throughout all the substrate. If the surface is not activated properly, the PDMS chains do not form uniformly and may induce pinning by patching or chain length variation on the surface [4, 62].

The activated sample is then hand dipped into the SOCAL reactive solution. The sample is left submerged in the solution for $5\,\mathrm{s}$ before it is slowly removed at a speed of $\sim 5\ \mathrm{mm/s}$.

The dipped substrate is then transferred to a bespoke relative humidity chamber (Figure 3.1) and left to dry at 60% RH and at room temperature of $25\,^{\circ}\mathrm{C}$ for 20 min. During this period, the rapid polycondensation of DMDS grafts a homogeneous layer of PDMS onto the substrate, as on the bottom-left panel schematics of Figure 3.2. Relative humidity is important since Wang & McCarthy showed that the variation of this parameter yields contact angle hysteresis values between 1° and 20° [62]. Additionally, Armstrong *et al* showed that under the drying conditions above, contact angle hysteresis values can be reduced to $\sim 1^{\circ}$ [4].

The last step in this process is the rinsing of the leftover acid and unreacted material from the surface of the sample. The sample is taken with a pair of ceramic tweezers and thoroughly rinsed with a continuous flow of DI water, ensuring that all parts of the surface are rinsed. Then, the sample is subjected to a second rinse using IPA, and again, ensuring to rinse the whole surface. The rinsing process is finished by an additional thorough rinse with toluene (Fisher Chemical). This rinsing process is repeated 3 times before the sample is then placed in a petri dish container and stored for surface characterisation.

3.1.4 Coating of capillary tubes with SOCAL

In literature, there is little research on the coating and characterization of SOCAL surfaces inside tube geometries. However, in 2019, Geyer, *et al.* [110] developed a method to coat the inside of long tubes (1 m) with liquid repellent layers similar to SOCAL, down to an Inner Diameter (ID) of ~ 1 mm. This method consist on the liquid activation of surface radicals in order to coat the surface with water-repellent coatings. In this work, they opted to use liquid activation of surface radicals due to the limited diffusion that plasma treatment encounters when one is dealing with high aspect ratio tube geometries (where aspect ratio = tube length/inner diameter). The higher the aspect ratio, the longer it takes the plasma to travel through the inside of the tube. This is particularly important because homogeneous coating of a surface with SOCAL is dependent on the controlled exposure to air plasma in order to have a well distributed activation of surface radicals, as shown in Wang and McCarthy's work [62].

Nonetheless, in 2021, Zhao, *et al.* [111] published a work on fouling reduction which succeeded in developing a method to coat metallic flat and tube substrates (length = $200\,\mathrm{mm}$, inner diamater = $5\,\mathrm{mm}$) by sintering a layer of silicon dioxide which is reactive with the SOCAL solution. On one hand, the contact angle hysteresis measurements on their flat samples

was measured to be between $3°$-$6°$, comparable to results to other SOCAL surface publications [62]. On the other hand, coated tubes were cut in half and low friction interactions were identified by running a flow on the tubes. Tubes that exhibited low Reynolds numbers were used to compare with uncoated ones and a clear smoothing of the surfaces was observed via Scanning Electron Microscopy (SEM) imaging. Although this method offers great potential in the coating of tubes, no direct measurement of the SOCAL surface inside the tubes has been made. Additionally, this process is limited to materials that are able to withstand temperatures of at least $500\,°\mathrm{C}$ [111], which can limit the applicability of this method.

Length dependent coating

For capillary tubes of 100 mm in length, 1.6 mm in outer diameter and 1.2 mm in inner diameter, a trial and error test determine that an aspect ratio of 0.06 was sufficient to achieve a complete coating of the tube. For aspect ratios larger than this, the coating becomes inhomogenous and the wettability of the inner tube transitions from a hydrophobic configuration to hydrophilic one after $\sim 20\,\mathrm{mm}$. Hence, for the following procedure, the capillary tube length is fixed at $20\,\mathrm{mm}$.

SOCAL process for capillary tubes

Capillary tubes (Outer Diameter (OD) = 1.6 mm, ID = 1.2 mm, length = 100 mm) are sectioned into samples of $20\,\mathrm{mm}$ in length. This is done by creating an imperfection of the crystal structure of the capillary tube by running a thin file on the outer surface of the capillary tube. The imperfection is then tapped lightly to induce a clean break of the glass. The samples are then placed in a separate container to await cleaning.

The cleaning procedure for the capillary tubes is analogous to the cleaning procedure for flat surfaces. Sectioned capillary tubes are submerged in a solution of DI water and detergent (Decon 90-Water, 2% solution) and placed in an ultra-sonic bath for 30 min. The samples are then taken out of the solution and, with the use of a syringe, they are rinsed thoroughly with acetone, IPA and DI water. The samples are then blown dry with an air gun to ensure no solvent traces are left inside the inner surface and then set aside in a container.

Once the capillary tube samples are clean, the OH radical of the surface are activated by exposure to air plasma using a plasma cleaner (Hennniker HPT-100) operating at $30\,\mathrm{W}$ for 30 minutes. The tubes are then immediately removed from the plasma oven with ceramic tweezers and hand dipped into SOCAL solution. The samples are then slowly removed at a speed of $\sim 5\,\mathrm{cm/s}$ and the bottom edge of the tube is pressed lightly against a paper tissue to remove excess liquid via imbibition, ensuring that there is no excess of liquid at the end on the tube to facilitate air flow. The sample is then placed to dry inside a humidity chamber at 60%

relative humidity and at room temperature ($T = 25\,^{\circ}\mathrm{C}$) for 40 minutes ensuring that air is able to flow as it dries. Subsequently, the sample removed from the humidity chamber and rinsed vigorously with toluene, IPA and DI water to stop the SOCAL reaction and remove unreacted material. The sample is then blown dry with an air gun and stored in a petri dish.

3.2 Surface characterisation

As mentioned in the previous chapter, the parameter that measures static friction on surfaces is known as contact angle hysteresis, $\Delta\theta$. This quantity is measured by obtaining two characteristic values: the advancing and receding contact angle, θ_A and θ_R, respectively. The difference between these two values is what determines the contact angle hysteresis, as shown in Equation 2.14.

The subtlety of measuring this quantity comes from the definition of the advancing and receding configurations. These configurations are defined as the onset of motion of the contact line, and in order to measure them accurately, Shirtcliffe, *et al.* [34] stated that one must approach these asymptotic values at infinitely slow speeds. This is the reason why most well known characterisation methods try to encapsulate these points with significantly slow moving contact lines to approach this limit and approximate a value of θ_A and θ_R, such as the slow inflation and deflation of a droplet or the careful tilting of a surface to induce motion.

The work in this thesis looks into four methods to determine contact angle hysteresis. The first and second methods are well-studied in the literature: the volumetric variation method [4, 5, 39, 112] and the sliding angle method [2, 38, 39, 113]. The third method is a novel characterisation that was developed in this thesis as a product of the unique static and dynamic friction attributes of SOCAL and is named as the contact line relaxation method. The fourth method is another novel method to measure contact angle hysteresis on SOCAL coated capillary tubes which uses the capillary action to approximate the advancing and receding contact angles.

3.2.1 Volumetric variation method

Consider a sessile droplet of $R < \kappa^{-1}$, resting on the surface at θ_e, with a needle centered and inserted directly on top of the droplet, as seen in Figure 3.3(a). After a stable state is reached, liquid is pumped into the droplet at a fixed flow rate (Figure 3.3(b)) which increases the apparent contact angle θ. The droplet then reaches the threshold advancing contact angle θ_A, the maximum angle the droplet can hold in a stable configuration, which forces the droplet to de-pin, resulting in the motion of the contact line (Figure 3.3(c)). Once the inflation of the droplet is stopped, the liquid is slowly pumped out of the droplet, decreasing the volume of the droplet and forcing the contact angle to decrease (Figure 3.3(e)). As with the pump-in procedure, the contact angle of the droplet continues to decrease until it reaches the receding contact angle θ_R and the contact line begins retract (Figure 3.3(f)).

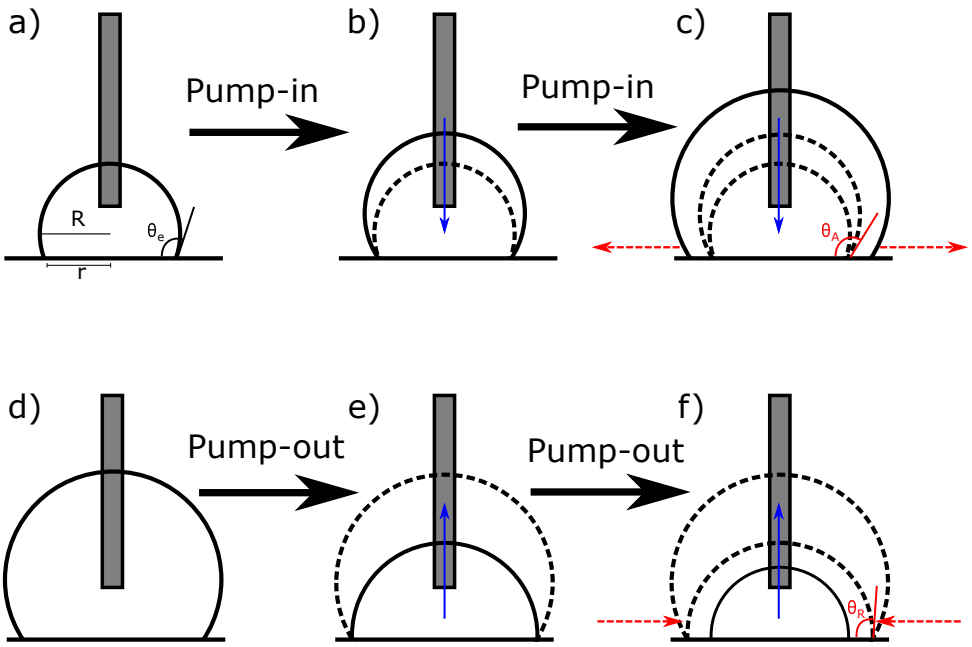

Figure 3.3: Volumetric variation method. a) Sessile droplet on solid surface. b) Inflation of the droplet by pumping in liquid through the needle. c) The droplet reaches θ_A and begins to move. d) Static droplet after pump-in period is stopped. e) Deflation of the droplet. f) The receding angle, θ_R is reached and the contact line moves.

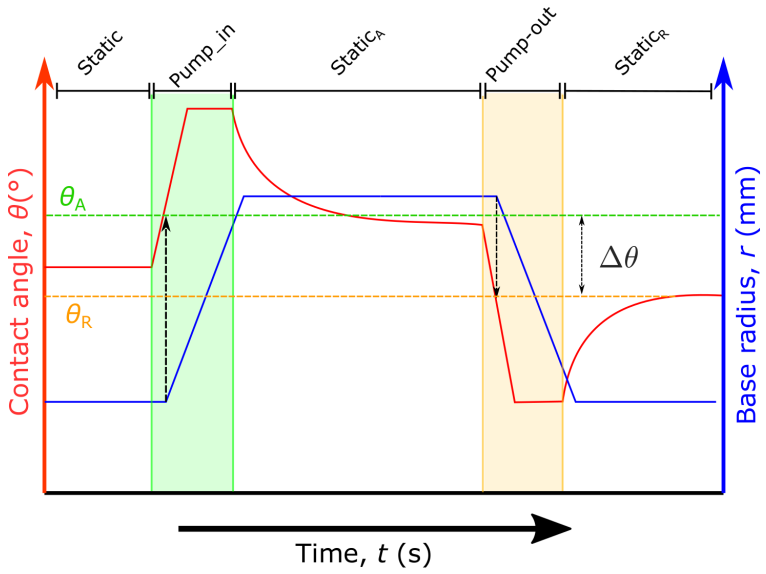

Figure 3.4: Schematic of typical $\Delta\theta$ measured with the volumetric variation method. The advancing angle θ_A is obtained by relating it to the onset of motion of the contact line in the pump-in period (dashed arrow in pump-in region). Analogously, the receding contact angle θ_R is defined as the instance in time where the base radius starts to retract (dashed arrow in pump-out region). The interval defined by these two limits is the contact angle hysteresis $\Delta\theta$.

Table 3.1: Initial θ_A, θ_R and $\Delta\theta$ results using the volumetric variation method. $\Delta\theta$ measurements of 8 different samples created with the production following parameters: $30\,\mathrm{W}$ plasma power, 30 min plasma time, and 20 min drying time at a relative humidity of 60% and a temperature $25\,^{\circ}\mathrm{C}$. Each value represents the average of three separate measurements with the corresponding standard deviation. The lower section of the table is the mean of all the measurements and the standard deviation (s.d).

Sample	θ_A (°)	θ_R (°)	$\Delta\theta$ (°)
1	104.0 ± 0.7	102.3 ± 0.4	1.6 ± 0.9
2	104.0 ± 0.4	102.3 ± 1.0	1.7 ± 1.2
3	104.9 ± 2.5	103.0 ± 1.8	1.9 ± 0.8
4	106.1 ± 0.3	104.0 ± 0.5	2.1 ± 0.6
5	105.1 ± 0.5	104.8 ± 0.2	0.2 ± 0.5
6	107.0 ± 0.6	106.0 ± 0.6	1.0 ± 0.1
7	106.2 ± 0.9	103.9 ± 0.9	2.3 ± 0.5
8	105.2 ± 0.9	104.3 ± 0.2	0.9 ± 0.7
mean (°)	105.3	103.8	1.5
s.d. (°)	1.3	1.4	0.9

Contact angle goniometry is used to obtain the contact angle and the base radius as a function of time [4, 62]. Figure 3.4 shows a schematic of how the results are expected to behave using the volumetric method. When the pump-in period is started, the contact angle increases first, while the base radius remains static. The base radius begins to move an instance in time, which is used to obtain a value of the contact angle to define θ_A. Similarly, in the pump-out period, the contact angle begins to decrease while the base radius remains pinned. θ_R is then measured at the point in time where the base radius is de-pinned and starts to retract. Then, the measured values of θ_A and θ_R are used to define the contact angle hysteresis as in Equation 2.14.

The most important aspect is in this method lies in choosing an appropriate flow rate, $\dot{q}$, to approach the onset of motion of the base radius. Since this method aims to approach an asymptotic limit in the motion of the contact line, the corresponding increase in volume of the droplet must be gradual and slow [34]. This is the reason why most works using this method move the contact line of the droplet at speeds in the scale of $\mu\mathrm{L/s}$ [4, 34, 114].

Table 3.1 shows the results of $\Delta\theta$ measurements using the parameters outlined in the previous section. The average contact angle hysteresis is comparable to that of previous works on SOCAL surfaces [4, 62], indicating that the process of coating has been achieved succesfully. However, error measurements account for a large fraction of the $\Delta\theta$ measurement itself. The limitations and improvements of this method, and particularly on SOCAL, is explored in more detail in Chapter 4.

3.2.2 Sliding angle method

This method of measuring contact angle hysteresis was developed to overcome scenarios where the side profile of the droplet is not clearly visible. For instance, this method is commonly used in LIS surfaces since the triple point of the interfaces is difficult to determine due to the formation of wetting ridges between the lubricating liquid and the liquid droplet. Figure 3.5 shows the procedure to measure contact angle hysteresis using the sliding angle method. A droplet of fixed volume is first placed on a levelled surface and left to reach the equilibrium configuration (Figure 3.5(a)). This surface is then gradually tilted, usually fractions of a degree at a time, creating a tilting angle, θ_{tilt}, with the initial levelled surface. The tilting of the surface forces the left and right contact angle (θ_l and θ_r, repectively) to change along θ_{tilt} (Figure 3.5(b)). θ_l and θ_r will continue to change until a critical tilting angle called the sliding angle, α, is reached, where $\theta_l = \theta_R$ and $\theta_r = \theta_A$, inducing the motion of the droplet down the inclined plane, as seen in Figure 3.5(c). The sliding angle, α, is characterised as the tilting angle at which the droplet begins to move [38, 115] and the dissipative force, F, is defined as [5]

$$F = mg\sin\alpha, \tag{3.1}$$

where m is the mass of the droplet and g is the acceleration due to gravity. This dissipative force is related to $\Delta\theta$ through Equation 2.15, which yields the following relationship.

$$\alpha = \arcsin\left(\frac{2r\gamma(\cos\theta_R - \cos\theta_A)}{mg}\right). \tag{3.2}$$

Note that this method is dependent on the mass of the droplet, so the sliding angle can vary depending on the size of the droplet.

On SOCAL surfaces, comparisons between the volumetric method and the sliding angle method show an apparent difference. For instance, while SOCAL is reported to exhibit low contact angle hysteresis, the sliding angle is apparently larger than one would expect for a surface with such low static friction [116]. This can be appreciated in Figure 2.9(b) in Section 2.3.5, where a water droplet on SOCAL is apparently static even at a tilting angle of 5°. This is significant because superhydrophobic surfaces and LIS both have similar, if not larger, values of contact angle hysteresis to SOCAL surfaces. Therefore, droplets of the same liquid and volume should slide at similar angles. Additionally, an interesting aspect is that at tilting angles of 15°, the droplets on SOCAL move much slower that other ultra-smooth surfaces [2]. This highlights the need to further understand the statics and dynamics of liquid fronts on surfaces such as SOCAL. The relationship of the static and dynamic friction on SOCAL surfaces is further discussed in Chapter 4.

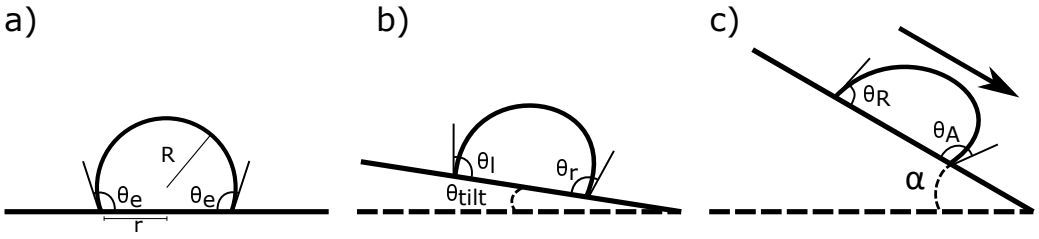

Figure 3.5: Sliding angle method. a) Droplet sitting flat on a surface at θ_e. b) The surface is gradually tilted at an angle θ_{tilt}, changing the value of the left and right contact angles, θ_l and θ_r. In the case shown here $\theta_l < \theta_r$. c) When the contact angles reach the advancing and receding configuration, θ_A and θ_R, the tilting angle reaches the sliding angle, $\theta_{tilt} = \alpha$, which forces the droplet slide downwards.

3.2.3 Contact line relaxation method

This method was developed in this thesis as an alternative to the volumetric variation method. One of the limiting factors when using the volumetric variation method is choosing the appropriate flow rate to drive the motion of the contact line. Shirtcliffe, *et al.* [34] stated that one can only measure the this transition if one approaches the advancing or receding contact angle at infitenely slow speeds. In the literature, contact line velocities do not normally exceed a couple of $\mu m/s$ with some studies using the recess of the contact line provoked by the evaporation of the droplet [4]. On SOCAL, as shown in further chapters, the transition of the droplet between static and dynamic states is smooth rather than a sharp change, making the determination of the initial motion of the contact line difficult. This impacts the determination of the advancing and receding contact angle due to the large changes in contact angle during the inflation or deflation period, which translate to human errors of $\sim 2^\circ$, a significant error considering the contact angle hysteresis reported in literature for low pinning surfaces [2, 4], i.e, with $\Delta\theta \approx 2^\circ$.

In order to overcome this limitation, a method based on the thermodynamic relaxation of the contact line is developed in this work using the relaxation of the contact line after it has been inflated/deflated to determine the advancing and receding contact angles. The regions of interest in this method are the ones labeled as $Static_a$, for the advancing relaxation, and $Static_r$, for the receding relaxation. Figure 3.6 shows an schematic of the procedure of the contact angle relaxation, the experiments are done at controlled relative humidity and temperature conditions. An water droplet of fixed volume and $R < \kappa^{-1}$ is deposited on a sample and let to relax to a stable state. The needle is positioned to one side of the droplet, ensuring that the shape of the droplet is not deformed. Then, a fixed volume of water is pumped into the droplet through the needle at a constant flow-rate, $\dot{q}$, until motion of the contact line is observed. The pumping is then stopped and the droplet is left to relax in order to adopt the minimum state of energy allowed by the surface, which corresponds to the

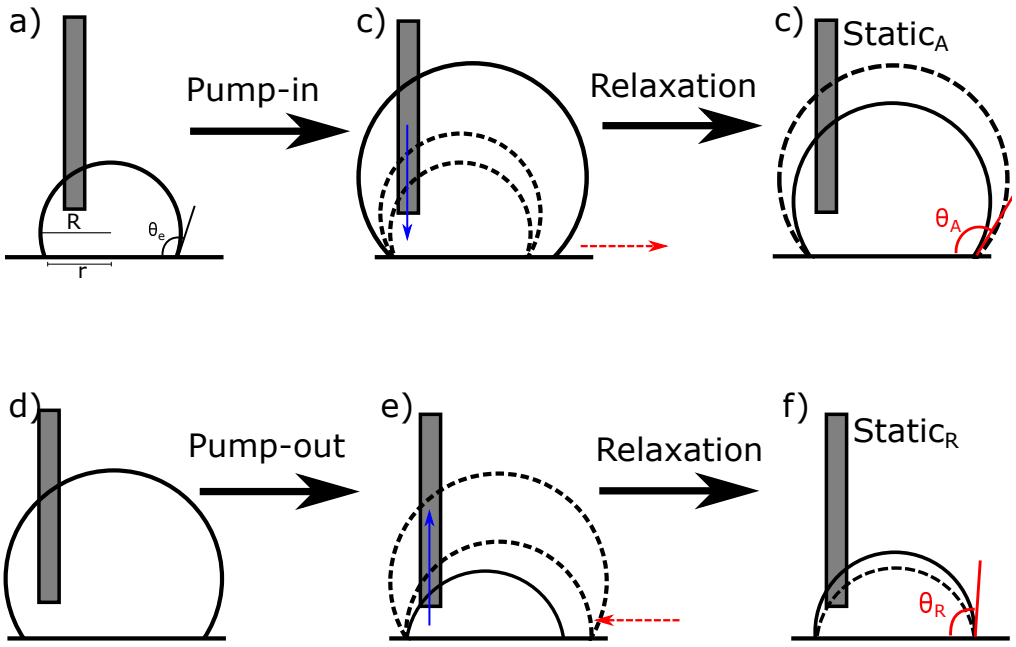

Figure 3.6: Contact angle relaxation method. a) Static droplet of fixed volume and static contact angle. b) Droplet is inflated a a fixed flow rate. c) Droplet is left to relax to the upper-bound stable configuration, θ_A. d) Static droplet after inflation. e) Liquid is pumped-out of the droplet to force the contact line to recede. f) Droplet relaxes to the lower-bound stable configuration, θ_R.

advancing contact angle θ_A. After the advancing relaxation period, a fixed amount of liquid is pumped-pumped out of the droplet through the needle, forcing the contact line to recede. After this dynamic period, the pump is turned off and the droplet is left to relax to the second stable energy state determined by the surface, the receding contact angle θ_R.

The contact angle measurements are then extracted from the droplet images and an exponential equation is used to obtain the asymptotic limit for both relaxation regimes,

$$\theta(t) = \theta_S + \delta\theta_0 \exp(-t/\tau) + \omega t, \tag{3.3}$$

where $\theta(t)$ is the contact angle as a function of time (t), θ_S is static contact angle defined by the asymptotic limit of the relaxation, $\delta\theta_0$ is the amplitude of the exponential, τ is the relaxation time and ω is a constant that accounts for the deviation of the contact angle caused by evaporation effects. The evaporation effect on the contact angle arises from the constant evaporation of the droplet due to the ambient conditions, however, when the relative humidity is set close to thermodynamic equilibrium, the contact angle relaxes to well defined flat plateaus. Hence, in the case of high relative humidity, the correction constant tends to zero, $\omega \longrightarrow 0$. Note that the θ_S defines the advancing or receding contact angle depending

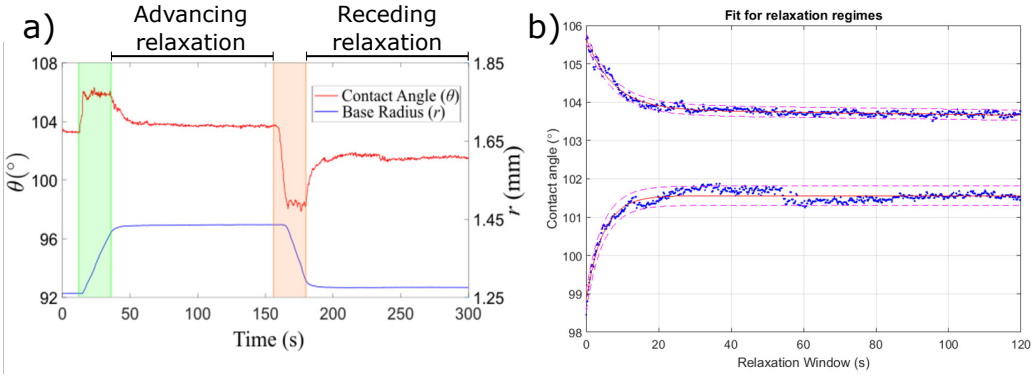

Figure 3.7: Contact line relaxation method. a) Advancing and receding relaxation regimes from a sample set of data. b) Exponential fits of the advancing and receding relaxation regimes.

on the regime of motion of the contact line, therefore

$$\theta_S = \begin{cases} \theta_A, & \text{for advancing relaxation} \\ \theta_R, & \text{for receding relaxation.} \end{cases} \tag{3.4}$$

Figure 3.7 shows a sample set of data where the advancing and receding relaxation are identified in panel a). The relaxation regimes are selected from the data and Equation 3.3 is used to obtain the advancing and receding contact angles. For the case shown in Figure 3.7(b), $\theta_A = 103.8^\circ$ and $\theta_R = 101.6^\circ$.

The accuracy of this method is further analyzed in Chapter 4 and a comparison with the volumetric method shows that this method is more accurate to measure contact angle hysteresis on SOCAL surfaces. Additionally, in Chapter 6, this method is used as a base to measure the contact angle hysteresis inside SOCAL coated capillary tubes by observing the relaxation of the contact line on a moving capillary action liquid front.

3.2.4 Characterization of SOCAL inside a capillary tube

One of the most important aspects of surface characterization is the measurement of contact angles. For flat surfaces, one can obtain the measurement of apparent contact angles of the droplet by looking at a side profile image of a droplet. In capillary tubes, this type measurement becomes challenging due to the optical limitations of a glass capillary tube geometry. Refractive index matching offers a solution to observe the contact line of the liquid front inside the tube, however, the measurement of precise apparent contact angles is challenging to determine due to the inner curvature of the capillary tube. An alternative way to measure the apparent contact angle inside a capillary tube is to make use of the spreading properties of liquids inside tube geometries known as capillary action.

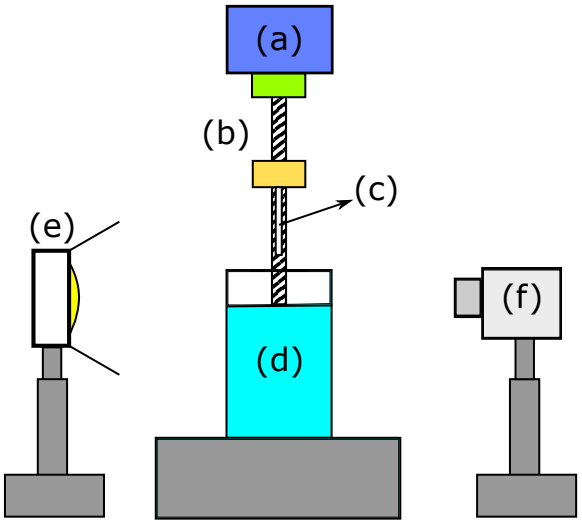

Figure 3.8: Schematic of experimental setup to measure CAH on capillary tubes. a) Arduino Uno microcontroller used to control stepper motor for the linear stage. b) Linear stage: Stepper motor (green) turns threaded metal bar with sample holder (yellow) which allows z-direction motion. c) SOCAL coated capillary tube sample ($20\,\mathrm{mm}$ in length). d) De-Ionized water reservoir ($18\,\mathrm{M\Omega-cm}$). e) LED white light source with diffuser. d) IDS camera running at 20 fps.

Jurin's Law (Equation 2.12) can be rearranged to provide an approximation of the apparent contact angle inside thin tubes as a function of Jurin's height, $\theta(H)$, which reads as

$$\theta(H) = \arccos\left(\frac{H\rho g r_t}{2\gamma}\right), \tag{3.5}$$

where r_t is the radius of the capillary tube.

Using Equation 3.5, one can design an experiment where a capillary tube normal to the surface of the liquid is dipped into water to measure Jurin's height. Moving the tube into the liquid moves results in the motion contact line of the liquid column and by allowing it to relax, one can obtain the values of the advancing and receding contact angles to calculate the contact angle hysteresis inside the tubes.

Figure 3.8 shows an schematic of the experimental design to measure contact angle hysteresis using capillary action. To achieve accurate measurements of Jurin's height for moving contact lines, an experiment that allows controlled motion and static states is necessary. A linear stage was created to be able to precisely control the dipping of a capillary tube into a water reservoir. The linear stage consists of two parallel metallic shafts, the first bar acts as a stabilizer for the sample holder and a second shaft is threaded, acting as the axis of rotation for the sample holder to move up or down. The rotation of the threaded shaft is done via the use of a stepper motor, driving the motion of the sample holder in the z-direction. The motion

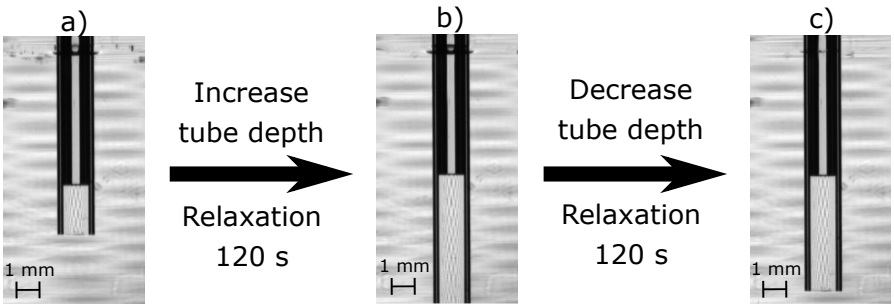

Figure 3.9: Experimental method for Contact angle hysteresis on SOCAL coated capillary tubes. The sample is lowered until the contact line of the water pillar starts to move, (a).The sample is then lowered further at a speed of 25 mm/s and stopped when the interface starts to move. The sample is let to relax for 120 s for the contact line to stabilize, (b). The sample is then lifted at 25 mm/s and stopped when the interface moves again. The interface is left to relax another 120 s, (c).

of the linear stage motor is controlled using an arduino based microcontroller connected to a touch screen display (Figure 3.8(a)), allowing the user to start or stop the motor and control the direction of rotation. The linear stage is placed directly above and perpendicular to a DI water reservoir (Figure 3.8(d)).

The optical array to gather experimental results consists of a camera and white LED light source carefully aligned with the surface of the water reservoir, ensuring that the inner surface of the liquid is clearly visible. The camera takes images at resolutions between $18 - 56$ pixels/mm and records video data at 20 fps. The high resolution allows to obtain height measurements precisely with an error of $24.4\,\mu m$, which translates to a contact angle error of 0.04° for the measurement.

SOCAL capillary tubes are placed on the sample holder, ensuring that the open end of the tube is perpendicular to the surface of the water reservoir. The sample is then lowered until the surface of the water is breached and the capillary is at a depth beyond Jurin's height. This is done by ensuring that the contact line of the water pillar inside the tube begins to move into the capillary tube, as seen in Figure 3.9(a). After a static state of the interface is determined, the capillary tube is lowered at a speed of $1\,mm/s$ and stopped once the contact line of the liquid pillar has moved. The contact line is then left to relax to the advancing contact angle configuration for 120 s (Figure 3.9(b)). After the first relaxation period, the sample is lifted at a constant speed of 25 mm/s and stopped when the contact line of the liquid pillar has retracted. The contact line is left to relax for a further 120 s to let the contact line reach the receding contact angle configuration (Figure 3.9(c)). The measurements of Jurin's heights are taken at the end of the relaxation periods and Equation 3.5 is applied to obtain the values of the contact angle at those points. The results of surface characterisation with this method can be appreciated in Chapter 6.

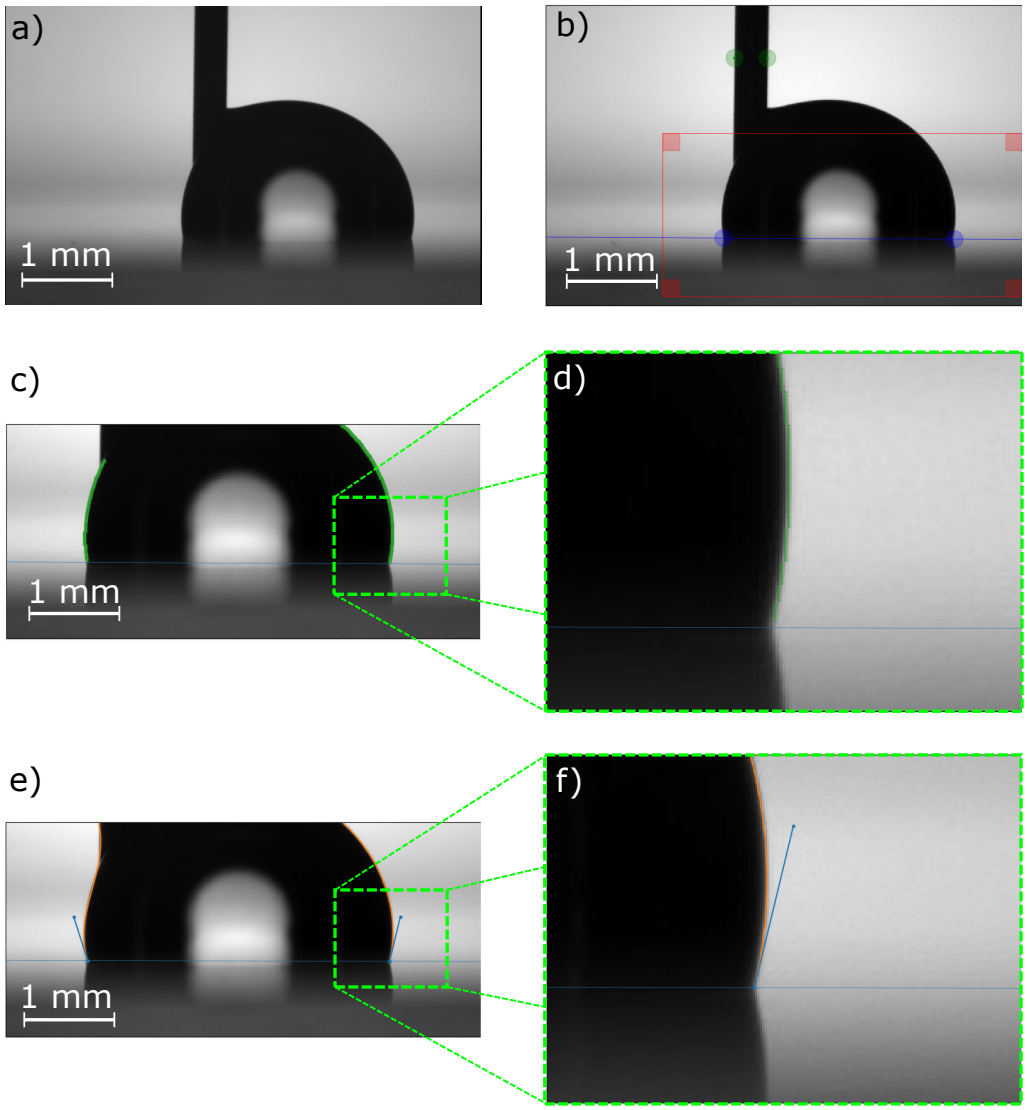

Figure 3.10: Fitting of the contour of a droplet using the Python Droplet Shape Analyzer (PyDSA) software. a) Image of a droplet extracted from the IDS CCD camera. b) Selection of regions of interest (red rectangle), baseline (blue line) and length scale (green dots). c) Identified contour (green dots) using the Canny edges algorithm. d) Zoomed up image of contour of interest. e) Third degree polynomial fitting to the contour of the droplet. f) Zoomed up image of the fitting of the interface.

3.3 Image analysis

3.3.1 Imaging of droplets

Contact angle goniometry refers to the technique of acquiring contact angle measurements of a droplet using its side profile and it is one of the most used methods to obtain contact angle measurements in the literature [117]. Although the measurement of a water droplet may seem simple, there are some key challenges that need to be overcome. The biggest challenge to

address is the transparency of the water droplet, which needs to be carefully addressed in order to obtain accurate measurements of the contour of the droplet. This is achieved by casting a shadow around the droplet using a small aperture light source. This creates a sharp contrast of the contour of the droplet, enabling the user to obtain a clear image of the shape of the droplet and facilitating the processing of the data. This is shown in panel (a) of Figure 3.10. In this work, two different software suites are used to obtain measurements from the video images taken in experiments: Krüss Advance software package [118] and the open source Python Droplet Shape Analyzer (PyDSA) analyser environment [31].

The Krüss Advance software is an off-the-shelf suite that allows the measurement of sessile droplet data. The software takes side profile images and obtains the contour of the droplet. It operates by fitting a function to the detected contour to determine droplet variables such as contact points, contact angles, base radius and volume. According to the manufacturers manual, this software is able to achieve measurement resolutions of 0.01° [119]. The software offers a variety of fitting functions, and for the works presented in this thesis, a tangent method fitting was employed.

The second image processing software is the most used throughout this thesis and is called PyDSA. This software is an open source Python based Droplet Shape Analyser (DSA) that allows the user to have additional input on the determination of the contour of the droplet and their contour fitting functions. The wide range of optimization options enables a better fit to the contour of the droplet, offering flexibility and accuracy to the analysis of the data.

In PyDSA, the image analysis process requires a side profile image of the droplet, as seen in Figure 3.10(a). In order to scale the image, an object of known length is needed to obtain the amount of pixels per millimeter in the image. In this case, the outer diameter of the needle ($0.361\,\mathrm{mm}$) is used to scale the image by defining two green markers that provides a length scaling factor (Figure 3.10(b)). The user then defines the region of interest delimited by a red rectangle in Figure 3.10(b), ensuring that the needle does not affect the measurement of the contact point of interest (the right contact point). The baseline is manually determined by zooming into the contact points where the droplet meets the surface, ensuring that it is clearly visible, and the reflection of the droplet on the surface is used to accurately determine the triple points (Figure 3.10(b)). The careful determination of these aspects allows the software to accurately determine the contour of the interface of the droplet.

To obtain the spatial coordinates of the contour of the droplet, PyDSA utilizes the Open Source Computer Vision Library (OpenCV). This library is used to run the Canny edge detection function developed by John Canny in 1986 [120]. This function uses a multi-stage algorithm which detects the boundary between two threshold contrast values. It filters the noise in the boundary to provide a continuous edge for the boundary. The canny edges algorithm is the process used to detect and map the points of the contour as discrete points in Cartesian coordinates, along with the units according to the scaling factor obtained from the needle width

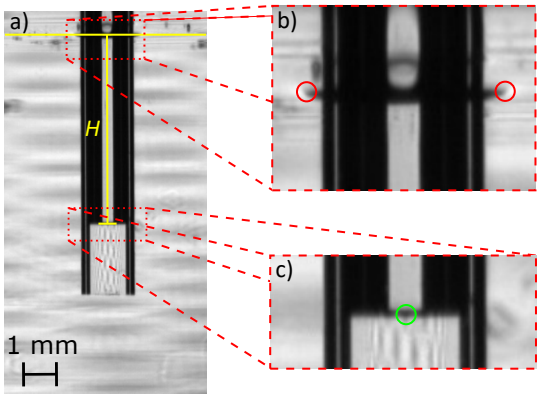

Figure 3.11: Jurin's height determination. a) Image of capillary tube submerged in water. H is determined by the difference between the base line (horizontal yellow line) and the meniscus of the liquid front(vertical yellow line). b) Zoomed image of the base of the capillary tube. The two points where the liquid stops being deformed by the solid (red circles) indicates the surface of the liquid, i.e., the baseline. c) Zoomed image of the liquid-gas interface inside the capillary tube. The meniscus is identified by the green circle.

(Figure 3.10(c-d)). These contour points are then used to interpolate a polynomial function to obtain a continuous line over the contour. The polynomial function used for the contour points is of third degree since it is the fitting method which follows the contour accurately for the interface of the droplet. PyDSA uses the third degree polynomial function to find the intersection with the pre-determined base line. A tangent line is calculated for the polynomial function at the points of the intersection and the contact angle is defined as the angle between the tangential and base line the direction of the centre of the droplet (Figure 3.10(e-f)). The base radius is defined as the distance between the two intersection points which allow us to determine other characteristic values such as the volume and spherical radius of the droplet.

In the study of droplet wetting phenomena, the key parameter is the value of the contact angle a droplet makes on the surface. Therefore, it comes as no surprise that the accuracy of contact angle measurement is a popular topic in the literature [117, 121]. Vuckovac *et al* published a research paper studying the accuracy of contact angle goniometry. They found that the error in the measurement of contact angles increased exponentially with higher values of contact angle caused by the deviation of a pixel in the determination of a baseline. However, in their studies, for contact angles below 150° the goniometric error associated with slight deviation of the true contact line is between 0.5° to 1° [117].

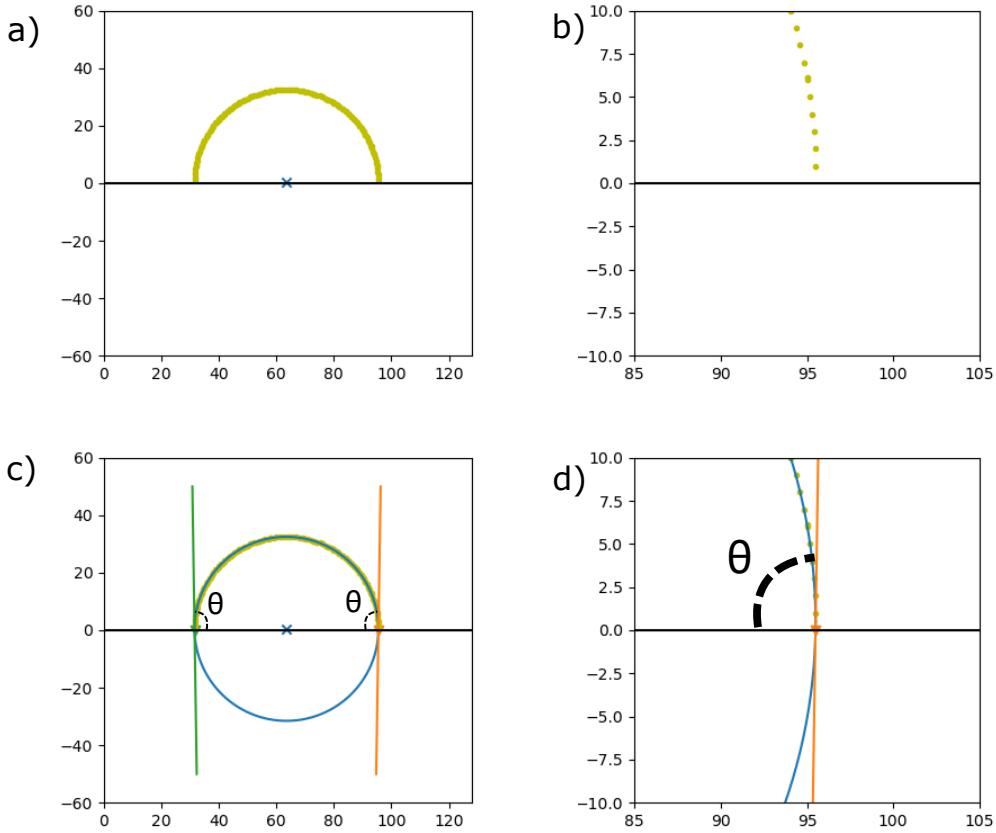

Figure 3.12: Contour fitting of simulation data. a) Contour where $\phi = 0$, defining the interface of the simulated droplet. b) Zoomed image of the contour points close to the solid interface. c) Ellipse fitted the contour of the droplet and contact angle measurements obtained from tangents at the triple point. d) Zoomed image of the tangent obtained according to the ellipse.

3.3.2 Measurement of Jurin's height

ImageJ, an open source imaging processing software, is used to obtain the values of Jurin's height from the video images obtained in the experiments. To determine this height, a baseline is identified as the intersection between the points where the liquid stops being deformed by the solid, which points to the surface of the water reservoir (Figure 3.11(b)). The meniscus of the liquid column is measured at the lowest or highest point of the liquid column inside the capillary tube (Figure 3.11(c)). A vertical line is then drawn between the baseline and the meniscus, which defines the value of H (Figure 3.11(a)).

3.3.3 Measurement of Lattice Boltzmann simulation data

Lattice Boltzmann simulations yield simulation data in the form of scalar or vector fields. In order to obtain information from this fields, it is necessary to be able to obtain the spatial coordinates of the boundary contour between the two phases. The phase field ϕ, is given as a scalar field where each element of the field contains a value between $-1 \leq 0 \leq 1$, where -1 and 1 denote if the region is in the liquid or the gas phase, repectively. The boundary between these two phases is where $\phi = 0$, which one can use to find the contour of the droplet. For this purpose, a bespoke Python program was written in order to be able to obtain and plot this type of information from the simulation outputs. The program loads the phase field and identifies the spacial coordinates where $\phi = 0$, as seen in Figure 3.12(a-b). Those coordinates are used to fit an ellipse function and,similar to the process followed in the PyDSA environment, the base radius is obtained by measuring the distance between the intersection points of the base line and the interpolated ellipse. To obtain the values of the contact angle, a tangent line is calculated at the intersection points of the base line and the ellipse. Then, the contact angle is measured between the tangent line and the base radius in the direction of the centre of the droplet, as seen in Figure 3.12(c-d).

3.4 Conclusion

This chapter has given details of the production of SOCAL surfaces and presented experimental techniques to characterise slippery surfaces. The SOCAL production is started by the thorough cleaning of a glass substrate in order to ensure no contaminants affect the growth of the polymer chains on the surface and that a homogeneous coating is achieved. The SOCAL process consists of the polycondensation of PDMS onto a plasma exposed activated surface. This is achieved through a acid-catalyzed reaction of DMDS and the OH radicals on the activated surface. The surface is then rinsed with Toluene and IPA to stop the reaction and wash away any left over non-reacted substances. The parameters used in the production are taken from the literature and initial results of the contact angle hysteresis show that SOCAL surfaces have been successfully produced.

The characterisation methods reviewed in this chapter include the volumetric variation method, the sliding angle method and the proposed contact angle relaxation method. The volumetric variation method is one of the most used method of droplet characterisation in the literature. As the name suggests, this method varies the volume of the droplet by pumping-in or pumping-out liquid from a fixed volume droplet which forces the contact line to move. The onset of contact line motion during the volume change period is used to determine the values of the advancing and receding contact angles, determining the value of contact angle hysteresis. The second method reviewed in this chapter is the sliding angle method. This

method consists in the gradual tilting of a surface which contains a sessile droplet. Once the tilting of the surface deforms the droplet to the advancing and receding configuration, the droplet begins to slide at a characteristic sliding angle, providing information about the contact angle hysteresis of the surface.

When compared to other slippery surfaces, there seems to be a disagreement between the static and dynamic on SOCAL surfaces. Hence to increase accuracy of measurements, a novel way to measure contact angle hysteresis is presented based on the minimization of surface energy. The method is named contact line relaxation method, which utilizes the relaxation of the droplet after is has been perturbed by a volume change and a exponential equation to asymptotically approach the values of the advancing and receding contact angles. The following chapter compares the results taken from the volumetric variation method and the contact line relaxation method. Additionally, the contact line relaxation method provides further details of the dynamics of the contact line which are used to understand how a liquid front moves on SOCAL surfaces.

This chapter also reviews some of the experimental designs and imaging techniques to obtain data from the experiments. A bespoke relative humidity chamber is built in order to facilitate the production of SOCAL surfaces at a fixed relative humidity. Additionally, a bespoke linear stage is created to enable the precise dipping of capillary tubes into liquid reservoirs. Lastly, the imaging processing techniques employed in this thesis are provided for droplets, liquid columns in tubes and simulation data.

Chapter 4

Static and dynamic friction of the contact line on SOCAL surfaces

This project aims to study the motion created by the intermolecular interaction of interfaces generated by a gradient in relative humidity. Molecular forces are small compared to the forces that resist the lateral motion of droplets on a normal solid surface due to their inherent roughness. For this reason, the interaction between droplets and low friction ultra-smooth surfaces are of particular importance at a fundamental level in this project. As discussed in previous chapters, although ultra-smooth surfaces are difficult to find in nature, current surface engineering technology allows us to create surfaces that allow motion of droplets with remarkable ease. These engineered surfaces have a many applications that span from ink-jet printing [122], coating [123] and lubrication [124] systems.

Minimizing the interaction, especially friction, between liquids and surfaces have the potential to allow parameters such as surface tension to dominate the behaviour of droplets on solids. A potential candidate for this endeavour are ultra-smooth topographies such as the ones found on SOCAL surfaces. This coating procedure is a novel type of engineered surface that exhibits remarkably low static friction for many liquids, which span from surface tension values of 18.4 to 78.2 mNm^{-1} [2, 4, 62]. SOCAL surfaces consist of a nanometric monolayer of polymer chains that are grafted onto a solid glass surface with the aid of a acid-catalyzed reaction with DMDS [62]. The polymer chains of a SOCAL surface are flexible, and play a role similar to that of an intermediary liquid lubricant film used to create SLIP surfaces [51] and LIS [60] (refer to Chapter 2), masking chemical and topographical imperfections. However, unlike SLIP surfaces or LIS, the polymer chains on SOCAL surfaces allow the droplet to maintain a solid-liquid-gas contact line, which enables the accurate use of classical approaches like the Young-Dupré equation. On SOCAL surfaces, droplets exhibit very low contact-angle hysteresis, typically of 5° or below [62]. Despite this low hysteresis, droplets on this surfaces exhibit a remarkably low mobility [2], with recorded slip angles higher than 5°, indicating the existence of a high dynamic friction taking part in the in the motion of the droplet. From a fundamental point of view, this raises important questions about the physical mechanism governing the motion of contact lines on SOCAL surfaces.

In this Chapter, the static and dynamic behaviour of water droplets is studied on SOCAL surfaces by utilizing surface characterisation to compare it with well known theories that aim to describe a contact line in motion. CCA evaporation experiments are presented and compared to literature to confirm that the surfaces produced show similar behaviour as those described in literature.

Subsequently, the static friction and dynamic friction on SOCAL surfaces is studied. Volumetric variation experiments of pure water droplets are performed at fixed flow rates, controlled relative humidity and temperature conditions. Initial results show a smooth transition of static to dynamic behaviour of the contact line which make the determination of the advancing and receding contact angle challenging. To overcome this, a novel method to measure contact angle hysteresis is developed by looking at the relaxation to equilibrium of the contact line after a fixed flow rate volume change. A comparison with classical methods of contact angle hysteresis measurements shows that the relaxation of the contact line at high relative humidity yields well-defined, more accurate and reproducible results for SOCAL surfaces. Using static and dynamic concepts of droplets on solid surfaces, it is predicted that the pinning force is proportional to the contact angle hysteresis and the surface tension. The expressions for the theoretical relaxation times of the contact line are calculated according to the hydrodynamic model (Cox-Voinov theory) [19] and the MKT [20]. A comparison with experimental data shows that the contact line of the droplets follows the kinematics described in the MKT.

Out of equilibrium experiments are performed for both different flow rates for the change in volume and in relative humidity conditions. For the variation in flow rate, which was varied between 1 to 10 $\mu L/min$, the results show that the contact angle relaxes to well defined delimiting values, regardless of the flow rate used. For the variation in relative humidity, it is found that there is a significant influence in the relaxation of the contact line which affects the determination of the relaxation contact angle and dynamically affects the value of the evaporation contact angle in a quasi-static state. Hence, the relaxation of the contact line is only well defined for higher values of relative humidity where the effects of evaporation are mitigated. This study concludes with the comparison of the experimental results with the theoretical curves predicted by the hydrodynamic and the MKT. The results show that the relaxation of the contact line is in remarkable agreement with prediction of the MKT [125].

The work presented in this Chapter is original work published as a journal paper and can be found in Appendix A.

4.1 Evaporation of SOCAL surfaces

One of the aspects that describes low friction interactions between droplets and surfaces is the behaviour of evaporation, first discussed by Picknett and Bexon [25], in which they predict that in perfectly smooth surfaces, liquids evaporate at a constant contact angle. As the droplet evaporates, it decreases in volume, which forces the droplet to either decrease the base radius, r, or to change the value of its apparent contact angle, θ, with the surface. CCA evaporation follows the behaviour of the former of those two cases, as shown in Chapter 2. In this mode, as the droplet decreases in volume, the apparent contact angle remains constant while the contact area, A, of the droplet decays linearly.

For SOCAL surfaces, this mode of evaporation was first observed by Armstrong, *et al.* [4]. Hence, evaporation experiments on a SOCAL surfaces produced with the parameters reported in the literature are performed to confirm that the SOCAL surfaces in this project have comparable properties.

Experimental setup

The samples are glass slides ($25\,\text{mm} \times 75\,\text{mm}$) coated with SOCAL which are cleaned and prepared following the methodology described in Chapter 3.

Figure 4.1 shows the schematic of the Krüss Droplet Shape Analyzer 25 (DSA25). This piece of equipment allows the collection of profile images of small droplets on surfaces, a technique known in literature as contact angle goniometry [117]. A commercial temperature-humidity chamber (TC30) is adapted to the main frame of the equipment which allows the precise leveling of the supporting stage, control of the surface temperature and control the relative humidity conditions inside the chamber.

The experimental procedure begins by placing the SOCAL sample inside the temperature and humidity chamber attached to the Krüss DSA25 in Figure 4.1. The temperature (T) and relative humidity (RH) conditions are set to stabilize at $T = 25 \pm 0.1\,^{\circ}\text{C}$ and $RH = 70\% \pm 0.5\%$. Then, a $4.0 \pm 0.3\,\mu\text{L}$ droplet of DI water (type III, purified in an Elga PURELAB Option-Q lab water purification system) is dispensed on top of the SOCAL sample and detached from the needle. Video recording is started at 1 frame every 10 s at a resolution of 2 µm/pixel and is stopped once the droplet has completely evaporated from the surface.

The images are analyzed using the Krüss Advance software package. To obtain accurate measurements of the base radius and contact angle, the base line is identified using the reflection of the droplet on the surface. The software package then identifies the contour of the droplet and a elliptical fit of the profile is used to approximate the shape of the droplet. The

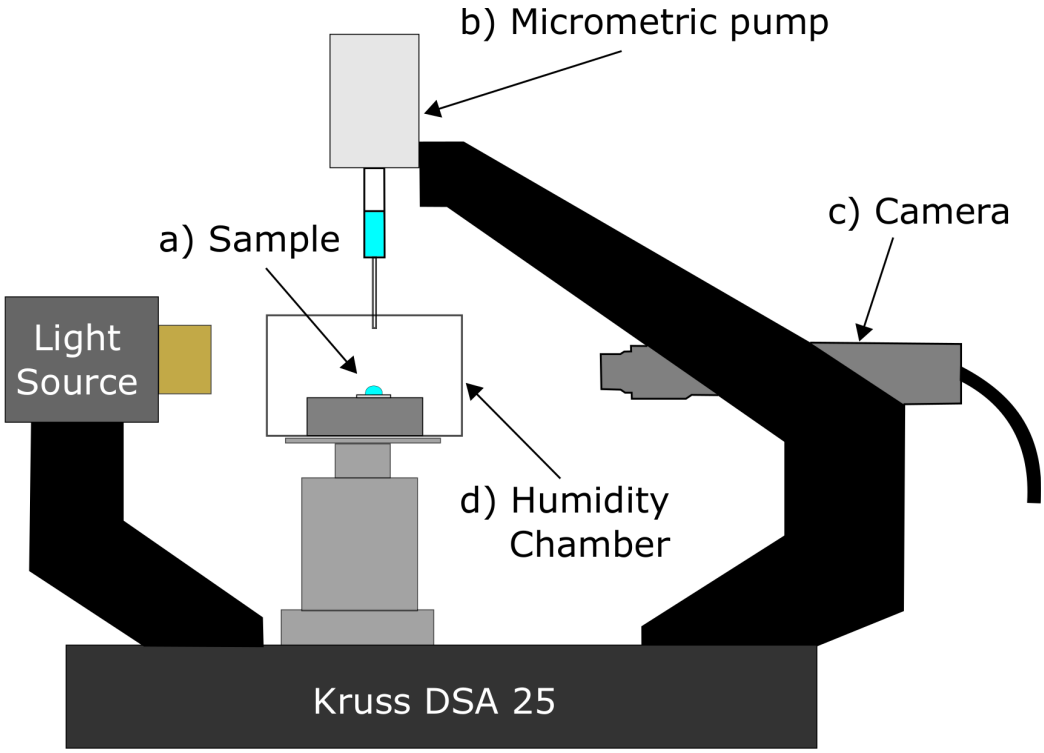

Figure 4.1: Krüss Droplet Shape Analyzer 25 (DSA25). Schematic of the Krüss Droplet Shape Analyzer (DSA). a) Water droplet resting on a SOCAL surface. b) Micrometric dosing system adapted to the body of the DSA. c) CCD camera from IDS taking images at 20 fps. d) Commercial temperature and humidity chamber (TC30) from Krüss.

base radius is calculated by measuring the distance between the two intersection points of the baseline and the fitted ellipse, where a tangent fit is used to obtain measurements of the contact angle. The contact angle data is given as a mean between the two angles measured at the intersection points, as no discrepancies between the two edges were observed.

Evolution of contact angle and base radius of the droplet

Figure 4.2(a) shows a typical evaporation sequence in the conditions outlined in the experimental setup of this section. The contact angle remains constant for the majority of the evaporation while the decay in contact area follows the linear trend as predicted in Equation 2.34 from the diffusion limited evaporation. The results in this panel are consistent with the results obtained by Armstrong, *et al.*, which are reproduced in panel (b), for similar experimental parameters. Panel (c) shows the contact angle as a function of the decrease in volume of the droplet as it evaporates. The contact angle remains constant for the majority of the volume decrease, as expected in CCA. This plot is used to identify the interval of interest of the CCA evaporation mode as reported in ref [4] to avoid initial thermal relaxation of the contact angle

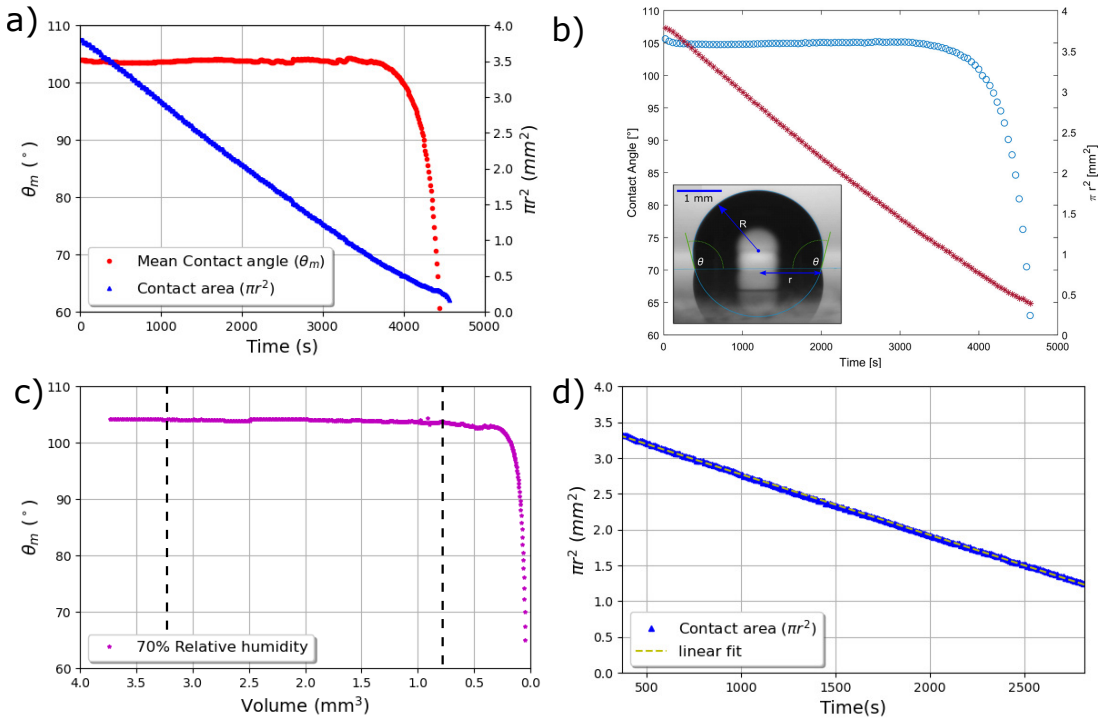

Figure 4.2: Constant contact angle (CCA) mode of evaporation on SOCAL surfaces. a) Typical evaporation sequence showing the evolution of the mean contact angle of the droplet and the calculated contact area of the droplet. b) Figure taken from Armstrong *et al* [4] showing the typical behaviour of constant contact angle mode evaporation on SOCAL surfaces. c) Plot of the mean contact angle as a function of volume loss, the dashed lines indicate the region of interest as per ref [4]. d) Decay of contact area in time in the region of interest with linear fit.

and the variations caused by the collapse of the droplet. Panel (d) shows the linear decay of the contact area of the droplet. This linear behaviour agrees well with the predicted behaviour of the contact area as predicted in the diffusion limited model of evaporation presented by Picknett and Bexon [25].

From the linear fit it is possible to obtain the rate of decay of the contact area, $\frac{d\pi r^2}{dt} = -0.0008$ mm^2/s. This value agrees well with the reported value reported for the 70% relative humidity of $\frac{d\pi r^2}{dt} = -0.0008$ mm^2/s [4]. Therefore, the surfaces presented in this work have comparable low-friction properties as those reported in Ref. [4].

4.2 Statics and dynamics of droplets on solid surfaces

4.2.1 Statics

The Young-Dupré equation (Equation 2.6 in Chapter 2) describes the relationship between the surface tension and the contact angle which defines the shape of a small droplet on a solid surface. However, as discussed in Chapter 2, this description of the relationship of the free surface energy dependent contact angle is only valid in an ideal case where there is no chemical or topographical roughness affecting this relationship. In reality, all surfaces are rough on small scales and generate a pinning force on the contact line of the droplet. This resistance is known as the static friction and in order for the contact line to move, this resistive force has to be overcome. The static friction exerted by a surface is quantified using contact angle hysteresis, $\Delta\theta$, which is defined the difference between the advancing and receding contact angles, θ_A and θ_R (Equation 2.14). $\Delta\theta$ can be seen as an interval that comprises all the values of the static contact angle, θ_S, where the droplet remains static on the surface, i.e, $\theta_R \leq \theta_S \leq \theta_A$.

The importance of contact angle hysteresis becomes evident when considering the pinning force acting on a droplet. At the onset of motion, the net force acting on the contact line is given by [38]

$$F_{\text{pinning}} = 2\gamma r(\cos\theta_R - \cos\theta_A), \tag{4.1}$$

where r is the base radius of the droplet [2]. Note that since θ_S is determined by $\Delta\theta$ (Equations 2.13 and 2.14), it follows that the advancing and receding angles can be expressed as

$$\theta_A = \theta_S + f\Delta\theta \tag{4.2}$$

and

$$\theta_R = \theta_S - (1-f)\Delta\theta, \tag{4.3}$$

where $0 \leq f \leq 1$. Inserting these expressions in Equation 4.1 and expanding in powers of $\Delta\theta$ gives

$$F_{\text{pinning}} \approx 2\gamma r \sin\theta_S \Delta\theta. \tag{4.4}$$

Hence, the pinning force scales with contact-angle hysteresis by a factor determined by the normal component of the surface tension force, $\gamma\sin\theta_S$.

4.2.2 Relaxation to equilibrium

The focus is now directed to the relaxation of the droplet towards a spherical-cap shape which allows the derivation of separate expressions for the typical relaxation time based on the Cox-Voinov and MKT models. The Cox-Voinov theory describes the motion of the contact line as dependent on the surface tension and viscous disspation effects while MKT proposes that the contact line is more dependent on kinematic properties, such as the frequency on pinning events and their intermolecular length (see Section 2.3.4 of Chapter 2 for more details). If one assumes ideal behaviour, then the droplet shape is a spherical cap of instantaneous base radius $r(t)$, contact-line velocity $v = \dot{r}$ and spatially uniform dynamic contact angle $\theta(t)$. Therefore, the deformation of the droplet in this dynamic state can be quantified in terms of a deformation angle, $\delta\theta$, which is expressed as

$$\delta\theta(t) = \theta(t) - \theta_S, \tag{4.5}$$

In this case, θ_S is taken as the limiting static values of the contact angle, i.e., either θ_A or θ_R depending on whether the contact line is advancing or receding during the relaxation process. In the limit of small deformations, it is expected that the velocity of the contact line varies linearly with $\delta\theta$, i.e.,

$$\dot{r} = m\delta\theta, \tag{4.6}$$

where the constant m is determined by the physical mechanism governing the motion of the contact line. For a spherical cap, the expression of the volume can be represented as a function of the contact angle and the base radius of the droplet, $V(\theta, r)$,

$$V(\theta, r) = \frac{\pi}{3}\frac{r^3(1-\cos\theta)^2(2+\cos\theta)}{\sin^3\theta}. \tag{4.7}$$

Solving this equation for the base radius, r, gives,

$$r = \left[\frac{3V\sin^3\theta}{\pi(1-\cos\theta)^2(2+\cos\theta)}\right]^{1/3}. \tag{4.8}$$

Expanding this expression in powers of $\delta\theta$ and differentiating with respect to time leads to the relation

$$\dot{r} = \left.\frac{\mathrm{d}r}{\mathrm{d}\theta}\right|_{\theta=\theta_S} \dot{\delta\theta}. \tag{4.9}$$

Combining Equations 4.6 and 4.9 and integrating with respect to time gives the exponential relaxation of the contact angle,

$$\theta(t) = \theta_S + \delta\theta_0 \exp(-t/\tau), \tag{4.10}$$

where $\delta\theta_0$ is the initial deformation and

$$\tau = \frac{1}{m}\left.\frac{\mathrm{d}r}{\mathrm{d}\theta}\right|_{\theta=\theta_S} \tag{4.11}$$

is the relaxation time.

For viscous-dominated dynamics, the microscopic contact angle is expected to be close to the static value [26], i.e., $\theta_m \approx \theta_S$. Setting $\theta = \theta_S + \delta\theta$ in Equation 2.18, expanding in powers of $\delta\theta$ and using Equations 4.6 and 4.11, leads to the following expression of the Cox-Voinov constant (m_{cv}) and the Cox-Voinov relaxation time (τ_{CV}):

$$m_{\mathrm{CV}} = \frac{\gamma\theta_S^2}{3\eta\ln(L/l_m)}, \tag{4.12}$$

and

$$\tau_{\mathrm{CV}} = \frac{\left[\frac{3V}{\pi(\cos\theta_S-1)^2(2+\cos\theta_S)}\right]^{1/3}}{2+\cos\theta_S}\left(\frac{3\eta\ln(L/l_m)}{\gamma\theta_S^2}\right). \tag{4.13}$$

One can obtain equivalent expressions using the MKT model. Expanding Equation 2.19 in powers of $\delta\theta$ and using Equations 4.6 and 4.11 results in the expression for the the MKT constant (m_{MKT}) and the MKT relaxation time (τ_{MKT})

$$m_{\mathrm{MKT}} = \frac{K_0\gamma\xi^3\sin\theta_S}{k_BT}, \tag{4.14}$$

and

$$\tau_{\mathrm{MKT}} = \frac{\left[\frac{3V}{\pi((\cos\theta_S-1)^2(\cos\theta_S+2))}\right]^{1/3}}{2+\cos\theta_S}\left(\frac{k_BT}{K_0\gamma\sin\theta_S\xi^3}\right). \tag{4.15}$$

Equations 4.13 and 4.15 allows us to compare with measured values of relaxation times in experiments to make a statement on the dynamics that drive the contact line on SOCAL surfaces.

4.3 Experimental setup

The following experiments were performed in the Krüss DSA25 as shown in Figure 4.1. Additionally, for the experiments performed from this point, a Cellix ExiGo micropump was installed on the main frame of the equipment, substituting the one provided in the original piece of equipment. This micropump is reported to be highly accurate, with a dispensing resolution of the order of ± 0.08 pL [126].

Figure 4.3 shows the experimental method to measure contact angle hysteresis. Firstly, a SOCAL sample is placed inside the temperature and humidity chamber and then sealed. The micropump and syringe are carefully lowered until the needle (outer diameter: $0.4\,\mathrm{mm}$) in is the field of view of the camera. A droplet of DI water (Water Ultrapur, Millipore) of volume $V = 8\,\mu\mathrm{l}$ is dispensed onto the SOCAL sample. To ensure that the shape of the droplet interface of the droplet is not deformed by pinning on the needle's surface, the needle is carefully positioned on one side of the droplet and the apparent contact angle is measured at the opposite edge of the drop, where the droplet maintains a shape close to a spherical cap.

Once the needle is in position, ensuring that the droplet is in a static state (Figure 4.3(a)), the inflation and deflation procedure is initialized. A volume $\Delta V = 4\,\mu\mathrm{l}$ of water is first injected into the droplet at a constant flow rate, $\dot{q}$, and different constant flow rates are used between $1\,\mu\mathrm{l/min}$ and $10\,\mu\mathrm{l/min}$ (Figure 4.3(b)). Once the increase in volume is finalized, the droplet is allowed to rest for 2 minutes before the deflation is done. Then, a volume $\Delta V = 4\,\mu\mathrm{l}$ of water is withdrawn from the droplet at the same flow rate (Figure 4.3(c)), and is left to rest for a further 2 minutes before video recording is stopped. The droplet is then removed from the surface and the process is repeated.

All experiments in this section are performed at controlled relative humidity, which are varied between $30\% \pm 0.5\%$ and $94\% \pm 0.5\%$, and at a constant temperature, $T = 25^{\circ}\mathrm{C} \pm 0.2^{\circ}\mathrm{C}$. For each set of parameters the experiment is repeated 5 times.

The experiments were recorded using a video camera and the resulting images analyzed using PyDSA, an in-house droplet shape analyzer [31], see Chapter 3 for more details. The resolution of the video footage is at least $257\mathrm{pixel/mm}$ and the apparent contact angle of the droplet is determined by image analysis as follows. First, a base line is defined using the droplet's reflection on the solid to determine the left and right contact point of the droplet with the surface. The droplet's free contour is determined using a brightness threshold function. A third-degree polynomial is fitted to the contour of the droplet over a region that ranges from the free edge of the drop to the point where the needle meets the droplet. The algorithm then determines the point at which the polynomial meets the contact line and computes the apparent contact angle as the local slope. The resolution of the images allows the algorithm to produce droplet contours formed by $\sim 250 - 500$ points, leading to a small fitting error. Therefore, the systematic measurement error in the apparent angle is $\delta\theta \sim 0.2^{\circ}$, which is commensurate with previous errors reported in the literature [117, 121].

To determine the advancing and receding contact angles, and, therefore, the contact angle hysteresis, two different methods of surface characterisation are used in this chapter. The first method, which is referred to as the volumetric variation method, consists of determining the onset of motion of the contact line upon increasing and decreasing the volume of the droplet [5, 39, 112, 113, 127]. This point is then mapped to the corresponding apparent contact

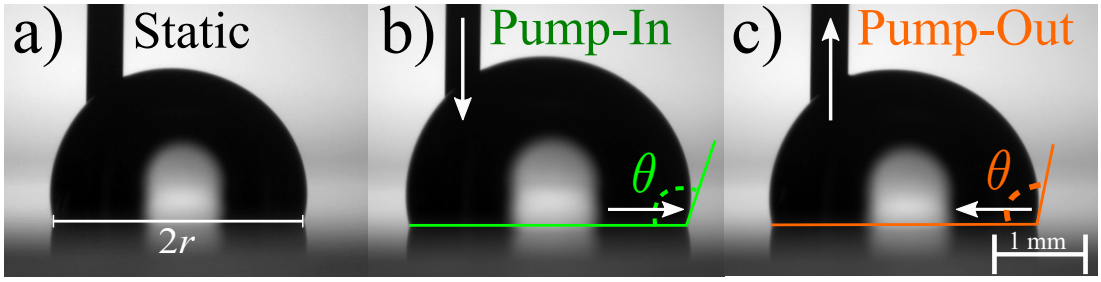

Figure 4.3: Experimental procedure. (a) A droplet of controlled initial volume V is placed on a SOCAL surface and connected to a micropump through a thin needle. (b) and (c) The micropump injects or withdraws liquid at a prescribed flow rate $\dot{q}$ (vertical arrows). The instantaneous apparent contact angle, θ, and base radius, r, are measured using image analysis. The scale bar is $1\,\mathrm{mm}$.

angle: θ_A for a volume increase and θ_R for a volume decrease. The second method consists of tracking the contact line velocity as the droplet is allowed to rest after an volume change, and identifying the corresponding limiting value of the apparent contact angle as either the advancing or the receding angle [34].

4.4 Experimental Results

4.4.1 Typical contact angle hysteresis experiment sequence

Figure 4.4 shows representative measurements of the evolution of the contact angle, $\theta(t)$ (red line), and the base radius of the droplet, $r(t)$ (blue line), for an $8\,\mu\mathrm{l}$ droplet subject to changes in volume at constant flow rate ($\Delta V = \pm 4\,\mu\mathrm{l}$; $\dot{q} = 10\,\mu\mathrm{l/min}$), followed by relaxation periods at zero flow rate ($\Delta t = 120\,\mathrm{s}$). The temperature and relative humidity are fixed at $T = 25\,^{\circ}\mathrm{C}$ and $\mathrm{RH} = 94\%$, ensuring that the droplet does not undergo significant evaporation during the experiment. This is confirmed by the steady plateau of the evolution of the contact angle and contact radius in time shown in Figure 4.4. During the injection phase (green shaded region) the apparent contact angle rises sharply from the initial value $\theta_i \approx 103^{\circ}$. This sharp increase is followed by a steady motion of the contact line, where $\theta \approx 106^{\circ}$ and where the base radius grows at a rate $\dot{r} = 9 \pm 1\,\mu\mathrm{m/s}$. A similar situation occurs during the withdrawal phase of the experiment (red shaded region), where the apparent contact angle sharply falls as the contact line starts to recede until it settles at $\theta \approx 99^{\circ}$ for a contact-line velocity, $\dot{r} = 12 \pm 1\,\mu\mathrm{m/s}$. Once the flow is switched off, the apparent contact angle relaxes to the well-defined constant values: $\theta_a \approx 103.8^{\circ}$ after injection and $\theta_r \approx 101.6^{\circ}$ after withdrawal.

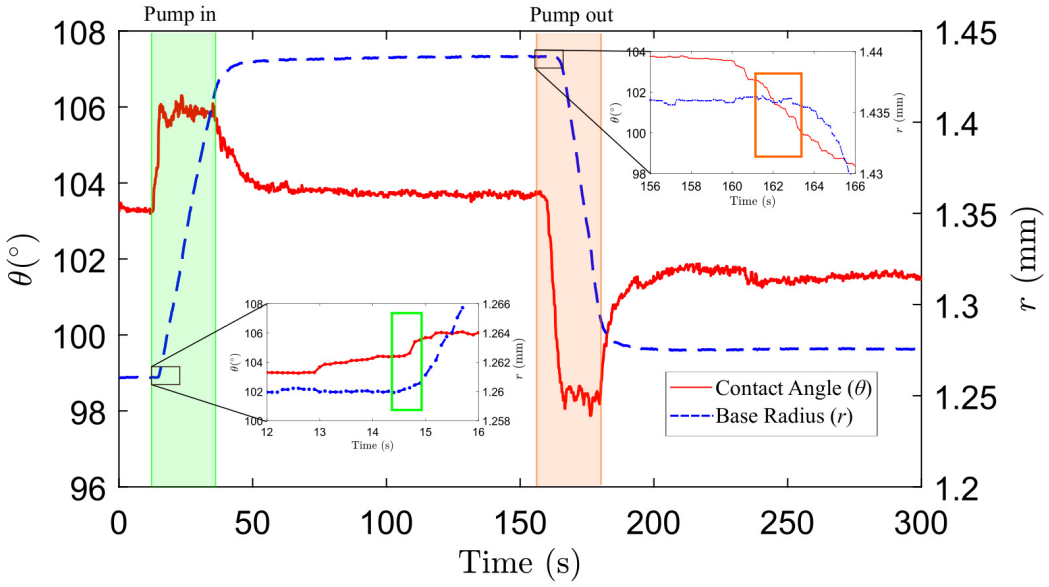

Figure 4.4: Apparent contact angle and base radius measurements at high relative humidity. Graph of a typical experimental set of data performed at a constant flow rate $\dot{q} = 10\,\mu\text{l/min}$ at $T = 25\ ^\circ\text{C}$ and a $\text{RH} = 94\%$. The zoomed-in regions show how the smooth transition from a static to a moving contact line introduces uncertainty in the measurement of the advancing and receding angles.

4.4.2 Effect of flow rate

The relaxation of the apparent contact angle reported in Figure 4.4 indicates that dynamical effects due to a finite flow rate affect the shape of the droplet [34]. To understand the relevance of this effect for droplets on SOCAL surfaces, experiments were performed on a fresh SOCAL sample considering three different flow rates: $\dot{q} = 1\,\mu\text{l/min}$, $5\,\mu\text{l/min}$ and $10\,\mu\text{l/min}$. As before, the experiment consisted of a change in the droplet volume $\Delta V = \pm 4\,\mu\text{l}$, followed by a relaxation at zero flow rate ($\Delta t = 300\,\text{s}$). The experiment was repeated three times for each flow rate. The temperature and relative humidity were kept at $T = 25\,^\circ\text{C}$ and $\text{RH} = 94\%$.

Figures 4.5(a-c) shows independent measurements of the apparent contact angle. As before, the presence two dynamical regimes is observed, corresponding to an increase or a decrease in the base radius, which are characterized by maximum and minimum values of the apparent contact angle, respectively. These regimes are followed by a relaxation to static values. Figure 4.5(d) shows a superposition of the data for the three flow rates studied. In the plot, arbitrary units of time are used to match the volume increase/decrease windows while the rest of the time data is unaltered (i.e., time units in the relaxation portions of the plot are the same for all flow rates). Although the effect of the input and output rate is subtle, in general,

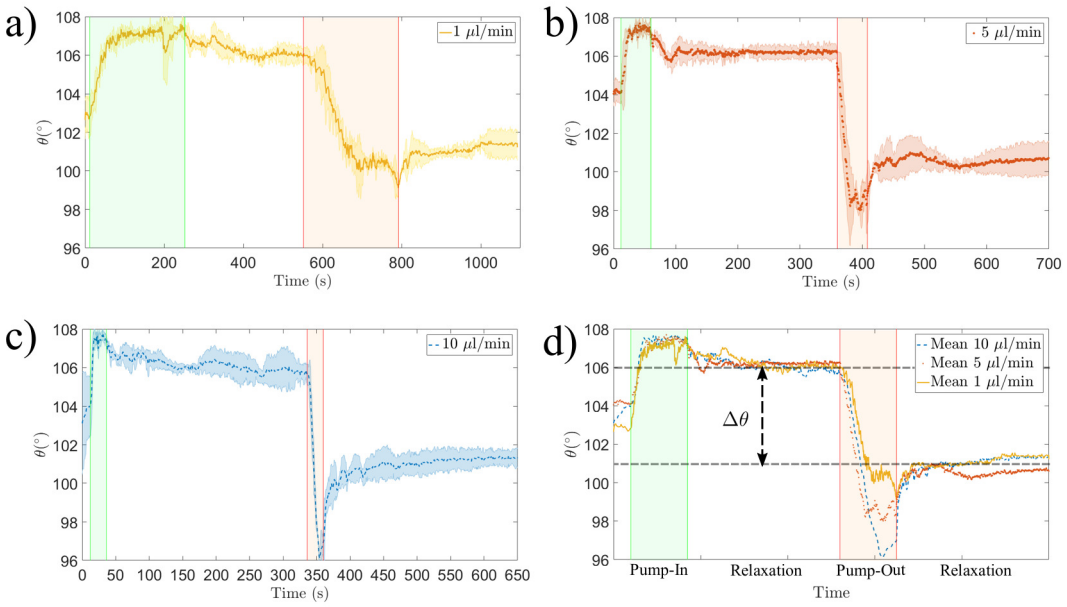

Figure 4.5: Effect of flow rate on the apparent contact angle. (a-c) Variation of the contact angle at different flow rates. (d) Overlap of the experimental data. The apparent contact angle relaxes to constant values which are independent of the flow rate. The difference between these values is identified as the contact-angle hysteresis.

the response of the dynamic contact angle during a change in the droplet volume depends on the flow rate. In contrast, when the droplet is allowed to relax, the curves follow similar shapes consistently and converge to a unique limiting value for the contact angle, independent of the flow rate use to change the volume of the droplet.

4.4.3 Effect of relative humidity

To understand the effect of relative humidity on the droplet's apparent contact angle, experiments are carried out at RH= 94%, 50% and 30%, at fixed flow rate, $\dot{q} = 10\,\mu\text{l/min}$, and temperature, $T = 25\,^{\circ}\text{C}$. For each experiment, the relaxation window was kept at $\Delta t = 120\,\text{s}$. Figure 4.6 shows the changes in apparent contact angle (a-c) and base radius (d-f) for the three relative humidities considered. In order to account for variation in the initial radius, r_0, the change in base radius is given as $\Delta r = r - r_0$. During the injection phase, the apparent contact angle reaches the same dynamic value regardless of the relative humidity $\theta = 105^{\circ} \pm 1.1^{\circ}$. However, during the subsequent relaxation, there is a significant change in the apparent contact angle at different relative humidities. Unlike the plateau behaviour observed at $\text{RH} = 94\%$, at RH=50% and 30% the apparent contact angle decreases with time at a rate that becomes stronger with decreasing relative humidity. During the same step, the base radius remains constant and independent of the relative humidity (see panels d-f in Figure 4.6). In the

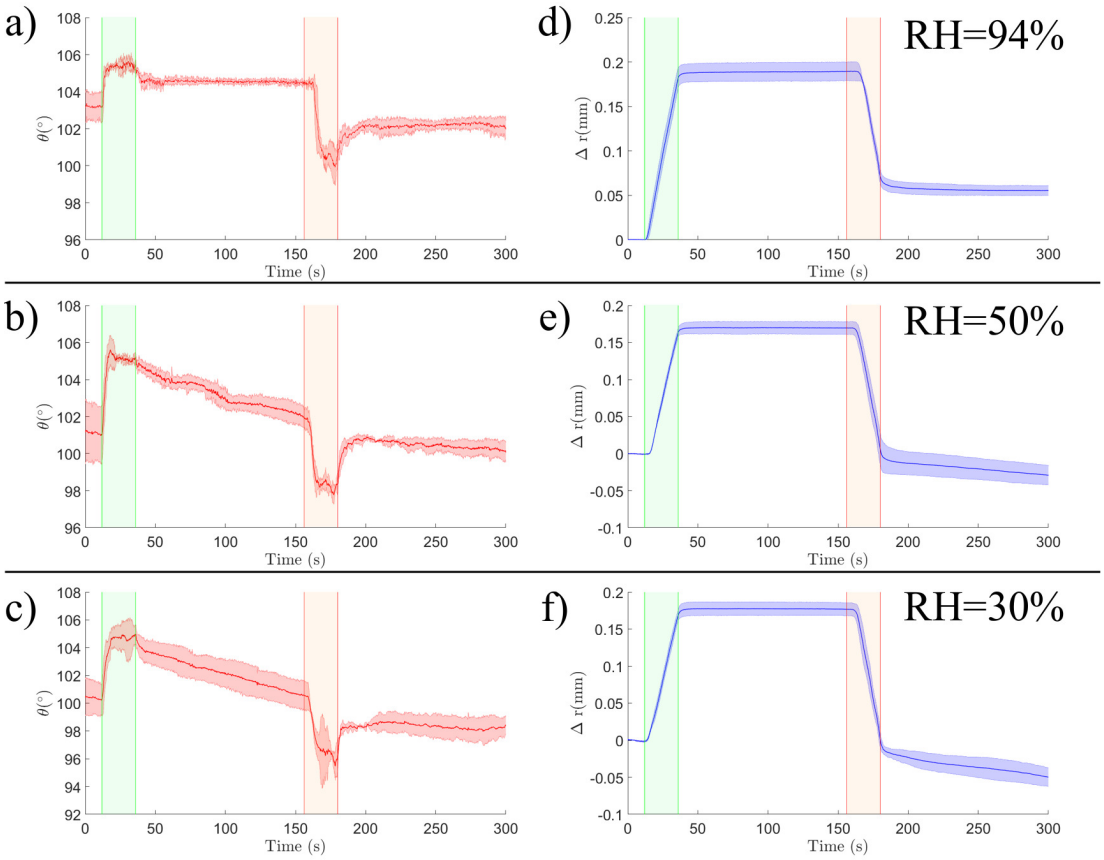

Figure 4.6: Influence of relative humidity on the apparent contact angle and the base radius. (a-c) Variation of the apparent contact angle at $\mathrm{RH} = 94\%$, 50% and 30%, respectively. (d-f) Corresponding change in the droplet base radius.

withdrawal phase, observe an initial decrease of the apparent contact angle. Once the flow is switched off, the apparent contact angle relaxes to a plateau while the base radius decreases at a roughly constant rate owed to evaporation phase change. Both the plateau value of the apparent contact angle and rate of change of the base radius depend on the relative humidity.

4.5 Reducing uncertainty in contact angle measurements

The first point of discussion is the uncertainty in the measurement of the advancing and receding contact angles on SOCAL surfaces, and its effect on the determination of the contact angle hysteresis.

Typically, θ_A and θ_R are identified as the apparent contact angles at the onset of motion of the contact line upon an increase or decrease of the volume of the droplet, respectively [4, 5, 39, 112, 113, 127]. On SOCAL surfaces, however, the onset motion is difficult to identify with precision. This is because, as shown in the zoomed-in regions of Figure 4.7, the apparent

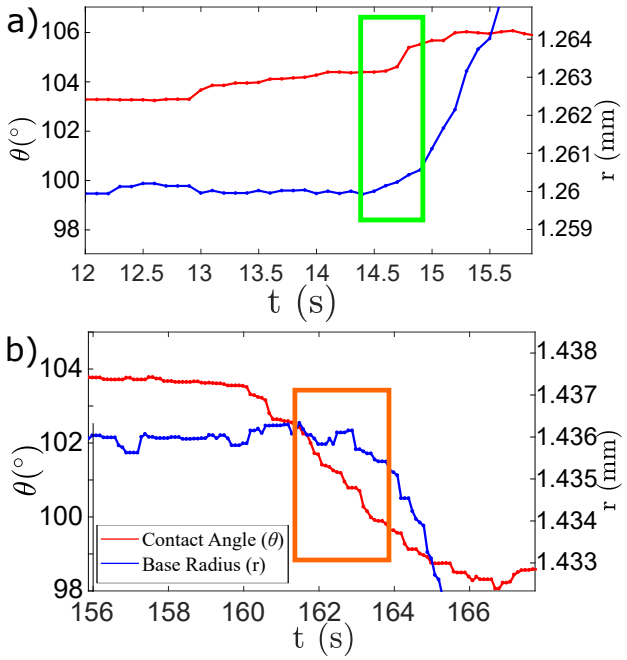

Figure 4.7: Close up to onset of motion on the contact line. Zoomed plots from Figure 4.4. a) The advancing configuration of the contact line. b) the receding configuration of the contact line.

Table 4.1: Apparent contact-angle measurements of water droplets on SOCAL surfaces. Volume change method: θ_A and θ_R are determined by estimating the onset of motion of the contact line at constant flow rate $\dot{q} = 10\,\mu\text{L/min}$. Contact-line relaxation method: θ_A and θ_R are determined as the limiting apparent contact angles that the droplet exhibits after relaxation to a static shape. The temperature and relative humidity are $T = 25\,^\circ\text{C}$ and $\text{RH} = 94\%$.

	Volume-change method			Contact-line relaxation method		
Trial number	θ_A (°)	θ_R (°)	$\Delta\theta$ (°)	θ_A (°)	θ_R (°)	$\Delta\theta$ (°)
1	104.4	100.3	4.1	103.8	101.6	2.2
2	105.5	101.3	4.2	104.2	102.2	2.0
3	104.6	104.3	0.3	104.6	102.3	2.3
4	105.4	104	1.4	104.3	102.8	1.5
5	105.1	102.4	2.7	104.9	102.3	2.6
mean (°)	105.0	102.4	2.5	104.4	102.2	2.1
s.d. (°)	0.5	1.7	1.7	0.4	0.4	0.4

contact angle and the base radius vary smoothly as the contact line starts to move. The typical range of transition of the base radius from the static value to a constant contact-line velocity is $\Delta r \approx 0.2\,\text{mm}$. The corresponding range of change in the apparent angle is $\Delta\theta \approx 2^\circ$, which is comparable to the overall change in θ during the volume change. As shown in Table 4.1, the uncertainty in the measurement of the advancing and receding contact angles is of the order of one degree. This leads to a contact-angle hysteresis $\Delta\theta = 2.5^\circ \pm 1.7^\circ$.

Shirtcliffe, *et al.* proposed that the advancing and receding angles can only be measured in the limit of a vanishingly small flow rate [34]. In our experiments, this limit corresponds to the relaxation of the apparent contact angle after the flow rate is stopped. Indeed, as shown in Figure 4.5, the contact angle relaxes to the same constant value, regardless of the flow rate, which shows that these plateaus are limiting thresholds for the static contact angle. Table 4.1 shows measurements of θ_A and θ_R obtained after the contact-line relaxation for the same experimental conditions of the volume-change method (refer to Chapter 3 for more details). The results show a significant (three-fold) reduction of the standard deviation of the measurements, which leads to a more consistent contact-angle hysteresis measurement, $\Delta\theta = 2.1^\circ \pm 0.4^\circ$.

Note that, even though the average contact-angle hysteresis obtained from both methods is similar, the relative error for the volume-change method amounts to 68%. This is clearly important, as the corresponding error in the pinning force is proportional to the error in the contact-angle hysteresis (see Equation 4.1). In contrast, the error in the measurement of $\Delta\theta$ obtained from the contact-line relaxation is consistently smaller (19% for the data reported in Table 4.1) and confirms the low pinning force exerted by the SOCAL surface on water droplets.

4.6 Contact angles out of thermodynamic equilibrium

Now, the effect of relative humidity on the contact-angle hysteresis is discussed. Figure 4.6(a,d) shows measurements of the apparent contact angle and droplet base radius upon a change in volume at high relative humidity ($\mathrm{RH} = 94\%$), corresponding to conditions close to thermodynamic equilibrium. After either an advancing or a receding motion of the contact line, both the apparent angle and droplet base radius relax to well-defined constant values, with no appreciable subsequent variation over the timescale of the experiments.

Figure 4.6(b,c,e,f) show the corresponding curves for lower relative humidity ($\mathrm{RH} = 50\%$ and $\mathrm{RH} = 30\%$). After a volume increase, the apparent contact angle undergoes a sustained decrease over time (Figure 4.6(b-c)), whilst the base radius of the drop remains constant (Figure 4.6(e-f)). This indicates that the droplet is out of thermodynamic equilibrium and undergoing a CCR mode of evaporation [25, 65]. Indeed, the rate at which the apparent contact angle decreases is larger for smaller relative humidity. This is likely due to a higher mass loss due to evaporation. On the other hand, after a volume decrease the apparent contact angle remains constant, while the base radius decreases. This is consistent with a CCA mode of evaporation [25, 65]. The apparent contact angle, however, is not equal to the receding contact angle measured at high relative humidity. It decreases with lower relative humidity (see Table 4.2). This indicates that the contact line is out of both thermodynamic and mechanical equilibrium and recedes from the solid surface at a rate controlled by evaporation.

Table 4.2: Effect of relative humidity on the apparent contact angle after a volume decrease.

Relative Humidity	94%	50%	30%
θ ($^\circ$)	102.1 ± 0.3	100.5 ± 0.3	98.4 ± 0.7

A relative humidity dependent change in evaporation contact angle has been observed before by Armstrong *et al.* work[4]. In this work, they attribute the change in evaporation contact angle to a difference in surface energy caused by an adsorption of water molecules on the surface, changing the balance of surface tension forces which determine the equilibrium contact angle. Although this explanation is highly plausible, further studies need to be made to confirm this effect, such as a study of the change in mass for substrates at different relative humidities. Moreover, the results of this study shows that there is a high dynamic dependence of the contact angle to motion of the contact line for SOCAL surfaces. Therefore, a contributing factor to this effect could be attributed to a changing contact line velocity at different relative humidities.

4.7 Dynamics of Relaxation

Now, a comparison is done of the prediction of the Cox-Voinov theory and the Molecular Kinetic Theory, Equations (4.13) and (4.15), to the experimental measurements of the relaxation of the droplet close to thermodynamic equilibrium ($\mathrm{RH} = 94\%$). As shown in Figure 4.4, the apparent contact angle seems to follow an exponential variation towards the limiting static value. To obtain an experimental measurement of the relaxation time, τ, the measurements of the instantaneous base radius of the droplet are fitted to an extended form of the exponential relaxation obtained in Equation 4.10, hence

$$\theta(t) = \theta_\infty + \Delta\theta_0 \exp(-t/\tau) + \omega t. \tag{4.16}$$

Here, $\theta_\infty = \theta_S$ corresponds to the limiting value of the contact angle after relaxation, i.e., either the advancing or receding contact angle. The final term, ω, on the right hand side of Equation 4.16 is a fitting constant introduced to account for the effect of evaporation on the constant decay of the contact angle, as can be appreciated in the first relaxation window in panels (b) and (c) of Figure 4.6. A fit of the data to this equation yields values of ω or the order of $1 \times 10^{-3\,\circ}/\mathrm{s}$, which leads to a variation of the contact angle of at most 0.2° over the period of relaxation. The data fits give an average relaxation time $\tau = 8.3 \pm 5.8$ s.

To obtain a prediction of the relaxation time from the Cox-Voinov theory, Eq. (4.13), the parameters used are $\gamma = 72$ mN/m, $\eta = 0.89$ mPa s, $L = 1.2$ mm and $l_m = 4$ nm, where the macroscopic length scale L is chosen as the typical size of the droplet, and the microscopic length scale l_m is chosen to be comparable to the polymer chain length reported for SOCAL [5, 62]. This leads to $\tau_{\mathrm{CV}} = 1.131 \times 10^{-4}$ s, which differs from the experimental measurement by several orders of magnitude. The free parameter in the Cox-Voinov model, which leads to the discrepancy, is the ratio L/l_m in Eq. (4.13). Keeping $L \approx 1$ mm and fitting the Cox-Voinov theory to the experimental data gives $l_m \approx 0.1$ pm, which seems unrealistic as it is orders of magnitude smaller than the smallest of the atoms.

To compare to the prediction of the Molecular Kinetic Theory, Eq. (4.15), one needs knowledge of the frequency of the adsorption-desorption events, K_0, and of the intermolecular distance, ξ. Daniel *et al.* [2] studied the dissipative force exerted on water and sucrose droplets on SOCAL surfaces. By fitting their experimental data to the MKT model they obtained $K_0 = 7500\ \mathrm{s}^{-1}$ and $\xi = 3$ nm. Using these values in Equation 4.15 yields $\tau_{\mathrm{MKT}} = 0.2324$ s, which is a better prediction of the experimental measurement of the relaxation time.

The difference between the prediction from the MKT model and the experimental measurement of the relaxation time are now discussed. The molecular scale, ξ, is unlikely to differ significantly from the experiments reported in Ref. [2]. On the other hand, the experiments of Ref. [2] do not report a specific value of relative humidity, but it is reasonable to assume that these were carried out at ambient conditions, i.e., $\mathrm{RH} < 94\%$. Our experiments were carried out at high relative humidity ($\mathrm{RH} = 94\%$), where the liquid is close to equilibrium with the surrounding vapour phase. Hence, it is expected that the frequency of adsorption-desorption events is smaller in these experiments. Indeed, treating K_0 as a single free parameter and fitting to the experimental measurement of the relaxation time yields a value $K_0 = 204.5\ \mathrm{s}^{-1}$. This suggests that at high relative humidity the contact line is slowed down by the rate of adsorption-desorption of molecules from the solid.

Fig 4.8 shows instantaneous measurements of the contact angle vs contact line velocity averaged over 5 independent trials. The prediction of the Cox-Voinov theory and that of the Molecular Kinetic Theory are superimposed for comparison. For the Cox-Voinov the parameters used are $\gamma = 72$ mN/m, $\eta = 0.89$ mPa s, $L = 1.2$ mm and $l_m = 4$ nm. For the advancing configuration, the static contact angle is set to $\theta_m = 104.4^\circ$ and for the receding configuration, the static contact angle is set at $\theta_m = 102.2^\circ$. For the MKT, the parameter values are $K_0 = 204.5\ \mathrm{s}^{-1}$ and $\xi = 3$ nm, with $\theta_S = 104.4^\circ$ for the advancing configuration and $\theta_S = 102.2^\circ$ for the receding configuration. The prediction of the MKT uses the parameter values fitted to match the relaxation time during the relaxation periods. The prediction of the MKT captures the experimental data to a better degree than the prediction of the Cox-Voinov theory.

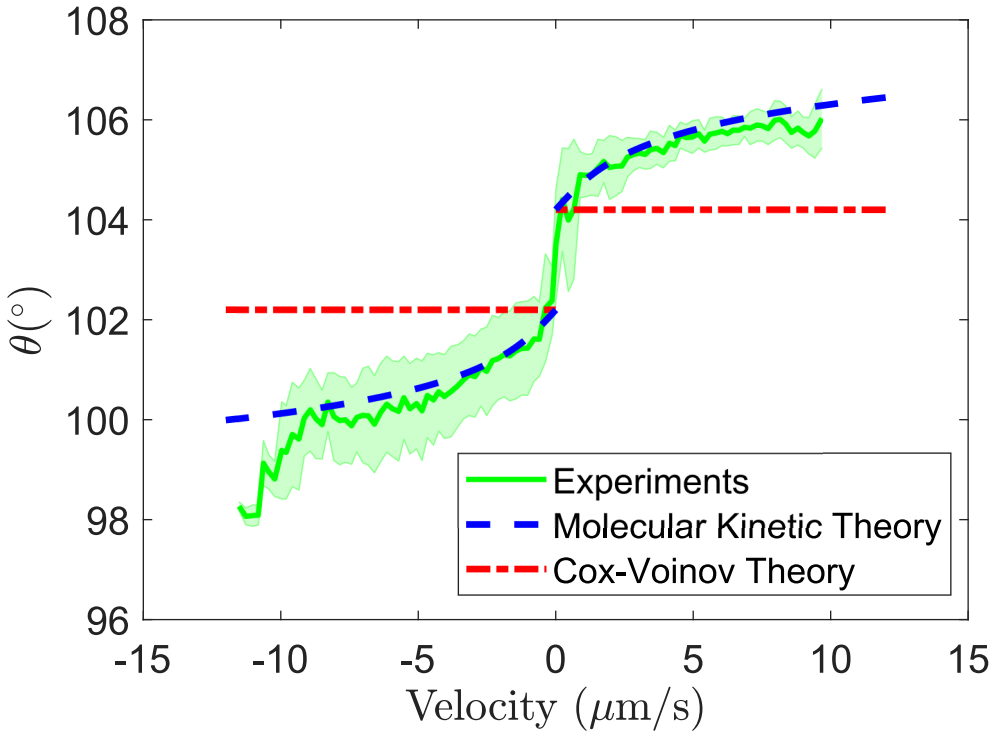

Figure 4.8: Instantaneous measurements of the contact angle vs and contact-line velocity. The experimental data is averaged across 5 trials. The contact angle hysteresis of the sample is $\Delta\theta = 2.1^\circ \pm 0.4^\circ$. The thick lines correspond to the predictions of the Cox-Voinov and Molecular Kinetic Theory.

4.8 Conclusion

In this chapter, the static and dynamic friction imparted by SOCAL surfaces on water droplets has been studied. Our study of static friction has focused on determining the contact-angle hysteresis of droplets under controlled temperature and ambient humidity conditions. Direct measurements of the advancing and receding contact angles are reported in the limit of mechanical and thermodynamic equilibrium by tracking the relaxation of a droplet's interface after a volume change. Such measurements are independent of the flow rate used to effect the volume change, leading to a significantly lower uncertainty in the measurement of the advancing and receding angles compared to the method of identifying the onset of contact-line motion.

Out of thermodynamic equilibrium, corresponding to an ambient relative humidity below the point of liquid-vapour phase coexistence, the droplet's interface does not relax to the advancing and receding angles. Instead, the droplet undergoes evaporation keeping a constant apparent contact angle which is always lower than the receding contact angle measured close to thermal equilibrium.

In regards to dynamic friction, a study was presented on the timescale of relaxation of the droplet to a static configuration and compared the experimental measurement of the relaxation time to a hydrodynamic model and a model based on molecular kinetic theory. The results support that the dynamic friction imparted by SOCAL surfaces on droplets is dominated not by the hydrodynamic flow close the droplet's edge, but by the motion of the contact line. The remarkable combination of low static friction and high dynamic friction can unlock applications in surface engineering, where SOCAL surfaces act as "low pinning-slow shedding" coatings.

These results highlight the remarkable low-pinning, slow motion of pure water droplets of SOCAL surfaces, and can motivate further studies of the statics and dynamics of droplets on other coatings achieved by polymer grafting [128].

In terms of the significance for hygrotaxis, this study shows that the contact line on SOCAL surfaces is sensitive to changes in ambient relative humidity which offers great potential in both surface tension and wettability gradient generation of motion.

Chapter 5

Simulations of Hygrotaxis of pure liquid droplets

The focus of this chapter is to explore the effect of hygrotaxis from a modelling and computational point of view. The model used in order to carry the simulations is the Lattice Boltzmann Method. The Lattice Boltzmann Method is a powerful modelling tool which allows the simulations to be described by continuum mechanics while considering both macroscopic and molecular interactions [93, 94]. This mesoscopic model simulates fluids by doing a lattice discretization of the domain and considers the average contribution of the particles around the lattice point. The Lattice Boltzmann algorithm implemented in this thesis is based on a framework built by Élfego Ruiz-Gutierrez [81–83], which has been adapted to simulate a 2D droplet undergoing phase changes regulated by variations of chemical potential in the domain.

This chapter begins by validating the phase transition dynamics of a 2D droplet, resting on a solid evaporating, in free space. The results are then compared to the theoretical predictions described in the Cahn-Hilliard equation. The comparison between the theoretical prediction and the simulation results show that the Lattice Boltzmann simulations are successful in modelling the evaporation of a droplet.

The following simulations consist of a droplet undergoing phase change in a channel configuration. A chemical potential gradient is produced by changing the boundary conditions of the chemical potential on the left and right edges of the domain. In order to counteract the pressure flows produced by a density difference in the domain, an additional background density gradient is produced to ensure that no advective flows are generated while maintaining the chemical potential gradient.

Then, an exploratory study into the evaporation, condensation and mixed states is done by varying the gradient in chemical potential in the domain. A consistent motion of the centre of mass towards higher values of chemical potential is observed in all the chemical potential gradients studied. Results stemming from mixed regimes of evaporation and condensation show the most significant amount of motion. Additionally, in situations where one side of the droplet is evaporating while the other is in equilibrium show motion of both contact points in the same direction. All of these results suggest the existence of a self-propulsion mechanism

produced by the chemical potential gradients. To elucidate the mechanism of this motion, velocity flow visualization show a significant amount of motion is happening on the interface of the droplet, pointing to a surface tension driven effect. This is further supported by the surface tension measurements done at the interface of the droplet, where there is a clear difference which drives the surface flows. Then, a study looking into the relationship of advective and diffusive flows shows that this effect is not a result of diffusive effects caused by the difference in phase change from both edges of the droplet.

Studies into the effects of different viscosities between the two phases show that this effects is not affected significantly for the viscosity range explored. Another confinement variation study, where simulations where run for different channel heights show that the dynamics generated by the chemical potential gradient are not affected. However, the lifetime of the droplet is significantly extended as the height of the channel decreases. Mass flow stream plots show that flux field around the droplet is rectified, which limits the evaporation of the droplet.

This chapter proves that hygrotaxis is possible under these conditions and motivate the experimental approaches in Chapter 6.

5.1 Evaporation of a 2D droplet

5.1.1 Theoretical prediction

To validate the numerical algorithm, control simulations of a droplet evaporating at a neutral wetting ($\theta_e = 90^\circ$) regime are carried out, where an exact solution of the Cahn-Hilliard model is available for comparison. Consider a 2D droplet sitting on a surface with an equilibrium contact angle, θ_e, of 90° (Figure 5.1). Additionally, consider a droplet is below its capillary length, under this condition the shape of the droplet is defined by the radius, R, with a fixed value of chemical potential at the interface, μ_i. A semicircular shell of radius $R_H > R$ to drive the evaporation of the droplet [80], where the boundary value of the chemical potential is fixed to an out-of-equilibrium state, μ_H. Hence the boundary conditions for the chemical potential in this system are,

$$\mu(R) = \mu_i, \tag{5.1}$$

$$\mu(R_H) = \mu_H. \tag{5.2}$$

Within the gas phase, the mass flux, J, obeys,

$$J = -M\nabla\mu \tag{5.3}$$

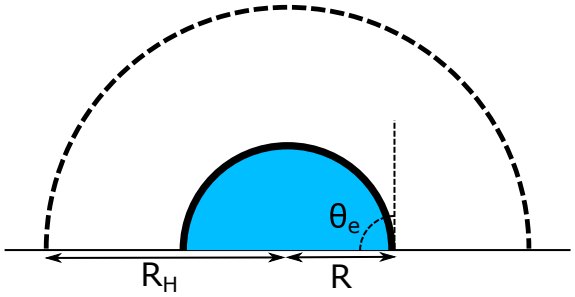

Figure 5.1: System description. The evaporation dynamics will consist of two characteristic length. The first one is the interface of the droplet represented by the length of the droplets' radius, R. The dynamics will be driven by outer shell represented by the radial length, RH.

where M is the mobility parameter. The last condition used for this calculation is that the process of evaporation is quasi-static, this implies that at any point in time the chemical potential must satisfy Laplace's equation,

$$\nabla^2 \mu = 0. \tag{5.4}$$

Under the assumption that the droplet retains its semicircular shape during evaporation, the dependence on the polar angle drops and Equation 5.4 can be simplified to,

$$\frac{d}{dr}\left(r\frac{d\mu}{dr}\right) = 0 \tag{5.5}$$

where $R \leq r \leq R_H$. Integrating Equation 5.5 with respect to r yields the expression for the spatially-dependent chemical potential

$$\mu(r) = C_1 \ln(r) + C_2, \tag{5.6}$$

where C_1 and C_2 are integration constants. Using the boundary conditions defined in Equation 5.1 and Equation 5.2, one obtains that Equation 5.6 is expressed as

$$\mu(r) = \mu_H + \frac{\mu_H - \mu_i}{\log\left(\frac{R_H}{R}\right)} \log\left(\frac{r}{R_H}\right). \tag{5.7}$$

Therefore, the flux (Equation 8.3) reads,

$$J_r = -M\frac{(\mu_H - \mu_i)}{r\log\left(\frac{R_H}{R}\right)}. \tag{5.8}$$

Integrating the flux over the liquid-gas interface returns an expression for the rate of change of area of the droplet, this is,

$$\frac{dA}{dt} = \frac{\pi M(\mu_H - \mu_i)}{\log\left(\frac{R_H}{R}\right)}, \tag{5.9}$$

where $A = \frac{\pi R^2}{2}$ is the area of the droplet. Equation 5.9 can now be expressed in terms of the base radius of the droplet as,

$$R\frac{dR}{dt} = \frac{M(\mu_H - \mu_i)}{\log\left(\frac{R_H}{R}\right)}. \tag{5.10}$$

Taking $R(0) = R_0$ as a boundary condition, one can integrate this equation to obtain the espression for the behaviour of the time dependent radius as predicted by the Cahn-Hilliard equation, thus,

$$\frac{1}{4}R^2(\log\left(\frac{R_H}{R}\right) + 1) = tM(\mu_H - \mu_i) + \frac{1}{4}R_0^2(\log\left(\frac{R_H}{R_0}\right) + 1). \tag{5.11}$$

5.1.2 Simulation setup

In the simulations, the initial radius is given as the ratio between the simulation units and the characteristic length, $L_c = L_x$, which is the horizontal length of the domain, therefore,

$$R_0 = \frac{R_i}{L_x}, \tag{5.12}$$

where R_i is the initial radius of the droplet in simulation units. The outer shell radius, R_H, is fixed as,

$$R_H = \frac{L_x - 1.5}{2}. \tag{5.13}$$

As shown in Chapter 2, in the diffuse interface approximation, the equation of state for the chemical potential is,

$$\mu(r) = \frac{3\gamma}{\sqrt{8}l}(\phi(r)^3 - \phi(r) - l^2\nabla^2\phi(r)). \tag{5.14}$$

At the edges of the domain the phase field is uniform and fixed to a value ϕ_H; therefore, equation 5.14 becomes,

$$\mu_H = \mu(R_H) = \frac{3\gamma}{\sqrt{8}l}(\phi_H^3 - \phi_H). \tag{5.15}$$

On the other hand, the chemical potential at the interface of the droplet, $\mu_i = \mu(R)$, is dominated by the Laplacian term in Equation 5.14. This is because the value of the phase field at the interface of the droplet is approximately zero, $\phi(R) \approx 0$. To estimate the value of the chemical potential at this point, the Gibbs-Thomson condition used since it provides an approximation of the small changes in chemical potential along the interface,

$$\mu_i \approx \Delta\mu = -\frac{2\gamma C}{\Delta\phi}, \tag{5.16}$$

where $\Delta\mu$ is the difference of the chemical potential close to the interface, C is the curvature of the interface and $\Delta\phi$ is the change of the phase field across the interface, which for the simulations $\Delta\phi \approx 2$.

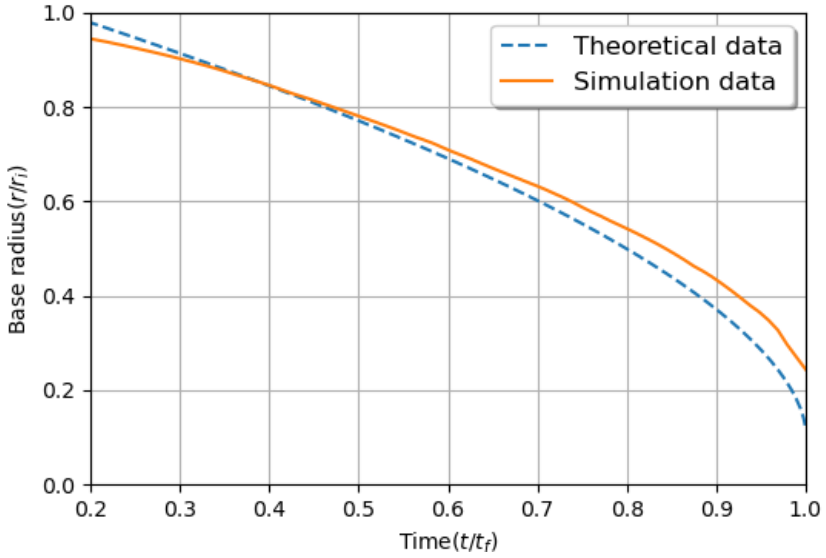

Figure 5.2: Cahn-Hilliard prediction vs Lattice Boltzmann simulations. Graph showing the comparison of the evolution of the radius of the droplet over time. The differences that are observed between the 2 lines can be justified by the difference that in the simulations, difference between μ_H and μ_i is not constant as it is taken in the construction of the theory.

Table 5.1: Simulation Parameters for 2D evaporation. Arbitrary units

Parameter	Value	Parameter	value
Channel height, L_y	32	Channel Width, L_x	64
Surface tension, γ_0	1×10^{-4}	Density, ρ	1
Interface width, l	1.6	Radius, $r = \frac{R}{L_x}$	0.2
Droplet viscosity, ν_1	1/6	Ambient viscosity, ν_2	1/6
Phase field, ϕ	-1.3	Chemical potential, μ_H	-5.95×10^{-5}
Chemical potential at R, μ_i	7.81×10^{-6}		

Table 5.1 shows the parameters used in order to run the simulation. Figure 5.2, shows the theoretical prediction and the simulation results for the behaviour of the base radius of the droplet. The overall behaviour of the simulation curve follows the one predicted by Cahn-Hilliard equation, where both curves decay and collapse similarly over time. Nonetheless, there are subtle differences between both curves. However, these slight differences can be justified since the difference $\mu_H - \mu_i$ are not strictly the same between the simulations and the Cahn-Hilliard model. This is because, in reality, μ_i is not constant and changes as the radius of the droplet is displaced as it evaporates. In the simulations, this difference is not taken as a constant which has an effect in the rate of evaporation of the droplet.

5.2 2D channel configuration

In the laboratory, it is challenging to expose a droplet to a humidity gradient in a room due to the difference in scale and the gradients expected to have a direct influence are those in the vicinity of the droplet. However, this can be achieved by localizing the ambient conditions to a domain comparable to the droplet size. In the literature, the strategies adopted to achieve a vapour driven motion for binary mixtures and pure droplets often require the existence of a second droplet in the near vicinity of each other to generate a gradient [15, 17, 18]. These strategies are successful in generating vapour gradients that influence the mechanics of the droplet, however, additional effects such as thermal interactions between the liquid-solid cannot be avoided in highly energetic systems [16, 129]. These interactions induce thermal gradients which contribute to the motion of droplets on such surfaces, making it a challenge to determine the precise role of vapour gradients in the mechanism of motion. To avoid this issue, the simulations are done in the absence of temperature to isolate the effect of chemical potential gradients. In order to bolster the formation of humidity gradients, the droplet is confined to a domain size no bigger than 5 times the initial radius of the droplet. Hence, the case proposed in this work is one where the droplet is sitting in the middle of a square channel and is exposed to a humidity gradient by setting each side of the channel to different values of chemical potential gradients.

Figure 5.3 shows the geometry of the domain exposed to a chemical potential gradient. The square channel is defined by the length L_x and the height L_y. A droplet is placed on the bottom surface directly in the centre of the channel and by changing the open boundary conditions on each side of the channel by setting differing values of the order parameter and chemical potential, one can generate a gradient of chemical potential throughout the channel. For clarity and without loss of generality, the chemical potential gradients are set to point to the left edge of the domain.

5.2.1 Pressure flows

One of the issues when trying to create a chemical potential gradient is that differences in the density field generate a pressure flow on the horizontal axis which inevitably affects the motion of the droplet in the simulations, as seen in Figure 5.4(a). In order to ensure that the simulations are not affected by this advective flow, the simulation setup must accommodate an additional chemical potential gradient in the x-direction such that the velocity of the flow generated is identically zero. This is achieved by considering that the total pressure in the Navier-Stokes equation (Equation 2.41) for $u = 0$ satisfies

$$0 = -\nabla \cdot \Pi = -c_s^2 \nabla \rho - \phi \nabla \mu, \tag{5.17}$$

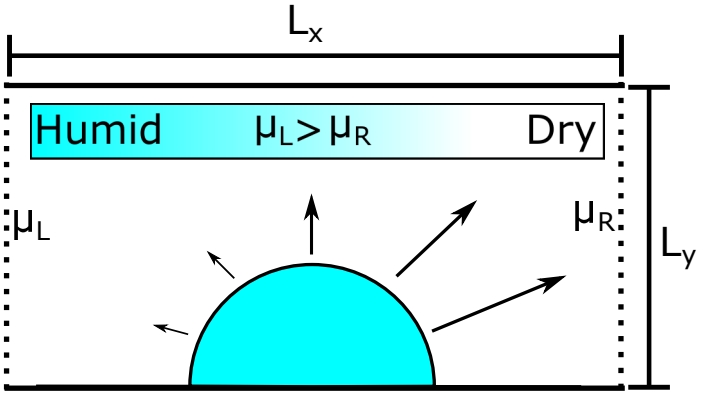

Figure 5.3: System proposal. The system consists of a droplet sitting in the middle of the domain, of horizontal length, L_x, and the vertical length, L_y. The bottom and top edges consist of solid walls. The left and right edges of the domain consist of open sides. A gradient in chemical potential, responsible for the phase change, is achieved by imposing a difference between the left and right chemical potentials, $\mu_l = \mu_0$ and $\mu_r = \mu_0'$, respectively.

which arises from from expressing the total pressure by is partial components. Hence, solving Equation 5.17 for ρ provides the correct density profile that cancels any mechanical motion while retaining the constant diffusive flux between the phases. This implies that one can define a density profile that counteracts the constant chemical potential gradient generated flows.

For a one dimensional system, the integration of Equation 5.17 yields

$$\int_V \nabla \cdot \Pi dV = \int_{\delta V} \Pi \cdot dS = [\rho_r - \rho_l] c_s^2 \hat{\mathbf{x}} + [\mathbf{P}(x = L_x) - \mathbf{P}(x = 0)] \cdot \hat{\mathbf{x}}], \tag{5.18}$$

where the first equality is found using the divergence theorem and ρ_l and ρ_r are the left and right densities at the open boundaries, respectively. Inputing the expression of the capillary pressure in Equation 5.18 yields the following expression for the difference in densities ρ_l and ρ_r, then

$$\rho_r - \rho_l = -\frac{1}{c_s^2} \left[\phi\mu - \psi + \frac{3\gamma l}{\sqrt{8}} \left(\frac{d\phi}{dx} \right)^2 \right]_{x=0}^{x=L_x}. \tag{5.19}$$

The chemical potential gradient is prescribes by a difference in the boundary values of the phase field, $\phi_l = \phi(x = 0)$ and $\phi_r = \phi(x = L_x)$, respectively, and evaluating Equation 2.53. For $\nabla\mu = \text{constant}$, the following consideration is taken

$$\frac{d\phi}{dx}(x = L_x) = \frac{d\phi}{dx}(x = 0), \tag{5.20}$$

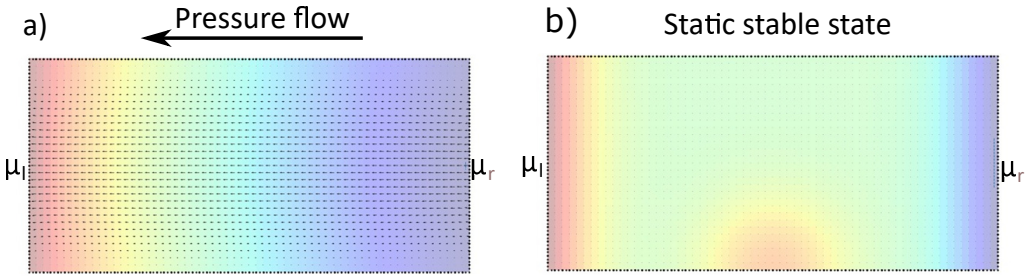

Figure 5.4: Pressure flows generated by gradients in chemical potential. a) Different boundary conditions for the chemical potential on the open sides of the channel generate a pressure flow from high to low chemical potential. b) Simulation domain after hygrostatic pressure considerations correct the generation of the pressure flow.

which gives a good approximation for small chemical potential gradients and small variations around the equilibrium values $\phi = \pm 1$, Moreover, as a consequence of Equation 5.20, the last term on the right hand side of Equation 5.19 vanishes and the difference in the boundary values of the density is given by

$$\rho_r - \rho_l = -\frac{1}{c_s^2}[\tilde{p}(x = L_x) - \tilde{p}(x = 0)], \tag{5.21}$$

where

$$\tilde{p}(\phi) = \phi\mu(\phi) - \psi(\phi, \nabla\phi = 0) = \frac{3\gamma_0}{8\sqrt{2}l}\phi^2(3\phi^2 - 2), \tag{5.22}$$

defines the interaction of an homogeneous system. Thus, the boundary values of the density are chosen to be

$$\rho_l = 1 - \frac{1}{c_s^2}\tilde{p}_l, \tag{5.23}$$

and

$$\rho = 1 - \frac{1}{c_s^2}\tilde{p}_r, \tag{5.24}$$

to satisfy Equation 5.21, where $\tilde{p}_l = \tilde{p}(\phi_l)$ and $\tilde{p}_r = \tilde{p}(\phi_r)$. Figure 5.4(b) shows the result of choosing these density boundary values, where a droplet under the same chemical potential gradient as panel was able to evaporate without mechanical motion observed, showing the ability to still exchange flux, and the absence of pressure flows in the dommain.

5.2.2 Boundary conditions

The top and at the bottom edges of the domain are solid boundaries, i.e.,

$$\mathbf{u}(\mathbf{x}_s) = 0, \tag{5.25}$$

$$\hat{n} \cdot \nabla \cdot (\Pi - \eta(\nabla \mathbf{u} + \nabla \mathbf{u}^T)(\mathbf{x}_s)) = 0, \tag{5.26}$$

$$\hat{n} \cdot \nabla \mu(\mathbf{x}_s) = 0, \tag{5.27}$$

where $\mathbf{x}_s$ are the coordinates of the solid boundaries.

On the other hand, the left and right edges of the channel are considered to be open and to allow exchanges of mass with its surroundings. At these boundaries, the pressure and the chemical potential are prescribed as,

$$\phi(\mathbf{x}_o) = \phi_o, \tag{5.28}$$

$$\nabla \cdot \mathbf{u}(\mathbf{x}_o) = 0, \tag{5.29}$$

$$\Pi(\mathbf{x}_o) = \Pi_o, \tag{5.30}$$

$$\mu(\mathbf{x}_o) = \mu_o = 3\frac{\gamma}{\sqrt{8}l}(\phi_o^3 - \phi_o), \tag{5.31}$$

where the x_o are the coordinates of the open boundary and ϕ_o, Π_o and μ_o are the boundary values of the order parameter, the pressure tensor and the chemical potential, respectively.

5.2.3 Normalization of key quantities

An important aspect of this study is to find significant quantities that helps to interpret data and provide physical meaning to the measurements. For hygrotaxis, the interest lies in the dynamics of the centre and the contact points of the droplet.

The characteristic length, L_c, is the distance that a molecule needs to traverse during diffusion,

$$L_c = L_x. \tag{5.32}$$

The characteristic velocity, u_c, is normalized by considering that the advective fluxes are equivalent to the diffusive ones in the system, hence

$$u_c = -M\frac{\mu_d}{\rho L_c}, \tag{5.33}$$

where $\mu_d = \mu_r - \mu_l$.

Equations 5.32 and 5.33 are then used to obtain the characteristic time of diffusion,

$$t_c = \frac{\rho L_c^2}{M|\mu_d|}. \tag{5.34}$$

Another quantity that plays an important part in the analysis is the chemical potential. The normalization of this quantity can be obtained if one considers the relationship between the initial surface tension and the density. Hence, the characteristic chemical potential is defined as,

$$\mu_c = \frac{\gamma_0}{\rho L_c}, \tag{5.35}$$

where μ_c is the characteristic chemical potential and γ_0 is the initial surface tension. For the simulations, these values will remain constant at $\mu_c = 7.8125 \times 10^{-7}$.

5.3 Chemical potential gradient simulations

5.3.1 Evaporation, condensation and mixed regimes

Evaporation and condensation are phase change phenomena that arise from the energy cost that is required to hold or release an species of liquid molecule into the surrounding phase. Phase change is usually driven by a mixture of temperature and chemical potential changes. Temperature effects are neglected in the simulations presented in this chapter, leaving phase change as an adsorptive or desorptive effect driven only by differences in chemical potential. Therefore, the key quantity that regulates phase change in this system is the chemical potential since it regulates the coexistence of the liquid and gas phases. Hence, the simulations presented here have an intrinsic dependence on the number of particles in the system for the dynamics of phase change, akin to relative humidity.

To better understand the effects of changes in the chemical potential in the evolution of evaporation or condensation, three representative gradient scenarios are outlined where hygrotaxis may occur. The first one, identified as the Evaporation-Evaporation (EE) regime, corresponds to a situation where the boundary conditions at each side of the channel are set to values that drive the evaporation of the droplet at different rates. The second scenario is where one boundary drives evaporation while the other induces condensation, such cases are referred to as Evaporation-Condensation (EC) to denote overall evaporation and Condensation-Evaporation (CE) for overall condensation. The third scenario is the Condensation-Condensation (CC), which comprises cases where both boundary values drive the condensation of the droplet.

Table 5.2: Constant simulation parameters for chemical potential gradients. Arbitrary units

Parameter	Value	Parameter	Value
Channel height, L_y	64	Channel Width, L_x	128
Surface tension, γ_0	1×10^{-4}	Viscosity, η	1/6
Interface thickness, l	1.6		

The parameters that regulate the chemical potential gradient are the boundary values of the chemical potential. These are the left boundary value of the chemical potential, μ_l, and the right value of the chemical potential, μ_r. In the evaporation-evaporation regime simulations, both sides of the domain are set to negative values of chemical potential, with the condition that $\mu_i \geq \mu_l > \mu_r$ to ensure that a gradient is produced. For the evaporation-condensation regime, the relationship between the chemical potential is set to follow $\mu_l > \mu_i > \mu_r$. In the evaporation-condensation regimes, the overall behaviour of evaporation or condensation in the simulations is prescribed by the relation,

$$\mu_T = \frac{\mu_r + \mu_l}{2} \tag{5.36}$$

where μ_T is the average value of the chemical potential in the domain. Overall evaporation occurs when $\mu_T < \mu_i$ and condensation when $\mu_T > \mu_i$. Lastly, for the condensation-condensation cases, the relationship between the values of the chemical potential is $\mu_l > \mu_r \geq \mu_i$. For all scenarios described to this point, table 5.2 details the simulation parameters shared by all chemical potential regimes. For clarity, and without loss of generality, the chemical potential gradients presented are always set to point to the left.

Figure 5.5 shows some examples of the results under the different gradient regimes described. In all of the regimes, there is a clear displacement of the centre of the droplet towards the humid, or higher chemical potential, side. This effect is stronger in the case shown in panel c) of Figure 5.5, where the combination of the evaporation and condensation regimes increase the lifetime of the droplet, allowing the droplet to move beyond its initial footprint. The overarching behaviour of these results is that motion of the centre of mass of the droplet is observed irrespective of the chemical potential gradient regime the droplet is subjected to.

The behaviour of the contact points of the droplet in Figure 5.5 is now discussed. Panel a) of Figure 5.5, shows a regime where one would expect to observe symmetric evaporation of the droplet. This is to say where both contact points move constantly towards each other until they collapse into one, albeit at different rates depending on the evaporation regime the particular side is subjected to. However, this is not the case in panel a), the behaviour observed is that the left contact point, which is exposed to an evaporating regime, remains static for the

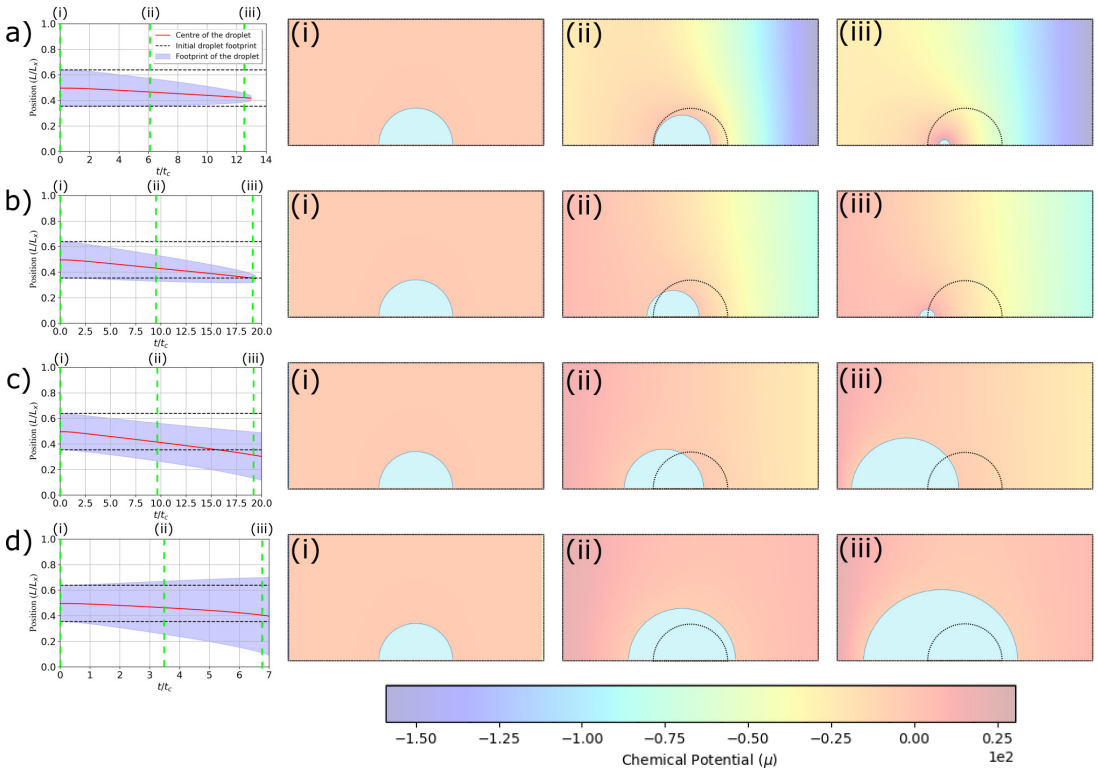

Figure 5.5: Chemical gradient regimes. a) Evaporation-evaporation regime where $\mu_l = -19.6$ and $\mu_r = -159.1$. b) Combination of evaporation and condensation where the former is predominant, $\mu_l = 14.5$ and $\mu_r = -76.1$. Similarly to b), c) Evaporation-condensation regime where there is a near equilibrium gradient between evaporation and condensation rates, $\mu_l = 24.4$ and $\mu_r = -19.6$. d) Condensation-condensation regime where both values of the chemical potential differ but are positive to drive condensation, $\mu_l = 30.3$ and $\mu_r = 14.5$. All initial radii are $R = 0.2$.

majority of the simulation until the radius of the droplet reaches the collapsing phase of the evaporation. This behaviour indicates that for the majority of the life of the droplet there is a force, contrary to the one driven by evaporation, that drives the contact points towards the left side.

This force explains the behaviour of the contact points in other chemical potential gradient regimes. In panel b) of Figure 5.5, the value of the negative chemical potential is ~ 5 times larger and since $\mu_T = -30.8$, retraction of both contact points should be observed since the regime corresponds to that of overall evaporation. However, the contact points move in the same direction, again, showing the existence of a driving force guiding the motion of the droplet. Panel c) shows a case where the difference between the chemical potential is minimal, $\mu_T < 2.5$, since the droplet is gaining and loosing mass at similar rates, it is expected that the contact points would remain static to a degree but what is observed is the continuous motion of the droplet towards the humid side. Panel d) shows a clear displacement of the

Table 5.3: Simulation Parameters. Arbitrary units

Parameter	Value	Parameter	value
Channel height, L_y	64	Channel Width, L_x	128
Surface tension, γ_0	1×10^{-4}	Density, ρ	1
Interface width, l	1.6	Radius, $r = \frac{R}{L_x}$	0.35
Droplet viscosity, η_1	1/6	Ambient viscosity, η_2	1/6
Left chemical potential, μ_l	0	Right chemical potential, μ_r	-211.8

centre of mass of the droplet and week motion of the right contact point. In this case, it is not enough to observe the behaviour of the contact points to determine if there is a dynamic effect contributing to the overall motion of the droplet, it is necessary to further understand the mechanism guiding the motion of the droplet in chemical gradient regimes. This effect is identified as hygrotaxis, and the following section explores the mechanism that makes this motion possible.

5.4 The driving mechanism of Hygrotaxis

To explore the hygrotactic behaviour, the boundary condition for the chemical potential on the left side is set to $\mu_l = 0$, while the right side is set to $\mu_r < 0$. In this gradient regime, the evaporation of the droplet is localized on the right side of the droplet while the left side of the droplet is kept close to equilibrium (Equilibrium-Evaporation (EQE)). Under these conditions, the left side of the droplet is not expected to present motion since no mass in being accreted. The parameters of this simulation is reported on table 5.3 and the results can be appreciated in Figure 5.6. Interestingly, in this chemical potential gradient regime, motion of both contact lines in the same direction.

Figure 5.7 shows the evolution of the contact radius, the average velocity of the centre of the droplet and the evolution of the contact angle. There is a transient where the base radius decreases faster in comparison to the rest of the simulation. This effect is a consequence of relaxation of the chemical potential reaching a quasi-static regime, this is to say when $\nabla^2 \mu = 0$. However, after the transient period in panel a), the radius of the droplet adopts a similar behaviour to that observed in the base simulation of Section 5.1.

One of the possible mechanisms considered for hygrotaxis, which stem from the results of Chapter 4, was that a difference in contact angle along the triple point may induce Laplace pressure driven motion of the droplet coming from wetting gradients, driving the motion from low wetting regions to high wetting ones [5, 61, 130]. By comparing the behaviour of the motion of the droplet and that of the contact angle values at the two contact points in panels b) and c) of Figure 5.5, it is possible to look into this possibility for hygrotaxis. Considering the initial difference in contact angle, $\sim 2^\circ$, this would result in a initial force opposing the motion of the

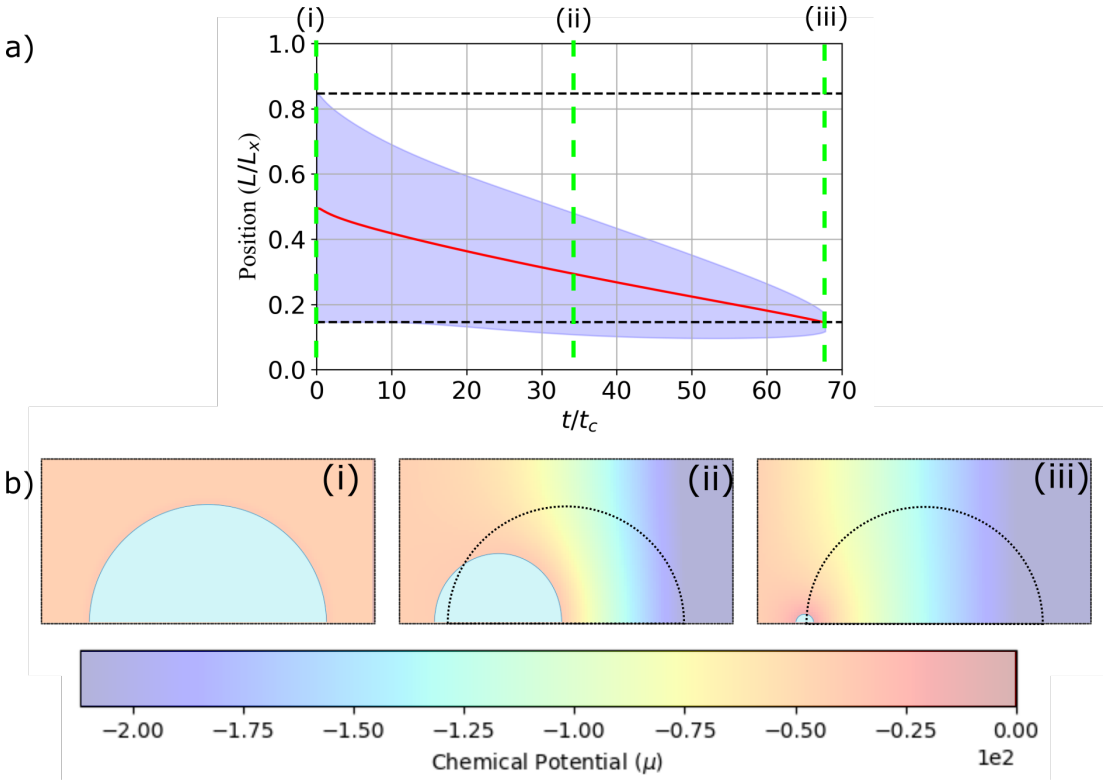

Figure 5.6: Equilibrium-evaporation (EQE) gradient. a) Shows the evolution of the centre of the droplet and the droplet contact points. b) snapshots of the evolution of the droplet. The left side of the channel is set to a zero and the right side is set to an evaporating regime, $\mu_l = 0.0$ and $\mu_r = -211.8$, respectively.

droplet. However, the change in position of the centre of the droplet during the evaporation is linear, reflecting a constant velocity towards the left of the channel, while the initial difference in contact angle vanishes over the course of the simulation without affecting the motion of the droplet. This suggests that the difference in contact angle has no significant effect on hygrotactic motion under the conditions set in the simulations and that the mechanism is dominated by another effect.

In the literature, vapour driven motion is a product of surface tension gradients that generate inner flows which drive the motion of the droplet, this effect is most commonly known as the Marangoni effect [131, 132] or Marangoni driven motion [15, 130, 133]. In multiphase fluids, surface tension can be described as the excess free energy that it costs to maintain an interface between two phases, which can be appreciated as the shaded area and the peak of the Helmholtz free energy in Figure 2.12b in Chapter 2. Figure. 5.8 shows an instance in time after the relaxation period of the droplet where the contact points of the droplet are moving in the same direction. In the same figure, plots of the mass flux streams around the droplet are shown, the velocity streams inside the channel and the surface tension change profile along the interface. This instance in time can be appreciated by the green dotted line in panel

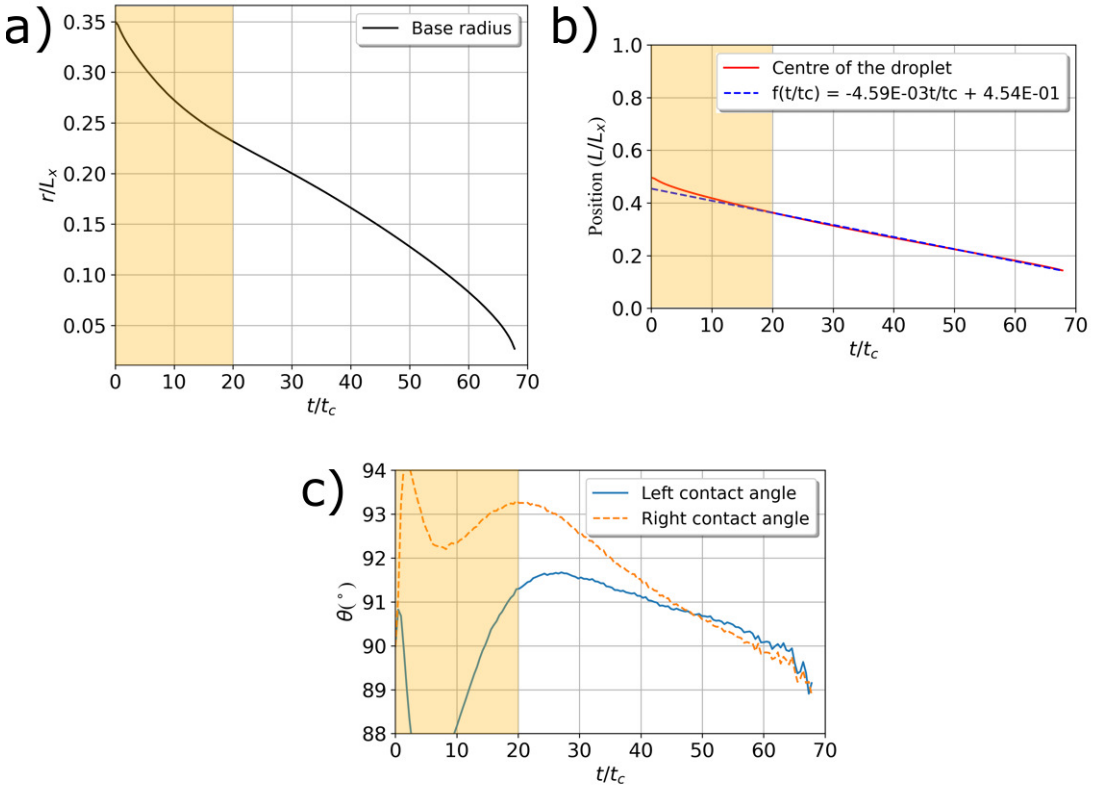

Figure 5.7: Droplet key parameters. The yellow shaded region is considered a relaxation phase, it is the time the chemical potential takes to reach a steady gradient. a) Shows the evolution of the base radius, b) shows the evolution of the centre of the droplet and the average velocity of the droplet considering the linear section after the relaxation phase, and c) shows the evolution of the contact angle of the left and right contact points.

a), which shows the evolution of centre of the droplet and the contact points. Panel b) shows the stream plot of the flux field as calculated from equation 2.42. The intensity of the flux in the domain represents the boundary values of the chemical potential where the flux stream lines coming out of the interface of the droplet are stronger on the right, where the boundary condition driving the evaporation of the drop is larger. This panel shows that the chemical gradient imposed induces anisotropic fluxes at the interface of the droplet. In panel c), it is evident that the the flow is stronger close to the interface of the droplet, driving liquid from the left side to the right side of the interface. This, in turn, generates a convective flow inside the droplet in the direction of the motion close to the solid interface, resulting in motion of the bulk towards the humid region. This behaviour of the flows on the surface of the droplet and the convective flows observed agree with the known mechanism of surface tension driven effects mentioned in literature [15, 133] which drive the motion of the droplet.

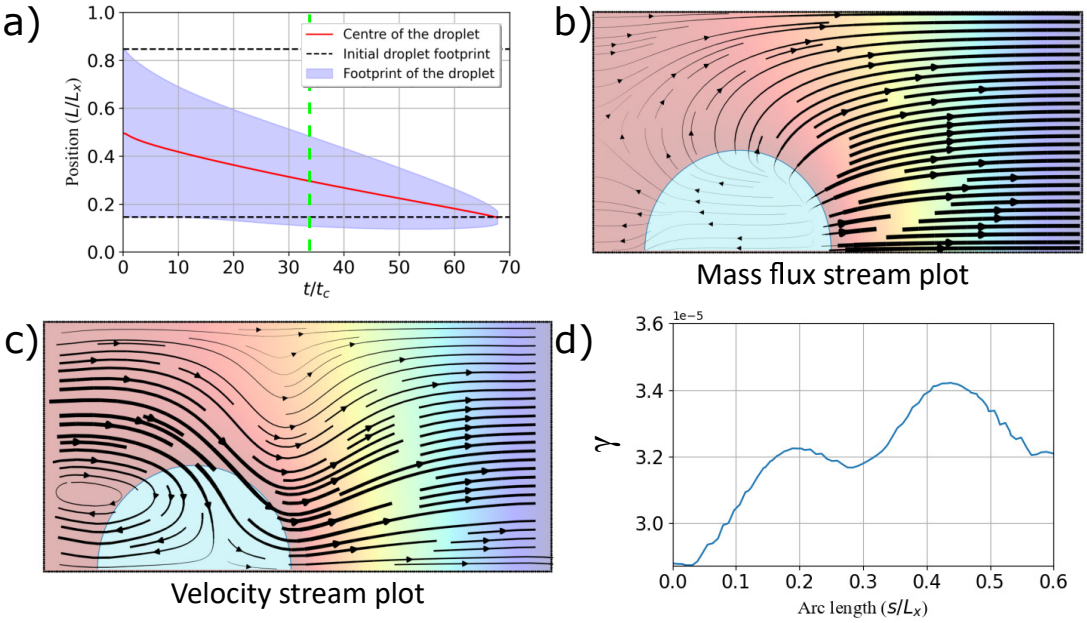

Figure 5.8: Dynamics of Hygrotaxis. a) Evolution of centre of the droplet and the contact points, the green dotted line is the instance in time where analysis for the next plots is taken. b) Stream plot showing the flux field of the droplet. c) Stream plot of the velocity field inside the domain of the simulation. The flows are strongest close to the interface of the droplet and generate vortices that propagate inside the droplet. d) Local surface tension, $\gamma(s) = \frac{3\gamma_0(\nabla\phi)}{\sqrt{8}}$, along the interface of the droplet. s are the points in space of the interface of the droplet

To confirm that there is a Marangoni flow being induced along the surface of the droplet, one needs to focus on the differences of surface tension along the interface of the droplet. One can approximate the surface tension in the interface by using Equation 2.57 and considering that $\phi = 0$ at the interface of the droplet. Therefore, the only contribution at the interface of the droplet will depend on $\Delta\phi$, hence

$$\gamma(s) \approx \frac{3\gamma_0 l(\nabla^2\phi)}{\sqrt{8}}, \tag{5.37}$$

where $s = s_{sim}/L_x$ is the contour, or arc-length, of the droplet. Panel d) shows the local values of the surface tension of the interface the droplet, higher surface tension values reflect stronger cohesive forces, explaining the generation of a flow in the direction seen in panel c). Since the only parameter varied is the chemical potential gradient, this shows that the presence of chemical potential gradients induce inhomogeneities in the surface tension at the interface of the droplet, driving the flow of liquid along the surface of the droplet.

Table 5.4: Phase field and chemical potential values for simulations.

Regime	ϕ_l	ϕ_r	μ_l	μ_r
EQE	-1.0	-1.6	0.0	-211.8
EC	-0.9	-1.3	14.5	-76.1
ECEQ	-0.8	-1.2	24.4	-44.8
EQC	-0.6	-1.0	32.6	0.0

5.4.1 Advection vs Diffusion

Hygrotaxis is not only present in the evaporative regime presented so far, the results show that it is a pervasive effect as long as a chemical potential gradient is present. This means that the chemical potential gradient can be set to obtain specific behaviours for hygrotactic motion. Figure 5.9 shows additional simulations for regimes where the values of the phase field have been adjusted to obtain specific behaviours. These phase field parameters are reported in Table 5.4. On panel a), the case corresponds to that of an EC case where the left edge of the interface of the droplet is set to one close to equilibrium which allows the droplet to move significantly beyond its initial footprint. Panel b) shows a EC case where the phase field has been set so that there is minimal loss of mass of the droplet which allows it to reach the end of the domain almost unchanged, this case is referred to as Evaporation-Condensation at Equilibrium (ECEQ). Panel c), analogous to the EQE case at the beginning of this section, shows a situation where condensation of the droplet is localized to the left side while the other is kept close to equilibrium. This case, referred to as Equilbrium-Condensation (EQC), shows that both contact points of the droplet can be influenced to move in the same direction.

To confirm that in the mechanism of motion is present in all of the cases mentioned in this section, Figure 5.10 shows the velocity flow plots, including that of the EQE case in panel a). In all cases, the mechanism of motion is present since there are strong flows being generated close the interface of the droplets. Additionally, in the cases where there is condensation and evaporation, a displacement of inner flow vortex to towards the center of the drop is observed. Table 5.4 shows the phase field value, the normalized values of the chemical potential and the corresponding velocity of motion for each regime. On can observe that the velocity, a value dependent on the diffusion velocity or the difference in chemical potential, does not vary significantly. This suggests that hygrotaxis is an effect that has little dependence on the diffusion. However, in regimes where the motion chemical gradient allows both evaporation condensation, it is to confirm that the droplet is moving due to hygrotaxis and not because of a kinematic effect caused by the accretion of liquid molecules on one side and depletion the loss of them on the other, resulting in the apparent movement of the droplet. In these cases, it is necessary to compare how the velocity of flow of the bulk compares to the velocity of diffusion to determine if the condensation and evaporation, which are directly linked with diffusion velocities, play a significant roll in the dynamics

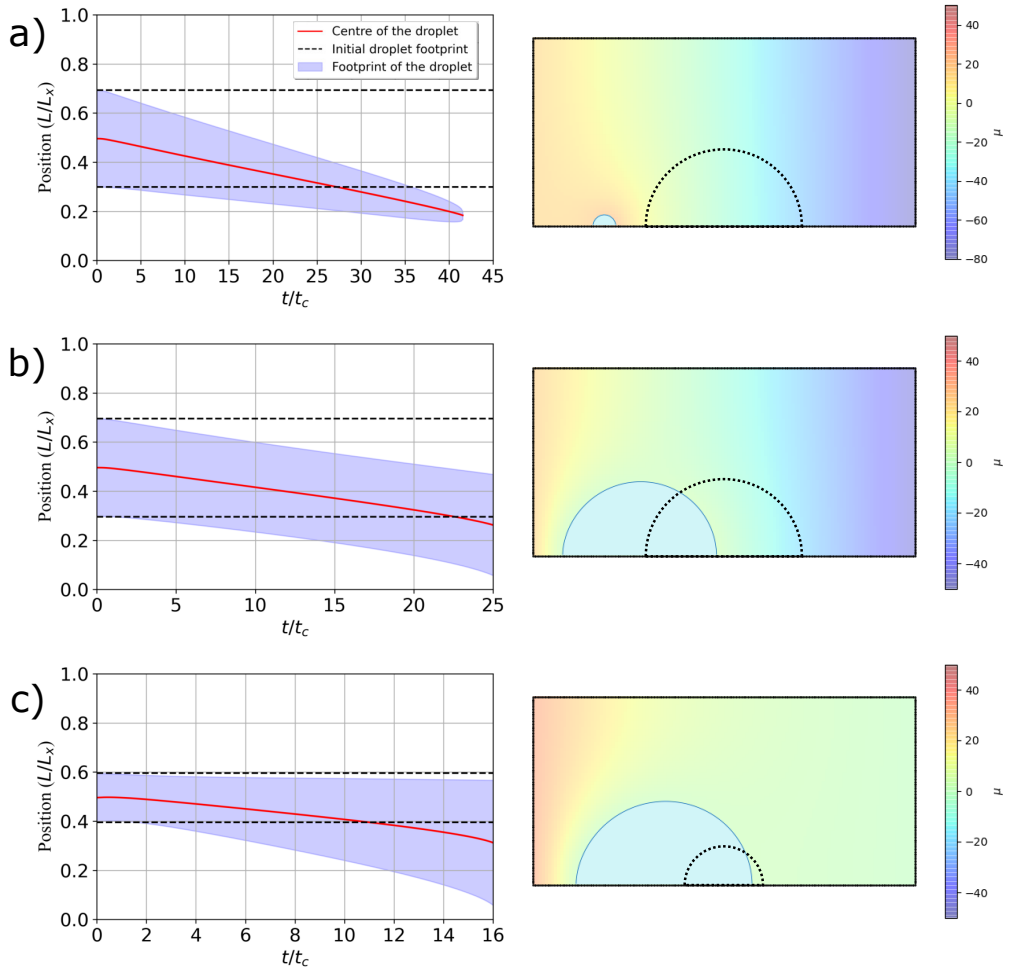

Figure 5.9: Optimized gradient regimes. a) Evaporation-Condensation (EC): regime where the phase field values are set as $\mu_l = 14.5$ and $\mu_r = -76.1$. In this regime there is condensation but more evaporation. b) Evaporation-Condesation Equilibrium (ECEQ): Regime where the phase field values are set to be symmetrical, $\mu_l = 24.4$ and $\mu_r = -44.8$. Under this regime, the droplet moves with minimal loss of mass. c) Equilibrium-evaporation (EQC): Regime where the phase field values are set to $\mu_l = 32.6$ and $\mu_r = 0.0$.

There are two dimensionless quantities that describe the relationship between advective transport and diffusive transport, these are the Péclet number (Pe) and the Marangoni number (Ma). The Péclet number is the ratio between the advective transport rate and the diffusive transport rate. In the simulations, the advective transport rate is the velocity at which the centre of the droplet moves, u_{cm}, while the diffusive transport rate is the characteristic velocity of diffusion defined in equation 5.33. The ratio between these two describes which effect is more significant in the motion of a liquid and is defined as

$$Pe = |Pe| = \frac{u_{cm}}{u_c}. \tag{5.38}$$

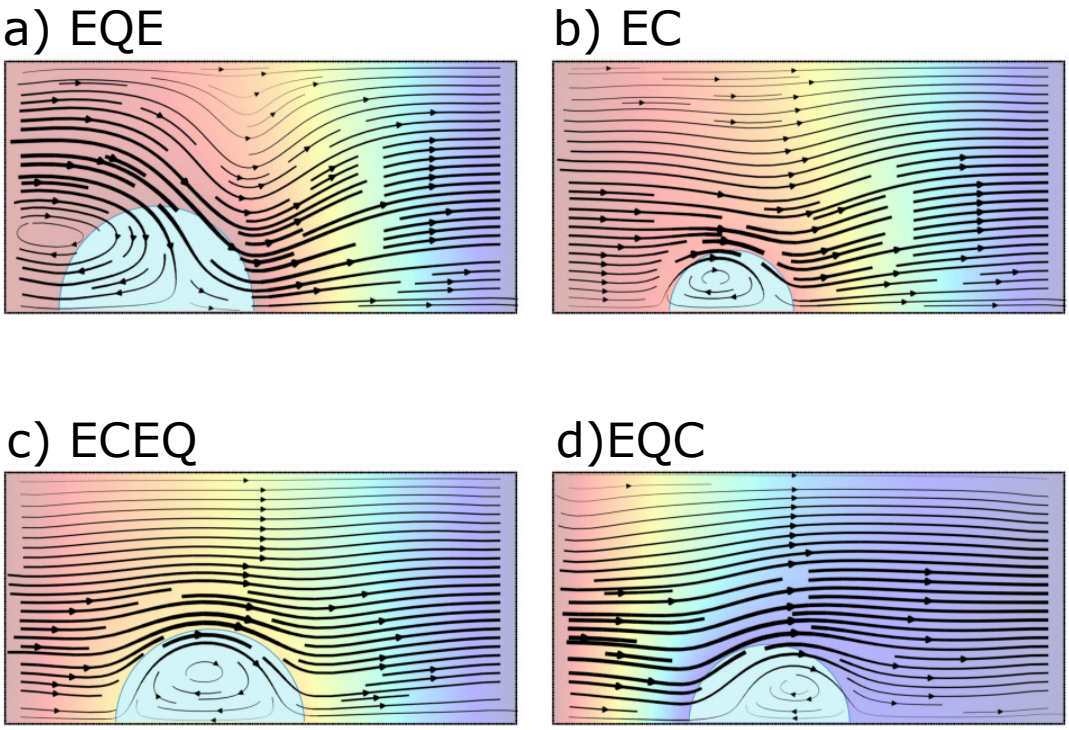

Figure 5.10: Velocity streams for different regimes. In all cases the velocity streams are stronger close to the interface of the droplet. The flow vortexes also experience displacement towards the centre of the droplet, depending on the nature of the gradient.

$Pe \gg 1$ indicates that advective flows are being generated and play a dominant part in the motion of the droplet. If the effect was dependent on the condensation or evaporation of the droplet then the velocity of the droplet and the Peclét number would be comparable with the diffusion velocity.

The Marangoni number , on the other hand, is another dimensionless number that describes the relationship between advective and diffusive forces. However, this number is tied to the advection and diffusion caused purely by surface tension gradients and is defined as

$$Ma = \frac{u_\tau s}{D}, \tag{5.39}$$

where u_τ is the tangential velocity along the interface of the droplet, s is the arc length of the droplet interface and D is the diffusion constant defined as $D = \frac{3\gamma_0}{l\sqrt{8}}$. As for the Péclet number, a positive value would show that that the surface tension on the interface of the surface is generating the flow. Additionally, the value of the Marangoni number also describes the type of vortex expected, as denoted in the work Diddens, *et al.* [133] where they related the value of this number to the type of convective flow present in droplets.

Table 5.5, shows the Pe and Ma values for the simulations along with the associated velocities of the centre of the droplet, v_d. These dimensionless quantities show two characteristics of

Table 5.5: Velocity, Péclet and Marangoni number values for the motion in different Regimes.

Regime	$v_d \times 10^{-3}$ (d_{norm}/t)	Pe	Ma
EQE	-5.0	197.2	13.9
EC	-7.5	736.9	2.1
ECEQ	-9.7	1269.7	5.6
EQC	-11.0	2944.2	2.3

the motion observed in this system. First, the Péclet number indicates that the advective contribution is larger by 2 to 3 orders of magnitude than the diffusive one, which strongly suggests that the motion of the droplet is not a consequence of a diffusive effect. On the other hand, the Marangoni number describes the flows generated inside the droplet stem from the surface tension effects. Additionally, Table 5.5 suggests that hygrotactic motion is more effective for condensing fronts since the Péclet number differs by an order of magnitude and faster velocities are recorded for the centre of the droplet.

5.5 Effect of viscosity

To this point, all the simulations have been done using matching viscosities for the liquid and vapour phases. Viscosity plays an important part in how a liquid behaves since it controls the friction the liquid experiences as it flows. In addition, the viscosity of the two fluid phases can be significantly different.

Two viscosity scenarios are studied, the first scenario corresponds to the case where the viscosity of the liquid phase, η_{in}, is larger than the ambient viscosity, η_{out}. Figure 5.11 shows the motion of the centre of the droplet in five different viscosity combinations. In this scenario, the viscosity has little impact of the motion of the droplet. However, at the largest viscosity contrast, $\eta_{in}/\eta_{out} = 0.5/0.1$, the droplet travels less distance by the slight decrease in velocity due to this difference in viscosity.

The second scenario is when the ambient viscosity is larger than the viscosity of the droplet. Figure 5.12 shows the results of this viscosity contrast sweep. Similarly to the first case, the viscosity has insignificant effects on the overall motion of the droplet, with the observation that larger values for the viscosity of the ambient phase allow for small increase in the velocity of the droplet which does not increase with increasing values of the ambient viscosity.

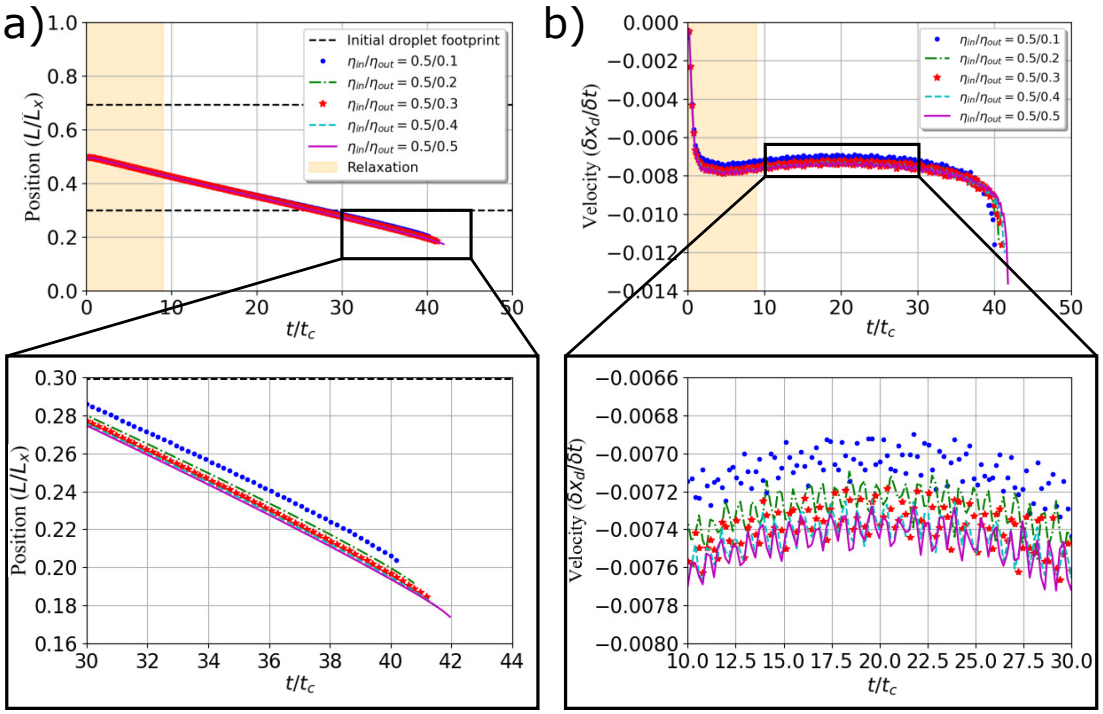

Figure 5.11: Inner viscosity larger than outer viscosity. a) Position of the centre of the droplet where the liquid viscosity of the droplet is larger. b) Instantaneous velocity of the centre of the droplet, where $x_d = L/L_x$.

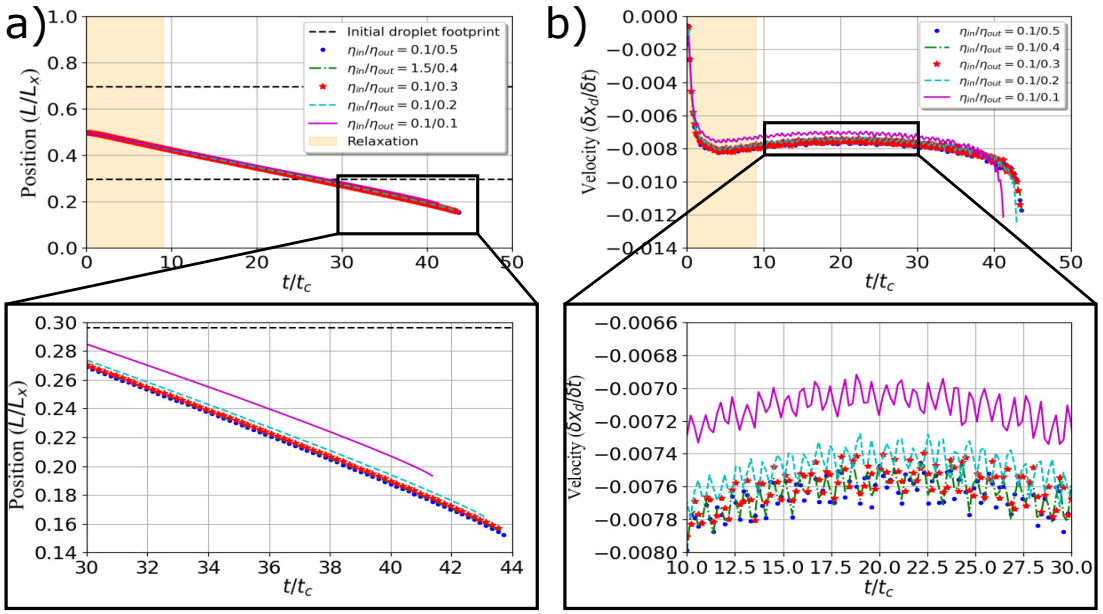

Figure 5.12: Outer viscosity larger than inner viscosity. a) Position of the centre of the droplet where the ambient viscosity of the droplet is larger. b) Instantaneous velocity of the centre of the droplet, where $x_d = L/L_x$.

Although the effect of the viscosity is small for hygrotactic motion, the fact that the droplet moves a fraction faster in more viscous environments shows that the ambient of the droplet plays a small part in the "traction" between the ambient and the liquid phase. Additionally, the low dependence in droplet viscosity also points to the conclusion that hygrotactic motion is an effect that largely depends on the contribution of the surface tension difference generated by the chemical potential gradient.

5.6 Effect of Channel height

The attention is now turned to the effect of the channel height on the dynamics of hygrotaxis. As mentioned before, this confined configuration was chosen because it was considered that chemical gradients would have a more significant effect if the size of the domain was comparable to the size of the droplet in laboratory conditions. In order to see how the confinement of the droplet affects the dynamics of hygrotaxis, five different values of channel height are chosen: 40, 50, 64, 96 and 128, which are given in simulation length scale units (L_y). All of the domains of different height are subjected to an identical EC regime, where $\mu_l = 14.5$ and $\mu_r = -76.1$. Figure 5.13 shows the effect of the channel height on the decay of the base radius of the drop. For channel heights which are large in comparison to the droplet, $L_y > 96$, the differences in the evolution of the base radius are insignificant. However, for channel heights $L_y = 96$ and $L_y = 64$, there is a transition in behaviour of the rate of decay of the base radius, becoming slower as the height of the domain is reduced. These differences in the evolution of the base radius, specially those close to the droplet size, suggest that confinement greatly affects the rate of evaporation of the droplet. The rate of evaporation is slowed to the extent that the droplet is able to reach the edge of the domain due to hygrotactic motion. The final increase in radius observed in the Figure 5.13 is a simulation artifact stemming from the boundary conditions, which are not discussed here.

The base radius of the droplet is plotted as a function position in Figure 5.14. This graph is helpful since one can find the position of the droplet in the channel where the boundary effects start to deviate from normal behaviour according to the changes in the base radius. This enables the identification of a relevant interval where it is possible to compare the results of the motion of the droplet for all channel heights. From this graph, this interval corresponds to $0.25 < x < 0.50$ since the behaviour of the radius follows a similar smooth decay until this 0.25.

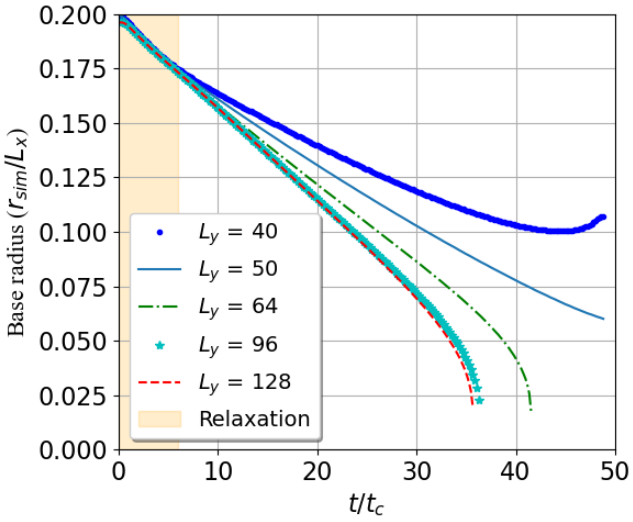

Figure 5.13: Evolution of base radius under different channel heights. As the height of the channel decreases, the evaporation of the droplet is mitigated and the rate of decrease in radius is slowed down.

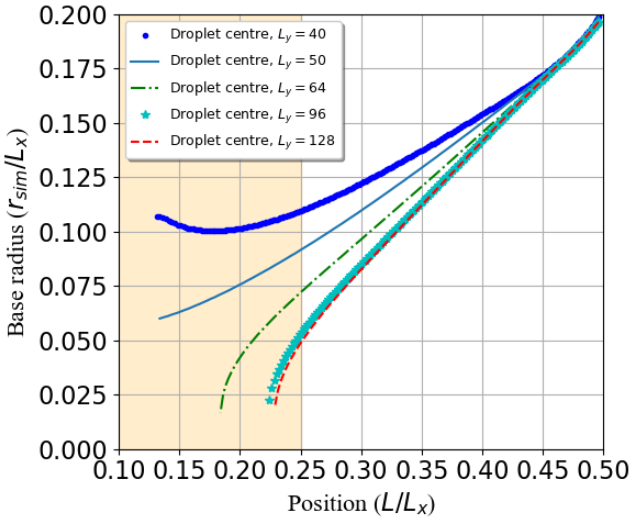

Figure 5.14: Base radius as a function of position The yellow shaded area is identified as the point the position where the influence of the edge of the domain starts to change the dynamics of the hygrotaxis

Figure 5.15 shows the position and droplet velocity as a function of time corresponding to the regime of interest identified in Figure 8.13. The position of the droplet and the velocities throughout the channel do not vary significantly throughout the different channel heights. This result is rather interesting since the change in rate of evaporation due to the height seems to bear no effect on the surface tension gradient generated on the interface of the droplet. This suggests that one can tune the height of the channel in order to extend the range of travel without the need to change the chemical potential gradient regime.

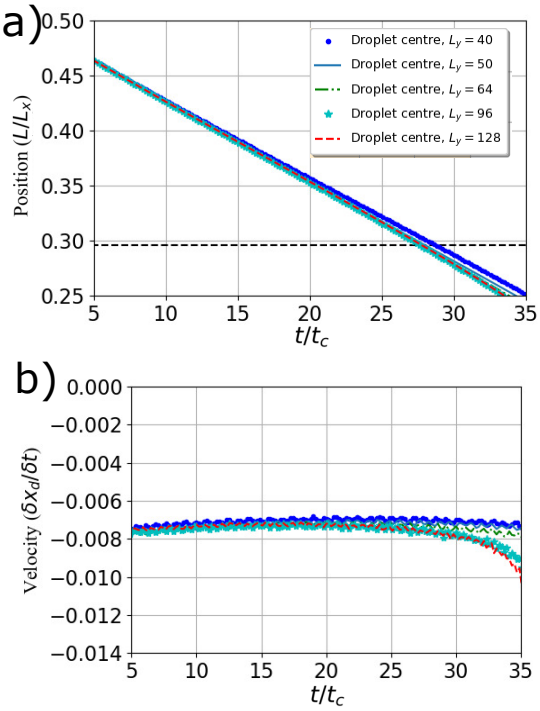

Figure 5.15: Evolution of position and velocity of the droplet in the relevant intervals. a) Position of the droplet and b) is the velocity of the droplet in the significant intervals defined. As before, $x_d = L/L_x$

To explain the change in rate of evaporation at different channel heights, Figure 5.16 shows the flux fields at $t/t_c = 20$ for heights of 128, 64 and 40 simulation units. As it can be appreciated in the behaviour of the flux inside the channel, when the height of the the channel becomes shorter, the flux streams are rectified so that they are oriented predominantly in the horizontal direction. This rectification displaces the position of the saddle point, or the inflexion point, of the flux near the interface of the droplet. As the channel height decreases, the saddle point is displaced towards the top of the droplet, reducing the flux at on largest surface are of the droplet, thus, slowing evaporation. This explains why the surface tension gradient is maintained to sustain a similar velocity for the transportation of the droplet.

5.7 Conclusion

In this chapter simulations of hygrotaxis in different chemical potential gradient scenarios have been presented. A validation of the evaporation dynamics for the Lattice Boltzmann was done which confirmed the simulations were suitable to model the dynamics of evaporation and condensation. Simulations under different chemical potential gradient regimes were presented and motion of the droplet was observed in all cases. A surface tension driven mechanism was identified to explain the motion generated by the presence of a chemical potential gradient.

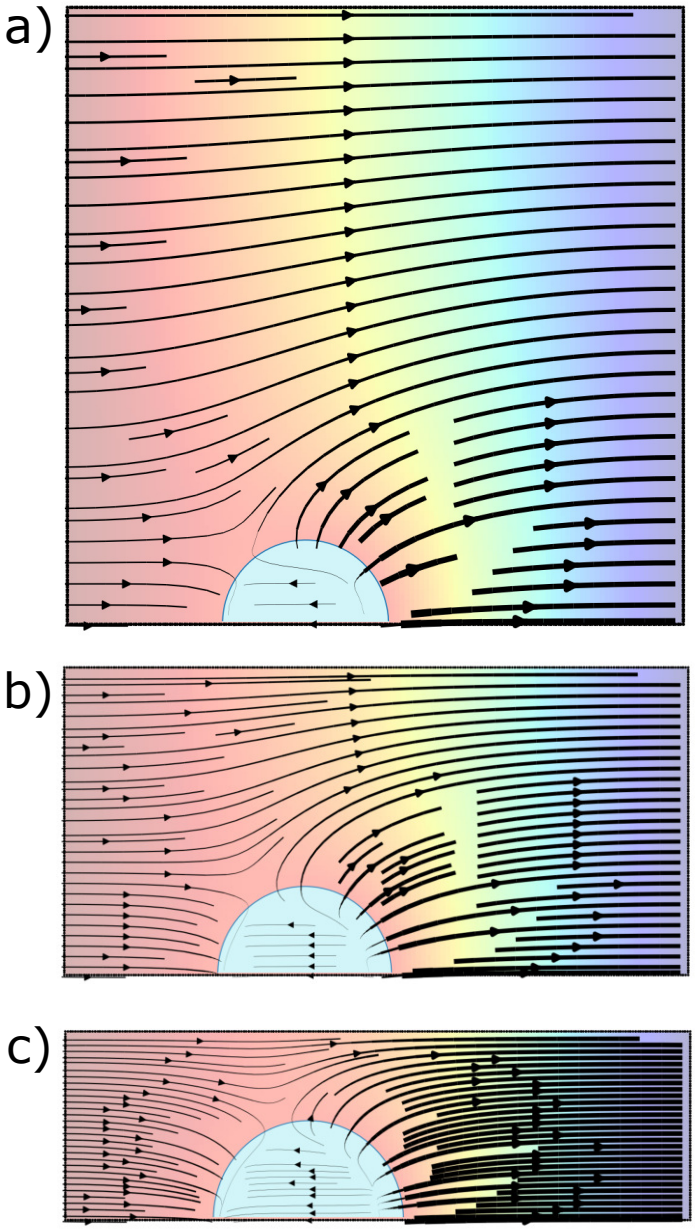

Figure 5.16: Flux stream plots for different heights a) Flux stream plot for channel height $L_y = 128$. b) Flux stream plot for channel height $L_y = 64$. c) Flux stream plot for channel height $L_y = 40$.

This was confirmed by looking into the behaviour of the velocity fluxes which showed strong interfacial flows on the surface of the droplet. The local surface tension was measured and showed that the chemical potential gradient induced a surface tension difference, explaining

the generation of surface flows on the interface of the droplet which drive convective flows in the droplet towards the more humid regions. A comparison between advective and diffusive transport rates showed that the motion of the droplet was an advective Marangoni effect, even for the cases where condensation and evaporation were present.

A study on the effects of viscosity for this phenomenon showed that the motion was driven by surface tension where viscosity does not play a large roll in this effect for differences in viscosities of a factor of 5. Lastly, the effect of the height of the channel revealed that there is no effect on the velocity of motion due to hygrotaxis, showing that the motion of the droplet is dependent of the chemical potential gradients. However, these results showed that confinement has a significant effect in the dynamics of evaporation due to a rectification of the flows around the droplet. This last result showed that hygrotaxis has the potential to be a flexible effect and could be tuned with confinement geometries to control the motion of droplets.

Chapter 6

Experimental approaches to hygrotaxis

Up to this point, simulations of droplets evaporating in different chemical potential gradients have been shown, where surface tension driven effect has been identified to enable droplets to flow towards more humid environments, i.e., hygrotaxis. Additionally, Chapter 4 showed that SOCAL surfaces are unique for they exhibit unusual behaviour in dynamic and static states. While the static friction of a SOCAL surface remains remarkably low, the dynamics of motion of the contact line are constrained by the kinetics of the contact line, yielding high dynamic friction and slow moving contact lines which impact the evaporative behaviour and the evolution of the contact angle and contact radius. This suggests this effect could lead to a surface energy driven motion of liquid droplets on ultra-smooth surfaces.

In this chapter, two experimental approaches to hygrotaxis are explored to demonstrate whether the occurrence of this effect can be determined experimentally. To test the effects of surface tension gradients, the first approach consists of making use of a large droplet acting as a humidity reservoir in a low humidity environment and then placing a significantly smaller droplet near the interface of the reservoir droplet, where both droplets are deposited on a SOCAL surface. Under these conditions, i.e., in the first approach, experimental results show a displacement of the centre of the droplet towards the humid side, which are similar to results obtained in simulations under near equilibrium conditions on one side of the droplet and evaporation of the other. The results of this section serve as a proof of concept of hygrotaxis but further experimental improvements need to be achieved.

The second approach consists in isolating two separate interfaces of a body of liquid by using a liquid slug inside a SOCAL coated capillary tube, a method developed and presented in Chapter 3. Each opening of the tube is exposed to different relative humidity conditions with the intent of creating a wettability gradient strong enough to induce motion of the liquid slug inside the SOCAL coated capillary tube. Preliminary results of evaporation of the liquid slugs

under this conditions show that the centre of the liquid slug apparently moves towards the dry side, a type of motion that would agree with a contact angle dependent wettability gradient. However, due to the inherent macroscopic roughness of the tubes, which seem to overcome the SOCAL coating, no concrete conclusion can be made.

Although the results of the hygrotaxis experiments in this chapter are not conclusive in terms of confirming the existence of this effect experimentally, they serve as base studies and motivation to continue exploring this effect in the future.

6.1 Droplet generated gradient

In order to obtain a humidity gradient around a droplet, it is necessary to place a droplet in the middle of two different relative humidity sources. In the literature, this is normally achieved by placing the droplet in close proximity to another droplet [15–18, 129, 134], treating the droplet as the source of saturated air while the ambient conditions are controlled separately to provide a contrast in relative humidity around the droplets. This method has shown great success in the motion of binary droplets in vapour gradients [7] and in the lifetime of pure droplet evaporation, producing the so called droplet shielding effect [135]. However, no report has been made of motion of pure water or pure liquid droplets under these conditions.

6.1.1 Experimental setup

Figure 6.1 show the experimental for the evaporation experiments. A SOCAL sample (refer to Chapter 3 for surface production) of surface dimensions 25 mm x 75 mm, is placed inside the humidity chamber (TC30) adapted to the Krüss DSA25, see Figure 4.1 for schematics of the apparatus. The temperature and relative humidity are left stabilize to $20 \pm 0.1\,^{\circ}\mathrm{C}$ and $10\% \pm 0.5\%$, respectively. Then, using a needle of OD of 0.235 mm, a 8 µL reservoir droplet is randomly placed on the SOCAL surface and a smaller droplet of 0.08 ± 0.03 µL is positioned next to the reservoir droplet. The needle is used to drag the reservoir droplet as close as possible to the small droplet (~ 0.1 mm in separation). It is important to note that the surface and the droplet temperature are constant which allows to assume that no thermal effects take place during the evaporation. Video footage is started at 1 fps for the duration of the evaporation and the image resolution used is no smaller than 188 pixels/mm. After the evaporation is completed, the needle is moved to another location and this process is done for 5 repetitions at different locations of the sample to avoid any systematic errors and ensure reproducibilty of the experiment.

The images extracted are analyzed using open source droplet analyser software PyDSA [31]. The apparent contact line is determined zooming into the contact points for of the droplets and using the reflection of the droplet on the surface. Similarly to the experimental method in Chapter 4, the droplet's contour is determined using a Canny edge approach [120]. Then,

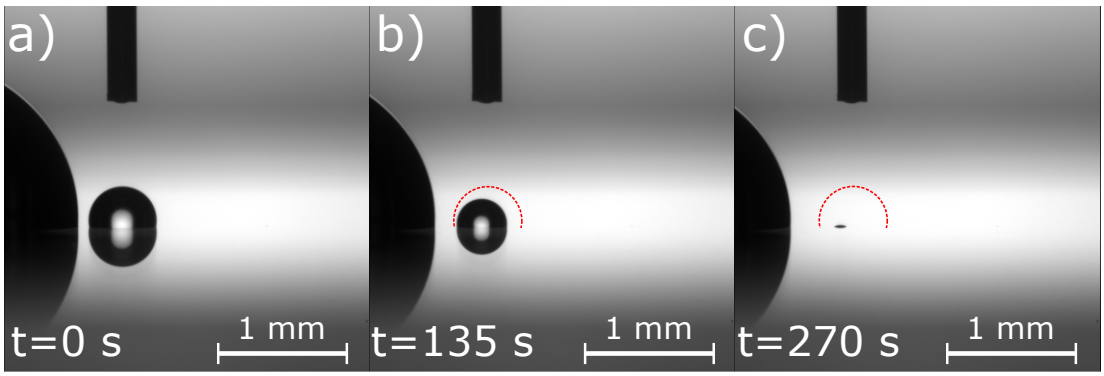

Figure 6.1: Experimental procedure for hygrotaxis evaporation. The temperature and relative humidity are lef to stabilize to $20 \pm 0.2\,^{\circ}$C and $10\% \pm 0.5\%$, respectively. a) $0.08 \pm 0.03\,\mu$L droplet (small droplet) placed beside a larger $8\,\mu$L droplet. b) Intermediate picture of the total evaporation time. c) Final position of the droplet before evaporating completely. For (b-c), the red dotted contour represents the initial size and position of the droplet.

a third degree polynomial is fitted to the contour of the droplet which covers the entirety of the droplet contour. The program then determines the point where the polynomial meets the baseline and returns droplet parameters such as the apparent contact angle, the base radius, the positions and velocity values for the contact points, and volume. As mentioned in Chapter 4, the systematic error associated with this measurement is $\delta\theta \sim 0.2^{\circ}$, which agrees with errors predicted by the literature [117, 121].

6.1.2 Typical evaporation sequence

According to the findings on the simulations of neutrally wetting droplets in chemical potential gradients (Chapter 5), it is expected that the relative humidity gradient created in this to be similar to an EE case, where the droplet is exposed to differential evaporation regime. In this configuration, one edge of the droplet to be close to saturation (left side of the small droplet), due to the proximity between the two droplets, while the other edge is evaporating at a rate corresponding to that associated with the relative humidity of the ambient phase (right side of the small droplet).

Figure 6.2 shows a typical result of the evaporation sequence under the conditions specified on the experimental setup. Panel a) shows a plot of the mean contact angle of the droplet and the decay of the contact area as the droplet evaporates, showing CCA evaporation [25]. The apparent contact angle slightly decays ($\sim 2^{\circ}$) throughout the evaporation, this decay is most likely due to the thermodynamic relaxation of the droplet on the surface, which can be in the order of 10^2 seconds as shown by Armstrong, *et al* [4]. Both the contact angle change in the relaxation phase and the relaxation time is comparable to the ones predicted in the literature [4, 136]. The behaviour of the contact area, πr^2, of the droplet further supports the

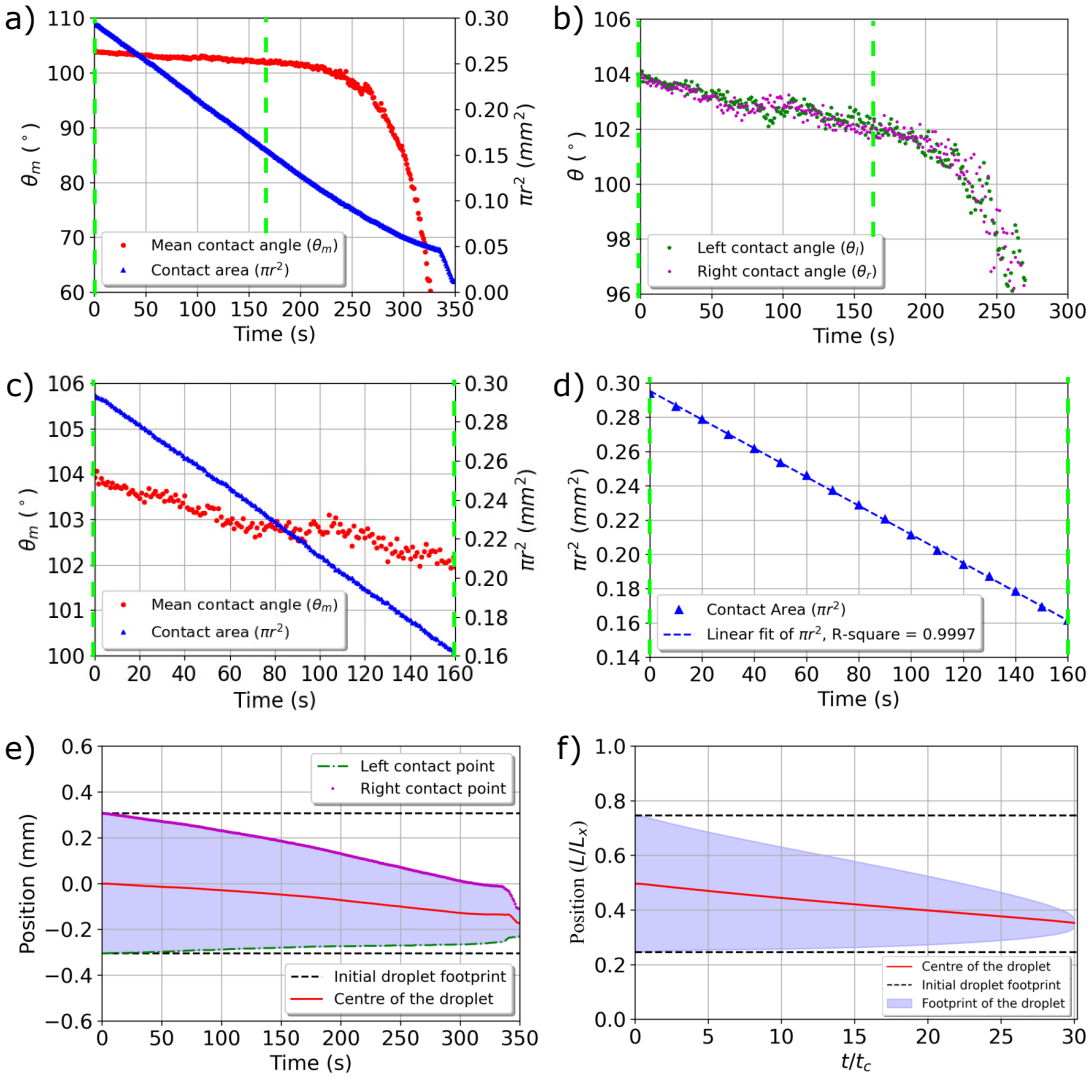

Figure 6.2: Typical evaporation result for droplet proximity evaporation experiments. a) Evolution of the mean contact angle (θ_m) and the contact area of the droplet. The green dashed lines encase the region of interest. b) Plot of the left and right contact angles. c) Mean contact angle and contact area in the region of interest. d) Linear fit to the change in contact area of the droplet. e) Evolution of the contact points and centre of the droplet. f) simulation of a droplet evaporating in chemical potential gradient of $\mu_l = -9.1\ \mu_{sim}/\mu_c$ and $\mu_r = -76.1\ \mu_{sim}/\mu_c$.

constant contact angle mode evaporation since it decays linearly, agreeing with the theoretical prediction presented in Equation 2.34. This can be seen clearly in panels (c-d), where the plots have been zoomed to the area of interest between 0 and 160 s. The contact area decays as a linear function as appreciated in panel d).

Figure 6.2(b) shows the apparent contact angle measurements on each side of the droplet. The constant behaviour of the contact angle on both sides of the droplet shows that there is no contact line pinning on either point throughout the evaporation.

Figure 6.2(e-f) shows the plot of the centre of the droplet along with the evolution of the left and right contact points according to the experiment (e) and the simulation (f). The black dashed lines represent the initial position of the contact points, or the initial footprint of the droplet, and the blue shaded regions represent the evolution of the footprint of the droplet. In the experimental result in panel e), one can appreciate that the centre of the droplet is displaced towards the near saturation side during the evaporation. Additionally, even though the contact area of the droplet decays linearly, as predicted in the theory for CCA mode evaporation, the contact points of the droplet recede at different rates. The left contact point, the edge exposed to the reservoir droplet, recedes at a slower speed ($\approx 1.7 \times 10^{-4}$ mm/s) than the right contact point exposed to the ambient relative humidity ($\approx 8.1 \times 10^{-4}$ mm/s), more than a four-fold difference.

Comparing this experiment with the simulations, similarities to the case in Figure 6.2(f) can be appreciated. This Evaporation-Evaporation case is set a chemical potential gradient of $\mu_l = -9.1\ \mu_{sim}/\mu_c$ and $\mu_r = -76.1\ \mu_{sim}/\mu_c$. In this scenario, the left edge of the droplet is exposed to a highly saturated environment, but still allowing evaporation, and the right side is exposed to a dryer environment. The overall behaviour of this scenario is similar to the experimental result.

6.1.3 Evolution of the droplet

Figure 6.3 shows the average results of the evaporation of five 0.08 ± 0.03 µL DI water droplets in the conditions specified in subsection 6.1.1. Figure 6.3(a) shows the evolution of the contact points of the droplet, along with the centre of the droplet. In this panel, it is evident that the centre of the droplet is displaced towards the region of higher relative humidity and that there is a difference in the rate of retraction for the contact points. The relatively constant error observed in the contact point is a systematic error stemming from inaccuracy of the dispensing of the droplet. This systematic error can be further appreciated at the end of the plot (t = 208 s) where the error increases significantly. This happens due to the different evaporation lifetime of the droplets since the total evaporation time interval goes from ~ 300 s to ~ 400 s. Figure 6.3(b) shows the the linear fits of the evolution of the contact points. The speed obtained from the fitting parameters for each fit can be appreciated in Table 6.1. The velocity of the right contact point exceeds both the velocity of the left contact point and the centre of the droplet by a factor of ~ 3. The velocity of the left contact point is similar to the one for the centre of the droplet, which is expected since both contact points are receding.

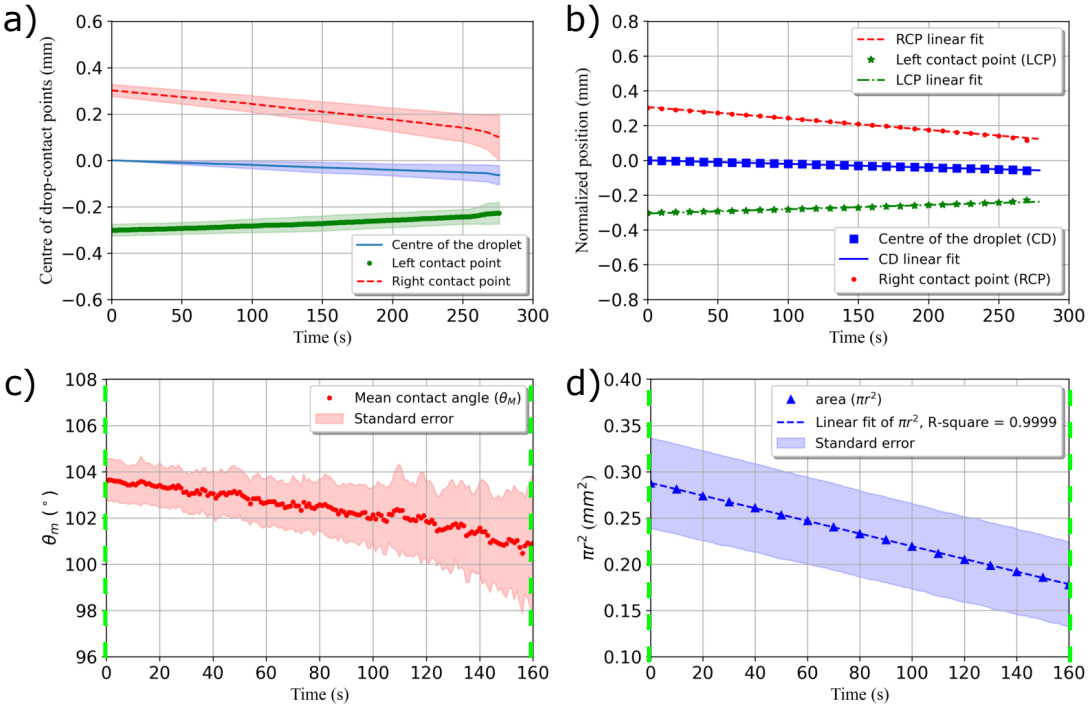

Figure 6.3: Averaged results of 5 evaporation runs. a) Evolution of the centre and contact points of the droplet. b) Linear fits of the data. c) Evolution of the contact angle in the interval of interest. d) Evolution of the contact area in the interval of interest. The shaded regions in the graphs represent the standard error.

Table 6.1: Velocity for the contact points and the centre of the droplet. In this case the sign of the velocity indicates motion towards the left (-) and right (+).

Position	velocity $\times 10^{-6}$ (mm/s)	s.d $\times 10^{-6}$ (mm/s)
Left contact point	242.3	1.8
Right contact point	-657.1	2.0
Centre of the droplet	-207.1	0.3

Panel c) of Figure 6.3 shows the evolution of the contact angle during the constant contact angle evaporation mode for the evaporation. During this period, the contact angle undergoes an slow and gradual change of 3°, which is still within the reported angle changes for the relaxation period for the evaporation [4], Panel d) shows the evolution of the contact area of the droplet and, as for the previous subsection and Figure 6.2(d), it is evident that the contact area is decaying linearly with time as expected from a CCA evaporation.

6.1.4 Experimental and simulation results comparison

To make an initial comparison to the simulations, Figure 6.4 shows the normalized experimental and simulation data. The positional coordinate, x, is normalized using the initial radius of the droplet, r_i, as the characteristic length, giving us,

$$x_{norm} = \frac{x}{r_i}, \tag{6.1}$$

where x_{norm} is the normalized position. The time, t, is normalized using the total evaporation time of the droplet, t_f, so,

$$t_{norm} = \frac{t}{t_f}, \tag{6.2}$$

where t_{norm} is the normalized time. Panel a) shows the average evolution of the centre and contact points of the droplet for 5 repetitions of the experiment. Panel b) shows the evolution of the same parameters for panel a) for a simulation with high humidity on the left side and low humidity on the right side. Table 6.2, shows the measured velocities under these normalization conditions.

The first point of discussion are the similarities between the experiment and the simulation. For both experimental and simulation results, the centre of the droplet shows a displacement towards the saturated environment caused by the reservoir droplet. In both experiments and simulation, there is a significant difference between the velocity of the left and right contact point. For the experiments, the difference between right contact point is ~ 3 times faster than the left contact point while for this simulation this relationship is defined by a factor of ~ 5. In terms of the velocity observed in the region of higher relative humidity (left side) of the droplet, the experiments and simulations differ by an order of magnitude in terms of velocity. This points out that the relative humidity on the left side of the droplet in the experiments is close to equilibrium, similar to the value set in the simulations. The difference observed in the velocities of the right side and centre of the droplet suggests that the relative humidity between the experiments and the simulations are significantly different. This suggests that the relative humidity on the right edge of the droplet is exposed to a higher humidity than the ones in the simulation. Furthermore, the ideal of the simulations conditions when compared to the non-ideal SOCAL substrate may also play a role on the lower velocities reported when comparing experiments and simulations.

Table 6.2: Velocity for the contact points and the centre of the droplet. In this case the sign of the velocity indicates motion towards the left (-) and right (+).

Position	v_{exp} (x_{norm}/t_{norm})	v_{sim} (x_{norm}/t_{norm})	Δv (%)
Left contact point	0.22	0.26	15
Right contact point	-0.60	-1.33	55
Centre of the droplet	-0.19	-0.54	65

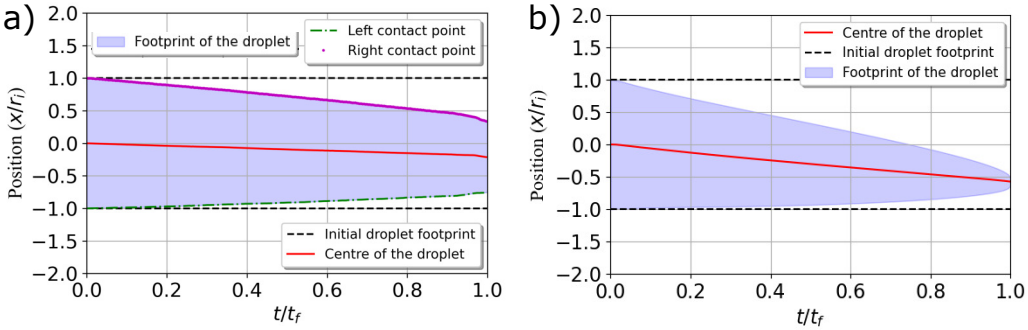

Figure 6.4: Normalized graphs for the evolution of the contact points and the centre of the droplet. The normalization is done according to the initial radius (r_i) for the position (x) and the time is normalized to the total time of evaporation (t_f). a) Averaged experimental data and b) simulation at $\mu_l = -9.1\ \mu_{sim}/\mu_c$ and $\mu_r = -76.1\ \mu_{sim}/\mu_c$

The differences between the experiments and the simulations are now discussed. The most important difference is the boundary conditions, on the experiments the relative humidity is bound to vary due to the decrease in volume from both droplets, hence the gradient is not expected to be constant. In simulations, the gradient is constant once the system relaxes. Another factor that may take part in affecting the dynamics of evaporation is the confinement conditions, which in narrow channels have been shown to affect the vapour density around the droplet [137, 138]. This suggests that the gradient of relative humidity around the droplet is not the same as the one in the simulations, however, the behaviour of the contact points are similar in terms of direction of motion and serves as a indication that hygrotaxis is possible.

6.1.5 Humidity gradients around the droplet

It is challenging to measure exact values for the gradient of relative humidity around the droplet. However, since the evaporation under these conditions follows the evaporation prediction given by the CCA theory, it seems sensible to use the diffusion limited theory of evaporation by Picknett & Bexon [25]. To give an indication of the effective relative humidity that the droplet is evaporating in, Equation 2.34 (in Chapter 2) is used to estimate this value according to the decay of the area of the droplet. The parameters used for this are Temperature = $20\,^{\circ}$C, diffusion of water vapor in air D_{lit} = 2.36×10^{-5} m^2 s^{-1}, density of water (ρ) = 997 kg m^{-3} and $\theta = 102.4^{\circ}$.

For a single droplet evaporating at a relative humidity of 10%, the contact area should decrease at a speed of -0.00188 mm^2 s^{-1}. However, the average decrease in contact area for the experiments is -0.00068 ± 0.00014 mm^2 s^{-1}, a value which is more than 3 times slower than the theory predicts. According to theoretical prediction, the droplet under the relative humidity gradient in these experiments is evaporating at rate that corresponds to that of a relative humidity of $67\% \pm 7\%$, near to the mean average between saturated $RH = 100\%$ and

ambient phase $RH = 10\%$. This shows that the presence of the larger droplet clearly affects the dynamics of evaporation of the smaller droplet, similar to the droplet shielding effect [135]. The error in the effective relative humidity suggests that the relative humidity gradient around the droplet is changing as it evaporates. This points to the idea that even small differences in the distance separating the droplets can have a significant impact the generation of the relative humidity gradient, even in the micrometric scale. In order to improve these experiments in the future, a system designed to improve the control of the relative humidity gradient in the system would allow this work to make more conclusive statements about the dynamics of evaporation in this type of system.

6.1.6 Consistency and reproducibility

In terms of the SOCAL surface, the literature [4, 62] and the results presented in Chapters 3 and 4 allow us to ensure that the consistency and the quality of the surfaces produced under those parameters remain reproducible, with an average contact angle hysteresis of $1.5^\circ \pm 0.9^\circ$. In terms of the experiment presented in this section, the biggest concern is that an effect caused by a surface imperfection may be responsible for the effect observed during the evaporation. However, the results of the experiments show otherwise. To avoid any systematic error stemming from a particular surface imperfection, the experiments were repeated always ensuring that the evaporation took place at a different location of the sample. This guarantees that the behaviour at the contact line remains unaffected by any possible pinning events that may occur during a single experimental run. Another aspect that shows that the experiment is not being affected by any pinning is the constant contact angle behaviour observed during the evaporation of the small droplet. As mentioned in Chapter 2, constant contact angle mode of evaporation consists of the linear decrease of the contact area accompanied by a constant contact angle during the evaporation of a liquid droplet on a surface. In panels (b) and (d) of Figure 6.2, this can be appreciated in the experiments. Panel (b), on one hand, shows that the contact angle is quasi-constant, with around a 2° change in the contact angle most likely due to the thermodynamic relaxation as shown by Armstrong *et al.*[4] On the other hand, in panel (d), the behaviour of the decrease of the contact area decays linearly, which fulfills the criteria of an evaporation cycle occurring on a ultra-smooth surface. Additionally, on Figure 6.4(a), the evolution of the average footprint of the droplet remains smooth for both contact points. This ensures that pinning is not responsible for the effects observed during the experiment and guarantees that this effect is reproducible under the experimental conditions presented.

6.1.7 Concluding remarks

In this section, evaporation experiments were done of a small ($0.08 \pm 0.03\,\mu L$) pure water droplet next to a bigger reservoir pure water droplet ($8\,\mu L$). The results show a clear displacement of the centre of the droplet and a significant difference in receding velocity between the contact points of a factor of ~ 3. Comparisons against a simulation with similar evaporation conditions, where the humid side of the droplet is set to a quasi-equilibrium value, shows similarities in the behaviour of the contact points and the centre of the droplet. However, difference in the boundary conditions and the confinement of the system require further improvement of experiments to allow a better comparison.

By measuring the decrease of contact area of the droplet under these conditions, it is estimated that the droplet was evaporating at a rate equivalent to a relative humidity much larger that the ambient one, clearly showing the effect of the vapour field of the reservoir droplet on the smaller one. The results show that the error of the change in contact area and the relative humidity values that the gradient is not constant throughout the evaporations. This alludes to the importance of the distance between the droplets in generating the humidity gradient around the small droplet.

Although additional studies need to be made in order to understand this effect to a greater degree, the results presented in this section serve as a proof of concept of hygrotaxis and serve to motivate further study of this effect.

6.2 Capillary tube configuration

Capillary tubes, usually of the order of 1 mm in ID, offer an ideal option of isolating two liquid fronts while allowing one to work in scales below the capillary length. In this length scale, effects from gravity on the shape of the meniscus can be neglected. The findings in Chapter 4 showed that the dynamic friction plays an important part in the value of the contact angle of evaporating droplets. Additionally, a study of evaporation done by Armstrong, *et al.* [4] showed that there is a step-like change in the values for evaporating contact angles for low and high relative humidity environments, alluding to a surface energy change due to the adsorption of water molecules onto the solid surface. For SOCAL surfaces, a difference of $\sim 4^\circ$ can be observed between high and low relative humidity conditions in the results for Chapter 4 and in the work done in Armstrong, *et al* [4]. As discussed in Chapter 2, differences in contact angle allude to existence of wettability gradient that are able to drive the motion of a droplet due to the difference in curvature, which induces a gradient of the Laplace pressure inside the droplets. Initial experiments on droplets showed that the gradient made in the presence of

another droplet was not enough to drive the motion of the droplet to any particular direction. A tube geometry allows the ability to expose each interface to a constant value for relative humidity, enabling any effects due to contact angle differences to play an important part in the evolution of the liquid column inside the capillary tube.

In this section, contact angle hysteresis measurements are performed of the SOCAL coated and uncoated glass capillary tubes. The results show that the SOCAL coating method developed in this thesis is successful in coating the inner surface of the glass capillary tubes with SOCAL. Subsequently, evaporation experiments are done inside capillary tubes, exposing each side to different values of relative humidity. Initial results point to the possibility of a wettabilty gradient induced motion due to changes in surface energy on the SOCAL surfaces exposed to different relative humidity conditions. However, excessive pinning, believed to come from the inherent macroscopic defects of the capillary tubes, makes the successful run experiments challenging. This limits the ability to draw concrete conclusions on the mechanism present but shed light on a possible alternative mechanism of a relative humidity driven motion.

6.2.1 Contact angle hysteresis in capillary tubes

One of the benefits of using glass capillary tubes is that they are completely transparent. Although direct apparent contact angle measurements inside tube geometries can be challenging due to the curvature of the surface, the meniscus of the liquid column is clearly visible in capillary tubes. Hence, it is possible to use the capillary action surface characterisation method developed and described in Chapter 3. This method uses Jurin's law to approximate the apparent contact angle of liquid columns in capillary tubes (Equation 3.5). This subsection intends to prove that SOCAL surfaces are achievable in thin tube geometries.

For this experiments, SOCAL coated capillary tubes are produced following the procedure outlined in Section 3.1.4. The experimental design consists of a motorized linear stage which allows the controlled descent and ascent of a capillary tube into a DI water reservoir, shown in Section 3.2.4.

The experiment is performed as follows. Capillary tube samples are submerged into a water reservoir at a depth of $\sim 5\,\mathrm{mm}$, ensuring that the liquid column in the tube is not pinned on the bottom edge of the tube. Then, the tube is submerged further at a speed of $1\,\mathrm{mm/s}$ until the contact line begins to move. The motor is then stopped and the liquid column is left to relax for a period of $120\,\mathrm{s}$, where θ_A is measured at the end of this period. After this prescribed time, the capillary tube is lifted at a speed of $1\,\mathrm{mm/s}$ and is stopped when the contact line begins to move. Then, the liquid column is allowed to relax for an additional $120\,\mathrm{s}$, and θ_R is measured at the end of this period. This procedure is repeated 4 times for both SOCAL coated and pure glass capillary tubes.

Table 6.3 shows results of $\Delta\theta$ measurements done with a SOCAL coated capillary tube and an uncoated glass capillary tube. On one hand, for SOCAL, the average of the advancing contact angle is $99.5 \pm 0.6^\circ$ and the average receding contact angle is $96.7 \pm 1.4^\circ$. These advancing and receding contact angle values are within the reported values for SOCAL in Wang and McCarthy's [62] development of the SOCAL procedure. The contact angle hysteresis value of $2.9 \pm 1.9^\circ$ is comparable to reported values for contact angle hysteresis in the literature for SOCAL surfaces [62, 111] and the ones reported in Chapter 4.

Although the values of the contact angle fall within the reported values for SOCAL, previous works [4, 62] have shown that the SOCAL process can be optimized to reach contact angle hysteresis values of $< 2^\circ$. According to these studies, the SOCAL production parameters used in our procedure are the ones associated to contact angle hysteresis values of $2.0 \pm 1^\circ$, with advancing and receding contact values of $\sim 108^\circ$ and $\sim 106^\circ$, respectively. In terms of the contact angle hysteresis observed, the measurement in this experiment falls within error. However, there is a significant difference in the values for the advancing and receding contact angle of $> 6^\circ$. This suggests that the optimization parameters for flat substrates are not the same for different geometries such as capillary tubes. This is to be expected since the aspect ratio of the tube affects the diffusion of plasma inside the capillary tube, as discussed in the length dependency of plasma activation (Section 3.1.4). This is likely to also affect the relative humidity inside the tube, an important parameter that regulates the growth of the nanometric polymer chains. Hence, the parameters regulating the growth of SOCAL on the inner surface of tube can be improved and there is room to make a systematic study to lower contact angle hysteresis in tube geometries.

On the other hand, the glass results show that the uncoated surface of the capillary tubes does exhibit significant amount of pinning, with a $\Delta\theta(H) = 27.2^\circ \pm 5.3^\circ$ for the glass inside the tube. For contrast, literature values for contact angle hysteresis on glass microscope slides present $\Delta\theta \approx 12.7^\circ$ [139]. This suggest that the inner surface roughness of the capillary tubes is more than double of that of flat glass. This is to be expected since polishing can be used to smooth the surfaces of glass slides and, on capillary tubes, this becomes a challenging task for capillary tubes due to small ID.

The contact angle hysteresis measurements on the SOCAL coated capillary tubes, in conjunction with the large change in surface charactersitic values (θ_A, θ_R and $\Delta\theta$) between coated and uncoated samples, confirms that a SOCAL coating method has been successfully implemented for tube geometries.

Table 6.3: Contact angle measurements using Jurin's height on SOCAL and glass capillary tubes. Table showing experimental results using Jurin's law to obtain θ_A, θ_R and $\Delta\theta$ inside SOCAL coated and glass capillary tubes. The measurement error for SOCAL is $\pm 0.04^\circ$ and for glass it is $\pm 1.4^\circ$.

	SOCAL			Glass		
Trial	$\theta_A(H)(^\circ)$	$\theta_R(H)(^\circ)$	$\Delta\theta(H)(^\circ)$	$\theta_A(H)(^\circ)$	$\theta_R(H)(^\circ)$	$\Delta\theta(H)(^\circ)$
1	99.7	96.4	3.3	54.9	21.4	33.5
2	100.2	95.8	4.4	52.7	23.5	29.2
3	99.5	95.7	3.7	45.9	20.9	25.0
4	98.8	98.7	0.1	44.5	23.3	21.1
mean(°)	99.5	96.7	2.9	49.5	22.3	27.2
s.d	0.6	1.4	1.9	1.3	5.1	5.3

6.2.2 Evaporation experiments inside SOCAL capillary tubes

Experimental setup

An experiment designed to expose each side of the capillary tube sample to a different value of relative humidity can be seen in Figure 6.5. The left side of the SOCAL capillary tube is exposed to a dry reservoir filled with silica beads. Silica beads remove moisture from the air, lowering the relative humidity inside the dry reservoir. Hourly measurements in ambient room conditions showed that the relative humidity inside the dry reservoir can be kept at $2\% \pm 1\%$ relative humidity for 5 hours at room conditions and daily measurements (3 days) showed that the relative humidity was kept under $5\% \pm 2\%$, ensuring that low relative humidity values are sustained throughout the experiments. Additionally, each time experiments were run, fresh or dry baked silica beads ($200\,^\circ$C for 40 minutes) were used to ensure relative humidity was kept as low as possible in the dry reservoir. The right side of the capillary tube is open to the ambient relative humidity controlled by the humidity chamber attached to the Krüss DSA 25. The nozzle (Figure 6.5(d)) is connected to a water reservoir which drives saturated air into the chamber, allowing the relative humidity inside the chamber to stabilize at values up to $94\% \pm 1\%$.

The SOCAL capillary tube sample (Length = 20 mm, OD = 1.6 mm and ID = 1.2 mm) is first rinsed with DI water and blown dry to ensure that there are no particles stuck on the inner surface. A liquid column of $2\,\mu$L is placed using a Celix micropump in the middle of the sample (Figure 6.5(d)) using a syringe connected to a thin needle (OD = 0.26 mm), being specially careful to avoid scraping the inner surface of the tube. The sample is then carefully connected to the dry reservoir and horizontally levelled using a sample holder aligned with the dry relative humidity source opening. The device is then placed inside the humidity chamber and sealed. The relative humidity is set to 90% and the video recording is not started until the relative humidity in the chamber stabilizes (~ 10 min). Video footage is recorded at 1 frame every 10 seconds at a resolution of 105 pixels/mm.

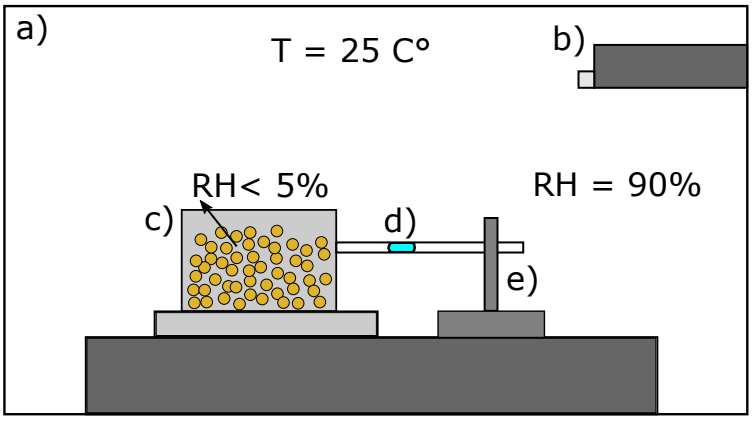

Figure 6.5: Hygrotaxis experiment inside a capillary tube. Schematic of experiment to expose each side of a capillary tube to different relative humidity values. a) Humidity chamber (TC30) adapted to the Krüss DSA 25. b) Nozzle providing saturated air driving ambient relative humidity to $90\% \pm 1\%$. c) Dry reservoir containing silica beads to ensure a low relative humidity ($< 5\%$) on one end of the capillary tube. d) SOCAL coated capillary tube where a liquid column is placed in the middle. e) Sample holder to ensure that capillary tube is horizontally level and aligned with dry reservoir.

Macroscopic pinning

In this geometry, the body of liquid is not exposed to a gradient in humidity but to a absolute difference at both interfaces. Although there are a significant differences in relative humidity conditions between both reservoirs, these ambient conditions are still within the evaporative regime in both interfaces. As a precaution to the reader, pinning was encountered during most of the evaporation experiments of the liquid column. This pinning had negative impact on the motion of the contact line, making it challenging to discern effects from the relative humidity conditions imposed and the motion of the contact lines. It is believed that this problem stems from the inherent macroscropic roughness in the inner part of the capillary tube due to production methods, since no polishing or smoothing procedure is done after drilling or heat drawing of the capillary tubes [140]. There is room to improve this experiment in the future via acid or alkaline treatments to smooth the inner surface of the capillary tubes [141, 142] before coating with SOCAL. Another possible issue is the difficulty in cleaning the coated inner surface of the capillary tube, which depends greatly on flows to remove contaminants. This means that if any particle, such as salt depositions, gets adhered to the surface beyond the washing capabilities of the solvent flow, the surface will retain the pinning point. However, in the following sections, results of those experimental runs where there was no visible pinning of the contact lines are presented.

Initial results

Figure 6.6 shows average results of 3 evaporation experiments of $2\,\mu$L liquid columns over 50 minutes. Panel a) shows that over the course of the evaporation of the liquid column, the center of mass of the liquid is displaced from the centre towards the low relative humidity region. Additionally, the receding of the contact lines is not symmetric and the contact line exposed to the high relative humidity environment moves while the other is quasi-static (qualitatively, the contact line moves a fraction of a millimeter to the low relative humidity side).

Previous evaporation studies on SOCAL [4] and results from Chapter 4 have shown that the contact line recedes faster as the relative humidity decreases, suggesting that under the experimental parameters, the contact line exposed to the low relative humidity conditions should recede faster than the one with high relative humidity. However, this is not the case for the experiments, as panel b) of Figure 6.6 shows the evolution of the centre of the liquid column with the left and right interfaces. The origin is considered to be the centre of the droplet and positive values are positions in the direction of the high relative humidity side while negative values represent positions towards the low relative humidity side. In this panel, it is clear that that the right contact line is moving at a greater rate than the left contact line. This difference is captured in the overall motion of the centre of mass of the liquid column towards one side of the channel. The apparent large error values ($\sim 0.2\,$mm) of the evolution of the left and right interfaces are due to the differences is the initial volume of the droplet. However, looking at the normalized positions of the contact lines to $\Delta x = x - x_i$, where x is the position and x_i is the initial position of the contact line. Panels c) and e) of Figure 6.6 show that in terms of the motion of the contact lines, the maximum value of the error is ~ 0.05 mm, or 15% of the overall motion. Additionally, the average value of the position of the left contact line is $-2.1 \times 10^{-3} \pm 3.4 \times 10^{-3}$ mm, suggesting that the left contact line does not recede but moves towards the low humidity region. The remarkably large error of this measurement indicates that no conclusion on the motion of this contact line can be made from these results. However, what is clear is that the left contact line remains in a quasi-static state during the evaporation of the liquid column.

Figure 6.7 shows linear fits of the data to obtain information on the overall motion of the droplet. The velocities associated with the fitting parameters are $-4.9 \times 10^{-5} \pm 1.8 \times 10^{-7}$ mm/s for the centre of the droplet, $-9.8 \times 10^{-5} \pm 1.4 \times 10^{-7}$ mm/s for the right contact point, and $-1.7 \times 10^{-7} \pm 2.3 \times 10^{-7}$ mm/s for the left contact point. For both the centre of the liquid droplet and the right interface, there is a constant velocity in the direction of the low relative humidity region, with the right interface moving ~ 2 times faster than the centre of the liquid column. For the left interface, the velocity measured is two orders of magnitude smaller than the other two. Additionally, the error of the measurement is bigger than the value of the velocity, indicating that motion of the left interface is not conclusive.

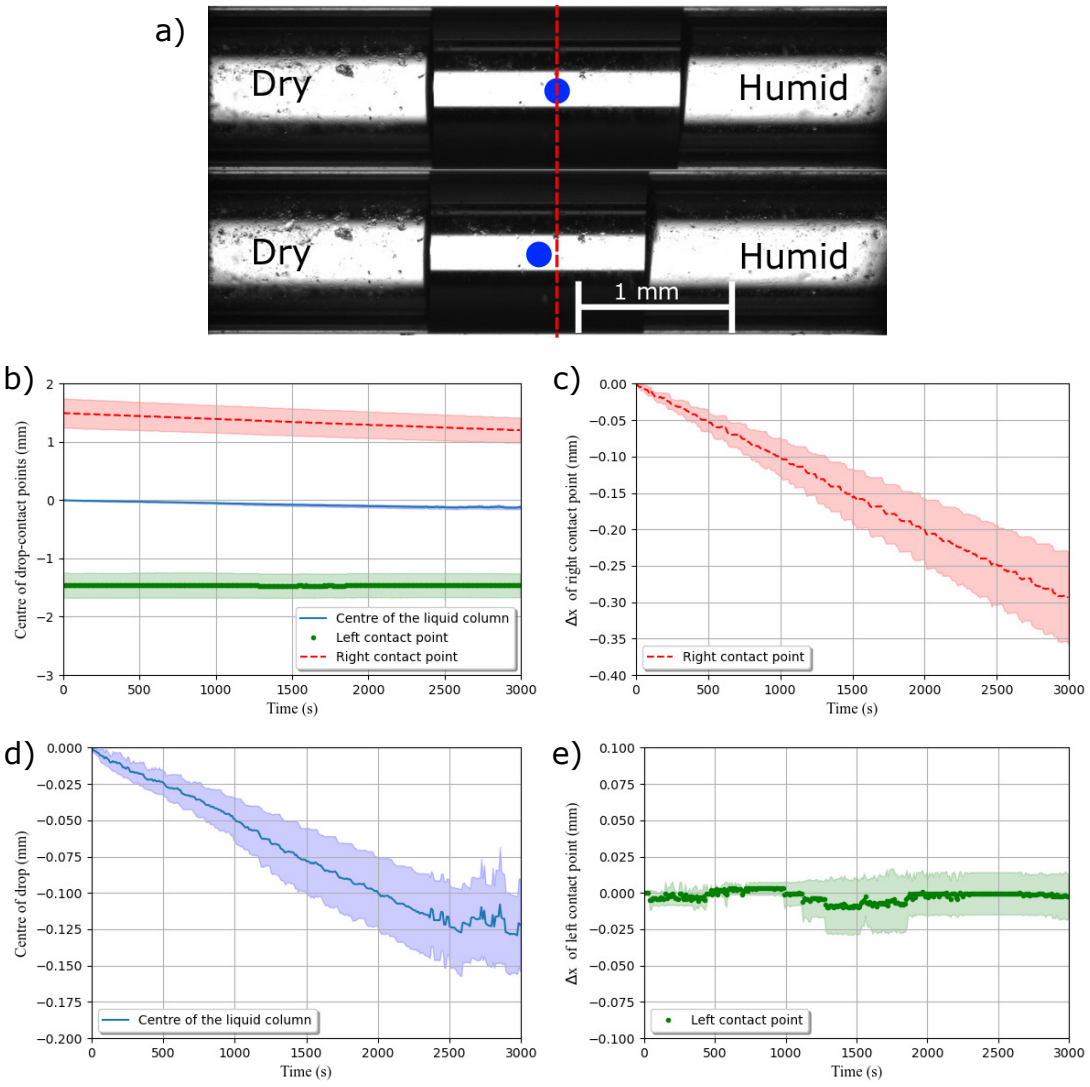

Figure 6.6: SOCAL capillary tube evaporation experiments. a) Snapshots of the initial state (top image) and the state of the droplet after 50 minutes (bottom image). The dotted red line indicates the initial position of the centre of the liquid column and the blue dot is the centre of the droplet. b) Graph showing the evolution of the contact lines of each interface and the position of the centre of the droplet. c-e) are the graphs of each interface and the centre of the droplet separately. The shaded regions represent the error of the measurement.

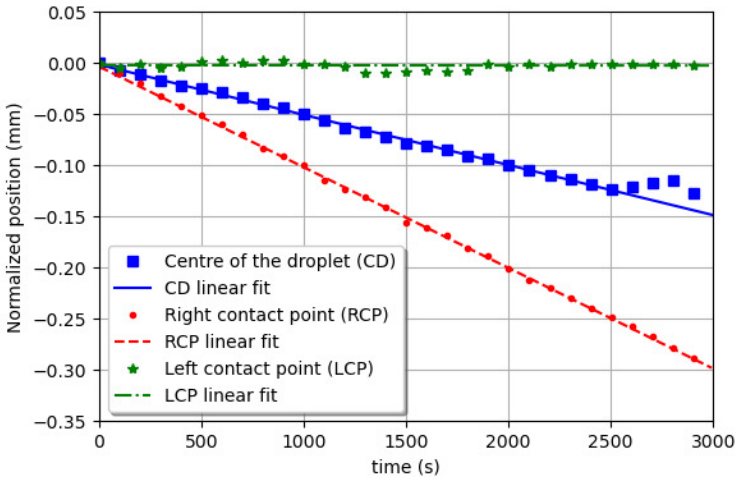

Figure 6.7: Linear fits for evaporation evolution. Figure showing the linear fits for the data for the centre of the droplet, the right contact point and the left contact point. The velocities associated with the fitting parameters are $-4.9 \times 10^{-5} \pm 1.8 \times 10^{-7}$ mm/s for the centre of the droplet, $-9.8 \times 10^{-5} \pm 1.4 \times 10^{-7}$ mm/s for the right contact point, and $-1.7 \times 10^{-7} \pm 2.3 \times 10^{-7}$ mm/s for the left contact point.

These results suggest that there might be a mechanism driving the motion of liquid column towards low humidity regions which competes against viscous and dynamic drag forces. The origin of this driving force could be explained by considering the relative humidity dependency for the contact angle found in Chapter 4 and in Ref. [4]. In addition, adsorption and desorption of water molecules in the ambient phase change the surface energy of the solid-gas interface. Higher relative humidity lowers the surface energy, resulting in higher static contact angles. Analogously, low relative humidity increases the surface energy of the solid, yielding lower values of static contact angle. The hygrostactic pressure, Δp, at the column boundaries is governed by the curvature, C, of the interfaces following the Laplace pressure equation,

$$\Delta p = \gamma C \tag{6.3}$$

where γ is the surface tension of the liquid-gas interface. The curvature of the droplet is dependent on the contact angle at the triple line. Hence, the curvature on the left interface, C_L, is smaller than the curvature on the right interface, C_R, which means that the right interface will experience an overpressure in comparison to the left side. To compensate for this pressure difference, the bulk of the liquid moves towards the left interface resulting in the motion of the right contact line and the quasi-static behaviour of the left contact line. However, in order to make this assertion, clear images of the liquid interface of the water column must be available.

6.2.3 Concluding remarks

In this section, I presented a method to coat the inside of thin capillary tubes (ID ≈ 1mm) with SOCAL, achieving contact angle hysteresis values comparable to those in the literature for flat substrates ($< 3^{\circ}$). I developed a method to measure contact angle hysteresis using the capillary action. I presented evaporation experiments of liquid columns inside the capillary tubes where each interface was exposed to a different values of relative humidity. Initial results appear show motion of the centre of the droplet in favour of the dry side, pointing to possible pressure driven flow generated by differences in contact angle along the 2 exposed liquid interfaces. However, significant challenges such as excessive pinning and lack of motion of one of the contact lines do not allow for consistency and reproducibility. This hinders the ability to draw any solid conclusions from the experimental results since it is not possible to discern if the contact line is pinned or moving. To overcome these challenges, one would require a smoothing treatment of the inner surface of the capillary tubes along with better images of the meniscus of the droplet.

6.3 Conclusion

In this chapter, the aim was to explore two different experimental approaches to hygrotaxis by developing experimental designs that allowed a liquid droplet or a liquid column inside a capillary tube to be exposed to differing values of relative humidity conditions. The first approach, consisting in placing a small droplet close to a bigger one (the latter acting as a humidity reservoir) in a dry humidity environment, showed that the evaporation dynamics are affected. The difference in the receding speeds of the contact lines displace the centre of mass of the droplet in favour of the region with higher relative humidity. When compared to the simulated work presented in Chapter 5, where one side is set to a quasi-equilibrium chemical potential and the other to a evaporating chemical potential, the results show similarities in the behaviour of the evolution of the contact points and the centre of the droplet. The influence of the bigger droplet is clear when measuring the rate of evaporation of the smaller droplet, which corresponds to a relative humidity of 67% rather than the 10% measured in the humidity chamber.

The second approach consists of placing a liquid column inside a capillary tube which required the development of a method to successfully coat the inside of capillary tubes with SOCAL. After running evaporation experiments of 2μL water columns inside the SOCAL coated capillary tubes, asymmetric evaporation towards the dry region was observed. The preferential evaporation observed does not agree with expected behaviour of the contact line under the given relative humidity parameters, suggesting that there could be an existing driving force affecting the motion of the contact line on the low relative humidity region. This

effect may stem from the difference in curvature between the 2 interfaces caused by the relative humidity dependence. However, frequent encounter of pinning points throughout the evaporations needs to be further improved as well as the experimental procedure so to be able to claim that such effect is taking place.

Chapter 7

Summary and Future Work

This thesis has explored the interactions between water droplets, relative humidity and a novel type of ultra-smooth surface called SOCAL. This was done in order to explore a novel effect, named “hygrotaxis", based on the self-propulsion generated by relative humidity gradients on pure water droplets. Hence, the unique relationship between water droplets, SOCAL and relative humidity gradients has been studied from both an experimental perspective and through the use of Lattice Boltzmann simulations.

Chapter 2 provides a review on the relevant theoretical framework and literature review needed to explore hygrotaxis and droplet physics. Then, in Chapter 3, the SOCAL surface production methodology is provided for flat glass substrates and glass capillary tubes, which includes the cleaning procedure, the plasma exposure parameters, the coating method and the drying conditions. To ensure that the drying conditions were controlled, a bespoke humidity control system was developed using microcontrollers to regulate the water saturation of air in a humidity chamber. The steps summarized above ensure that a homogeneous acid-catalyzed polycondensation of nanometric polymer chains is created on glass substrates, producing a pinning-free, low contact angle hysteresis surface. This chapter then provides a description of the wetting based surface characterization methods utilized in this thesis. The first two methodologies described are well-known in literature and are named the volumetric variation method, which uses in-flow and out-flow of liquid to move the contact line of a droplet, and the sliding angle method, which characterises the surface based on the critical sliding angle of a droplet. The following two methods provided are novel ways to characterise contact angle hysteresis in SOCAL surfaces on flat and capillary tube configurations. The flat characterization method is named “contact line relaxation" method, based on the relaxation of the contact angle after the contact line is perturbed, and the capillary tube is named “capillary action" method, which uses capillary invasion in tubes to approximate contact angles. The last section of this chapter provides an overview of the imaging processing techniques to obtain characterisation parameters from the image data.

The first results chapter, Chapter 4, studied the statics and dynamics of liquid droplets on flat SOCAL surfaces. Baseline evaporation experiments show that the surfaces created in this study exhibit CCA evaporation associated with ultra-smooth surface and exhibit results comparable to those in the literature. An analysis into the statics and dynamics of droplets on solid surfaces is then provided, based on the contact line relaxation method. On one hand, the results of the static analysis predict that the pinning force scales according to a factor normal to the surface tension and the static contact angle on the surface. On the other hand, for the analysis of the dynamics of relaxation to equilibrium, the hydrodynamic theory and the Molecular Kinetic Theory are used to obtain expressions for the relaxation times according to the physics described in each theory. Then, the characterization of contact angle hysteresis on SOCAL surfaces was studied in detail. Initial results on the behaviour of the base radius showed that the transition from static to dynamic states of liquid contact lines went through a smooth transition. This smooth transition made the utilization of classic methods of surface characterization difficult since the determination of the onset of contact line motion becomes challenging to determine This slow transition increases the error of contact angle hysteresis measurement due to the qualitative nature of this method, resulting in errors comparable to the measurements themselves. To overcome this, a new method named “contact line relaxation" was developed to quantitatively measure contact angle hysteresis using the exponential relaxation to equilibrium of a liquid contact line after motion is induced. This method approaches the value of the advancing and receding contact angles through the asymptotic limit of the relaxation, allowing for the approach of these values at the sought infinitely slow flow speeds. The results of this method show a significant decrease in the standard deviation error in the determination of the advancing and receding contact angles, resulting in a more accurate measurement of contact angle hysteresis on SOCAL surfaces. Subsequently, studies at different flow rates and at different relative humidities showed that this method can reliably measure contact angle hysteresis on high relative humidities, independent of the flow rate used. Additionally, the results at different relative humidities showed that the evaporation contact angle on SOCAL surfaces decreases $\sim 4^{\circ}$, alluding to the possibility of designing a wetting gradient to induce self propulsion. Then, experimental relaxation times were obtained from the fitting parameters and compared to the ones predicted by theory. The results show a remarkable agreement with the MKT, indicating that the droplet dynamics is dependent on kinetic variables determined by the surface, such as the frequency of jumps and the distance between them.

Chapter 5 showed that hygrotaxis is possible under the influence of chemical potential gradients. This was done by implementing simulations based on the Lattice Boltzmann method. Firstly, a baseline study of the evaporation of a droplet resting on a solid in free space showed that the simulations are successful in modelling the evaporation according to the Cahn-Hilliard equation. Then, Lattice Boltzmann simulations which model the phase change of liquid droplets subjected to chemical potential gradients in confined systems were performed.

In order to generate chemical potential gradients, each boundary of the channel was set to a different equilibrium chemical potential. To avoid advective flows stemming from the density changes in the channel, an additional chemical potential gradient was introduced to ensure that the overall pressure was zero, allowing for the generation of a stable chemical potential gradient in the domain. Different chemical potential gradient configurations were explored, focusing on evaporation gradients, evaporation-condensation gradients and condensation gradients. The results show that there is a prevalent motion of the centre of the mass of the droplet towards higher values of the chemical potential in all the gradients explored. Most significantly, motion of the contact lines in the same direction was observed in the cases were evaporation and condensation are present, and in the case where there is equilibrium on one side and evaporation on the other. To understand the mechanism taking place, plots of the velocity flows of the droplet showed the strong presence of droplet surface flows which drive the motion of the droplet. Analysis into the surface tension profile of the droplet showed the existence of a difference in surface tension which proved to be the reason why strong surface flows are generated on the droplet. An advection against diffusion analysis was conducted to confirm that the motion of the droplets observed was not a product of kinematic effects by calculating the values of the Péclet number and Marangoni number in the system. This studies determined that the motion was indeed generated by the surface tension flows which induce the advection of the droplet. This showed that the mechanism driving the motion of hygrotaxis in these types of gradients is caused by a chemical potential generated Marangoni flow.

Subsequently, additional computational studies on the effect of varying viscosity of the phases and the channel height were performed. The viscosity contrast between the phases showed no significant effects in the dynamics of motion in the range explored. Although the dynamics of motion was not affected significantly in terms of the motion generated for the different channel heights, there was a large effect in the rate of evaporation of the droplet. Flux plots showed that as the height of the channel decreases, the mass flux flows in the system are rectified, effectively slowing the evaporation of the droplet. This shows that hygrotaxis can be amplified by confinement in narrow channels.

The final results chapter, Chapter 6, explored hygrotaxis in an experimental perspective. Evaporation experiments of small droplets ($0.08\,\mu$L) in close proximity to a larger one ($8\,\mu$L showed displacement of the centre of mass towards the larger droplet. The normalized results were compared with simulations in evaporation gradients which showed agreement in the general behaviour of the droplets. To confirm that a gradient in humidity was achieved, contact area decay measurements were performed and showed that the small droplet is evaporating at a rate corresponding an effective humidity gradient of 67%, as opposed to the ambient relative humidity of 10%. The second approach consisted in separating the interface of a small body of liquid which are exposed to different values of relative humidity. To achieve this,

a method to coat the inside of capillary tubes with SOCAL is developed and characterised using the capillary action method described in Chapter 3. Measurements done in coated samples showed that the SOCAL coating was successfully applied with contact angle hysteresis measurements comparable to those in literature for flat surfaces ($2.9^\circ \pm 1.9^\circ$). This was further confirmed with measurements on uncoated glass capillary tubes which recorded large values of contact angle hysteresis, this alludes to the inherent roughness inside the tubes. Evaporation experiments of $2\,\mu$L liquid slugs were performed, where one end of the capillary tube sample was exposed to a relative humidity of 5%, while the other was exposed to a relative humidity of 94%. Initial results show preferential evaporation towards the side with low relative humidity. However, prevalent pinning events in the evaporation experiment require improvements in order to confirm a relative humidity induced motion. Although the results in this chapter require further improvements in order to provide more conclusive results, they serve as proof on concept for hygrotaxis and motivate further study into this phenomenon.

The results from this thesis expand in the understanding of liquid fronts on ultra-smooth surfaces, such as SOCAL, and their potential they can provide in the self-propulsion of droplets. Self propulsion of droplets, particularly those induced by a humidity gradient, offer great potential in applications such as optimization of heat transfer systems, water harvesting and particle deposition [7].

In terms of studies that could stem from the findings of this thesis, future simulations could explore the effect of different confinement geometries since the mass flux around the droplet is influenced by the confinement condititions. For instance, simulation domains where the upper solid boundary of the channel is angled into a wedge or made into a step-like geometry could have a significant effect on the evaporation and the chemical potential gradient around the droplet. Additionally, simulations of liquid slugs where a wetting gradient is introduced on the solid boundaries would provide further understanding of the evaporation results obtained in Chapter 6.

Experimentally, future hygrotaxis experiments could be made inside a narrow channel configuration where each opening of the channel is exposed to different, and constant, relative humidity to ensure that the gradient around the droplet is consistent throughout the duration of the experiments, making the results more comparable to the simulations in Chapter 5.

Future studies involving capillary tube geometries could be focused in the optimization of the SOCAL coating parameters to minimize contact angle hysteresis inside the capillary tubes. Additionally, chemical etching procedures could be applied to the glass capillary tubes in order to smooth their inner surface before the coating procedure is performed. Lastly, to overcome the aspect ratio dependent surface activation in capillary tubes, future experiments could

explore the efficacy of the Fenton reaction for the SOCAL procedure. This reaction utilizes a liquid reagent rather than plasma for surface activation and holds a significant amount of potential to be applicable on SOCAL since it has been shown to be effective in bonding polymer groups inside long capillary tubes [110].

Bibliography

[1] M. Villegas, Y. Zhang, N. Abu Jarad, L. Soleymani, and T. F. Didar, “Liquid-Infused Surfaces: A Review of Theory, Design, and Applications,” *ACS Nano*, vol. 13, pp. 8517–8536, 8 2019.

[2] D. Daniel, J. V. Timonen, R. Li, S. J. Velling, M. J. Kreder, A. Tetreault, and J. Aizenberg, “Supplementary information for "Origins of extreme liquid-repellency on structured, flat, and lubricated hydrophobic surfaces",” *Physical Review Letters*, vol. 120, no. 24, p. 244503, 2018.

[3] I. M. Alhamad, W. K. Ahmed, and H. Z. Ali, “Boosting Teaching Experience in Mechanical Engineering Courses Using Additive Manufacturing Technologies,” in *2019 Advances in Science and Engineering Technology International Conferences, ASET 2019*, Institute of Electrical and Electronics Engineers Inc., 5 2019.

[4] S. Armstrong, G. McHale, R. Ledesma-Aguilar, and G. G. Wells, “Pinning-Free Evaporation of Sessile Droplets of Water from Solid Surfaces,” *Langmuir*, vol. 35, no. 8, pp. 2989–2996, 2019.

[5] P.-G. de Gennes, F. Brochard-Wyart, and D. Quéré, *Capillarity and Wetting Phenomena*. New York: Springer, 1st ed., 2004.

[6] S. Lach, S. M. Yoon, and B. A. Grzybowski, “Tactic, reactive, and functional droplets outside of equilibrium,” *Chemical Society Reviews*, vol. 45, pp. 4766–4796, 8 2016.

[7] R. Malinowski, I. P. Parkin, and G. Volpe, “Advances towards programmable droplet transport on solid surfaces and its applications,” 11 2020.

[8] T. M. Squires and S. R. Quake, “Microfluidics: Fluid physics at the nanoliter scale,” *Reviews of Modern Physics*, vol. 77, no. 3, pp. 977–1026, 2005.

[9] D. Quéré, “Rough ideas on wetting,” *Physica A: Statistical Mechanics and its Applications*, vol. 313, pp. 32–46, 10 2002.

[10] P. J. Van Haastert and P. N. Devreotes, “Chemotaxis: signalling the way forward,” *Nature Reviews Molecular Cell Biology 2004 5:8*, vol. 5, pp. 626–634, 8 2004.

[11] T. W. Grebe and J. Stock, “Bacterial chemotaxis: The five sensors of a bacterium,” *Current Biology*, vol. 8, pp. R154–R157, 2 1998.

[12] R. Blakemore, “Magnetotactic bacteria,” *Science*, vol. 190, pp. 377 LP – 379, 10 1975.

[13] R. W. Style, Y. Che, S. J. Park, B. M. Weon, J. H. Je, C. Hyland, G. K. German, M. P. Power, L. A. Wilen, J. S. Wettlaufer, and E. R. Dufresne, “Patterning droplets with durotaxis,” *Proceedings of the National Academy of Sciences*, vol. 110, pp. 12541–12544, 7 2013.

[14] R. Dreyfus, J. Baudry, M. L. Roper, M. Fermigier, H. A. Stone, and J. Bibette, “Microscopic artificial swimmers,” *Nature*, vol. 437, no. 7060, pp. 862–865, 2005.

[15] N. J. Cira, A. Benusiglio, and M. Prakash, "Vapour-mediated sensing and motility in two-component droplets," *Nature*, vol. 519, no. 7544, pp. 446–450, 2015.

[16] H. Sadafi, S. Dehaeck, A. Rednikov, and P. Colinet, "Vapor-Mediated versus Substrate-Mediated Interactions between Volatile Droplets," *Langmuir*, vol. 35, pp. 7060–7065, 5 2019.

[17] B. Majhy and A. K. Sen, "Evaporation-induced transport of a pure aqueous droplet by an aqueous mixture droplet," *Physics of Fluids*, vol. 32, p. 032003, 3 2020.

[18] P. Kabi, R. Pal, and S. Basu, "Moses Effect: Splitting a Sessile Droplet Using a Vapor-Mediated Marangoni Effect Leading to Designer Surface Patterns," *Langmuir*, vol. 36, pp. 1279–1287, 2 2020.

[19] R. G. Cox, "The dynamics of the spreading of liquids on a solid surface. Part 2. Surfactants," *Journal of Fluid Mechanics*, vol. 168, no. April 2006, pp. 195–220, 1986.

[20] R. A. Hayes and J. Ralston, "The molecular-kinetic theory of wetting," *Langmuir*, vol. 10, pp. 340–342, 1 1994.

[21] R. J. Pelham and Y. l. Wang, "Cell locomotion and focal adhesions are regulated by substrate flexibility.," *Proceedings of the National Academy of Sciences of the United States of America*, vol. 94, pp. 13661–5, 12 1997.

[22] Z. Izri, M. N. Van Der Linden, S. Michelin, and O. Dauchot, "Self-propulsion of pure water droplets by spontaneous marangoni-stress-driven motion," *Physical Review Letters*, vol. 113, no. 24, pp. 1–5, 2014.

[23] J. M. Stauber, S. K. Wilson, B. R. Duffy, and K. Sefiane, "On the lifetimes of evaporating droplets," *Journal of Fluid Mechanics*, vol. 744, pp. 1–12, 2014.

[24] H. Y. Erbil, "Evaporation of pure liquid sessile and spherical suspended drops: A review," *Advances in Colloid and Interface Science*, vol. 170, no. 1-2, pp. 67–86, 2012.

[25] R. G. Picknett and R. Bexon, "The evaporation of sessile or pendant drops in still air," *Journal of Colloid And Interface Science*, vol. 61, no. 2, pp. 336–350, 1977.

[26] D. Bonn, J. Eggers, J. Indekeu, and J. Meunier, "Wetting and spreading," *Reviews of Modern Physics*, vol. 81, no. 2, pp. 739–805, 2009.

[27] T. Lim, S. Han, J. Chung, J. T. Chung, S. Ko, and C. P. Grigoropoulos, "Experimental study on spreading and evaporation of inkjet printed pico-liter droplet on a heated substrate," *International Journal of Heat and Mass Transfer*, vol. 52, pp. 431–441, 1 2009.

[28] M. C. Yuen and L. W. Chen, "Heat-transfer measurements of evaporating liquid droplets," *International Journal of Heat and Mass Transfer*, vol. 21, pp. 537–542, 5 1978.

[29] E. Bertrand, D. Bonn, D. Broseta, H. Dobbs, J. O. Indekeu, J. Meunier, K. Ragil, and N. Shahidzadeh, "Wetting of alkanes on water," *Journal of Petroleum Science and Engineering*, vol. 33, pp. 217–222, 4 2002.

[30] K. C. Park, P. Kim, A. Grinthal, N. He, D. Fox, J. C. Weaver, and J. Aizenberg, "Condensation on slippery asymmetric bumps," *Nature*, vol. 531, no. 7592, pp. 78–82, 2016.

[31] Gaby Launay, "PyDSA Droplet Shape Analysis in Python," 2018.

[32] M. S. Sadullah, G. Launay, J. Parle, R. Ledesma-Aguilar, Y. Gizaw, G. McHale, G. G. Wells, and H. Kusumaatmaja, "Bidirectional motion of droplets on gradient liquid infused surfaces," *Communications Physics 2020 3:1*, vol. 3, pp. 1–7, 9 2020.

[33] B. E. Rapp, "Microfluidics: Modeling, mechanics and mathematics," *Microfluidics: Modeling, Mechanics and Mathematics*, pp. 1–766, 12 2016.

[34] N. J. Shirtcliffe, G. McHale, S. Atherton, and M. I. Newton, "An introduction to superhydrophobicity," *Advances in Colloid and Interface Science*, vol. 161, no. 1-2, pp. 124–138, 2010.

[35] P. Roach, N. J. Shirtcliffe, and M. I. Newton, "Progess in superhydrophobic surface development," *Soft Matter*, vol. 4, pp. 224–240, 1 2008.

[36] D. Quéré, "Wetting and Roughness," *Annual Review of Materials Research*, vol. 38, no. 1, pp. 71–99, 2008.

[37] N. J. Shirtcliffe, G. McHale, and M. I. Newton, "The superhydrophobicity of polymer surfaces: Recent developments," *Journal of Polymer Science Part B: Polymer Physics*, vol. 49, pp. 1203–1217, 9 2011.

[38] C. Fumridge, "Studies At Phase Interfaces I. the Sliding of Liquid Drops on Solid Surfaces and a Theory for Spray Retention," *Journal of Colloid Science*, vol. 17, pp. 309–324, 1962.

[39] H. B. Eral, D. J. C. M. 't Mannetje, and J. M. Oh, "Contact angle hysteresis: a review of fundamentals and applications," *Colloid and Polymer Science*, vol. 291, pp. 247–260, 2 2013.

[40] A. B. D. Cassie and S. Baxter, "Wettability of porous surfaces," *Transactions of the Faraday Society*, vol. 40, no. 5, pp. 546–551, 1944.

[41] Robert N. Wenzel, "Resistance of solid surfaces to wetting by water," *Industrial and Engineering Chemistry Research*, vol. 28, no. 8, pp. 988–994, 1936.

[42] G. McHale, "CHAPTER 9 Wetting Properties of Surfaces and Drag Reduction," *RSC Soft Matter*, vol. 2017-January, no. 5, pp. 253–284, 2016.

[43] P. G. De Gennes, "Wetting: statics and dynamics," *Reviews of Modern Physics*, vol. 57, pp. 827–863, 1985.

[44] O. V. Voinov, "Hydrodynamics of wetting," *Fluid Dynamics*, vol. 11, no. 5, pp. 714–721, 1976.

[45] E. Lauga, M. Brenner, and H. Stone, "Microfluidics: The No-Slip Boundary Condition," *Springer Handbooks*, pp. 1219–1240, 2007.

[46] T. D. Blake and J. M. Haynes, "Kinetics of liquid liquid displacement," *Journal of Colloid And Interface Science*, vol. 30, no. 3, pp. 421–423, 1969.

[47] M. J. De Ruijter, J. De Coninck, T. D. Blake, A. Clarke, and A. Rankin, "Contact angle relaxation during the spreading of partially wetting drops," *Langmuir*, vol. 13, no. 26, pp. 7293–7298, 1997.

[48] W. Barthlott and C. Neinhuis, "Purity of the sacred lotus, or escape from contamination in biological surfaces," *Planta*, vol. 202, no. 1, pp. 1–8, 1997.

[49] C. Neinhuis and W. Barthlott, "Characterization and distribution of water-repellent, self-cleaning plant surfaces," *Annals of Botany*, vol. 79, pp. 667–677, 6 1997.

[50] U. Bauer and W. Federle, "The insect-trapping rim of Nepenthes pitchers: surface structure and function.," 2009.

[51] T. S. Wong, S. H. Kang, S. K. Tang, E. J. Smythe, B. D. Hatton, A. Grinthal, and J. Aizenberg, "Bioinspired self-repairing slippery surfaces with pressure-stable omniphobicity," *Nature*, vol. 477, no. 7365, pp. 443–447, 2011.

[52] D. Wang, Q. Sun, M. J. Hokkanen, C. Zhang, F. Y. Lin, Q. Liu, S. P. Zhu, T. Zhou, Q. Chang, B. He, Q. Zhou, L. Chen, Z. Wang, R. H. Ras, and X. Deng, "Design of robust superhydrophobic surfaces," *Nature 2020 582:7810*, vol. 582, pp. 55–59, 6 2020.

[53] T. Onda, S. Shibuichi, N. Satoh, and K. Tsujii, "Super-Water-Repellent Fractal Surfaces," *Langmuir*, vol. 12, pp. 2125–2127, 5 1996.

[54] J. Bico, C. Marzolin, and D. Quéré, "Pearl drops," *Europhysics Letters*, vol. 47, p. 220, 7 1999.

[55] D. Öner and T. J. McCarthy, "Ultrahydrophobic Surfaces. Effects of Topography Length Scales on Wettability," *Langmuir*, vol. 16, pp. 7777–7782, 10 2000.

[56] H. Y. Erbil, A. L. Demirel, Y. Avci, and O. Mert, "Transformation of a simple plastic into a superhydrophobic surface," *Science*, vol. 299, pp. 1377–1380, 2 2003.

[57] A. Asher, V. L. Alexeev, A. V. Goponenko, A. C. Sharma, I. K. Lednev, C. S. Wilcox, D. N. Finegold, B. J. Neil Shirtcliffe, G. McHale, M. I. Newton, G. Chabrol, and C. C. Perry, "Dual-Scale Roughness Produces Unusually Water-Repellent Surfaces," *Advanced Materials*, vol. 16, pp. 1929–1932, 11 2004.

[58] N. Geraldi, R. Morris, G. McHale, and M. Newton, "Snail Deterrent Properties of a Soot based Flexible Superhydrophobic Surface," p. a001, 2014.

[59] J. T. Luo, N. R. Geraldi, J. H. Guan, G. McHale, G. G. Wells, and Y. Q. Fu, "Slippery Liquid-Infused Porous Surfaces and Droplet Transportation by Surface Acoustic Waves," *Physical Review Applied*, vol. 7, p. 014017, 1 2017.

[60] J. D. Smith, R. Dhiman, S. Anand, E. Reza-Garduno, R. E. Cohen, G. H. McKinley, and K. K. Varanasi, "Droplet mobility on lubricant-impregnated surfaces," *Soft Matter*, vol. 9, pp. 1772–1780, 1 2013.

[61] G. Launay, M. S. Sadullah, G. McHale, R. Ledesma-Aguilar, H. Kusumaatmaja, and G. G. Wells, "Self-propelled droplet transport on shaped-liquid surfaces," *Scientific Reports 2020 10:1*, vol. 10, pp. 1–8, 9 2020.

[62] L. Wang and T. J. McCarthy, "Covalently Attached Liquids: Instant Omniphobic Surfaces with Unprecedented Repellency," *Angewandte Chemie - International Edition*, vol. 55, no. 1, pp. 244–248, 2016.

[63] Y. Jin, L. Zhang, P. Wang, Y. Jin, P. Wang, and L. Zhang, "Atmospheric Water Harvesting: Role of Surface Wettability and Edge Effect," *Global Challenges*, vol. 1, p. 1700019, 7 2017.

[64] S. D. Lourenço, Y. Saulick, S. Zheng, H. Kang, D. Liu, H. Lin, and T. Yao, "Soil wettability in ground engineering: fundamentals, methods, and applications," *Acta Geotechnica*, vol. 13, pp. 1–14, 2 2018.

[65] A. M. Cazabat and G. Guéna, "Evaporation of macroscopic sessile droplets," *Soft Matter*, vol. 6, no. 12, pp. 2591–2612, 2010.

[66] R. G. Larson, "Transport and deposition patterns in drying sessile droplets," *AIChE Journal*, vol. 60, pp. 1538–1571, 5 2014.

[67] R. D. Deegan, O. Bakajin, T. F. Dupont, G. Huber, S. R. Nagel, and T. A. Witten, "Capillary flow as the cause of ring stains from dried liquid drops," *Nature 1997 389:6653*, vol. 389, no. 6653, pp. 827–829, 1997.

[68] H. Y. Erbil, G. McHale, and M. I. Newton, "Drop evaporation on solid surfaces: Constant contact angle mode," *Langmuir*, vol. 18, pp. 2636–2641, 4 2002.

[69] J. M. Stauber, S. K. Wilson, B. R. Duffy, and K. Sefiane, "On the lifetimes of evaporating droplets with related initial and receding contact angles," *Phys. Fluids*, vol. 27, p. 122101, 2015.

[70] H. Gelderblom, A. G. Marín, H. Nair, A. Van Houselt, L. Lefferts, J. H. Snoeijer, and D. Lohse, "How water droplets evaporate on a superhydrophobic substrate," *Physical Review E - Statistical, Nonlinear, and Soft Matter Physics*, vol. 83, p. 026306, 2 2011.

[71] G. McHale, S. Aqil, N. J. Shirtcliffe, M. I. Newton, and H. Y. Erbil, "Analysis of Droplet Evaporation on a Superhydrophobic Surface," *Langmuir*, vol. 21, pp. 11053–11060, 11 2005.

[72] X. Zhang, S. Tan, N. Zhao, X. Guo, X. Zhang, Y. Zhang, and J. Xu, "Evaporation of Sessile Water Droplets on Superhydrophobic Natural Lotus and Biomimetic Polymer Surfaces," *ChemPhysChem*, vol. 7, pp. 2067–2070, 10 2006.

[73] M. L. McLauchlin, D. Yang, P. Aella, A. A. Garcia, S. T. Picraux, and M. A. Hayes, "Evaporative Properties and Pinning Strength of Laser-Ablated, Hydrophilic Sites on Lotus-Leaf-like, Nanostructured Surfaces," *Langmuir*, vol. 23, pp. 4871–4877, 4 2007.

[74] S.-x. Tan, X.-y. Zhang, N. Zhao, and J. Xu, "Simulation of Sessile Water-Droplet Evaporation on Superhydrophobic Polymer Surfaces," *Chinese Journal of Chemical Physics*, vol. 20, pp. 140–144, 4 2007.

[75] Y. C. Jung and B. Bhushan, "Wetting behaviour during evaporation and condensation of water microdroplets on superhydrophobic patterned surfaces," *Journal of Microscopy*, vol. 229, pp. 127–140, 1 2008.

[76] S. A. Kulinich and M. Farzaneh, "Effect of contact angle hysteresis on water droplet evaporation from super-hydrophobic surfaces," *Applied Surface Science*, vol. 255, pp. 4056–4060, 1 2009.

[77] J. H. Guan, G. G. Wells, B. Xu, G. McHale, D. Wood, J. Martin, and S. Stuart-Cole, "Evaporation of Sessile Droplets on Slippery Liquid-Infused Porous Surfaces (SLIPS)," *Langmuir*, vol. 31, pp. 11781–11789, 11 2015.

[78] G. W. C. Kaye and T. H. Laby, *Tables of Physical and Chemical Constants*. NPL (National Physical Laboratory), 16th edition ed., 1995.

[79] D. R. Lide, "CRC Handbook of Chemistry and Physics," *Journal of Molecular Structure*, vol. 268, p. 320, 1992.

[80] R. Ledesma-Aguilar, D. Vella, and J. M. Yeomans, "Lattice-Boltzmann simulations of droplet evaporation," *Soft Matter*, vol. 10, pp. 8267–8275, 11 2014.

[81] E. Ruiz-Gutiérrez, J. H. Guan, B. Xu, G. McHale, G. G. Wells, and R. Ledesma-Aguilar, "Energy Invariance in Capillary Systems," *Physical Review Letters*, vol. 118, no. 21, 2017.

[82] E. Ruiz-Gutiérrez, C. Semprebon, G. McHale, and R. Ledesma-Aguilar, "Statics and dynamics of liquid barrels in wedge geometries," *Journal of Fluid Mechanics*, vol. 842, pp. 26–57, 5 2018.

[83] E. Ruiz-Gutiérrez, A. M. Edwards, G. McHale, M. I. Newton, G. G. Wells, C. V. Brown, and R. Ledesma-Aguilar, "Lattice Boltzmann Simulations of Multiphase Dielectric Fluids," *Langmuir*, vol. 37, pp. 7328–7340, 6 2021.

[84] X. Liu and P. Cheng, "Dropwise condensation theory revisited Part II. Droplet nucleation density and condensation heat flux," *International Journal of Heat and Mass Transfer*, vol. 83, pp. 842–849, 4 2015.

[85] J. W. Cahn and J. E. Hilliard, "Free Energy of a Nonuniform System. I. Interfacial Free Energy," *The Journal of Chemical Physics*, vol. 28, p. 258, 8 2004.

[86] F. Magaletti, F. Picano, M. Chinappi, L. Marino, and C. M. Casciola, "The sharp-interface limit of the Cahn–Hilliard/Navier–Stokes model for binary fluids," *Journal of Fluid Mechanics*, vol. 714, pp. 95–126, 1 2013.

[87] M. R. Swift, E. Orlandini, W. R. Osborn, and J. M. Yeomans, "Lattice Boltzmann simulations of liquid-gas and binary fluid systems," *Physical Review E - Statistical Physics, Plasmas, Fluids, and Related Interdisciplinary Topics*, vol. 54, no. 5, pp. 5041–5052, 1996.

[88] H. B. Callen, *Thermodynamics and an Introduction to Thermostatistics*. John Wiley & Sons, 2006.

[89] L. M. Pismen, "Mesoscopic hydrodynamics of contact line motion," *Colloids and Surfaces A: Physicochemical and Engineering Aspects*, vol. 206, pp. 11–30, 7 2002.

[90] J. Rowlinson and B. Widom, *Molecular theory of capillarity*, vol. 167. New York: Dover Publications, 2002.

[91] J. W. Cahn, "Critical point wetting," *The Journal of Chemical Physics*, vol. 66, pp. 3667–3672, 8 1977.

[92] A. J. Briant, A. J. Wagner, and J. M. Yeomans, "Lattice Boltzmann simulations of contact line motion. I. Liquid-gas systems," *Physical Review E - Statistical, Nonlinear, and Soft Matter Physics*, vol. 69, no. 3 1, 2004.

[93] J. David and J. Wendt, *Computational fluid dynamics*, vol. 26. Springer, 1995.

[94] T. Kruger, H. Kusumaatmaja, A. Kuzmin, O. Shardt, G. Silva, and E. M. Viggen, *The Lattice Boltzmann Method: Principles and Practice*. Springer, first edit ed., 2016.

[95] T. L. Hill and J. Gillis, "An Introduction to Statistical Thermodynamics," *Physics Today*, vol. 14, p. 62, 1 2009.

[96] S. Succi, *The Lattice Boltzmann Equation: for Fluid Dynamics and Beyond*. Oxford University Press, 1 ed., 2001.

[97] R. L. Liboff, *Kinetic Theory*. Springer, third ed., 1983.

[98] X. He and L. S. Luo, "A priori derivation of the lattice Boltzmann equation," *Physical Review E*, vol. 55, p. R6333, 6 1997.

[99] D. D'Humières, I. Ginzburg, M. Krafczyk, P. Lallemand, and L. S. Luo, "Multiple-relaxation-time lattice Boltzmann models in three dimensions," in *Philosophical Transactions of the Royal Society A: Mathematical, Physical and Engineering Sciences*, vol. 360, pp. 437–451, The Royal Society, 3 2002.

[100] C. M. Pooley and K. Furtado, "Eliminating spurious velocities in the free-energy lattice Boltzmann method," *Physical Review E - Statistical, Nonlinear, and Soft Matter Physics*, vol. 77, no. 4, 2008.

[101] F. Brochard, "Motions of droplets on solid surfaces induced by chemical or thermal gradients," *Langmuir*, vol. 5, pp. 432–438, 3 2002.

[102] J. Li and Z. Guo, "Spontaneous directional transportations of water droplets on surfaces driven by gradient structures," *Nanoscale*, vol. 10, pp. 13814–13831, 7 2018.

[103] S. Daniel, M. K. Chaudhury, and J. C. Chen, "Fast drop movements resulting from the phase change on a gradient surface," *Science*, vol. 291, pp. 633–636, 1 2001.

[104] P. Agrawal, T. T. Salomons, D. S. Chiriac, A. C. Ross, and R. D. Oleschuk, "Facile Actuation of Organic and Aqueous Droplets on Slippery Liquid-Infused Porous Surfaces for the Application of On-Chip Polymer Synthesis and Liquid-Liquid Extraction," *ACS Applied Materials and Interfaces*, vol. 11, pp. 28327–28335, 8 2019.

[105] M. K. Tan, J. R. Friend, and L. Y. Yeo, "Microparticle collection and concentration via a miniature surface acoustic wave device," *Lab on a Chip*, vol. 7, pp. 618–625, 5 2007.

[106] D. Daniel, J. V. Timonen, R. Li, S. J. Velling, and J. Aizenberg, "Oleoplaning droplets on lubricated surfaces," *Nature Physics*, vol. 13, pp. 1020–1025, 10 2017.

[107] T. Mizutani, U. Satake, and T. Enomoto, "Surgical diamond wheels for minimally invasive surgery in bone resection under small quantity of coolant supply," *Precision Engineering*, vol. 56, no. August 2018, pp. 80–86, 2019.

[108] X. Wang, Z. Wang, L. Heng, and L. Jiang, "Stable Omniphobic Anisotropic Covalently Grafted Slippery Surfaces for Directional Transportation of Drops and Bubbles," *Advanced Functional Materials*, vol. 30, no. 1, pp. 1–10, 2020.

[109] S. Armstrong, G. McHale, R. Ledesma-Aguilar, and G. G. Wells, "Evaporation and electrowetting of sessile droplets on slippery liquid-like surfaces and slippery liquid-infused porous surfaces (SLIPS)," *Langmuir*, vol. 36, pp. 11332–11340, 9 2020.

[110] F. Geyer, M. D'Acunzi, C. Y. Yang, M. Müller, P. Baumli, A. Kaltbeitzel, V. Mailänder, N. Encinas, D. Vollmer, and H. J. Butt, "How to Coat the Inside of Narrow and Long Tubes with a Super-Liquid-Repellent Layer—A Promising Candidate for Antibacterial Catheters," *Advanced Materials*, vol. 31, no. 2, 2019.

[111] H. Zhao, S. Khodakarami, C. A. Deshpande, J. Ma, Q. Wu, S. Sett, and N. Miljkovic, "Scalable Slippery Omniphobic Covalently Attached Liquid Coatings for Flow Fouling Reduction," *ACS Applied Materials and Interfaces*, vol. 13, pp. 38666–38679, 8 2021.

[112] L. Gao and T. J. McCarthy, "Contact Angle Hysteresis Explained," *Langmuir*, vol. 22, pp. 6234–6237, 7 2006.

[113] G. McHale, N. J. Shirtcliffe, and M. I. Newton, "Contact-angle hysteresis on super-hydrophobic surfaces," *Langmuir*, vol. 20, no. 23, pp. 10146–10149, 2004.

[114] K. Grundke, K. Pöschel, A. Synytska, R. Frenzel, A. Drechsler, M. Nitschke, A. L. Cordeiro, P. Uhlmann, and P. B. Welzel, "Experimental studies of contact angle hysteresis phenomena on polymer surfaces - Toward the understanding and control of wettability for different applications," *Advances in Colloid and Interface Science*, vol. 222, pp. 350–376, 2015.

[115] D. Quéré, M. J. Azzopardi, and L. Delattre, "Drops at Rest on a Tilted Plane," *Langmuir*, vol. 14, pp. 2213–2216, 4 1998.

[116] J. H. Guan, G. G. Wells, B. Xu, G. McHale, D. Wood, J. Martin, and S. Stuart-Cole, "Evaporation of Sessile Droplets on Slippery Liquid-Infused Porous Surfaces (SLIPS)," *Langmuir*, vol. 31, no. 43, pp. 11781–11789, 2015.

[117] M. Vuckovac, M. Latikka, K. Liu, T. Huhtamäki, and R. H. A. Ras, "Uncertainties in contact angle goniometry," *Soft Matter*, vol. 15, no. 35, pp. 7089–7096, 2019.

[118] Kruss, "Advance Software," 12 2020.

[119] Kruss, "Drop Shape Analyzer - DSA25," 1 2022.

[120] J. Canny, "A Computational Approach to Edge Detection," *IEEE Transactions on Pattern Analysis and Machine Intelligence*, vol. PAMI-8, no. 6, pp. 679–698, 1986.

[121] K. Liu, M. Vuckovac, M. Latikka, T. Huhtamäki, and R. H. Ras, "Improving surface-wetting characterization," 3 2019.

[122] B. J. De Gans, P. C. Duineveld, and U. S. Schubert, "Inkjet printing of polymers: State of the art and future developments," *Advanced Materials*, vol. 16, no. 3, pp. 203–213, 2004.

[123] L. Introzzi, J. M. Fuentes-Alventosa, C. A. Cozzolino, S. Trabattoni, S. Tavazzi, C. L. Bianchi, A. Schiraldi, L. Piergiovanni, and S. Farris, ""Wetting Enhancer" Pullulan Coating for Antifog Packaging Applications," *ACS Applied Materials & Interfaces*, vol. 4, pp. 3692–3700, 7 2012.

[124] P. Kim, T. S. Wong, J. Alvarenga, M. J. Kreder, W. E. Adorno-Martinez, and J. Aizenberg, "Liquid-infused nanostructured surfaces with extreme anti-ice and anti-frost performance," *ACS Nano*, vol. 6, no. 8, pp. 6569–6577, 2012.

[125] T. D. Blake, "The physics of moving wetting lines," *Journal of Colloid and Interface Science*, vol. 299, pp. 1–13, 7 2006.

[126] we are cellix, "Microfluidic pumps."

[127] C. Lam, R. Wu, D. Li, M. Hair, and A. Neumann, "Study of the advancing and receding contact angles: liquid sorption as a cause of contact angle hysteresis," *Advances in Colloid and Interface Science*, vol. 96, pp. 169–191, 2 2002.

[128] H. Teisala, P. Baumli, S. A. Weber, D. Vollmer, and H. J. Butt, "Grafting Silicone at Room Temperature-a Transparent, Scratch-resistant Nonstick Molecular Coating," *Langmuir : the ACS journal of surfaces and colloids*, vol. 36, no. 16, pp. 4416–4431, 2020.

[129] Y. Wen, P. Y. Kim, S. Shi, D. Wang, X. Man, M. Doi, and T. P. Russell, "Vapor-induced motion of two pure liquid droplets," *Soft Matter*, vol. 15, no. 10, pp. 2135–2139, 2019.

[130] R. Malinowski, I. P. Parkin, and G. Volpe, "Contactless Manipulation of Binary Droplets via Sensing of Localized Vapor Sources," *Science Advances*, vol. 6, 9 2019.

[131] J. W. M. Bush, "Lecture 4: Marangoni Flows," *MIT Lecture Notes on Surface Tension*, pp. 1–5, 2004.

[132] A. Askounis, Y. Kita, M. Kohno, Y. Takata, V. Koutsos, and K. Sefiane, "Influence of Local Heating on Marangoni Flows and Evaporation Kinetics of Pure Water Drops," *Langmuir*, vol. 33, pp. 5666–5674, 6 2017.

[133] C. Diddens, Y. Li, and D. Lohse, "Competing Marangoni and Rayleigh convection in evaporating binary droplets," *Journal of Fluid Mechanics*, vol. 914, p. 23, 2021.

[134] R. Malinowski, I. P. Parkin, and G. Volpe, "Nonmonotonic contactless manipulation of binary droplets via sensing of localized vapor sources on pristine substrates," *Science Advances*, vol. 6, p. eaba3636, 10 2020.

[135] F. G. Schofield, A. W. Wray, D. Pritchard, and S. K. Wilson, "The shielding effect extends the lifetimes of two-dimensional sessile droplets," *Journal of Engineering Mathematics*, vol. 120, pp. 89–110, 2 2020.

[136] G. McHale, S. M. Rowan, M. I. Newton, and M. K. Banerjee, "Evaporation and the Wetting of a Low-Energy Solid Surface," *The Journal of Physical Chemistry B*, vol. 102, pp. 1964–1967, 2 1998.

[137] L. Bansal, S. Chakraborty, and S. Basu, "Confinement-induced alterations in the evaporation dynamics of sessile droplets," *Soft Matter*, vol. 13, pp. 969–977, 2 2017.

[138] S. Hatte, R. Dhar, L. Bansal, S. Chakraborty, and S. Basu, "On the lifetime of evaporating confined sessile droplets," *Colloids and Surfaces A: Physicochemical and Engineering Aspects*, vol. 560, pp. 78–83, 1 2019.

[139] E. Chibowski, A. Ontiveros-Ortega, R. Perea-Carpio, A. Ontiveros-ortega, and R. Perea-carpio, "On the interpretation of contact angle hysteresis," *Journal of Adhesion Science and Technology*, vol. 16, no. 10, pp. 1367–1404, 2002.

[140] H. GmbH, "Glass capillaries."

[141] N. Chada, K. P. Sigdel, R. R. Sanganna Gari, T. R. Matin, L. L. Randall, and G. M. King, "Glass is a Viable Substrate for Precision Force Microscopy of Membrane Proteins," *Scientific Reports*, vol. 5, pp. 1–8, 2015.

[142] C. A. Hamlett, S. Atherton, N. J. Shirtcliffe, G. Mchale, S. Ahn, S. H. Doerr, R. Bryant, and M. I. Newton, "Transitions of water-drop impact behaviour on hydrophobic and hydrophilic particles," *European Journal of Soil Science*, vol. 64, no. 3, pp. 324–333, 2013.

Appendix A

Peer reviewed journal publication

Publication details:

- **Journal:** Langmuir
- **Year:** 2020
- **Title:** Contact-Angle Hysteresis and Contact-Line Friction on Slippery Liquid-like Surfaces
- **Authors:** Hernán Barrio-Zhang, Élfego Ruiz-Gutiérrez, Steven Armstrong, Glen McHale, Gary G. Wells, and Rodrigo Ledesma-Aguilar
- **Permission:** Reprinted with permission from Langmuir 2020, 36, 15094-15101. Copyright 2020 American Chemical Society. For online access: *ACS Articles on Request*

LANGMUIR

pubs.acs.org/Langmuir Article

Contact-Angle Hysteresis and Contact-Line Friction on Slippery Liquid-like Surfaces

Hernán Barrio-Zhang, Élfego Ruiz-Gutiérrez, Steven Armstrong, Glen McHale, Gary G. Wells, and Rodrigo Ledesma-Aguilar*

Cite This: *Langmuir* 2020, 36, 15094−15101 Read Online

ACCESS | Metrics & More | Article Recommendations

ABSTRACT: Contact-line pinning and dynamic friction are fundamental forces that oppose the motion of droplets on solid surfaces. Everyday experience suggests that if a solid surface offers low contact-line pinning, it will also impart a relatively low dynamic friction to a moving droplet. Examples of such surfaces are superhydrophobic, slippery porous liquid-infused, and lubricant-impregnated surfaces. Here, however, we show that slippery omniphobic covalently attached liquid-like (SOCAL) surfaces have a remarkable combination of contact-angle hysteresis and contact-line friction properties, which lead to very low droplet pinning but high dynamic friction against the motion of droplets. We present experiments of the response of water droplets to changes in volume at controlled temperature and humidity conditions, which we separately compare to the predictions of a hydrodynamic model and a contact-line model based on molecular kinetic theory. Our results show that SOCAL surfaces offer very low contact-angle hysteresis, between 1 and 3°, but an unexpectedly high dynamic friction controlled by the contact line, where the typical relaxation time scale is on the order of seconds, 4 orders of magnitude larger than the prediction of the classical hydrodynamic model. Our results highlight the remarkable wettability of SOCAL surfaces and their potential application as low-pinning, slow droplet shedding surfaces.

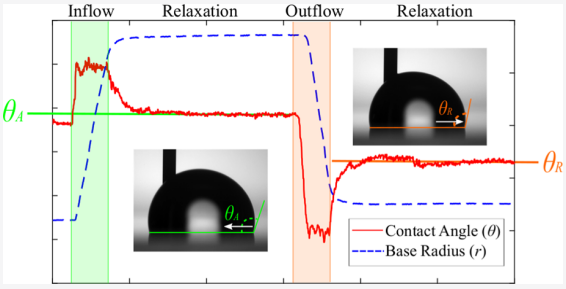

INTRODUCTION

The interaction of droplets with engineered solid surfaces has relevance from both a fundamental and an applied perspective. On the one hand, understanding the mechanisms involved in the interaction between droplets and complex surfaces can unveil new physics in the context of solid−liquid interactions. On the other hand, engineered surfaces can be used to solve problems in applications such as ink-jet printing,[1] coating,[2] and lubrication.[3]

Recently, there has been a sustained interest in slippery omniphobic covalently attached liquid-like (SOCAL) surfaces, which are a type of engineered, ultrasmooth solid surface that offers remarkably low static friction to the motion of droplets.[4−6] SOCAL surfaces are achieved by acid-catalyzed graft polycondensation of dimethyldimethoxysilane, where short polymer chains are covalently bound to a solid substrate creating a nanometric monolayer that shields a droplet from the underlying solid substrate.[4] The polymer coating of a SOCAL surface plays a similar role to the intermediary liquid lubricant film used to create slippery liquid-infused porous surfaces (SLIPS)[7] and lubricant-impregnated surfaces (LIS):[8] it creates a smooth surface that masks the chemical and topographical heterogeneity of the solid substrate. However, unlike SLIPS or LIS, on SOCAL surfaces, a droplet is in contact with a polymer coating covalently attached to the solid and not with a liquid layer. On SOCAL surfaces, droplets are subject to a very low contact-angle hysteresis, typically of 1° or below. Despite this low hysteresis, droplets on SOCAL surfaces exhibit a remarkably low mobility,[5] indicating an unexpected high dynamic friction imparted by the surface on a moving droplet. From a fundamental perspective, this raises important questions about the physical mechanism governing the motion of contact lines on SOCAL surfaces. On the other hand, the remarkable combination of low static friction but high dynamic friction can unlock applications in surface engineering, where SOCAL surfaces act as "low-pinning-slow shedding" coatings.

In this paper, we study the static and dynamic friction of water droplets on SOCAL surfaces. We start by reviewing relevant concepts in the study of statics and dynamics of sessile droplets on solid surfaces. We report experiments of the droplet transition to a steady state driven by either an inflow or

Received: September 9, 2020
Revised: November 12, 2020
Published: December 1, 2020

https://dx.doi.org/10.1021/acs.langmuir.0c02668
Langmuir 2020, 36, 15094−15101

an outflow at a fixed flow rate and the subsequent relaxation to equilibrium once the flow is suppressed. We characterize static friction using the relaxation of the contact line toward a static configuration, which allows us to measure the contact-angle hysteresis directly from measurements of the apparent contact angle. In the limit of mechanical and thermodynamic equilibria, corresponding to a vanishing contact-line velocity and high relative humidity (94%), we measure well-defined, reproducible values of the advancing and receding contact angles, which yield a contact-angle hysteresis as low as $\Delta\theta = 2.1 \pm 0.4°$. Out of thermodynamic equilibrium, we show that the apparent contact angle deviates from the advancing and receding values due to the effect of evaporation. Out of mechanical equilibrium but at high relative humidity, we find a variation of the apparent contact angle with interface velocity. The corresponding relaxation time to mechanical equilibrium is in good agreement with an analytical model based on molecular kinetic theory.[9]

STATICS AND DYNAMICS OF DROPLETS ON SOLID SURFACES

Statics. Consider a droplet sitting on a perfectly flat and smooth surface. Within the framework of classical thermodynamics, the equilibrium state of the droplet is given by a minimum in the total surface energy of the system. For droplets whose size is below the capillary length, this corresponds to a spherical cap shape defined by an equilibrium contact angle θ_e, also known as Young's angle, which is determined by the Young–Dupré equation

$$\cos\theta_e = \frac{\gamma_{SG} - \gamma_{SL}}{\gamma} \tag{1}$$

where γ is the liquid–gas surface tension, γ_{SG} is the solid–gas surface tension, and γ_{SL} is the solid–liquid surface tension.

Equation 1 implies that the equilibrium contact angle is uniquely determined by the combination of the surface tensions. However, this assertion is only valid in the ideal case of a perfectly flat and smooth solid. In practice, any solid surface is heterogeneous at small scales because of either chemical defects or topographic roughness. Therefore, instead of a unique equilibrium contact angle, one observes a static contact angle, θ_S, which varies over a range controlled by the surface heterogeneity.

An important consequence of the heterogeneity of a solid surface is contact-line pinning, which is the static friction that a droplet needs to overcome to start moving on the solid.[10] A familiar situation where contact-line pinning is evident occurs when a droplet is placed on an incline: one observes that the droplet resists motion up to a maximum inclination angle at which point it moves down. At the onset of motion, the contact angle of an advancing liquid–gas interface is referred to as the advancing contact angle, θ_A. Similarly, the contact angle at the onset of a receding motion is called the receding angle, θ_R. Therefore, the range of the static contact angle, θ_S, is given by

$$\theta_R \le \theta_S \le \theta_A \tag{2}$$

and the amplitude of this range is a measure of the hysteresis caused by the surface heterogeneity, typically called the contact-angle hysteresis

$$\Delta\theta = \theta_A - \theta_R \tag{3}$$

The importance of contact-angle hysteresis becomes evident when considering the pinning force acting on a droplet. At the onset of motion, the net force acting on the contact line is given by

$$F_{pinning} = 2\gamma r(\cos\theta_A - \cos\theta_R) \tag{4}$$

where r is the base radius of the droplet.[5] From eqs 2 and 3, it follows that the advancing and receding angles obey $\theta_A = \theta_S + f\Delta\theta$ and $\theta_R = \theta_S - (1-f)\Delta\theta$, where $0 \le f \le 1$. Inserting these expressions in eq 4 and expanding in powers of $\Delta\theta$ gives

$$F_{pinning} \approx -2\gamma r \sin\theta_S \Delta\theta \tag{5}$$

Hence, the pinning force scales with contact-angle hysteresis by a factor determined by the normal component of the surface tension force, $\gamma \sin\theta_S$.

Relaxation to Equilibrium. Beyond the onset of motion, the shape of the droplet can be characterized in terms of a dynamic angle, $\theta(v)$, which depends on the velocity of the contact line, v.[10,11] For an advancing contact line, the dynamic angle is higher than the advancing angle, i.e., $\theta(v) > \theta_A$, and one expects that θ approaches θ_A as $v \to 0$. Similarly, for a receding contact line, $\theta(v) < \theta_R$, and $\theta \to \theta_R$ as the contact line comes to a rest.

The deviation of the dynamic contact angle from the static value is governed by the competition between driving and dissipative forces. On the one hand, the large-scale deformation of the liquid–gas interface is governed by the competition between viscous stresses and surface tension. This is described by the Cox–Voinov theory,[12,13] which gives the following prediction of the apparent contact angle as a function of the velocity of the interface

$$\theta^3 = \theta_m^3 + 9\mathrm{Ca}\ln\left(\frac{L}{l_m}\right) \tag{6}$$

where $\mathrm{Ca} = \eta v/\gamma$ is the capillary number, L is the typical macroscopic length scale where the dynamic contact angle is measured, and θ_m is the microscopic contact angle, measured at a microscopic cutoff length scale l_m.[11]

In addition, the effect of the solid surface on the motion of the contact line is controlled by microscopic processes. Haynes and Blake developed a model for the contact-line dynamics based on molecular kinetic theory (MKT),[14] which was subsequently used to describe the spreading of droplets on solid surfaces.[15] In the framework of MKT, the contact-line motion is governed by the rate of adsorption and desorption of molecules from the solid. The balance between both processes sets the contact-line velocity[5]

$$v = 2K_0\xi \sinh\left(\frac{\gamma\xi^2(\cos\theta_S - \cos\theta)}{2k_BT}\right) \tag{7}$$

where K_0 is the frequency of adsorption–desorption of molecules at the contact line, ξ is the average distance of molecular displacements, and k_{BT} is the thermal energy.

We now study the relaxation of the droplet toward a spherical cap shape and derive separate expressions for the typical relaxation time based on the Cox–Voinov and MKT models. We start by assuming that the droplet shape is a spherical cap of instantaneous base radius $r(t)$, contact-line velocity $v = \dot{r}$, and spatially uniform dynamic contact angle $\theta(t)$. Therefore, deviations of the droplet shape from the static

https://dx.doi.org/10.1021/acs.langmuir.0c02668
Langmuir 2020, 36, 15094–15101

configuration can be quantified in terms of the deformation angle

$$\delta\theta(t) = \theta(t) - \theta_S \tag{8}$$

where θ_S is the limiting static value of the contact angle, i.e., either θ_A or θ_R depending on whether the contact line is advancing or receding during the relaxation process. In the limit of small deformations, we expect that the velocity of the contact line varies linearly with $\delta\theta$, i.e.

$$\dot{r} = m\delta\theta \tag{9}$$

where the constant m is determined by the physical mechanism governing the motion of the contact line. For a spherical cap, one has the geometrical relation

$$r = \left[\frac{3V \sin^3\theta}{\pi(1+\cos\theta)^2(2+\cos\theta)}\right]^{1/3} \tag{10}$$

Expanding this expression in powers of $\delta\theta$ and differentiating with respect to time lead to the relation

$$\dot{r} = \frac{\mathrm{d}r}{\mathrm{d}\theta}\Big|_{\theta=\theta_S}\dot{\delta\theta} \tag{11}$$

Combining eqs 9 and 11 and integrating with respect to time give the exponential relaxation

$$\theta(t) = \theta_S + \delta\theta_0 \exp(-t/\tau) \tag{12}$$

where $\delta\theta_0$ is the initial deformation and

$$\tau = \frac{1}{m}\frac{\mathrm{d}r}{\mathrm{d}\theta}\Big|_{\theta=\theta_S} \tag{13}$$

is the relaxation time.

For viscous-dominated dynamics, the microscopic contact angle is expected to be close to the static value,[11] i.e., $\theta_m \approx \theta_S$. Setting $\theta = \theta_S + \delta\theta$ in eq 6, expanding in powers of $\delta\theta$, and using eqs 9 and 13 lead to the following expressions

$$m_{CV} = \frac{\gamma\theta_S^2}{3\eta \ln(L/l_m)} \tag{14}$$

and

$$\tau_{CV} = \frac{\left[\frac{3V}{\pi(\cos\theta_S - 1)^2(2+\cos\theta_S)}\right]^{1/3}}{2+\cos\theta_S}\left(\frac{3\eta\ln(L/l_m)}{\gamma\theta_S^2}\right) \tag{15}$$

One can obtain equivalent expressions using the MKT model. Expanding eq 7 in powers of $\delta\theta$ and using eqs 9 and 13, we obtain

$$m_{MKT} = \frac{K_0\gamma\xi^3 \sin\theta_S}{k_B T} \tag{16}$$

and

$$\tau_{MKT} = \frac{\left[\frac{3V}{\pi((\cos\theta_S - 1)^2(\cos\theta_S + 2))}\right]^{1/3}}{2+\cos\theta_S}\left(\frac{k_B T}{K_0\gamma \sin\theta_S \xi^3}\right) \tag{17}$$

EXPERIMENTAL METHODS

SOCAL Surfaces. SOCAL surfaces were prepared following the methodology outlined by Wang and McCarthy[4] and optimized using the experimental parameters reported by Armstrong et al.[6] Glass slides (25 mm × 75 mm) were cleaned in a solution of deionized (DI) water and detergent (Decon 90, 2% solution) placed into a 30 min ultrasonic bath followed by rinsing with DI water, acetone, and isopropanol (IPA). The clean slides were then put in an air plasma oven (Henniker HPT-100) operating at a power of 30 W for 30 min, which creates OH^- radicals on the glass substrate. The slides were immersed for 5 s in a solution of isopropanol, dimethyldimethoxysilane, and sulfuric acid (100, 10, and 1 wt %, respectively) and withdrawn manually. This solution reacts with the exposed OH^- groups, inducing the polycondensation of PDMS chains on the surface. The result is the grafting of an ∼4 nm thick liquid-like polymer coating on the surface of the glass substrate.[4]

Contact-Angle Measurements. Figure 1a shows the experimental setup. A SOCAL surface sample is positioned within a drop

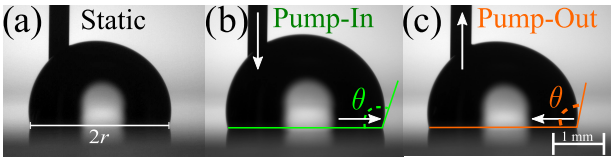

Figure 1. Experimental setup. (a) Droplet of controlled initial volume V is placed on a SOCAL surface and connected to a micropump through a thin needle. (b, c) Micropump injects or withdraws liquid at a prescribed flow rate $\dot{q}$ (vertical arrows). The instantaneous apparent contact angle, θ, and base radius, r, are measured using image analysis. The scale bar is 1 mm.

shape analyzer (Krüss, DSA25), equipped with a leveling stage, a thermostat, and humidity control. The experimental procedure consists of depositing a droplet of deionized water and controlled volume, V = 8 μL, on the SOCAL surface. A thin needle (outer diameter: 0.4 mm) is connected to a micropump (Cellix ExiGo) and used to feed or withdraw liquid from the edge of the droplet. At the same time, the apparent contact angle is measured at the opposite edge of the drop, where the droplet maintains a shape close to a spherical cap. The volume variation is carried out as follows. A volume ΔV = 4 μL of water is first injected into the droplet at a prescribed flow rate, $\dot{q}$, which we vary between 1 and 10 μL/min (Figure 1b). The droplet is then left to rest with the needle in for a period of 2 min to allow the contact line enough time to return to a static position. Subsequently, a volume ΔV = 4 μL of water is withdrawn from the droplet at the same flow rate (Figure 1c) and is then left to rest for 2 min before video recording is stopped. The droplet is then removed from the surface, and the process is repeated.

All experiments are performed at a controlled relative humidity, which we vary between 30 ± 0.5 and 94 ± 0.5% and at a constant temperature, T = 25 ± 0.2 °C. For each set of parameters, the experiment is repeated 5 times.

The experiments were recorded using a video camera, and the resulting images were analyzed using pyDSA, an in-house droplet shape analyzer.[16] The resolution of the video footage was at least 2 pixels/μm, and the apparent contact angle of the droplet is determined by image analysis as follows. First, the apparent contact line is detected using the droplet's reflection on the solid. The droplet's free contour is determined using a brightness threshold function. A third-degree polynomial is fitted to the contour of the droplet over a region that ranges from the free edge of the drop to the point where the needle meets the droplet. The algorithm then determines the point at which the polynomial meets the contact line and computes the apparent contact angle as the local slope. The resolution of the images allows the algorithm to produce droplet contours formed by ∼250−500 points, leading to a small fitting error. Therefore, the systematic measurement error in the apparent angle is $\delta\theta \sim 0.2°$, which is commensurate with previous errors reported in the literature.[17,18]

To determine the advancing and receding contact angles and, therefore, the contact-angle hysteresis, we used two different methods. As a first method, we determined the onset of motion of the contact

https://dx.doi.org/10.1021/acs.langmuir.0c02668
Langmuir 2020, 36, 15094−15101

line upon increasing and decreasing the volume of the droplet.[10,19−22] This point is then mapped to the corresponding apparent contact angle: θ_A for a volume increase and θ_R for a volume decrease. The second method consists of tracking the apparent contact angle as the velocity of the contact line vanishes after a change in volume, and identifying the corresponding limiting value of the apparent contact angle as either the advancing or the receding angle.[23]

EXPERIMENTAL RESULTS

Figure 2 shows representative measurements of $\theta(t)$ (red line) and $r(t)$ (blue line) for an 8 μL droplet subject to changes in volume at a constant flow rate ($\Delta V = \pm 4$ μL; $\dot{q} = 10$ μL/min), followed by relaxation periods at a zero flow rate ($\Delta t = 120$ s). The temperature and relative humidity are fixed at $T = 25$ °C and RH = 94%, ensuring that the droplet does not undergo significant evaporation during the experiment. During the injection phase (green-shaded region), the apparent contact angle increases sharply from the initial value $\theta_i \approx 103°$. This sharp increase is followed by a steady motion of the contact line, where $\theta \approx 106°$ and where the base radius grows at a rate $\dot{r} = 9 \pm 1$ μm/s. A similar situation occurs during the withdrawal phase of the experiment (red-shaded region), where the apparent contact angle sharply falls as the contact line starts to recede until it settles at $\theta \approx 99°$ for a contact-line velocity, $\dot{r} = 12 \pm 1$ μm/s. Once the flow is switched off, the apparent contact angle relaxes to well-defined constant values: $\theta = 103.8$ ° after injection and $\theta = 101.6°$ after withdrawal.

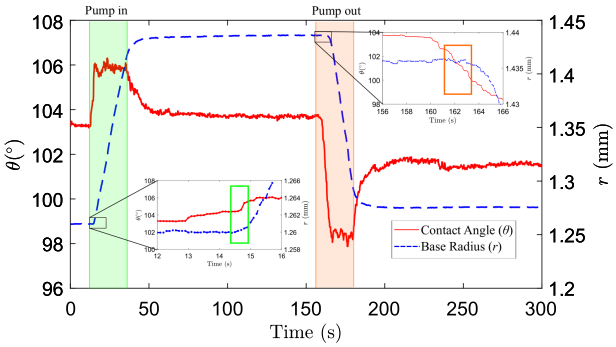

Figure 2. Apparent contact angle and base radius measurements at high relative humidity. The graph of a typical experimental set of data performed at a constant flow rate $\dot{q} = 10$ μL/min at $T = 25°$ C and RH = 94%. The zoomed-in regions show how the smooth transition from a static to a moving contact line introduces uncertainty in the measurement of the advancing and receding angles.

Effect of Flow Rate. The relaxation of the apparent contact angle reported in Figure 2 indicates that dynamical effects due to a finite flow rate affect the shape of the droplet.[23] To understand the relevance of this effect for droplets on SOCAL surfaces, we performed experiments on a fresh SOCAL sample considering three different flow rates: $\dot{q} = 1$, 5, and 10 μL/min. As before, the experiment consisted of a change in the droplet volume $\Delta V = \pm 4$ μL, followed by a relaxation at a zero flow rate ($\Delta t = 300$ s). The experiment was repeated three times for each flow rate. The temperature and relative humidity were kept at $T = 25$ °C and RH = 94%.

Figure 3a−c shows measurements of the apparent contact angle. As before, we observe two dynamical regimes, corresponding to an increase or a decrease in the base radius, which are characterized by maximum and minimum values of the apparent contact angle, respectively. These regimes are followed by a relaxation to static values. Figure 3d shows a superposition of the data for the three flow rates studied. In the plot, we use arbitrary units of time to match the volume increase/decrease windows while we leave the rest of the time data unaltered (i.e., time units in the relaxation portions of the plot are the same for all flow rates). Although the effect of the input and output rates is subtle, it is clear that, in all cases, the response of the apparent contact angle during a change in the droplet volume depends on the flow rate. In contrast, the relaxation at zero flow rate consistently leads to the same relaxation curves and limiting static values of the apparent contact angle regardless of the flow rate.

Effect of Relative Humidity. To understand the effect of relative humidity on the droplet's apparent contact angle, we carried out experiments at RH = 94, 50, and 30%, at a fixed flow rate, $\dot{q} = 10$ μL/min, and temperature, $T = 25$ °C. For each experiment, the relaxation window was kept at $\Delta t = 120$ s. Figure 4 shows the changes in the apparent contact angle (a−c) and base radius (d−f) for the three relative humidities considered. We report the change in base radius, $\Delta r = r - r_0$, to account for variations in the initial radius, r_0. During

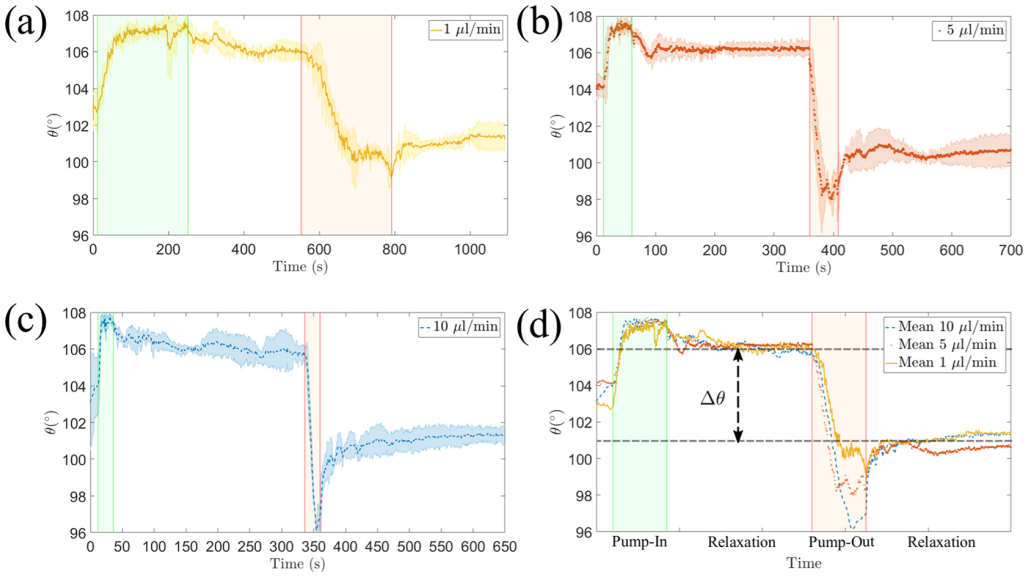

Figure 3. Effect of flow rate on the apparent contact angle. (a−c) Variation of the contact angle at different flow rates. (d) Overlap of the experimental data. The apparent contact angle relaxes to constant values, which are independent of the flow rate. The difference between these values is identified as the contact-angle hysteresis.

https://dx.doi.org/10.1021/acs.langmuir.0c02668
Langmuir 2020, 36, 15094−15101

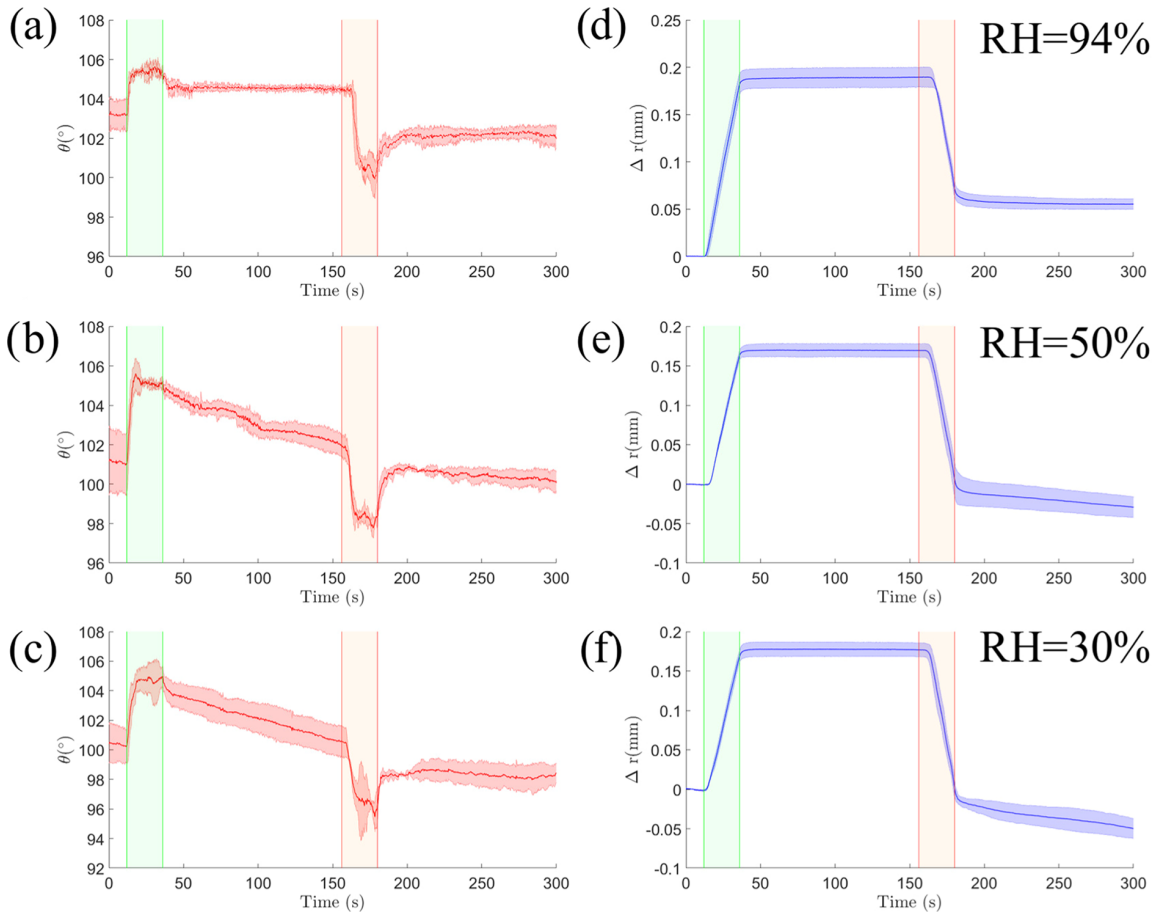

Figure 4. Influence of relative humidity on the apparent contact angle and the base radius. (a–c) Variation of the apparent contact angle at RH = 94, 50, and 30%, respectively. (d–f) Corresponding change in the droplet base radius.

the injection phase, the apparent contact angle reaches the same dynamic value regardless of the relative humidity $\theta = 105 \pm 1.1°$. However, during the subsequent relaxation, there is a significant change in the apparent contact angle at different relative humidities. Unlike the plateau behavior observed at RH = 94%, at RH = 50 and 30%, the apparent contact angle decreases with time at a rate that becomes stronger with decreasing relative humidity. During the same step, the base radius remains constant and independent of the relative humidity (see panels d–f in Figure 4). In the withdrawal phase, we observe an initial decrease of the apparent contact angle. Once the flow is switched off, the apparent contact angle relaxes to a plateau while the base radius decreases at a roughly constant rate. Both the plateau value of the apparent contact angle and rate of change of the base radius depend on the relative humidity.

DISCUSSION AND ANALYSIS

Contact-Angle Hysteresis Measurement and Uncertainty. We first discuss the uncertainty in the measurement of the advancing and receding contact angles on SOCAL surfaces and its effect on the determination of the contact-angle hysteresis.

Typically, θ_A and θ_R are identified as the apparent contact angles at the onset of motion of the contact line upon an increase or decrease of the volume of the droplet, respectively.[6,10,19−22] On SOCAL surfaces, however, the onset motion is difficult to identify with precision. This is because, as shown in the zoomed-in regions of Figure 2, the apparent contact angle and the base radius vary smoothly as the contact line starts to move. The typical range of transition of the base radius from the static value to a constant contact-line velocity is $\Delta r \approx 0.2$ mm. The corresponding range of change in the apparent angle is $\Delta\theta \approx 2°$, which is comparable to the overall change in θ during the volume change. As shown in Table 1, the uncertainty in the measurement of the advancing and receding contact angles is on the order of 1°. This leads to a contact-angle hysteresis $\Delta\theta = 2.5 \pm 1.7°$.

Shirtcliffe et al. proposed that the advancing and receding angles can only be measured in the limit of a vanishingly small flow rate.[23] In our experiments, this limit corresponds to the relaxation of the apparent contact angle after the flow rate is stopped. Indeed, as shown in Figure 3, such a relaxation leads to the same limiting static values of the apparent contact angle regardless of the flow rate. Table 1 shows measurements of θ_A and θ_R obtained after the contact-line relaxation for the same experimental conditions of the volume-change method. The results show a significant (3-fold) reduction of the standard deviation of the measurements, which leads to a more consistent contact-angle hysteresis measurement, $\Delta\theta = 2.1 \pm 0.4°$.

Note that, even though the average contact-angle hysteresis obtained from both methods is similar, the relative error for the volume-change method amounts to 68%. This is clearly important, as the corresponding error in the pinning force is proportional to the error in the contact-angle hysteresis (see eq 4). In contrast, the error in the measurement of $\Delta\theta$ obtained

https://dx.doi.org/10.1021/acs.langmuir.0c02668
Langmuir 2020, 36, 15094−15101

Table 1. Apparent Contact-Angle Measurements of Water Droplets on SOCAL Surfaces[a]

	volume-change method			contact-line relaxation method		
trial number	θ_A (deg)	θ_R (deg)	$\Delta\theta$ (deg)	θ_A (deg)	θ_R (deg)	$\Delta\theta$ (deg)
1	104.4	100.3	4.1	103.8	101.6	2.2
2	105.5	101.3	4.2	104.2	102.2	2.0
3	104.6	104.3	0.3	104.6	102.3	2.3
4	105.4	104	1.4	104.3	102.8	1.5
5	105.1	102.4	2.7	104.9	102.3	2.6
mean (deg)	105.0	102.4	2.5	104.4	102.2	2.1
s.d. (deg)	0.5	1.7	1.7	0.4	0.4	0.4

[a]Volume-change method: θ_A and θ_R are determined by estimating the onset of motion of the contact line at a constant flow rate $\dot{q}$ = 10 μL/min. Contact-line relaxation method: θ_A and θ_R are determined as the limiting apparent contact angles that the droplet exhibits after relaxation to a static shape. The temperature and relative humidity are T = 25 °C and RH = 94%.

from the contact-line relaxation is consistently smaller (19% for the data reported in Table 1) and confirms the low-pinning force exerted by the SOCAL surface on water droplets.

Contact Angles In and Out of Thermodynamic Equilibrium. We now discuss the effect of relative humidity on the contact-angle hysteresis. Figure 4a,d shows measurements of the apparent contact angle and droplet base radius upon a change in volume at a high relative humidity (RH = 94%), corresponding to conditions close to thermodynamic equilibrium. After either an advancing or a receding motion of the contact line, both the apparent angle and droplet base radius relax to well-defined constant values, with no appreciable subsequent variation over the time scale of the experiments.

Figure 4b,c,e,f shows the corresponding curves for a lower relative humidity (RH = 50 and 30%). After a volume increase, the apparent contact angle undergoes a sustained decrease over time (Figure 4b,c), while the base radius of the drop remains constant (Figure 4e,f). This indicates that the droplet is out of thermodynamic equilibrium and undergoing a constant contact-area mode of evaporation.[24] Indeed, the rate at which the apparent contact angle decreases is larger for smaller relative humidity. This is likely due to a higher mass loss due to evaporation. On the other hand, after a volume decrease, the apparent contact angle remains constant, while the base radius decreases. This is consistent with a constant contact-angle mode of evaporation.[24] The apparent contact angle, however, is not equal to the receding contact angle measured at high relative humidity. It decreases with lower relative humidity (see Table 2). This indicates that the contact line is out of both thermodynamic and mechanical equilibria and recedes from the solid surface at a rate controlled by evaporation.

Relaxation to Equilibrium. We now compare the prediction of the Cox–Voinov theory and the molecular kinetic theory (eqs 15 and 17) to the experimental measurements of the relaxation of the droplet close to thermodynamic equilibrium (RH = 94%). As shown in Figure 2, the apparent contact angle seems to follow an exponential variation toward the limiting static value. To obtain an experimental measurement of the relaxation time, τ, we fitted the measurements of the instantaneous base radius of the droplet to the function

$$\theta(t) = \theta_\infty + \Delta\theta \exp(-t/\tau) + \alpha t \quad (18)$$

Here, θ_∞ corresponds to the limiting value of the contact angle after relaxation, i.e., either the advancing or receding contact angle, and $\Delta\theta$ is the difference between the contact angle at the initial data point of the fit with θ_∞. The final term is introduced to account for the effect of evaporation, where α is a constant. A fit of the data to this equation yields values of α or the order of 1×10^{-3}°/s, which leads to a variation of the contact angle of at most 0.2° over the period of relaxation. The data fits give an average relaxation time τ = 8.3 ± 5.8 s.

To obtain a prediction of the relaxation time from the Cox–Voinov theory (eq 15), we use γ = 72 mN/m, η = 0.89 mPa s, L = 1.2 mm, and l_m = 4 nm, where the macroscopic length scale L is chosen as the typical size of the droplet, and the microscopic length scale l_m is chosen to be comparable to the polymer chain length reported for SOCAL.[4,10] This leads to τ_{CV} = 1. 131 × 10^{-4} s, which differs from the experimental measurement by several orders of magnitude. The free parameter in the Cox–Voinov model, which leads to the discrepancy, is the ratio L/l_m in eq 15. Keeping $L \approx 1$ mm and fitting the Cox–Voinov theory to the experimental data give $l_m \approx 0.1$ pm, which seems unrealistic.

To compare to the prediction of the molecular kinetic theory (eq 17), one needs knowledge of the frequency of the adsorption–desorption events, K_0, and of the intermolecular distance, ξ. Daniel et al.[5] studied the dissipative force exerted on water and sucrose droplets on SOCAL surfaces. By fitting their experimental data to the MKT model, they obtained K_0 = 7500 s^{-1} and ξ = 3 nm. Using these values in eq 17 yields τ_{MKT} = 0. 2324 s, which is a better prediction of the experimental measurement of the relaxation time.

We now discuss the difference between the prediction from the MKT model and the experimental measurement of the relaxation time. The molecular scale, ξ, is unlikely to differ significantly from the experiments reported in ref 5. On the other hand, the experiments of ref 5 do not report a specific value of relative humidity, but it is reasonable to assume that these were carried out at ambient conditions, i.e., RH < 94%. Our experiments were carried out at a high relative humidity (RH = 94%), where the liquid is close to equilibrium with the surrounding vapor phase. Hence, we expect that the frequency of adsorption–desorption events is smaller in our experiments. Indeed, treating K_0 as a single free parameter and fitting to the experimental measurement of the relaxation time yield a value K_0 = 204.5 s^{-1}. This suggests that at high relative humidity the contact line is slowed down by the rate of adsorption–desorption of molecules from the solid.

Figure 5 shows instantaneous measurements of the contact angle vs contact-line velocity averaged over five independent trials. The prediction of the Cox–Voinov theory and of the molecular kinetic theory is superimposed for comparison. For the Cox–Voinov, we use the parameter values γ = 72 mN/m, η = 0.89 mPa s, L = 1.2 mm, and l_m = 4 nm. For the advancing configuration, we use θ_m = 104.4° and for the receding configuration, we use θ_m = 102.2°. For MKT, we use the parameter values of K_0 = 204.5 s^{-1} and ξ = 3 nm, with θ_S =

Table 2. Effect of Relative Humidity on the Apparent Contact Angle after a Volume Decrease

relative humidity	94%	50%	30%
θ (deg)	102.1 ± 0.3	100.5 ± 0.3	98.4 ± 0.7

https://dx.doi.org/10.1021/acs.langmuir.0c02668
Langmuir 2020, 36, 15094−15101

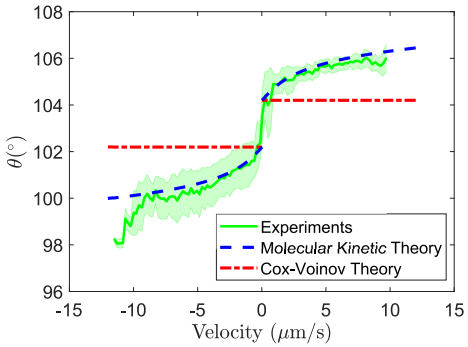

Figure 5. Instantaneous measurements of the contact angle vs contact-line velocity. The experimental data is averaged across five trials. The contact-angle hysteresis of the sample is $\Delta\theta = 2.1 \pm 0.4°$. The thick lines correspond to the predictions of the Cox–Voinov and molecular kinetic theories.

104.4° for the advancing configuration and $\theta_S = 102.2°$ for the receding configuration. The prediction of the MKT uses the parameter values fitted to match the relaxation time during the relaxation periods. The prediction of the molecular kinetic theory captures the experimental data to a better degree than that of the Cox–Voinov theory.

CONCLUSIONS

In this work, we have studied the static and dynamic friction imparted by SOCAL surfaces on water droplets. Our study of static friction has focused on determining the contact-angle hysteresis of droplets under controlled temperature and ambient humidity conditions. We have reported direct measurements of the advancing and receding contact angles in the limit of mechanical and thermodynamic equilibria by tracking the relaxation of a droplet's interface after a volume change. Such measurements are independent of the flow rate used to affect the volume change, leading to a significantly lower uncertainty in the measurement of the advancing and receding angles compared to the method of identifying the onset of contact-line motion.

Out of thermodynamic equilibrium, corresponding to an ambient relative humidity below the point of liquid–vapor phase coexistence, the droplet's interface does not relax to the advancing and receding angles. Instead, the droplet undergoes evaporation keeping a constant apparent contact angle, which is always lower than the receding contact angle measured close to thermal equilibrium.

In regard to dynamic friction, we have studied the time scale of relaxation of the droplet to a static configuration and compared the experimental measurement of the relaxation time to a hydrodynamic model and a model based on the molecular kinetic theory. Our results support that the dynamic friction imparted by SOCAL surfaces on droplets is dominated not by the hydrodynamic flow close to the droplet's edge, but by the motion of the contact line.

Our results highlight the remarkable wettability of SOCAL surfaces and can motivate further studies of the statics and dynamics of droplets on other coatings achieved by polymer grafting.[25]

AUTHOR INFORMATION

Corresponding Author

Rodrigo Ledesma-Aguilar − *Smart Materials and Surfaces Laboratory, Northumbria University, Newcastle upon Tyne NE1 8ST, United Kingdom; Institute for Multiscale Thermofluids, School of Engineering, University of Edinburgh, The King's Buildings, Edinburgh EH9 3FB, United Kingdom;* orcid.org/0000-0001-8714-0556; Email: rodrigo.ledesma@ed.ac.uk

Authors

Hernán Barrio-Zhang − *Smart Materials and Surfaces Laboratory, Northumbria University, Newcastle upon Tyne NE1 8ST, United Kingdom; Institute for Multiscale Thermofluids, School of Engineering, University of Edinburgh, The King's Buildings, Edinburgh EH9 3FB, United Kingdom*

Élfego Ruiz-Gutiérrez − *Smart Materials and Surfaces Laboratory, Northumbria University, Newcastle upon Tyne NE1 8ST, United Kingdom; Institute for Multiscale Thermofluids, School of Engineering, University of Edinburgh, The King's Buildings, Edinburgh EH9 3FB, United Kingdom;* orcid.org/0000-0003-3073-8957

Steven Armstrong − *Smart Materials and Surfaces Laboratory, Northumbria University, Newcastle upon Tyne NE1 8ST, United Kingdom; Institute for Multiscale Thermofluids, School of Engineering, University of Edinburgh, The King's Buildings, Edinburgh EH9 3FB, United Kingdom;* orcid.org/0000-0002-0520-8498

Glen McHale − *Smart Materials and Surfaces Laboratory, Northumbria University, Newcastle upon Tyne NE1 8ST, United Kingdom; Institute for Multiscale Thermofluids, School of Engineering, University of Edinburgh, The King's Buildings, Edinburgh EH9 3FB, United Kingdom;* orcid.org/0000-0002-8519-7986

Gary G. Wells − *Smart Materials and Surfaces Laboratory, Northumbria University, Newcastle upon Tyne NE1 8ST, United Kingdom; Institute for Multiscale Thermofluids, School of Engineering, University of Edinburgh, The King's Buildings, Edinburgh EH9 3FB, United Kingdom;* orcid.org/0000-0002-8448-537X

Complete contact information is available at: https://pubs.acs.org/10.1021/acs.langmuir.0c02668

Notes

The authors declare no competing financial interest.

ACKNOWLEDGMENTS

H.B.-Z. acknowledges financial support from Northumbria University and The University of Edinburgh via a Ph.D. Studentship. H.B.-Z. would like to thank P. Agrawal and B.V. Orme for their advice and valuable discussions. R.L.-A. acknowledges support from EPSRC (grant no. EP/P024408/1).

REFERENCES

(1) de Gans, B.-J.; Duineveld, P. C.; Schubert, U. S. Inkjet printing of polymers: State of the art and future developments. *Adv. Mater.* **2004**, *16*, 203–213.

(2) Introzzi, L.; Fuentes-Alventosa, J. M.; Cozzolino, C. A.; Trabattoni, S.; Tavazzi, S.; Bianchi, C. L.; Schiraldi, A.; Piergiovanni, L.; Farris, S. "Wetting enhancer" pullulan coating for antifog packaging applications. *ACS Appl. Mater. Interfaces* **2012**, *4*, 3692–3700.

https://dx.doi.org/10.1021/acs.langmuir.0c02668
Langmuir 2020, 36, 15094–15101

(3) Kim, P.; Wong, T. S.; Alvarenga, J.; Kreder, M. J.; Adorno-Martinez, W. E.; Aizenberg, J. Liquid-infused nanostructured surfaces with extreme anti-ice and anti-frost performance. *ACS Nano* **2012**, *6*, 6569−6577.
(4) Wang, L.; McCarthy, T. J. Covalently Attached Liquids: Instant Omniphobic Surfaces with Unprecedented Repellency,. *Angew. Chem., Int. Ed.* **2016**, *55*, 244−248.
(5) Daniel, D.; Timonen, J. V.; Li, R.; Velling, S. J.; Kreder, M. J.; Tetreault, A.; Aizenberg, J. Origins of Extreme Liquid Repellency on Structured, Flat, and Lubricated Hydrophobic Surfaces. *Phys. Rev. Lett.* **2018**, *120*, No. 244503.
(6) Armstrong, S.; McHale, G.; Ledesma-Aguilar, R.; Wells, G. G. Pinning-Free Evaporation of Sessile Droplets of Water from Solid Surfaces. *Langmuir* **2019**, *35*, 2989−2996.
(7) Wong, T. S.; Kang, S. H.; Tang, S. K.; Smythe, E. J.; Hatton, B. D.; Grinthal, A.; Aizenberg, J. Bioinspired self-repairing slippery surfaces with pressure-stable omniphobicity. *Nature* **2011**, *477*, 443−447.
(8) Smith, J. D.; Dhiman, R.; Anand, S.; Reza-Garduno, E.; Cohen, R. E.; McKinley, G. H.; Varanasi, K. K. Droplet mobility on lubricant-impregnated surfaces. *Soft Matter* **2013**, *9*, 1772−1780.
(9) Blake, T. D. The physics of moving wetting lines. *J. Colloid Interface Sci.* **2006**, *299*, 7.
(10) de Gennes, P.-G.; Brochard-Wyart, F.; Quéré, D. *Capillarity and Wetting Phenomena*, 1st ed.; Springer: New York, 2004.
(11) Bonn, D.; Eggers, J.; Indekeu, J.; Meunier, J.; et al. Wetting and spreading. *Rev. Mod. Phys.* **2009**, *81*, 739−805.
(12) Voinov, O. V. Hydrodynamics of wetting,. *Fluid Dynamics* **1977**, *11*, 714−721.
(13) Cox, R. G. The dynamics of the spreading of liquids on a solid surface. Part 2. Surfactants. *J. Fluid Mech.* **1986**, *168*, 195−220.
(14) Blake, T. D.; Haynes, J. M. Kinetics of liquid liquid displacement. *J. Colloid Interface Sci.* **1969**, *30*, 421−423.
(15) de Ruijter, M. J.; De Coninck, J.; Blake, T. D.; Clarke, A.; Rankin, A. Contact angle relaxation during the spreading of partially wetting drops. *Langmuir* **1997**, *13*, 7293−7298.
(16) Launay, G. *PyDSA Droplet Shape Analysis in Python*, 2018.
(17) Vuckovac, M.; Latikka, M.; Liu, K.; Huhtamäki, T.; Ras, R. H. A. Uncertainties in contact angle goniometry. *Soft Matter* **2019**, *15*, 7089−7096.
(18) Liu, K.; Vuckovac, M.; Latikka, M.; Huhtamäki, T.; Ras, R. H. Improving Surface-Wetting Characterization. *Science* **2019**, *3*, 1147−1148.
(19) Lam, C.; Wu, R.; Li, D.; Hair, M.; Neumann, A. Study of the advancing and receding contact angles: liquid sorption as a cause of contact angle hysteresis. *Adv. Colloid Interface Sci.* **2002**, *96*, 169−191.
(20) McHale, G.; Shirtcliffe, N. J.; Newton, M. I. Contact-angle hysteresis on super-hydrophobic surfaces,. *Langmuir* **2004**, *20*, 10146−10149.
(21) Gao, L.; McCarthy, T. J. Contact Angle Hysteresis Explained. *Langmuir* **2006**, *22*, 6234−6237.
(22) Eral, H. B.; 't Mannetje, D. J. C. M.; Oh, J. M. Contact angle hysteresis: a review of fundamentals and applications. *Colloid Polym. Sci.* **2013**, *291*, 247−260.
(23) Shirtcliffe, N. J.; McHale, G.; Atherton, S.; Newton, M. I. An introduction to superhydrophobicity. *Adv. Colloid Interface Sci.* **2010**, *161*, 124−138.
(24) Cazabat, A. M.; Guéna, G. Evaporation of macroscopic sessile droplets. *Soft Matter* **2010**, *6*, 2591−2612.
(25) Teisala, H.; Baumli, P.; Weber, S. A.; Vollmer, D.; Butt, H. J. Grafting Silicone at Room Temperature-a Transparent, Scratch-resistant Nonstick Molecular Coating. *Langmuir: ACS J. Surfaces and Colloids* **2020**, *36*, 4416−4431.

https://dx.doi.org/10.1021/acs.langmuir.0c02668
Langmuir 2020, 36, 15094−15101